

Copyright

by

Yuan Li

2006

**The Dissertation Committee for Yuan Li Certifies that this is the approved version
of the following dissertation:**

Self-Assembly of Block Copolymer Thin Films in Compressible Fluids

Committee:

Keith P. Johnston, Supervisor

Peter F. Green, Co-Supervisor

Arumugam Manthiram

Donald R. Paul

Venkat Ganesan

Self-Assembly of Block Copolymer Thin Films in Compressible Fluids

by

Yuan Li, B. S.; M. S. E.

Dissertation

Presented to the Faculty of the Graduate School of

The University of Texas at Austin

in Partial Fulfillment

of the Requirements

for the Degree of

Doctor of Philosophy

The University of Texas at Austin

December 2006

Dedication

To my husband Di,

And my parents,

For their endless love, support and encouragement

Acknowledgements

I owe a debt of gratitude to many people who have helped me in this journey of pursuing a doctoral degree. First of all, I have been privileged to have the guidance under two excellent advisors, Professor Peter F. Green and Professor Keith P. Johnston. I am grateful for this opportunity to work in their groups and to be inspired by them to love research. I thank them for their invaluable insights, directions and patience during the course of my graduate studies. Their trust and faith in me motivates me to give my best; their passion for research will exert a lasting impact in my life.

I also want to express my sincere thanks to many people whom I have collaborated with on various projects that contribute to this dissertation. I thank Prof. Isaac C. Sanchez and Xiaochu Wang for helping me with the SLEOS calculation of CO₂-polymer systems. I thank Prof. Lim from Pukyong National University for synthesizing various fluorinated polymers for me. Many thanks are also due to numerous past and present members of both Green and Johnston research groups, and in particular, to Dr. Joseph Pham, Luciana Meli, Dr. Brian Besancon, Jamie Kropka, Abraham Arceo, Dr. Jasper Dickson, John Keagy, Gaurav Gupta and Xi Chen. I also want to thank following professors, Prof. Donald R. Paul, Prof. Arumugam Manthiram and Prof. Venkat Ganesan for graciously serving as members of my dissertation committee.

I wouldn't be where I am today without the experience that I had as an undergraduate in Peking University, China. It is a place that I dreamed of going to as a little kid, that taught me invaluable lessons about both life and science, and that really opened my eyes for this world. I am also deeply indebted to The University of Texas at Austin for this challenging and forever memorable experience. I want to thank all the friends I made during my studies at both universities: my life wouldn't be so joyful without them.

I owe much to my parents for always believing in me and encouraging me to achieve my goals. As their only child, I only spent about ten days with them in the past five years. I regret for not being able to ease their trouble and to take good care of them when they needed me. Therefore, I want to sincerely thank them for their unconditional support and encouragement to pursue my interests, even when the interests go beyond the boundaries of language and geography. All I want to do in my life is to make them proud and I hope that I have achieved so by finishing this dissertation. My heartfelt appreciation also goes to my parents-in-law, who always love and support me as if I were their own daughter and I cannot possibly ask for more from them.

Finally, I want to especially thank my husband, Di Xiao, whose company and emotional support have been invaluable in this journey. I am so grateful to having found such a brilliant, talented and caring person as not only my best friend, but also my love in life. His enthusiasm and generosity have always been an inspiration for me. His love, encouragement and trust are the true source of this dissertation.

Self-Assembly of Block Copolymer Thin Films in Compressible Fluids

Publication No. _____

Yuan Li, Ph.D.

The University of Texas at Austin, 2006

Supervisors: Keith P. Johnston and Peter F. Green

In recent years, rapid progress has been reported toward exploiting self-assembly in block copolymer thin films to create periodically ordered nano-patterned substrates for potential applications, including nanolithography and “bottom up” microelectronic device fabrication. Compressible fluids, such as supercritical carbon dioxide (CO₂), have been widely used in many polymer related processes. Unlike conventional liquid solvents, the density and hence the “solvent strength” of supercritical CO₂, can be tuned by small variations in pressure, temperature or both. This tunability, along with the low interfacial tension and high diffusion coefficient makes supercritical CO₂ a strategic solvent to pattern block copolymer templates. This dissertation demonstrates how to effectively modify interfacial interactions and hence to control the self-assembly of asymmetric block copolymer thin films exposed to compressible fluids.

We firstly investigated how interfacial forces determine the morphology of supported asymmetric polyethylene-*b*-poly(styrene-*r*-ethylene-*r*-butene) (E-*b*-SEB)

diblock films under vacuum condition. It was shown that the relative strengths of intermolecular forces associated with crystallization, with block copolymer ordering and with long-range van der Waals forces influence the structure of the films. These interactions depend on temperature and on film thickness. In the second series of studies, supercritical CO₂ was used as a selective solvent to modify interfacial interactions and to control the morphological structures of asymmetric block copolymer films. Specifically, supercritical CO₂ annealing was found to (1) promote microphase segregation into spherical domains for poly(ethylene oxide)-b-poly(1,1'-dihydroperfluorooctyl methacrylate) (PEO-b-PFOMA) thin films; (2) invert core-shell structure of the surface micelles formed by polystyrene-b-poly(1,1',2,2'-tetrahydroperfluorooctyl methacrylate) (PS-b-PFOMA) thin films. Finally, studies involving the swelling of polymer films and the wetting characteristics of liquids on polymer films under CO₂ environments were performed in order to gain further insights into the thermodynamics of polymer-CO₂ interfaces.

Table of Contents

List of Tables	xiii
List of Figures	xvi
Chapter 1: Introduction	1
1.1 Motivation and Research Objectives	1
1.2 Self-Assembly Behavior of Block Copolymer Thin Films.....	3
1.2.1 Block Copolymers in Bulk	3
1.2.2 Ordered Block Copolymer Thin Films: Interfacial Effects	4
1.3 Self-Assembly Behavior of Block Copolymer Thin Films in CO ₂	8
1.3.1 Effects of CO ₂ Dilation on the Phase Behavior of Block Copolymers in Bulk.....	8
1.3.2 Block Copolymer Thin Films in CO ₂ : Phase Behavior	13
1.3.3 Micellization in Block Copolymer Thin Films	14
1.4 Polymer Thin Films in CO ₂ : Polymer-CO ₂ Interactions.....	15
1.5 Dissertation Outline	17
1.6 References.....	19
Chapter 2: Influence of Interfacial Constraints on the Morphology of Asymmetric Crystalline-Amorphous Diblock Copolymer Films.....	26
2.1 Introduction.....	27
2.2 Experimental Section	29
2.3 Results and Discussion	31
2.3.1 Films in the Temperature Range $T_m < T < T_{ODT}$	32
2.3.1a Films with Thickness $h > 12$ nm ($h > L_0$)	32
2.3.1b Films with Thickness below 12 nm ($h < L_0$)	37
2.3.2 Effect of Crystallization on the Structure	41
2.3.2a Morphology of Films Annealed in the Temperature Range T_g $< T < T_m$	42
2.3.2b Morphology of Films Annealed in Temperature Range $T_m <$ $T_1 < T_{ODT}$ and Subsequently in the Range $T_g < T_2 < T_m$...	44
2.4 Concluding Remarks.....	49

2.5 References.....	50
Chapter 3: Ordering in Asymmetric Block Copolymer Films by a Compressible Fluid	53
3.1 Introduction.....	54
3.2 Experimental Sections	56
3.2.1 Materials and Thin Film Preparation	56
3.2.2 Supercritical CO ₂ Annealing.....	58
3.2.3 <i>In-situ</i> Swelling Experiments.....	58
3.3 Results.....	59
3.3.1 The Absence of Order in Vacuum vs. an Order-Disorder Transition in Sc-CO ₂ at the Same Temperature Range	59
3.3.2 The Periodic Spacing of Ordered PEO-b-PFOMA Films in Sc-CO ₂	64
3.3.3 Sanchez-Lacombe Equation of State (SLEOS) Fitting of Swelling Isotherms for PFOMA and PEO in CO ₂	68
3.4 Discussion	76
3.5 Conclusions.....	81
3.6 References.....	82
Chapter 4: Structural Inversion of Micellar Block Copolymer Thin Films.....	86
4.1 Introduction.....	87
4.2 Experimental Sections	88
4.2.1 Synthesis of Materials.....	88
4.2.1a Preparation of PSt-Br Macroinitiator	88
4.2.1b Synthesis of PSt-b-PFOMA Block Copolymer	89
4.2.2 Thin Film Preparation and Characterization.....	91
4.2.3 Supercritical CO ₂ Annealing.....	91
4.2.4 Morphological Analysis Using Scanning Force Microscopy (SFM) and Scanning Transmission Electron Microscopy (STEM)	92
4.2.5 X-Ray Photoelectron Spectroscopy (XPS)	93
4.2.6 <i>In-Situ</i> Swelling Experiments	96
4.3 Results and Discussion	96

4.3.1 Self-Assembly of PS-b-PFOMA Diblock into Micelle-like Aggregates in Thin Films after Spin-Casting	96
4.3.2 Effects of Supercritical CO ₂ Annealing on the Morphologies of PS-b-PFOMA Thin Films.....	101
4.3.2a Inversion of the Core-Shell Composition of PS-b-PFOMA Aggregates in Sc-CO ₂	101
4.3.2b Shape of the PS-b-PFOMA Micellar Aggregates	105
4.3.3 Effects of Supercritical CO ₂ Annealing Temperature on the Core Sizes of PS-b-PFOMA Aggregates.....	108
4.4 Conclusions.....	120
4.5 References.....	121
Chapter 5: Role of Interfacial Interactions on the Anomalous Swelling of Polymer Thin Films in Supercritical Carbon Dioxide.....	126
5.1 Introduction.....	127
5.2 Experimental Sections	129
5.2.1 Materials	129
5.2.2 <i>In-situ</i> Swelling Experiments.....	130
5.2.3 Ellipsometry Fitting	132
5.3 Results.....	132
5.4 Discussion: Interfacial Effects on the Anomalous Swelling of Polymer Thin Films.	148
5.5 Conclusions.....	156
5.6 References.....	159
Chapter 6: Contact Angle of Water on Polystyrene Thin Films: Effects of CO ₂ Environment and Film Thickness	163
6.1 Introduction.....	164
6.2 Experimental Sections	166
6.2.1 Thin Film Preparation	166
6.2.2 High-Pressure Contact-Angle Measurements.....	166
6.3 Results and Discussion	167
6.3.1 Effects of CO ₂ Pressure on the Contact Angle: Experimental Results and the Macroscopic Model.....	167
6.3.2 Contact-Angle Hysteresis in CO ₂	176

6.3.3 Effects of Film Thickness on the Contact Angle: Experimental Results and the Microscopic Model.....	180
6.3.3a The Microscopic Model in Air.....	183
6.3.3b The Microscopic Model in CO ₂	189
6.4 Conclusions.....	194
6.5 References.....	195
Chapter 7: Conclusions and Recommendations for Future Work	199
7.1 Conclusions.....	199
7.1.1 Crystalline-Amorphous Block Copolymer Thin Films.....	199
7.1.2 Self-Assembly of Asymmetric Block copolymer Thin Films in CO ₂	200
7.1.3 Swelling and Wetting Properties of Polymer Films in CO ₂	201
7.2 Recommendations for Future Work.....	202
7.2.1 Nanopatterning Using Block Copolymer Films in CO ₂	202
7.2.2 Interfacial Phenomena of Polymer Films in CO ₂	203
7.3 References.....	204
Appendix A: Tabular Data for the Swelling Experiments in Chapter 5	206
Appendix B: Supporting Information for Chapter 6.....	219
B.1 Swelling Data	219
B.2 Contact Angle Data in Tabulate Form	220
B.3 Comparison between Calculated PS-CO ₂ Interfacial Tension in this Work and Reference.....	222
B.4 Extending the Microscopic Model to Sc-CO ₂ Environment.....	223
Bibliography	226
Vita	239

List of Tables

Table 2.1: Characteristics of the Crystalline-Amorphous Diblock Copolymer E-b-SEB	30
Table 3.1: Characteristic Properties of PEO and PFOMA in the Diblock.....	57
Table 3.2: Measured layer heights for PEO-b-PFOMA Films after Sc-CO ₂ Annealing..	67
Table 3.3: Sanchez-Lacombe Pure Component Characteristic Parameters.....	72
Table 3.4: Estimated Cohesive Energy Density (CED) from the Parameters in Table 3.3	72
Table 3.5: SLEOS Fitting Results for PFOMA and PEO in Sc-CO ₂	72
Table 4.1: Characteristic Properties of PS and PFOMA in the Copolymer.....	90
Table 4.2: Atomic Ratio between Fluorine and Carbon from XPS Data for As-Cast Films	99
Table 4.3: Atomic Ratio between Fluorine and Carbon from XPS Data for PS-b-PFOMA Films after Sc-CO ₂ Annealing at 35 °C and 13.8 MPa	104
Table 4.4: The Swelling % of PS and PFOMA in CO ₂ under Four Conditions	113
Table 4.5: Estimation of the Interfacial Tension between PS (27k) and CO ₂	118
Table 4.6: Effects of CO ₂ Annealing Temperature on the Sizes of Micelles Cores	118
Table 5.1: Molecular Weights and Sources of Polymers.....	131
Table 5.2: Analysis of Anomalous Swelling Maximum for Polymer Films at 35 °C	139
Table 5.3: Summary of the Initial and Swollen Film Thicknesses at the Anomalous Maximum for Various Polymer Films in CO ₂ , 35 °C.....	151

Table 5.4: Summary of the Fitting Results Obtained from Figure 5.6	153
Table 6.1: The Polar and Dispersion Components of Surface Tension for Water, PS and CO ₂	173
Table 6.2: The Hamaker Constants of Pure Substances	186
Table 6.3: The Fitted Hamaker Constants for PS films as a Function of Film Thickness	186
Table A.1a: Swelling data for a PFOMA film with $h_0 = 109$ nm during pressurization at 35 °C in CO ₂	206
Table A.1b: Swelling data for a PFOMA film with $h_0 = 109$ nm during depressurization at 35 °C in CO ₂ (continued from Table A.1a).....	207
Table A.2: Swelling data for a PS-b-PFOMA film with $h_0 = 100$ nm at 35 °C in CO ₂ ..	208
Table A.3: Swelling data for a PS film with $h_0 = 128$ nm at 35 °C in CO ₂	209
Table A.4: Swelling data for a PEO film with $h_0 = 104$ nm at 35 °C in CO ₂	210
Table A.5: Swelling data for a PFOMA film with $h_0 = 153$ nm at 35 °C in CO ₂	211
Table A.6: Swelling data for a PFOMA film with $h_0 = 179$ nm at 35 °C in CO ₂	212
Table A.7: Swelling data for a PFOMA film with $h_0 = 282$ nm at 35 °C in CO ₂	213
Table A.8: Swelling data for a PFOMA film with $h_0 = 115$ nm at 50 °C in CO ₂	214
Table A.9: Swelling data for a PFOMA film with $h_0 = 150$ nm at 50 °C in CO ₂	215
Table A.10: Swelling data for a PFOMA film with $h_0 = 198$ nm at 50 °C in CO ₂	216
Table A.11: Swelling data for a PS-b-PFOMA film with $h_0 = 100$ nm at 50 °C in CO ₂	217

Table A.12: Swelling data for a PS film with $h_0 = 131$ nm at 50 °C in CO_2	218
Table B.1: Effects of CO_2 Pressure on the Contact Angle of Water on PS films with Various Thicknesses at 23 °C (typical error bar $\pm 2^\circ$)	220
Table B.2: Contact Angles of Water on an $h = 120$ nm PS Film at 23 °C during Pressurization and Depressurization	221
Table B.3: Calculation of the Hamaker Constants of PS- CO_2 Mixture ($h = 120$ nm)....	223
Table B.4: Calculation of the Van der Waals Contribution in the Spreading Coefficient, $S_{\text{CO}_2}^{\text{vdw}}$	224
Table B.5: Calculation of the Polar Contribution in the Spreading Coefficient, $S_{\text{CO}_2}^{\text{P}}$..	225
Table B.6: Calculation of the Contact Angles from the Microscopic Model in CO_2	225

List of Figures

FIGURE 1.1: (a) Schematic drawing of an A-b-B diblock copolymer. (b) The mean-field theory calculated phase diagram of a typical diblock copolymer. Phase diagram is reproduced from The Physics of Block Copolymers. ⁶²	5
FIGURE 1.2: The structures of phase segregated block copolymer thin films: lamellae aligned parallel (a) and perpendicular (b) to the interfaces; cylinders aligned parallel (c) and perpendicular (d) to the interfaces; spheres (e). All pictures are taken from Segalman. ¹⁵	6
FIGURE 1.3: (a, b) Schematics of ordered films on a solid surface with the parallel stacking of lamellae for the symmetric (a) and asymmetric (b) wetting conditions. (c, d) Representative topographies of ordered PS-b-PMMA block copolymer thin films ($f = 0.5$) that form islands (c) or holes (d) structures. The scanning force microscopy (SFM) images (c and d) are taken from Limary. ⁷⁰	9
FIGURE 1.4: Schematic diagram of the lamellar ordering induced by a solid surface and the undulation which develops to match onto the hexagonal phase at the hexagonal-lamellar interface. The view is a slice through the y-z plane with symmetry in the x-direction. The dotted lines represent the position of the interfaces between the blocks of the copolymers. This figure is originally taken from the work of Turner et al. ⁷¹ and has been slightly modified.	10
FIGURE 1.5: Schematic diagrams illustrating the effects of CO ₂ sorption on the T vs. ϕ phase diagram of block copolymers. Solid curves show the phase diagram under air/vacuum condition whereas dashed curves show the phase diagram under CO ₂ condition. (a) CO ₂ lowers the upper order-disorder transition (UODT) temperature and favors phase mixing. (b) CO ₂ reduces the lower disorder-order transition (LDOT) temperature and induces phase segregation.	12

FIGURE 2.1: Topographical structure formed by annealing an E-b-SEB film with $h = 14$ nm at $170\text{ }^{\circ}\text{C}$ for 24 h. The leftmost point shows the position of a scratch and is used as a reference point to measure the height of each layer.	33
FIGURE 2.2: Topographies of samples with varying thickness after annealing at $170\text{ }^{\circ}\text{C}$. (a) $h = 30$ nm, (b) $h = 28$ nm, (c) $h = 25$ nm, (d) $h = 22$ nm, (e) $h = 19$ nm, (f) $h = 17$ nm, (g) $h = 14$ nm. The edge of each sample contains a scratch made to bare the substrate. All images sizes are $20\text{ }\mu\text{m}$	34
FIGURE 2.3: Topographical structure formed by annealing an E-b-SEB sample of $h = 178$ nm at $180\text{ }^{\circ}\text{C}$ for 25 h. The black line in the 3-D image shows the location of the line scan.	35
FIGURE 2.4: (a) Schematic of the case where a lamellar structure is formed at the surface. (b) Schematic of the case where a spherical layer is formed next to the substrate.	39
FIGURE 2.5: Topographical structure of a sample with $h = 8$ nm ($< L_0$), annealed at $170\text{ }^{\circ}\text{C}$	40
FIGURE 2.6: SFM images of (a) an $h = 8.5$ nm E/SEB film crystallized at $77\text{ }^{\circ}\text{C}$ for 5 h and (b) an $h = 11$ nm E/SEB film crystallized at $77\text{ }^{\circ}\text{C}$ for 5 h.	45
FIGURE 2.7: Optical microscopy (a), scanning force topographies (b), and line scans (c) of a film of thickness $h = 33$ nm annealed (crystallized) at $77\text{ }^{\circ}\text{C}$ for 23 h. The parameters identified in the diagram are $h_1 = 11.2 \pm 1.5$ nm ($\sim L_0$), $h_2 = 33.7 \pm 2.4$ nm ($\sim L + L_0$) and $h_3 = 61.0 \pm 3.0$ nm. The scale bar in (a) is $70\text{ }\mu\text{m}$	46
FIGURE 2.8: Optical microscopy (right) and SFM images (left) of samples crystallized at $76\text{-}77\text{ }^{\circ}\text{C}$: (a) an $h = 94$ nm film crystallized at $75\text{ }^{\circ}\text{C}$ for 3 h; (b) an $h = 67$ nm film crystallized at $75\text{ }^{\circ}\text{C}$ for 3 h. The scale bars in both optical microscopy images are $70\text{ }\mu\text{m}$	47

FIGURE 2.9: SFM images of (a) an $h = 41$ nm E-b-SEB film annealed at $170\text{ }^{\circ}\text{C}$ for 24 h and (b) an $h = 41$ nm E-b-SEB film annealed at $170\text{ }^{\circ}\text{C}$ for 3 h and then crystallized at $75\text{ }^{\circ}\text{C}$ for 3 h. 48

FIGURE 3.1: SFM images of PEO-b-PFOMA films with (a, b) $h = 67$ nm after annealing in vacuum ovens at $170\text{ }^{\circ}\text{C}$ for 240 hours; (c, d) $h = 57$ nm after annealing at CO_2 , $145\text{ }^{\circ}\text{C}$, 13.9 MPa for 48 hours; (e, f) $h = 55$ nm after annealing at CO_2 , $75\text{ }^{\circ}\text{C}$, 13.9 MPa for 76 hours. Left column shows $20\text{ }\mu\text{m}$ height images from contact mode SFM, whereas right column shows $1.5\text{--}2\text{ }\mu\text{m}$ phase images from tapping mode SFM. 61

FIGURE 3.2: A representative small angle X-ray scattering (SAXS) spectrum of bulk PEO-b-PFOMA at $135\text{ }^{\circ}\text{C}$ 63

FIGURE 3.3: SFM images and the corresponding line scans for PEO-b-PFOMA films annealed in Sc- CO_2 : (a) an $h = 46$ nm film after annealing at CO_2 , $145\text{ }^{\circ}\text{C}$, 13.9 MPa for 48 hours; (b) an $h = 57$ nm film after annealing at CO_2 , $116\text{ }^{\circ}\text{C}$, 13.9 MPa for 48 hours; (c) an $h = 47$ nm film after annealing at CO_2 , $60\text{ }^{\circ}\text{C}$, 13.9 MPa for 30 hours. Notice that except (a), both (b) and (c) show formation of terrace near the scratch. (d) Schematic drawing of the layered structure in phase segregated PEO-b-PFOMA films. 66

FIGURE 3.4: SFM topography of PEO-b-PFOMA films with thicknesses (a) $h = 63$ nm and (b) $h = 55$ nm after annealing at CO_2 , $75\text{ }^{\circ}\text{C}$, 13.9 MPa for 76 hours. Notice that the flower-like patterns in both images (marked by the circles) are the results of PEO chains crystallization when subsequently quenching to ambient condition from Sc- CO_2 annealing. 67

FIGURE 3.5: (a) Experimentally measured % swelling as the function of CO_2 activity for PFOMA films ($h \sim 110$ nm). 73

FIGURE 3.5: (b) SLEOS fitting of the experimental and extrapolated swelling isotherms for PFOMA films in Sc- CO_2 74

FIGURE 3.5: (c) SLEOS fitting of the mass fraction of CO ₂ in PEO based on the work by Weidner et al. ⁴⁸	75
FIGURE 3.6: Calculated interaction parameters, $\chi_{\text{PFOMA-CO}_2}$ and $\chi_{\text{PEO-CO}_2}$, vs. temperature (1/T).	79
FIGURE 3.7: (a) Schematic phase diagrams for a typical diblock copolymer to show the effects of both neutral and selective solvents. (b) Schematic phase diagrams for PEO-b-PFOMA diblock copolymer ($T_1 < T_2$). Squares represent the case in vacuum while dots represent the case in CO ₂ . At lower temperature T_1 (such as 116 °C), the diblock is disordered in vacuum and ordered in CO ₂ , 13.9 MPa; while at higher temperature T_2 (such as 145 °C), the diblock is disordered in both vacuum and CO ₂ , 13.9 MPa.....	80
FIGURE 4.1: SFM topography (a) and the corresponding line scan (b) of a PS-b-PFOMA film ($h = 90$ nm) after spin-casting from solution onto Si/SiO _x substrate. The scan sizes are 5 μm in (a) and 2 μm in (b). The colored triangles in the topography (b) are corresponding to those in the line scan. This particular circular feature has a diameter of 101.56 nm (between leftmost and rightmost triangles) and a height of 7.3 nm (between leftmost and middle triangles).	94
FIGURE 4.2: HAADF-STEM images of RuO ₄ stained PS-b-PFOMA films after spin casting: (a) a 72 nm film presenting two layers of micellar aggregates; (b) an even thicker film with more layers of micellar aggregates. The scale bars in both images are 100 nm.	95
FIGURE 4.3: (a) SFM topography of a PS-b-PFOMA film ($h = 88$ nm) after annealing at Sc-CO ₂ , 75 °C, 13.8 MPa for 3 days. (b) HAADF-STEM image of a RuO ₄ stained PS-b-PFOMA thin film sample supported on SiN grid after annealing at Sc-CO ₂ , 75 °C, 13.8 MPa for 3 days. The scale bar represents 200 nm.	102

FIGURE 4.4: (a) (b) HAADF-STEM images of a PS-b-PFOMA thin film sample supported on SiN grid after annealing at Sc-CO₂, 75 °C, 13.8 MPa for 3 days. (c) The size distribution of PS cores in (a). 103

FIGURE 4.5: Schematic representations of the PS-b-PFOMA surface aggregates after spin-casting from the solution onto Si/SiO_x substrate (a) and annealing under Sc-CO₂ (b). Light blue chains are PFOMA; red chains are PS. Note in (a) an ultrathin layer of PFOMA segregated layer (with the fluorinated side groups aligned towards the outer face) is drawn on free surface. On the substrate interface, a layer of highly deformed PFOMA cored hemimicelles is drawn due to the strong interaction between the carbonyl group and SiO₂. 106

FIGURE 4.6: HAADF-STEM images of PS-b-PFOMA samples (h ~ 150-200 nm) after annealing under various Sc-CO₂ conditions. The annealing conditions are as the following: (a) 35 °C, 6 days; (b) 50 °C, 3 days; (c) 75 °C, 3 days; (d) 140 °C, 25 h; the CO₂ pressure was fixed at 13.8 MPa (2000 psig) for all temperatures. (e) The sizes of PS cores measured from (a-d) as increasing CO₂ annealing temperature. Typical error bars for the diameter of PS cores are 11-13 nm and those for the center-to-center distance of the PS cores are 12-15 nm. 110

FIGURE 4.7: (a) Swelling isotherm for PS and PDHFOMA (for simplicity, indicated by PFOMA on the plot legends) films in Sc-CO₂. 111

FIGURE 4.7: (b) Swelling vs. CO₂ activity for PS and PDHFOMA films. 112

FIGURE 4.8: The diameters of PS cores after Sc-CO₂ annealing measured from STEM images vs. $\gamma/\ln(\xi)$, where γ is the interfacial tension between PS and CO₂, and $\xi = H/R$ is the relative stretching between corona and core chains. The broken line has a slope of 2/5. The solid line, a fit to the data, has a slope of 0.31..... 119

FIGURE 5.1: Representative swelling isotherm and the change in average refractive indices at 35 °C for an h₀ = 109 nm PFOMA film. Filled symbols (■, ▲) represent %

swelling and open symbols (\square , Δ) represent the change in average refractive indices. Squares (\blacksquare , \square) represent data obtained during the pressurization run and triangles (\blacktriangle , \triangle) represent data obtained during the depressurization run..... 135

FIGURE 5.2: (a) Swelling isotherms for PFOMA films with various thicknesses at 35 °C. 136

FIGURE 5.2: (b) Swelling isotherms at 35 °C for various polymer films with thickness around 100 nm. The solid line in each isotherm represents the interpolated baseline, which is used to estimate the excess % swelling at the anomalous peak. 137

FIGURE 5.2: (c) Swelling isotherms of PS and PEO films with magnified normal axis.138

FIGURE 5.3: Swelling isotherms for PFOMA films with various thicknesses at 50 °C. 143

FIGURE 5.4: (a) Swelling of PFOMA films with various thicknesses at both 35 °C and 50 °C plotted against CO₂ activity. 144

FIGURE 5.4: (b) Swelling of PS-b-PFOMA films plotted against CO₂ activity..... 145

FIGURE 5.4: (c) Swelling of PS films plotted against CO₂ activity. 146

FIGURE 5.5: Comparison between our PS swelling isotherms at 35 °C (a) and 50 °C (b) with two reference works.^{44, 53} 147

FIGURE 5.6: Film thicknesses for the swollen films at the anomalous maximum (7.9-8.0 MPa) vs. the initial film thicknesses for a variety of polymer films at 35 °C. Linear lines are the fit from the experimental data. 152

FIGURE 5.7: Film thicknesses for the swollen films vs. the initial film thicknesses at pressure points other than the anomalous maximum for PFOMA films at 35 °C. Linear lines are the fit from the experimental data. 157

FIGURE 5.8: The swelling coefficients for the middle layer, α_m , vs. CO ₂ pressure for PFOMA films at 35 °C.....	158
FIGURE 6.1: Schematic of the water contact angle measurements in (a) air/water/PS/SiO _x /Si and (b) CO ₂ /water/PS/SiO _x /Si systems.	168
FIGURE 6.2: Photographs of the water contact angle for an h = 120 nm PS film at 23 °C: (a) in air; (b) 41 bar, vapor CO ₂ ; (c) 59 bar, vapor CO ₂ ; (d) 138 bar, liquid CO ₂	169
FIGURE 6.3: Effects of CO ₂ pressure on the contact angle of water on an h = 120 nm PS film at 23 °C.	170
FIGURE 6.4: Comparison between experimentally measured contact angles of water on an h = 120 PS film in CO ₂ at 23 °C and the predicted values by a macroscopic model. The filled triangles (▲) are experimental data; the empty squares (□) are predicted on the basis of water-CO ₂ interfacial tension from ref 16; the empty circles (○) are predicted using water-CO ₂ interfacial tension from ref 48.	172
FIGURE 6.5: Estimated interfacial tension between PS and CO ₂ , γ_{PS-CO_2} from geometric-mean combining rule at 23 °C and experimental measured interfacial tension between water and CO ₂ , $\gamma_{water-CO_2}$ at 23 °C by Dickson et al. ¹⁶ Dashed line shows the interfacial tension between PS and water, $\gamma_{PS-water}$, which is assumed to be fixed at a certain temperature.	178
FIGURE 6.6: Contact angle of water on an h = 120 nm PS film at 23 °C during both pressurization and depressurization.	179
FIGURE 6.7: Effect of film thicknesses on the contact angle of water on PS films at 23 °C. Typical error bars for contact angle (not shown for figure clarity) are $\pm 2^\circ$	181
FIGURE 6.8: The contact angle of water and the calculated surface energy for PS films with different thicknesses in air at 23 °C.	182

FIGURE 6.9: Calculated contact angle of water on PS films as a function of PS film thickness from the microscopic model at 23 °C.....	187
FIGURE 6.10: Comparison between experimentally measured and fitted refractive index of PS films vs. film thickness at 23 °C.....	188
FIGURE 6.11: Comparison between the microscopic model prediction and the experimentally measured water contact angle of an $h = 120$ nm PS film in CO_2 at 23 °C.	192
FIGURE 6.12: Comparison between the microscopic model prediction and the experimentally measured water contact angle of PS films with different thicknesses in CO_2 at 23 °C.	193
FIGURE B.1: The measured swelling % of a PS film with $h = 172$ nm in CO_2 at 25 °C.	219
FIGURE B.2: Comparison between prediction from the geometric-mean model for PS- CO_2 interfacial tension and the work by Li et al.(Li, Y.; Meli, L.; Lim, K. T.; Green, P. F.; Johnston, K. P. <i>Macromolecules</i> 2006 , 39, 7044).....	222

Chapter 1: Introduction

1.1 MOTIVATION AND RESEARCH OBJECTIVES

During the past decade, much progress has been made toward understanding polymeric films in a confined geometry, much owing to their emerging applications¹⁻¹⁶ and appreciable deviated properties as compared with bulk polymers^{5, 17-33}. Polymer thin films play critical roles in applications such as lubricating films, protective coatings, adhesive layers, photoresists in lithography as well as active components in organic electronic devices including light emitting diodes (LED) and thin film transistors (TFT).¹⁻¹⁰ A key issue in these applications is understanding materials properties, such as the glass transition temperature (T_g)^{21, 31, 34, 35}, chain dynamics^{19, 26, 27} and phase behavior of blends³⁶ or copolymers^{18, 29, 37, 38}. Numerous studies indicate that as the film thicknesses approach to the radius of gyration (R_g) of polymer chains, significant deviations from bulk properties are observed.^{5, 19, 21, 26, 27, 29-33} These deviations are caused by the interfacial interactions associated with interfaces as well as the confinement effect.

The ability of block copolymer thin films to self-organize into mesoscopic structures (spheres, cylinders, and lamellae) renders them attractive candidates for various applications. Consequently, research on block copolymer thin films has blossomed in recent years.^{15, 18, 29, 38-40} Block copolymers films have been used as templates to create periodic patterns for the “bottom up” fabrication in microelectronics, for patterning in nanolithography and for the synthesis of porous materials.^{1, 2, 6, 8, 11-16} Recently, IBM has successfully fabricated nanocrystal FLASH memory using the self-assembled poly(styrene-*b*-methyl methacrylate) (PS-*b*-PMMA) cylinders that are aligned perpendicular to the substrate.^{1, 6, 16} Many attempts have also been made to incorporate

inorganic components into block copolymer scaffolds to make functional hybrid materials.^{8, 41, 42} In these applications, the self-assembly of the chains in block copolymer thin films is straightforward; however, a precise control of the desired morphological structures is challenging. Therefore, new and creative methodologies to control the lateral ordering of self-segregated domains are needed in order to exploit self-assembly in block copolymers films for nanoscale patterning.

Liquid and supercritical carbon dioxide (CO₂) have been studied extensively as alternatives to water or organic solvents in many polymer and semiconductor processes.⁴³⁻⁴⁷ CO₂ is an appealing solvent because it is inexpensive, non-toxic, environmentally benign and has an easily accessible critical temperature and pressure. In addition, the solvent properties of CO₂ can be finely tuned by varying processing pressure or temperature. These tunable solvent properties render supercritical CO₂ a promising annealing medium to induce ordering in copolymer thin film templates and to tune the geometry of self-assembled patterns.^{8, 42} However, studies of the structures and phase behavior of block copolymers, especially of asymmetric block copolymer thin films in CO₂ have been rare. In addition, the low viscosity and low surface tension of CO₂ enable its applications in processing wafers with high aspect ratio features to enhance solvent penetration and to avoid capillary collapse.⁴⁸⁻⁵⁷ For example, supercritical CO₂ has being used in almost every aspect of photo resist process, including spin-casting, developing and stripping of resist films.⁵⁷⁻⁵⁹ Considerable research has also focused on the cleaning, repairing and drying of low-k dielectric layers in supercritical CO₂.^{48, 51-56} There, nevertheless, remains much work to be done to investigate how CO₂ environment influences the structures and physical properties of confined polymer films.

This dissertation demonstrates how to effectively modify interfacial interactions and hence to control the self-assembly of asymmetric block copolymer thin films exposed

to compressible fluids. First, the influence of interfacial constraints on the morphology of an asymmetric crystalline-amorphous block copolymer is examined under vacuum condition. Second, we investigate the methodology of using supercritical CO₂ annealing to finely control the morphology of block copolymer thin films. The effects of supercritical CO₂ as a selective solvent to further adjust interfacial interactions are examined in two fluorinated block copolymers. Third, in the attempt to explain the phase behavior of block copolymer thin films in CO₂, further understanding on the interactions between CO₂ and polymer interfaces is gained by studying the swelling and wetting properties of various polymer films in CO₂.

The following sections of this chapter are intended to provide a background and context for the work described in the body of this dissertation.

1.2 SELF-ASSEMBLY BEHAVIOR OF BLOCK COPOLYMER THIN FILMS

1.2.1 Block Copolymers in Bulk

A typical diblock copolymer, A-b-B, is composed by two chemically distinct chains, A and B, that are jointed together by covalent bonds (Figure 1.1a). Due to the incompatibility of the two block component, a diblock copolymer can phase segregated into A-rich and B-rich domains below its corresponding order-disorder transition (ODT) temperature. However, this phase segregation only occurs at nanometer length scales because of the imposed connectivity between the two blocks. Specifically, the scale of the self-assembled structure depends on the number of monomers, N , segment size, a_0 , and the strength of interaction between the blocks, represented by the Flory-Huggins interaction parameter, χ .⁶⁰⁻⁶² The ordered morphology depends on the composition of the copolymer, represented by the volume fraction of one block, f . As the compositional

symmetry goes from low values ($f \sim 0$) to high values ($f \sim 0.5$), the phase-segregated microstructures evolve from body-centered cubic arrays of spheres, to hexagonally packed cylinders, then to bicontinuous structures, and finally to lamellae (as shown in Figure 1.1b).⁶⁰⁻⁶² For each volume fraction, f , there is a critical χN above which the diblock will phase separate into its designated morphology. For instance, mean-field theory indicates that $(\chi N)_{\text{crit}} = 10.5$ for a symmetrical diblock copolymer ($f = 0.5$) and $(\chi N)_{\text{crit}} \sim 27$ for an asymmetrical diblock copolymer with $f = 0.15$.⁶⁰

1.2.2 Ordered Block Copolymer Thin Films: Interfacial Effects

Generally, interfacial forces influence the morphological structure of thin films. For example, homopolymeric, liquid films in the nanometer thickness range may be morphologically unstable or metastable because they are potentially subject to destabilizing long-range intermolecular forces.^{18, 63-66} If the molecules exhibit a tendency to crystallize, then crystallization would oppose any structural destabilization process, depending on film thickness. In the case of A-b-B diblock copolymers, the situation may be slightly more complex.

When a phase-segregated block copolymer is confined in a less than 100 nm thick film supported by a solid substrate, the interfacial interactions associated with both interfaces can strongly affect the morphological structures. In the simplest cases, a single phase structure (spheres, cylinders, or lamellae) exists throughout the films and the phase segregated domains aligns either parallel or perpendicular to the interfaces, as shown in Figure 1.2.¹⁵ Parallel aligned domains are more common because one block segments often possess more favorable interaction with interfaces than the other, e.g. one block has lower surface tension or it has stronger short-range attractive interaction with the substrate. However, perpendicular aligned domains can be induced by chemically modifying the substrate to neutralize any existing preferential interactions. Such

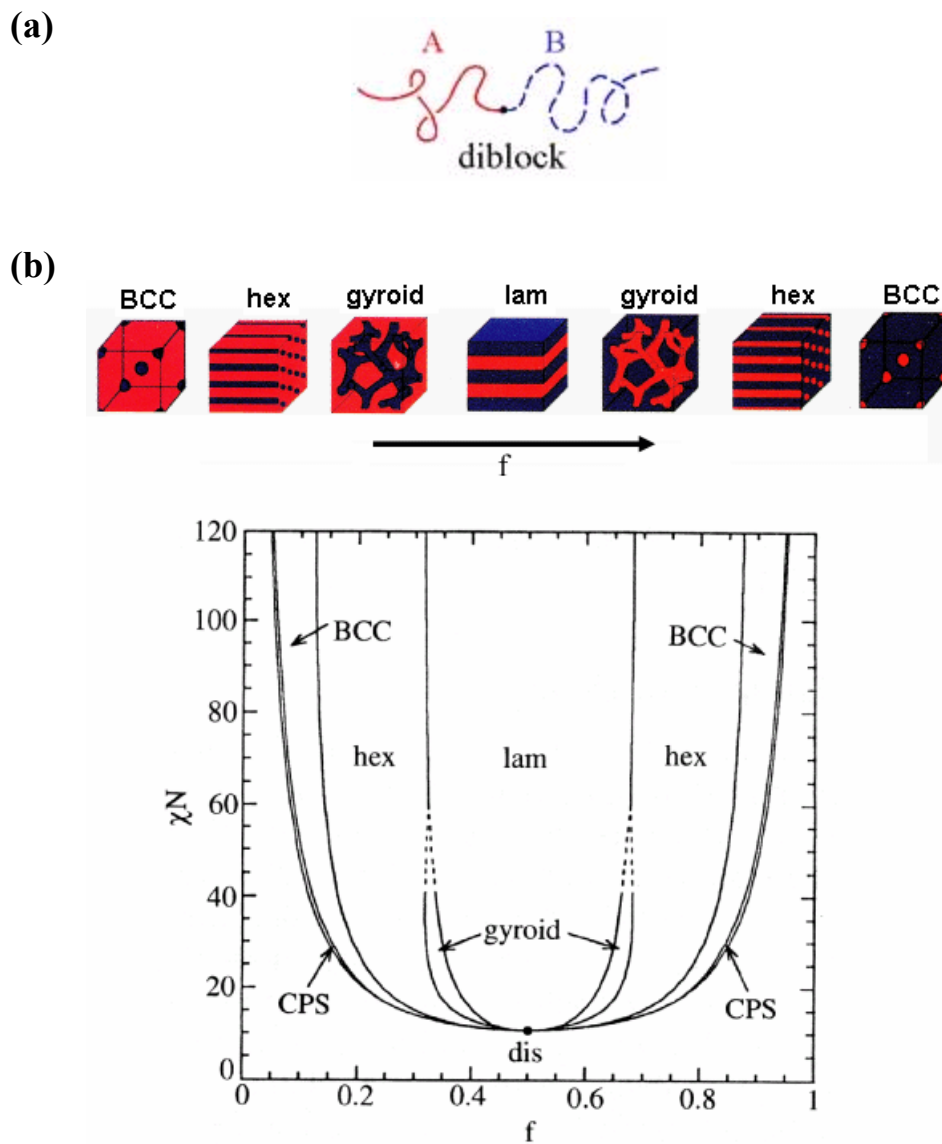


FIGURE 1.1: (a) Schematic drawing of an A-b-B diblock copolymer. (b) The mean-field theory calculated phase diagram of a typical diblock copolymer. Phase diagram is reproduced from *The Physics of Block Copolymers*.⁶²

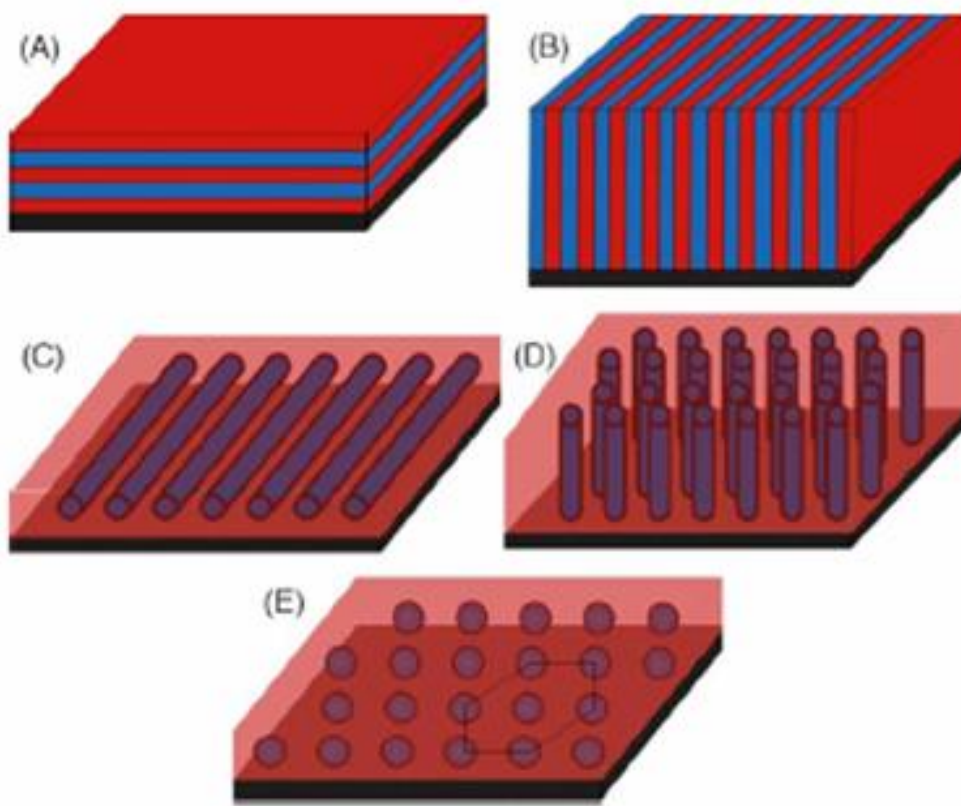


FIGURE 1.2: The structures of phase segregated block copolymer thin films: lamellae aligned parallel (a) and perpendicular (b) to the interfaces; cylinders aligned parallel (c) and perpendicular (d) to the interfaces; spheres (e). All pictures are taken from Segalman.¹⁵

modification can be achieved by depositing a brush layer of random copolymers between the block copolymer layer and the substrate.⁶⁷⁻⁶⁹

If phase-segregated domains align parallel to the surfaces (Figures 1.2a, c, e), we can consider that the interactions with both surfaces induce an oscillating profile on the interfacial free energy (or equivalently, the effective interface potential) of the film.²² As a result, the effective interface potential is a periodic function of film thickness, where locations of the minima in the potential, separated by the periodic spacing, L , denote the stable film thicknesses.²² For instance, if we simply consider symmetric block copolymer films ($f = 0.5$), then there exist two cases as shown in Figures 1.3a and b. For symmetric wetting (Figure 1.3a), wherein the same block resides at the substrate and at the free surface, the minima reside at locations nL ; hence, films of thickness $h = nL$ remain stable. In the asymmetric wetting case (Figure 1.3b), films of $h = (n + 1/2)L$ remain stable, with uniform thickness. When the film thickness deviates by an amount, δh , from the appropriate quantization criterion, the excess material forms a discontinuous layer of thickness L , provided that the film is below the ODT. If δh is small ($\delta h < 1/2L$), then the discontinuous layer forms islands (Figure 1.3c) whereas as δh approaches L , the layer contains holes (Figure 1.3d).⁷⁰

In more complicated cases, more than one structure can coexist in phase-segregated asymmetric block copolymer films. For instance, a minor block that constitutes the spherical or cylindrical domain may tend to wet one interface because of its preferential interactions. Thus, the equilibrium morphology at the surface is determined by whether the energy penalty of forming the lamellar phase and any deformation required to make the transition from the bulk structure to lamellae can be balanced by covering the surface with the more preferential wetted component.⁷¹ In addition, if the lamellar phase is indeed induced at the interface, how far would it extend

into the inner of the film is also an interesting question.^{71, 72} Figure 1.4 illustrates the case where the lamellar ordering is induced by a solid surface and an undulation develops to match onto the bulk cylindrical phase. Theoretical study by Turner et al.⁷¹ found that the extent of the region with lamellar ordering, L_0 , increases logarithmically with decreasing free-energy difference between the cylindrical and lamellar phases. This implies that L_0 is rarely very large. Experimentally, this interface induced lamellar phase is called brush layer and the thickness, L_0 , is often found to be close to one half of the lamellar spacing.⁴⁰

In Chapter 2 of this dissertation, we use a crystalline-amorphous block copolymer as an exemplary system to examine the influence of interfacial interactions on the morphological structure of block copolymer thin films.

1.3 SELF-ASSEMBLY BEHAVIOR OF BLOCK COPOLYMER THIN FILMS IN CO₂

1.3.1 Effects of CO₂ Dilation on the Phase Behavior of Block Copolymers in Bulk

In order to better control the orientation and lateral ordering of phase segregated domains in block copolymer films, most recent research activities have been focused on using external forces such as electric fields,^{73, 74} graphoepitaxy,^{75, 76} and chemical patterned substrates⁷⁷⁻⁷⁹. However, in this dissertation, our approach is to simply use supercritical CO₂ as an alternative annealing medium. We want to take advantage of the tunable properties of supercritical CO₂ to control the morphologies of block copolymer thin films.

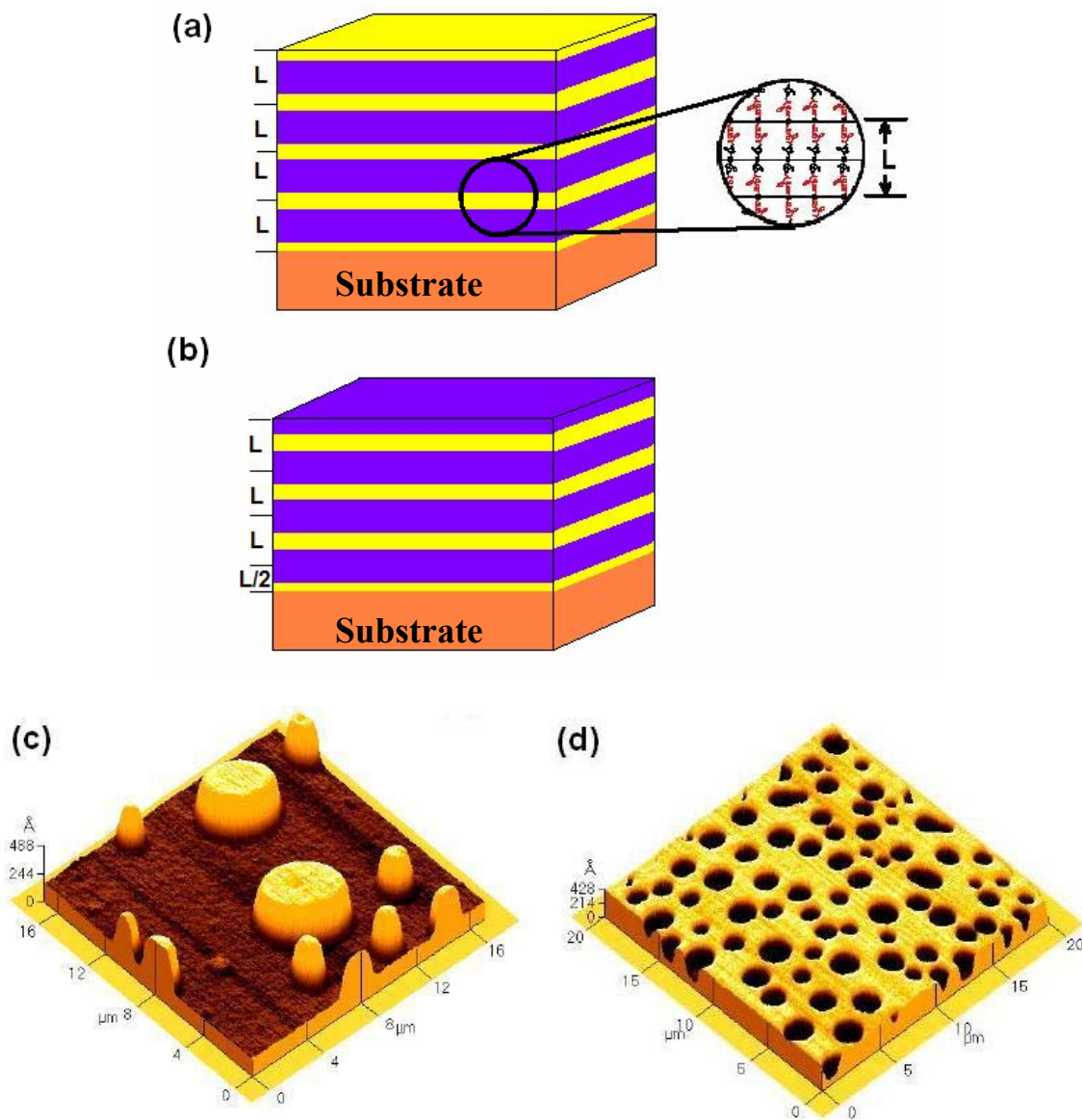


FIGURE 1.3: (a, b) Schematics of ordered films on a solid surface with the parallel stacking of lamellae for the symmetric (a) and asymmetric (b) wetting conditions. (c, d) Representative topographies of ordered PS-*b*-PMMA block copolymer thin films ($f = 0.5$) that form islands (c) or holes (d) structures. The scanning force microscopy (SFM) images (c and d) are taken from Limary.⁷⁰

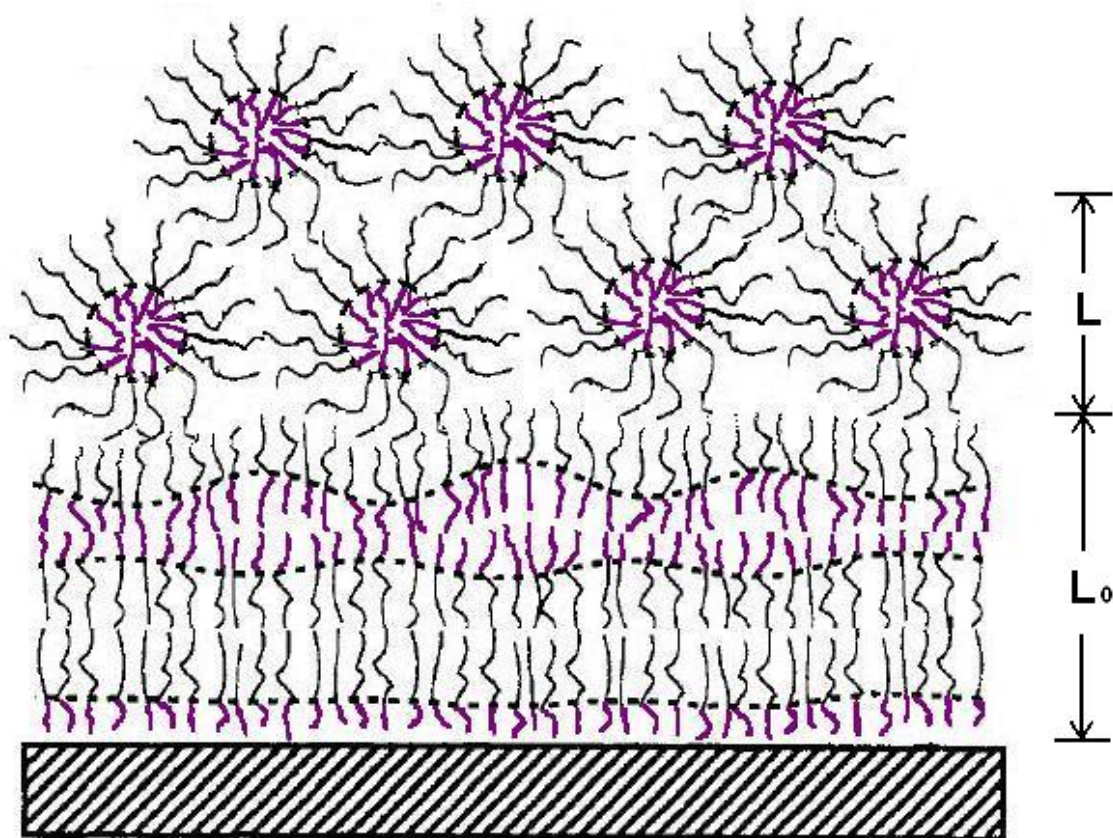


FIGURE 1.4: Schematic diagram of the lamellar ordering induced by a solid surface and the undulation which develops to match onto the hexagonal phase at the hexagonal-lamellar interface. The view is a slice through the y-z plane with symmetry in the x-direction. The dotted lines represent the position of the interfaces between the blocks of the copolymers. This figure is originally taken from the work of Turner et al.⁷¹ and has been slightly modified.

It is useful to first examine the effects of supercritical CO₂ annealing on the phase segregation behavior of bulk block copolymers. Dependent on whether CO₂ acts as a non-selective solvent or selective solvent, two cases exist.⁸⁰⁻⁸² Watkins and coworkers have systematic studied the cases where supercritical CO₂ acts as a non-selective solvent for block copolymers and polymer blends.⁸³⁻⁸⁶ They found that CO₂ sorption has two distinct contributions on the phase behavior of block copolymers as illustrated in Figure 1.5. For systems that have an enthalpic driven upper order-disorder transition (UODT) temperature, CO₂ can effectively screen the unfavorable segmental interactions and induce phase mixing. As a result, the UODT is reduced in CO₂ compared with under air/vacuum conditions (Figure 1.5a). For systems that have an entropic driven lower disorder-order transition temperature (LDOT), the entropy change upon mixing is negative. As temperature increases, disparities between the free volume of the two phases increases, and thus the enthalpic contribution to phase mixing weakens until phase segregation is reached. In CO₂, the increasing of free volume mismatch by CO₂ sorption can induce phase separation more than 100 °C below the ambient transition (Figure 1.5b). In general, the magnitude of the transition shift in LDOT is larger than that in UODT.

Despite the amount of work on CO₂ as a non-selective solvent on the phase behavior of bulk block copolymer, analogical works that examine CO₂ as a selective solvent have been rare.^{29, 87} For a bulk block copolymer, A-b-B, adding a selective solvent for A block can lead to changes in both the equilibrium phase structure and the order-disorder transition.^{88, 89} The apparent volume fraction, f_A , increases because block A is much more swollen by the selective solvent than block B. Consequently, the equilibrium phase structure always shifts toward the larger f_A side in the phase diagram. On the other hand, it is complicated with regard to the effects of selective solvent dilation on the order-disorder transition. Theoretical works^{90, 91} predicted that at high polymer

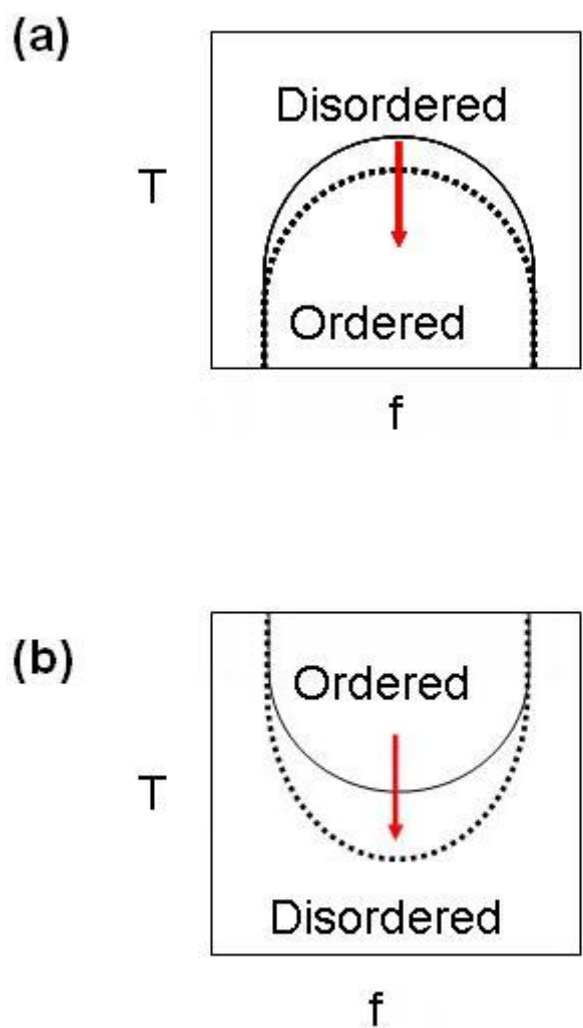


FIGURE 1.5: Schematic diagrams illustrating the effects of CO₂ sorption on the T vs. f phase diagram of block copolymers. Solid curves show the phase diagram under air/vacuum condition whereas dashed curves show the phase diagram under CO₂ condition. (a) CO₂ lowers the upper order-disorder transition (UODT) temperature and favors phase mixing. (b) CO₂ reduces the lower disorder-order transition (LDOT) temperature and induces phase segregation.

concentrations, the interaction parameter between A and B blocks, χ_{AB} determines the compatibility of A-b-B diblock. However, at low polymer concentrations, one needs to consider the difference between the A-solvent and B-solvent interaction parameters, or the so called “ $\Delta\chi$ ” effect ($\Delta\chi = |\chi_{A-S} - \chi_{B-S}|$). If $\Delta\chi$ is large enough, the phase segregation between A and B block can be induced due to enthalpic reasons.^{83,92}

1.3.2 Block Copolymer Thin Films in CO₂: Phase Behavior

When block copolymer thin films is exposed to CO₂ environment, in addition to the dilation effects of CO₂ as a solvent on the phase behavior of block copolymer, more factors have to be taken into consideration. Firstly, the presence of CO₂ on the free surface of thin films can strongly influence the interfacial interactions and thus substantially affect the wetting behavior.^{29,37} Under CO₂ environment, the block that has relatively more preferential interaction with CO₂, rather than the one that possesses lower surface tension will wet the free surface. Secondly, the sorption of CO₂ into polymer films can highly plasticize the films and thus effectively modify the kinetics of phase segregation.³⁷

To the best of our knowledge, there are only two prior experimental studies that examined the effects of CO₂ environment on the morphologies of block copolymer thin films. RamachandraRao et al. proved that sorption of Sc-CO₂ highly enhanced the ordering kinetics of high molecular weight, symmetric, polystyrene-b-polymethylmethacrylate (PS-b-PMMA) films (~0.3 μm) and that the wetting symmetry was reversed in Sc-CO₂ compared with vacuum.³⁷ Arceo et al. examined much thinner, symmetric, PS-b-PMMA films (~30 nm), and showed that Sc-CO₂ decreased the order-disorder transition temperature and favored microphase segregation.²⁹ Theoretically, Shah et al. showed that the solvent compressibility and selectivity toward one block can significantly affect the ordering of symmetric diblock copolymer thin films.⁸⁷ However,

all the above works were focused on symmetric block copolymer films. In Chapter 3 of this dissertation, we are interested in investigating the phase behavior of asymmetric block copolymer thin films under CO₂ environment, wherein the ordered domain has a spherical structure.

1.3.3 Micellization in Block Copolymer Thin Films

To further utilize the self-assembly ability of block copolymers, new strategies of employing solvent annealing to induce micellization in amphiphilic copolymer thin films have been developed.^{93, 94} Similarly, CO₂ annealing can potentially evoke the formation of interfacial micelles in fluorinated block copolymer thin films. The formation mechanism of micelles as well as the structures of surface micelles in block copolymer thin films will be briefly discussed next.

When amphiphilic block copolymers are dissolved in a selective solvent, they spontaneously self-assemble into micelles provided that the concentration is well above the critical micelle concentration (CMC). Micelles often display a spherical geometry, where the micelle core is formed by the insoluble block and the corona is formed by soluble block. The growth of micelles is driven by high surface tension between the core and the solvent. Consequently, the core chains are highly stretched and the repulsion of the swollen corona chains increases. Therefore an entropy loss arises as an opposing effect against the micelle growth. This problem can be resolved by reducing the micelle size or by a geometrical rearrangement from spheres to cylinders, vesicles, or even lamellae, where the chains of the cores become more relaxed.

The morphological structure of block copolymer micelles supported by a solid substrate have been examined previously; however, many issues remain unclear.⁹⁵⁻¹⁰⁴ Most block copolymer micelles are spherical, regardless of the volume fraction of one block. For example, symmetric block copolymers can form spherical micelles, while

their equilibrium solid-state structure is lamellae. Because the equilibrium solid-state structure of block copolymers films often differs from spherical micelles, the adsorption of polymer micelles to solid surfaces can be accompanied by complicated structural transformation. This structural rearrangement requires long relaxation time and thus extensive annealing. As the result, in many cases, micellization in copolymer thin films leads to metastable morphologies. In addition, the structures of block copolymer micelles supported by solid surfaces can be strongly influenced by confinement effect and interfacial interactions. When film thicknesses become comparable with the size of unperturbed micelles, block copolymer micelles can change shape from spherical to more ellipsoidal. In cases where the micelle cores have more preferential interactions with the substrate than the coronae, hemimicelles can form at the interface.¹⁰⁰

Chapter 4 of this dissertation focuses on the structure of block copolymer micelles in thin films, where supercritical CO₂ is employed to invert the core-shell structures and to tune the sizes of the micellar cores.

1.4 POLYMER THIN FILMS IN CO₂: POLYMER-CO₂ INTERACTIONS

To gain more control over the self-assembly behavior of block copolymer systems in CO₂, it is also important to examine the interactions between CO₂ and various polymers. It is well known that CO₂ has no dipole moment and extremely weak van der Waals forces. Consequently, CO₂ possesses a low cohesive energy density and most hydrocarbon polymers only have limited solubility in supercritical CO₂. The so called “CO₂ philic” polymers are either polysiloxanes or fluorocarbons, both of which have low cohesive energy density and thus small surface energy, just like CO₂. However, Beckman et al. recently designed CO₂ soluble hydrocarbon copolymers by optimizing the

balance between the enthalpy and entropy contribution to the solubility of polymers in CO₂.¹⁰⁵

Generally speaking, the solubility of CO₂ in polymers increases with increasing CO₂ pressure while decreases with increasing CO₂ temperature. Polymers-CO₂ interactions also influence the solubility of CO₂ in polymers. For example, specific intermolecular interactions were found between CO₂ and the carbonyl group in poly(methyl methacrylate) (PMMA).¹⁰⁶ Hence the solubility of PMMA in CO₂ is almost twice as much as polystyrene under the same conditions.¹⁰⁷

With regard to thin films, experimental works in our laboratory have explored many aspects on the physical properties of various polymer films under pressurized CO₂ environment.^{23-25, 34, 35, 108, 109} Pham and coworkers discovered a CO₂ induced devitrification transition in PS and PMMA thin films, and examined its dependence on pressure, temperature, and film thickness.^{34, 35} Meli et al. studied the morphological instability of PS thin films in supercritical CO₂, and found that the dewetting dynamics of polymer thin films is greatly suppressed.¹⁰⁸ The effects of CO₂ on the welding kinetics of PS colloidal crystals were examined by *in-situ* measurement of Bragg diffraction and by scanning electron microscopy (SEM).¹⁰⁹ In addition, the structure of end-graphed polymer brush in CO₂ has also been investigated by neutron reflectivity.²⁴ However, the effects of CO₂-polymer, CO₂-substrate and polymer-substrate interactions on the structure and physical properties of polymer thin films in CO₂ are still unclear.

One of the most fundamental and best studied properties of polymer thin film is swelling. Many studies have pointed out that the swelling and sorption of CO₂ into polymer thin films are higher than that of the bulk values, and increase substantially as the films thickness decreases.^{25, 32, 110} This excess swelling in polymer thin films compared with bulk polymers can be attributed to the adsorption of CO₂ at both

interfaces.^{17, 28} In addition, several studies have consistently found that the swelling isotherms of polymer thin films in CO₂ have an anomalous peak in the regime where the compressibility of CO₂ is at maximum.^{25, 32, 110} Despite the large amount of work¹¹¹⁻¹¹³ that has been devoted to understanding the anomalous swelling maximum, its origin still remains debatable. Hence, Chapter 5 of this dissertation is intended to further investigate the roles of interfacial interactions on the anomalous swelling phenomenon.

Finally, we are also interested in the wetting characteristics of liquids on polymer thin films in CO₂. This wetting phenomenon has not been examined before, yet it provides useful information in understanding CO₂-polymer interactions and designing thin film applications such as photoresist drying and stripping in CO₂.^{49, 50} In Chapter 6 of this dissertation, we explore the effects of pressured CO₂ and film thickness on the contact angle of water on top of polystyrene films that are supported by silicon wafer.

1.5 DISSERTATION OUTLINE

This dissertation is devoted to understand the effects of compressible fluids on the self-assembly behavior of block copolymer films. The main significance of this work is that it demonstrates how to effectively manipulate interfacial interactions and hence to control the self-organized morphologies of block copolymer thin films through varying film thicknesses, polymer properties and annealing environments.

The main body of this dissertation is divided into five chapters. Chapter 2 studies the morphological structures of asymmetric polyethylene-b-poly(styrene-r-ethylene-r-butene) (E-b-SEB) diblock copolymer thin films as the results of varying annealing temperatures in vacuum ovens and film thicknesses. The present interfacial interactions in this diblock system include the molecular forces associated with crystallization, with long-range van der Waals forces, and with block-copolymer ordering. This study

provides us a fundamental understanding on the influence of these molecular interactions on the phase behavior of block copolymer thin films.

Chapters 3 and 4 extend the study of morphological structures of asymmetric diblock copolymer thin films from under vacuum/air conditions to under supercritical CO₂ environment. In Chapter 3, we examine the morphological structures of asymmetric poly(ethylene oxide)-b-poly(1,1'-dihydroperfluorooctyl methacrylate) (PEO-b-PFOMA) thin films upon annealing in supercritical CO₂. The strong affinity between PFOMA and CO₂ is found to promote phase segregation into spherical domains for PEO-b-PFOMA films as compared with vacuum annealing under the same temperature. The results are explained based on Sanchez-Lacombe Equation of State (SLEOS) modeling on the relative interaction parameters, $\chi_{\text{PFOMA-CO}_2}$ and $\chi_{\text{PEO-CO}_2}$.

In Chapter 4, supercritical CO₂ annealing is found to invert the surface micellar structures formed by polystyrene-b-poly(1,1',2,2'-tetrahydroperfluorooctyl methacrylate) (PS-b-PFOMA) thin films. After spin-casting, the micellar cores are composed of PFOMA chains with a PS corona, whereas upon exposing the films to supercritical CO₂ PS chains forms the core of the micelles and PFOMA chains constitute the corona. The size variation of the PS cores as a function of Sc-CO₂ activity is discussed based on the change in PS-CO₂ interfacial tension and in chain stretching of the corona versus the core. The ability to tune the self-assembled structures of copolymer films with Sc-CO₂ is of practical interests for templating inorganic nanocrystals in block copolymer scaffolds.

Chapters 5 and 6 examine two phenomena of polymer thin films exposed to CO₂ environment, which were encountered when attempting to explain the observed self-assembly behavior of copolymers films in CO₂ by preferential polymer-CO₂ interactions. In Chapter 5, *in-situ* spectroscopic ellipsometry is used to investigate the effects of film thickness, polymer-substrate interaction and polymer-CO₂ interaction on anomalous

swelling maximum of polymer thin films exposed to supercritical CO₂. We show that the experimental data of various polymer films can be rationalized by considering the contribution of three layers in the total swelling % of the film: the CO₂/polymer interfacial layer, the middle layer, and the polymer/substrate interfacial layer.

Chapter 6 examines the effects of pressurized CO₂ and film thickness on the contact angle of water on top of polystyrene (PS) thin films supported by silicon wafer. At 23 °C, the contact angle increases upon increasing CO₂ pressure in the vapor regime and then levels off in the liquid regime; at a fixed CO₂ pressure, contact angle is also found to decrease with decreasing PS film thickness. These experimental results are well predicted by considering the effective van der Waals potential of the system, which reflects the influence of both CO₂ sorption and film thicknesses on the Hamaker constant of the PS films.

1.6 REFERENCES

1. Black, C. T.; Bezencenet, O. *IEEE Transactions on Nanotechnology* **2004**, 3, 412.
2. Black, C. T.; Guarini, K. W.; Milkove, K. R.; Baker, S. M.; Russell, T. P.; Tuominen, M. T. *Appl. Phys. Lett.* **2001**, 79, 409.
3. Cintavey, L. A.; Clarson, S. J.; Husband, D. M.; Brabander, G. N.; Boyd, J. T. *J. Appl. Polym. Sci.* **2000**, 76, 1448.
4. Dimitrakopoulos, C. D.; Mascaro, D. J. *IBM Journal of Research and Development* **2001**, 45, 11.
5. Frank, C. W.; Rao, V.; Despotopoulou, M. M.; Pease, R. F.; Hinsberg, W. D.; Miller, R. D.; Rabolt, J. F. *Science* **1996**, 273, 912.
6. Guarini, K. W.; Black, C. T.; Milkove, K. R.; Sandstrom, R. L. *J. Vac. Sci. Technol. B* **2001**, 19, 2874.
7. Ibn-Elhaj, M.; Schadt, M. *Nature* **2001**, 410, 796.

8. Pai, R. A.; Humayun, R.; Schulberg, M. T.; Sengupta, A.; Sun, J. N.; Watkins, J. *J. Science* **2004**, 303, 507.
9. Ziemelis, K. *Nature* **1998**, 393, 619.
10. Kawase, T.; Sirringhaus, H.; Friend, R. H.; Shimoda, T. *Digest of Technical Papers* **2001**, 32, 40.
11. Chou, S. Y.; Wei, M. S.; Krauss, P. R.; Fischer, P. B. *J. Appl. Phys.* **1994**, 76, 6673.
12. De Rosa, C.; C., P.; Thomas, E. L.; Lotz, B. *Nature* **2000**, 405, 433.
13. Fink, Y.; Winn, J. N.; Fan, S.; Michel, J.; Joannopoulos, J. D.; Thomas, E. L. *Science* **1998**, 282, 1679.
14. Park, M.; Harrison, C.; Chaikin, P. M.; Register, R. A.; Adamson, D. H. *Science* **1997**, 276, 1401.
15. Segalman, R. A. *Materials Science and Engineering R* **2005**, 48, 191.
16. Guarini, K. W.; Black, C. T.; Zhang, Y.; Kim, H.; Sikorski, E. M.; Babich, I. V. *J. Vac. Sci. Technol. B* **2002**, 20, 2788.
17. Beck Tan, N. C.; Wu, W. L.; Wallace, W. E.; Davis, G. T. *J. Poly. Sci. B: Polym. Phys.* **1998**, 36, 155.
18. Green, P. F. *J. Polym. Sci. B: Polym. Phys.* **2003**, 41, 2219.
19. Inoue, R.; Kanaya, T.; Nishida, K.; Tsukushi, I.; Shibata, K. *Phys. Rev. Lett.* **2005**, 95, 056102.
20. Li, Y.; Park, E. J.; Lim, K. T.; Johnston, K. P.; Green, P. F. *Submitted to J. Polym. Sci. B* **2006**.
21. Pham, J. Q.; Green, P. F. *Macromolecules* **2003**, 36, 1665.
22. Shull, K. R. *Macromolecules* **1996**, 29, 8487.
23. Sirard, S. M.; Green, P. F.; Johnston, K. P. *J. Phys. Chem. B* **2001**, 105, 766.
24. Sirard, S. M.; Gupta, R. R.; Russell, T. P.; Watkins, J. J.; Green, P. F.; Johnston, K. P. *Macromolecules* **2003**, 36, 3365.
25. Sirard, S. M.; Ziegler, K. J.; Sanchez, I. C.; Green, P. F.; Johnston, K. P. *Macromolecules* **2002**, 35, 1928.

26. Soles, C. L.; Douglas, J. F.; Wu, W.-L. *J. Polym. Sci. B: Polym. Phys.* **2004**, 42, 3218.
27. Soles, C. L.; Douglas, J. F.; Wu, W.-L. *Macromolecules* **2004**, 37, 2901.
28. Vogt, B. D.; Soles, C. L.; Jones, R. L.; Wang, C. Y.; Lin, E. K.; Wu, W. L.; Satija, S. K. *Langmuir* **2004**, 20, 5285.
29. Arceo, A.; Green, P. F. *J. Phys. Chem. B* **2005**, 109, 6958.
30. Ashley, K. M.; Raghavan, D.; Douglas, J. F.; Karim, A. *Langmuir* **2005**, 21, 9518.
31. Besancon, B. M.; Soles, C. L.; Green, P. F. *Phys. Rev. Lett.* **2006**, 97, 057801.
32. Koga, T.; Seo, Y. S.; Shin, K.; Zhang, Y.; Rafailovich, M. H.; Sokolov, J. C.; Chu, B.; Satija, S. K. *Macromolecules* **2003**, 36, 5236.
33. Reiter, G. *J. Polym. Sci. B: Polym. Phys.* **2003**, 41, 1869.
34. Pham, J. Q.; Johnston, K. P.; Green, P. F. *J. Phys. Chem. B* **2004**, 108, 3457.
35. Pham, J. Q.; Sirard, S. M.; Johnston, K. P.; Green, P. F. *Phys. Rev. Lett.* **2003**, 91, 175503.
36. Kropka, J. M.; Green, P. F. *Macromolecules* **2006**, in press.
37. RamachandraRao, V. S.; Gupta, R. R.; Russell, T. P.; Watkins, J. J. *Macromolecules* **2001**, 34, 7923.
38. Limary, R.; Green, P. F. *Macromolecules* **2002**, 35, 2535.
39. Seemann, R.; Herminghaus, S.; Jacobs, K. *J. Phys.: Condens. Matter* **2001**, 13, 4925.
40. Segalman, R. A.; Hexemer, A.; Hayward, R.; Kramer, E. J. *Macromolecules* **2003**, 36, 3272.
41. Chiu, J. J.; Lim, B. J.; Kramer, E. J.; Pine, D. J. *J. Am. Chem. Soc.* **2005**, 127, 5036.
42. Lin, Y.; Boker, A.; He, J.; Sill, K.; Xiang, H.; Abetz, C.; Li, X.; Wang, J.; Emrick, T.; Long, S.; Wang, Q.; Balazs, A.; Russell, T. P. *Nature* **2005**, 434, 55.
43. Cooper, A. I. *J. Mater. Chem.* **2000**, 10, 207.
44. DeSimone, J. M. *Science* **2002**, 297, 799.

45. Jones, C.; Zweber, A.; DeYoung, J.; McClain, J.; Carbonell, R.; DeSimone, J. *Critical Reviews in Solid State and Materials Science* **2004**, 29, 97.
46. Kazarian, S. G. *Polymer Science, Ser. C* **2000**, 42, 78.
47. Yeo, S. D.; Erdogan, K. *Journal of Supercritical Fluids* **2005**, 34, 287.
48. Keagy, J. A.; Zhang, X.; Busch, E.; Weber, F.; Wolf, P. J.; Rhoad, T.; Martinez, H. J.; Johnston, K. P. *J. Supercritical Fluids* **2006**, in press.
49. Namatsu, H. *J. Vac. Sci. Technol. B* **2000**, 18, 3308.
50. Namatsu, H.; Yamazaki, K.; Kurihara, K. *J. Vac. Sci. Technol. B* **2000**, 18, 780.
51. O'Neill, A.; Watkins, J. J. *MRS Bulletin* **2005**, 30, 967.
52. Xie, B.; Muscat, A. J. *Microelectronic Engineering* **2004**, 76, 52.
53. Zhang, X.; Pham, J. Q.; Martinez, H. J.; Wolf, J.; Green, P. F.; Johnston, K. P. *J. Vac. Sci. Technol. B* **2003**, 21, 2569.
54. Zhang, X.; Pham, J. Q.; Ryza, N.; Green, P. F.; Johnston, K. P. *J. Vac. Sci. Technol. B* **2004**, 22, 818.
55. Goldfarb, D. L.; de Pablo, J. J.; Nealey, P. F.; Simons, J. P.; Moreau, W. M.; Angelopoulos, M. *J. Vac. Sci. Technol. B* **2000**, 18, 3313.
56. Gorman, B. P.; Orozco-Teran, R. A.; Zhang, Z.; Matz, P. D.; W., M. D.; Reidy, R. F. *J. Vac. Sci. Technol. B* **2004**, 22, 1210.
57. Weibel, G. L.; Ober, C. K. *Microelectronic Engineering* **2003**, 2003, 145.
58. Sundararajan, N.; Yang, S.; Ogino, K.; S., V.; Wang, J.; Zhou, X.; Ober, C. K. O., S. K.; Allen, R. D. *Chem. Mater.* **2000**, 12, 41.
59. Taylor, D. K.; Carbonell, R.; Desimone, J. M. *Annu. Rev. Energy Environ.* **2000**, 25, 115.
60. Bates, F. S.; Fredrickson, G. H. *Annu. Rev. Phys. Chem.* **1990**, 41, 525.
61. Semenov, A. N. *Sov. Phys. JETP* **1985**, 61, 733.
62. Hamley, I. W., *The Physics of Block Copolymer*. Oxford University Press: New York, **1998**.
63. Brochard-Wyart, F.; Debrageas, G.; Fondécave, R.; Martin, P. *Macromolecules* **1997**, 30, 1211.

64. Reiter, G. *Langmuir* **1993**, 9, 1344.
65. Seemann, R.; Herminghaus, S.; Jacobs, K. *Phys. Rev. Lett.* **2001**, 86, 5534.
66. Sharma, A.; Reiter, G. *J. Colloid and Interface Sci.* **1996**, 178, 383.
67. Mansky, P.; Liu, Y.; Huang, E.; Russell, T. P.; Hawker, C. J. *Science* **1997**, 275, 1458.
68. Mansky, P.; Russell, T. P.; Hawker, C. J.; Mays, J.; Cook, D.; Satija, S. K. *Phys. Rev. Lett.* **1997**, 68, 67.
69. Xu, T.; Hawker, C. J.; Russell, T. P. *Macromolecules* **2005**, 38, 2802.
70. Limary, R. Block Copolymer Thin Films: Interfacial and Confinement Effects. The University of Texas at Austin, **2002**.
71. Turner, M. S.; Rubinstein, M.; Marques, C. M. *Macromolecules* **1994**, 27, 4986.
72. Chen, X.; Gardella, J. J. A.; Kumler, P. A. *Macromolecules* **1992**, 25, 6631-6637.
73. Morkved, T. L.; Lu, M.; Urbas, A. M.; Ehrichs, E. E.; Jaeger, H. M.; Mansky, P.; Russell, T. P. *Science* **1996**, 273, 931.
74. Thurn-Albrecht, T.; Schotter, J.; Kastle, G. A.; Emley, N.; Shibauchi, T.; Krusin-Elbaum, L.; Guarini, K.; Black, C. T.; Tuominen, M. T.; Russell, T. P. *Science* **2000**, 290, 2126.
75. Segalman, R. A.; Yokoyama, H.; Kramer, E. J. *Adv. Mater.* **2001**, 15, 1152.
76. Sundrani, D.; Darling, S. B.; Sibener, S. J. *Langmuir* **2004**, 20, 5091.
77. Fasolka, M. J.; Harris, D. J.; Mayes, A. M.; Yoon, M.; Mochrie, S. G. J. *Phys. Rev. Lett.* **1997**, 79, 3018.
78. Kim, S. O.; Solak, H. H.; Stoykovich, M. P.; Ferrier, N. J.; dePablo, J. J.; Nealey, P. F. *Nature* **2003**, 424, 411.
79. Rockford, L.; Russell, T. P.; Yoon, M.; Mochrie, S. G. J. *Macromolecules* **2001**, 34, 1487.
80. Banaszak, M.; Whitmore, M. D. *Macromolecules* **1992**, 25, 3406.
81. Whitmore, M. D.; Noolandi, J. *J. Chem. Phys.* **1990**, 93, 2946.
82. Whitmore, M. D.; Vavasour, J. D. *Macromolecules* **1992**, 25, 2041.

83. RamachandraRao, V. S.; Watkins, J. J. *Macromolecules* **2000**, 33, 5143.
84. Vogt, B. D.; Brown, G. D.; RamachandraRao, V. S.; Gupta, R. R.; Lavery, K. A.; Francis, T. J.; Russell, T. P.; Watkins, J. J. *Macromolecules* **2003**, 36, 4029.
85. Vogt, B. D.; Brown, G. D.; RamachandraRao, V. S.; Watkins, J. J. *Macromolecules* **1999**, 32, 7907.
86. Watkins, J. J.; Brown, G. D.; RamachandraRao, V. S.; Pollard, M. A.; Russell, T. P. *Macromolecules* **1999**, 32, 7737.
87. Shah, M.; Pryamitsyn, V.; Ganesan, V. *Manuscript in preparation* **2006**.
88. Hanley, K. J.; Lodge, T. P. *J. Poly. Sci., Part B: Poly. Phys.* **1998**, 36, 3101.
89. Helfand, E.; Tagami, Y. *J. Chem. Phys.* **1972**, 56, 3592.
90. Hsu, C. C.; Prausnitz, J. M. *Macromolecules* **1974**, 7, 320.
91. Zeman, L.; Patterson, D. *Macromolecules* **1972**, 5, 513.
92. Robard, A.; Patterson, D.; Delmas, G. *Macromolecules* **1977**, 10, 706.
93. Lin, Z.; Kim, D. H.; Wu, X.; Boosahda, L.; Stone, D.; LaRose, L.; Russell, T. P. *Adv. Mater.* **2002**, 14, 1373.
94. Kim, S. H.; Misner, M. J.; Russell, T. P. *Adv. Mater.* **2004**, 16, 2119.
95. Webber, G. B.; Wanless, E. J.; Armes, S. P.; Baines, F. L.; Biggs, S. *Langmuir* **2001**, 17, 5551.
96. Webber, G. B.; Wanless, E. J.; Butun, V.; Armes, S. P.; Biggs, S. *Nano Letters* **2002**, 2, 1307.
97. Webber, S. E. *J. Phys. Chem. B* **1998**, 102, 2618.
98. Breulmann, M.; Forster, S.; Antonietti, M. *Macromol. Chem. Phys.* **2000**, 201, 204.
99. Connell, S. D.; Collins, S.; Fundin, J.; Yang, Z.; Hamley, I. W. *Langmuir* **2003**, 19, 10449.
100. Ligoure, C. *Macromolecules* **1991**, 24, 2968.
101. Meiners, J. C.; Quintel-Ritzi, A.; Mlynek, J.; Elbs, H.; Krausch, G. *Macromolecules* **1997**, 30, 4945.

102. Regenbrecht, M.; Akari, S.; Forster, S.; Mohwald, H. *J. Phys. Chem. B* **1999**, 103, 6669.
103. Spatz, J. P.; Sheiko, S.; Moller, M. *Macromolecules* **1996**, 29, 3220.
104. Li, Z.; Zhao, W.; Liu, Y.; Rafailovich, M. H.; Sokolov, J.; Khougaz, K.; Eisenberg, A.; Lennx, R. B.; Krausch, G. *J. Am. Chem. Soc.* **1996**, 118, 10892.
105. Sarbu, T.; Styranec, T.; Beckman, E. J. *Nature* **2000**, 405, 165.
106. Kazarian, S. G.; Vincent, M. F.; Bright, F.; Liotta, C. L.; Eckert, C. A. *J. Am. Chem. Soc.* **1996**, 118, 1729.
107. Wissinger, R. G.; Paulaitis, M. E. *J. Poly. Sci. B: Polym. Phys.* **1987**, 25, 2497.
108. Meli, L.; Pham, J. Q.; Johnston, K. P.; Green, P. F. *Phys. Rev. E* **2004**, 69, 051601.
109. Abramowitz, H.; Shah, P. S.; Green, P. F.; Johnston, K. P. *Macromolecules* **2004**, 048961b.
110. Koga, T.; Seo, Y. S.; Zhang, Y.; Shin, K.; Kusano, K.; Nishikawa, K.; Rafailovich, M. H.; Sokolov, J. C.; Chu, B.; Peiffer, D.; Occhiogrosso, R.; Satija, S. K. *Phys. Rev. Lett.* **2002**, 89, 125506.
111. Carbonell, R. G.; Carla, V.; Hussain, Y.; Doghieri, F. In *The Role of Gibbs Excess Adsorption on Submerged Surface in Explaining the Complex Swelling Behavior of Supported Polymeric Thin Films in Supercritical Carbon Dioxide*, Eighth Conference on Supercritical Fluids and Their Applications, Ischia, Italy, 28-31 May, **2006**.
112. Koga, T.; Jerome, J. L.; Seo, Y. S.; Rafailovich, M. H.; Sokolov, J. C.; Satija, S. K. *Langmuir* **2005**, 21, 6157.

Chapter 2: Influence of Interfacial Constraints on the Morphology of Asymmetric Crystalline-Amorphous Diblock Copolymer Films

Through control of the temperature, T , and film thickness, h , the relative influence of forces associated with crystallization, long-range van der Waals forces, and block-copolymer ordering were manipulated to control the structure of films of asymmetric polyethylene-*b*-poly(styrene-*r*-ethylene-*r*-butene) (E-*b*-SEB) diblock copolymers. The bulk equilibrium structure of this copolymer consists of spheres of the crystallizable E block embedded in the amorphous SEB matrix. In thin films, the E component resides at the free surface and the SEB block resides in contact with the substrate. Within the temperature range of $T > T_m$, where T_m is the melting temperature, yet below the order-disorder transition (ODT) temperature, T_{ODT} , all films of thickness $h > 12$ nm were ordered throughout. The thickness of the brush layer L_0 , in contact with the substrate, of these films was 12 nm; this thickness is about one-half of the intersphere spacing of the bulk copolymer. Films equal or thinner than 12 nm dewet, forming droplets on the substrate. However, at temperatures below the melting temperature but above the glass transition temperature of the amorphous block, films in the same thickness range ($h \leq 12$ nm) were structurally stable. While thicker films were stable as well, crystallization had a significant effect on the topography of these films, particularly as the film thickness increased.

Reprinted with permission from Li, Y.; Loo Y. -L.; Register R. A., Green P. F. *Macromolecules* **2005**, 38, 7745-7753. Copyright © 2005 American Chemical Society.

2.1 INTRODUCTION

Interfacial forces influence the morphological structure of thin films, regardless of chemical structure. The topographies of thin films often are indicative of the nature of the dominant interfacial forces. For example, thin homopolymer (or simple) liquid films in the nanometer thickness range may be morphologically unstable or metastable because they are potentially subject to destabilizing long-range intermolecular forces.¹⁻⁵ The stability is determined by an effective interface potential, $\Phi(h)$, which has both long and short-range contributions. Such films may rupture and form patterns that reflect the nature of the interfacial forces. Metastable films are destabilized by nucleation and growth of holes whereas unstable films form spinodal patterns. Typically, these patterns evolve into droplets on an underlying substrate over a sufficiently long time interval.

In the case of an A-b-B diblock copolymer, the situation is often more interesting because these molecules self-organize into various mesoscopic geometric arrangements of A-rich and B-rich phases (spheres, cylinders, and lamellae) below an order-disorder transition (ODT) temperature.⁶⁻¹⁴ The ODT of an A-b-B copolymer is determined by the total number of monomers that compose the chain, N , by the Flory-Huggins interaction parameter, χ , and by the fraction of A-monomers on the chain, f .^{6-8, 15} Interfaces influence the structure and the orientation of the phases in diblock copolymer thin films. Often, one block preferentially interacts with an interface (free surface or substrate) and this interaction determines the local segmental concentration profile.^{1, 16} For lamellar structures, a modulation of the concentration profile propagates normal to boundaries because the dissimilar blocks are connected. The effective interface potential of the copolymer is a periodic function of film thickness, where the locations of the minima in the potential, separated by distance L , denote the stable film thicknesses.¹⁶ For the case

where a different block resides at the substrate and at the free surface (asymmetric wetting), the minima reside at locations $(n + 1/2)L$; hence, films of thickness $h = (n + 1/2)L$ remain stable, with uniform thickness. In the symmetric wetting case, films of $h = nL$ remain stable. When the film thickness deviates by an amount, δh , from the appropriate quantization criterion, the excess material forms a discontinuous layer of thickness L , provided the film is below the ODT. If δh is small, then the discontinuous layer forms islands whereas as δh approaches L , the layer contains holes. In cases where the attraction of one component to the substrate occurs but the film is above the bulk ODT, then the effective interface potential is a damped oscillatory function of h and the undulations of the topographies, away from the minima, bear no relation to L .¹

In a third situation, the molecules may exhibit a tendency to crystallize. If the molecules are homopolymers and they exhibit a tendency to crystallize, then crystallization may oppose structural destabilization and could preserve the integrity of even very thin films. In the case of an A-b-B diblock where one component crystallizes, there is evident that, depending on the χN , the diblock copolymer domain structure may be destroyed by crystallization.¹⁷⁻²⁸

It is evident from the foregoing discussion that the structure of the molecule largely determines the nature of the intermolecular forces that are active and that these interactions determine the morphology of the film. Because the morphology is intimately connected to material performance, an understanding of these issues is critical for the design and processing of thin film polymeric materials for various applications. To this end, it is important to learn how the relative strengths of different forces, ordering, crystallization, and van der Waals forces, determine the structure of a thin film. We examine this question by considering an A_c -b-B diblock copolymer in which one component, A_c , is crystallizable. Such a system is particularly attractive because the

microstructural details of the system can be controlled through temperatures. This system exhibits an ODT, a melting temperature and a glass transition temperature. We show that changing the temperature and film thickness determines the relative influence of these three types of molecular interactions on the structure of the film.

2.2 EXPERIMENTAL SECTION

The polyethylene-b-poly(styrene-r-ethylene-r-butene) diblock copolymer (E-b-SEB) contains a short polyethylene (E) block connected to a longer styrene-ethylene-butene (70/14/16 by weight) random terpolymer block (SEB). The molecular weights of E and SEB blocks are 5 kg/mol and 30 kg/mol respectively. The bulk ODT of the copolymer is $T_{\text{ODT}} = 200$ °C, the T_g of the amorphous SEB block is $T_g = 25$ °C and the melting point of the E block is $T_m = 103$ °C. The diblock was synthesized by sequential anionic polymerization of butadiene, then of a styrene/butadiene mixture, followed by catalytic hydrogenation. The E block contains 8 wt% butene because of the microstructure of the precursor polybutadiene.²⁷ The properties of this copolymer are summarized in Table 2.1.

Thin films were prepared by dissolving E-b-SEB in toluene and spin casting the solutions onto silicon wafers. By controlling spin rate and the concentration of polymer solution, we obtained different thickness (ranging from 7 to 200 nm), measured by spectroscopic ellipsometry. Analyses of the topographies of the films were performed in contact mode using an Autoprobe CP scanning force microscope (SFM) from Park Instruments. In some cases, tapping mode scanning force microscopy measurements were performed using a Nanoscope IV Dimension 3100 (Digital Instruments). Scanning force and optical microscopy images of the films, quenched to room temperature after undergoing heat treatment for specified durations at elevated temperatures under vacuum

Table 2.1: Characteristics of the Crystalline-Amorphous Diblock Copolymer E-b-SEB

Properties	Bulk	This study
Molecular weight, M_n	35.1 kg/mole	
Volume fraction of E block, f_E^*	0.16	
Weight fraction of E block, w_E	0.14	
Glass transition temperature of SEB block, T_g	25 °C	
Crystallization temperature of E block, T_{cr}	57 °C	76 ± 1 °C
Melting temperature of E block, T_m	103 °C	
Order-disorder transition temperature, T_{ODT}	200 °C	
Interaction parameter, χ	$-0.052 + 52.9/T$ (K)	
Distance between microdomains, L	20 nm	21.7 ± 2.2 nm
Thickness of the brush layer, L_0		11.6 ± 1.8 nm

* Calculated using the method from D. W. Van Krevelen's Properties of Polymers (ref 31), $\rho_{PE} = 0.855$ g/cm³, $\rho_{PS} = 1.05$ g/cm³ and $\rho_{PB} = 0.86$ g/cm³.

conditions, revealed the development of a range of topographies that reflect the influences of various interfacial forces. The surfaces of all spin cast films were smooth prior to annealing.

2.3 RESULTS AND DISCUSSION

This section is divided into two parts. In the first, topographies of thin films of varying thickness, $7 \text{ nm} < h < 178 \text{ nm}$, annealing at the temperature of 170°C , were examined. This temperature is above the melting temperatures and below the order-disorder transition temperatures of the films. This temperature enabled an assessment of the relative influence of the molecular forces associated with block connectivity (ordering of the copolymer) versus the long-range van der Waals forces toward the structure of the film; the crystallization forces are active at appreciably lower temperatures. In the second, the effect of crystallization on the structure of films in the thickness range $7 \text{ nm} < h < 100 \text{ nm}$ is examined. While there is evidence of a small film thickness dependence of the crystallization rate and melting temperature, all samples were annealed at $T = 76 \pm 1^\circ\text{C}$ as this temperature proved optimal for the development of crystallization within the films (development of crystallization below 70°C was unreasonably slow for thin films, whereas it is known to be relative fast in the bulk at this temperature). Our choice of this temperature enabled examination of the relative influence of the three forces, the long-range van der Waals forces, block connectivity, and crystallization, on the structure of the films.

2.3.1 Films in the Temperature Range $T_m < T < T_{ODT}$

In this temperature range, the long-range destabilizing van der Waals forces determine the structure of films of thickness $h < 12$ nm, whereas the structural forces associated with block connectivity determine the structure of films with thickness $h > 12$ nm. This critical value of h is the thickness of the brush layer $L_0 \cong 12$ nm, and it is also approximately one-half of the bulk intersphere spacing, $L_0 = L/2$. Section 2.3.1a below discusses the structure of films with $h > L_0$, while section 2.3.1b addresses the behavior of films with $h < L_0$.

2.3.1a Films with Thickness $h > 12$ nm ($h > L_0$)

A typical image of the topography of a film annealed at $T = 170$ °C, is shown in Figure 2.1. This sample, whose initial thickness was $h = 14$ nm, was scratched prior to annealing to expose the underlying substrate. Numerous line scans of the sample topography, and of the region containing the scratch, consistently showed that the islands were of height $L = 21.7 \pm 2.2$ nm and that the layer in contact with the substrate was $L_0 = 11.6 \pm 1.8$ nm. A series of images of films ranging in thickness from 30 nm to 14 nm are shown in Figure 2.2. The topographies are similar to those formed by symmetric diblock copolymers, and it is well known that they develop in order to accommodate the excess material, δh , needed to create a complete layer.²⁹ The topographies were observed in films ranging in thickness from 30 nm to 178 nm ($h \sim 8L$). In fact, the SFM tapping mode scans of the edge of the thickest a film ($h = 178$ nm) is shown in Figure 2.3; this films was annealed at 180 °C for 25 h, and the image reveals steps, evidence of order throughout the film.³⁰

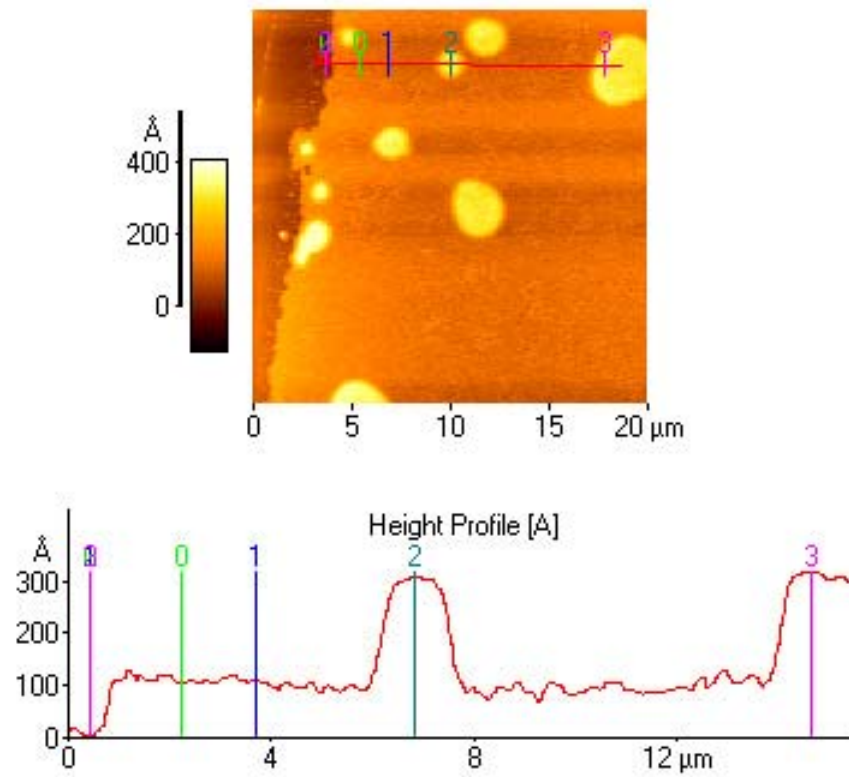


FIGURE 2.1: Topographical structure formed by annealing an E-b-SEB film with $h = 14$ nm at $170\text{ }^{\circ}\text{C}$ for 24 h. The leftmost point shows the position of a scratch and is used as a reference point to measure the height of each layer.

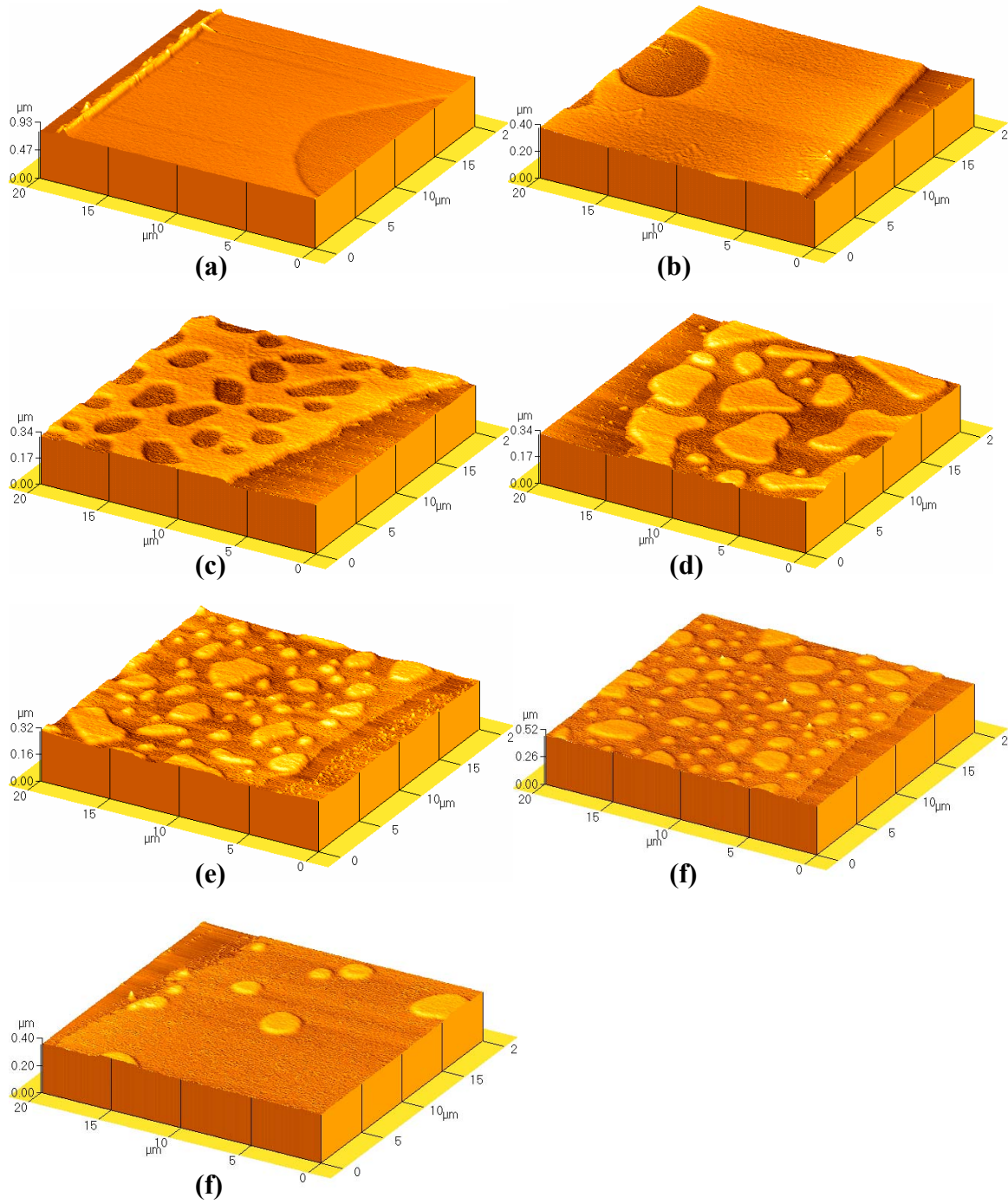


FIGURE 2.2: Topographies of samples with varying thickness after annealing at 170 °C. (a) $h = 30$ nm, (b) $h = 28$ nm, (c) $h = 25$ nm, (d) $h = 22$ nm, (e) $h = 19$ nm, (f) $h = 17$ nm, (g) $h = 14$ nm. The edge of each sample contains a scratch made to bare the substrate. All images sizes are 20 μm.

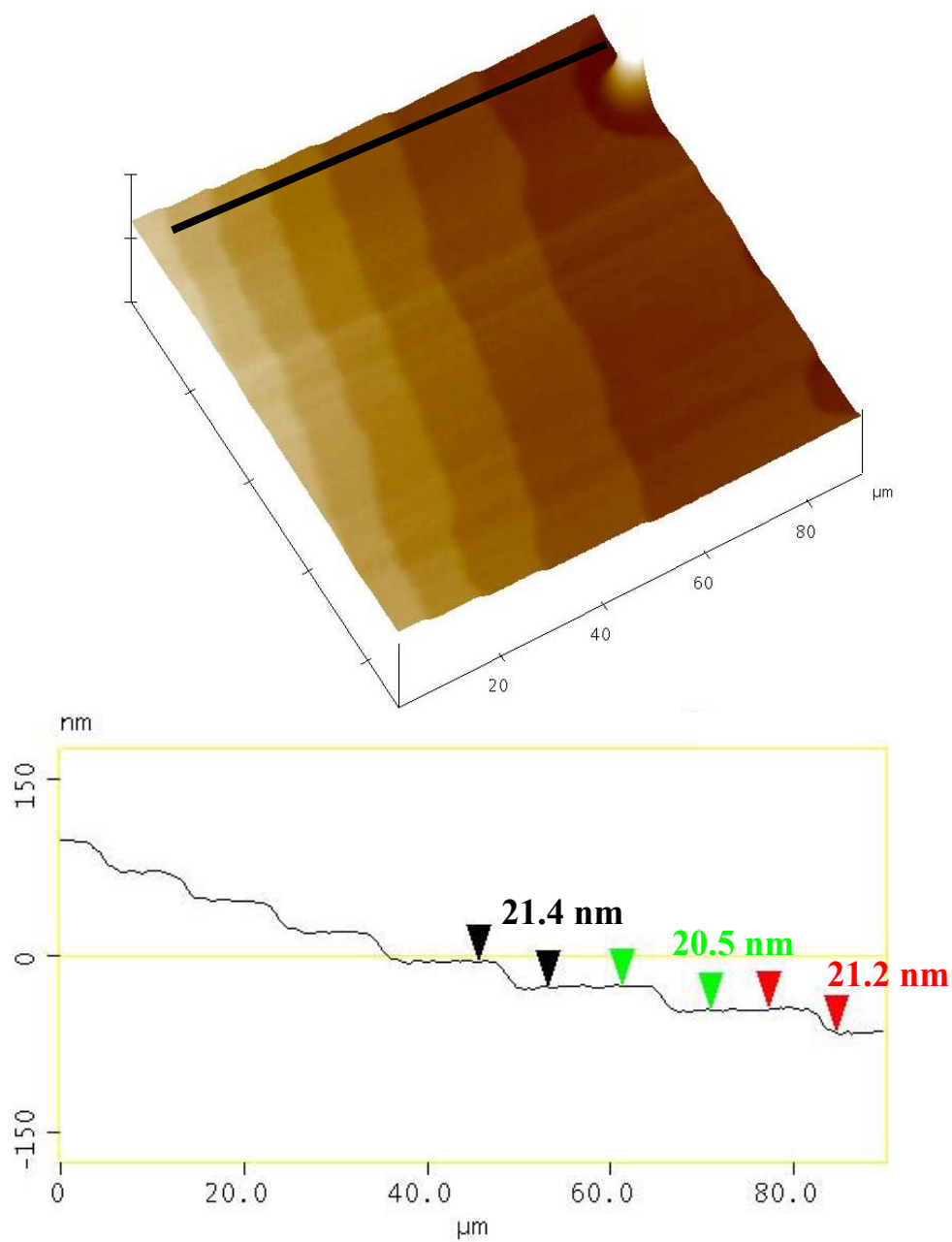


FIGURE 2.3: Topographical structure formed by annealing an E-b-SEB sample of $h = 178$ nm at $180\text{ }^{\circ}\text{C}$ for 25 h. The black line in the 3-D image shows the location of the line scan.

The bulk phase structure of this diblock is body-centered cubic, where the spheres of E blocks are embedded in a matrix of SEB block.^{27,28} In thin films, an asymmetric wetting condition occurs wherein the E-component resides at the free surface and the amorphous SEB component resides at the substrate. The surface energies of polyethylene, polystyrene and polybutene are 36.7, 43.0 and 33.1 mJ/m², respectively.^{31,32} On the basis of group contribution calculations, the surface energy of the SEB-block is 39.4 mJ/m² while that of the E-block is 36.4 mJ/m². Clearly, the E-component possesses a lower surface energy than the random block, which would indicate that this component should reside at the free surface. The interfacial tension between aromatic hydrocarbons (PS) and polar native oxide is much less than that between completely saturated alkane (PE) chains, so the SEB block resides at the substrate.³³

Interactions between the substrate and the copolymer segments have been known to modify the structure of the copolymer from hexagonal or spherical to lamellar. Turner et al. examined conditions under which the hexagonal phase of a bulk asymmetric diblock copolymer would be suppressed in favor of a lamellar phase in thin films.³⁴ For the lamellar region to exist, the free energy penalty associated with the formation of the lamellar phase at the expense of the equilibrium phase as well as the distortion energy associated with the transition from a lamellar to the equilibrium phase must be compensated elsewhere. Within a factor of order unity, this occurs when

$$\Delta\gamma > \gamma_{AB} \quad (2.1),$$

where γ_{AB} is the interfacial energy between the two blocks, and $\Delta\gamma$ is the difference between the surface energies of the two components of the copolymer. Such a reconstruction from cylinders to lamellae has been reported in the PS-b-PDMS system.³⁵ It turned out that, in this PS-b-PDMS system, the criterion specified by eq 2.1 does indeed predict such a substrate-induced transition, $\Delta\gamma > \gamma_{AB}$ ($\Delta\gamma \cong 23$ mJ/m²). For the

E/SEB system, $\Delta\gamma = \gamma_A - \gamma_B \cong 3 \text{ mJ/m}^2$ and an estimate of the interfacial energy is $\gamma_{AB} \sim 1.7 \text{ mJ/m}^2$,^{36, 37} which suggests the possibility of a surface-induced lamellar structure. If an E-b-SEB film of $h = L_0$ is layered, then how far would the lamellar structure persist in thicker films? If the lamellar structure extends beyond the brush layer, then the structure in Figure 2.4a arises. However, Figure 2.4b suggests an alternate possibility that should be considered because eq 2.1 represents a rough approximation.

To address this question, it is worthwhile to consider the behavior of an asymmetric polystyrene-b-butadiene (PS-b-PBD), 65 k: 10 k, a diblock copolymer whose interfacial characteristics and asymmetry are similar to those of the E-b-SEB copolymer. For example, the minority PBD block wets the free surface of PS-b-PBD thin films. On the basis of eq 2.1, the criterion $\Delta\gamma < \gamma_{AB}$ ($\Delta\gamma = 7.6 \text{ mJ/m}^2$, $\gamma_{AB} = 0.84 \text{ mJ/m}^2$, $\gamma_{PS} = 43 \text{ mJ/m}^2$ and $\gamma_{PBD} = 35.4 \text{ mJ/m}^2$) would predict a spherical-to-lamellar transition for PS-b-PBD thin films. However, unlike the PS-b-PDMS copolymer, this transition does not occur, as revealed by an assessment of the experiments of Harrison et al.³³ Spheres are observed beyond the first layer. Therefore, on the basis of the relative surface energies of E-b-SEB copolymer compared to those the other two copolymers, we expect that Figure 2.4b best describes the structure of the E-b-SEB thin films. The critical issue of this current study is that the samples are ordered in the vicinity of the substrate for films thicker than $L_0 \cong 12 \text{ nm}$. This is of particular importance in light of the findings in the next section regarding the structure of thinner films at this temperature.

2.3.1b Films with Thickness below 12 nm ($h < L_0$)

The morphology of films of thicknesses $h < L_0$ at $T = 170 \text{ }^\circ\text{C}$ ($T_m < T < T_{ODT}$) is now discussed. The E-b-SEB films in this thickness range dewet the substrate, forming droplets, as illustrated in Figure 2.5 for a film of thickness 8 nm. In fact, films of thickness 8, 10, and 12 nm dewet the substrate to form droplets. As mentioned earlier,

thin liquid films may exist in a morphological stable, metastable, or unstable state, and this behavior is determined by an effective interface potential.¹⁻⁵ For an apolar homopolymer film, this potential is determined by short-range interactions and, more importantly, by long-range van der Waals forces. For this sample, the dewetting is due to destabilizing van der Waals interactions, which may be understood as follows. If a net attraction exists between the interfaces (liquid/vapor and liquid/substrate), then the sample is unstable to local fluctuations of the film thickness. The stability is determined by the curvature of the effective interface potential, where the effective interface potential is

$$\Phi(h) = -\frac{A_{\text{air-poly-siox}}}{12\pi h^2} + \frac{(A_{\text{air-poly-siox}} - A_{\text{air-poly-si}})}{12\pi(h+d)^2} \quad (2.2).$$

Here $A_{\text{air-poly-siox}}$ and $A_{\text{air-poly-si}}$ are Hamaker constants, h is the film thickness and $d \sim 15\text{\AA}$ is the thickness of the SiO_x layer on the surface of Si wafer. Using Lifshitz theory, we estimate that $A_{\text{air-poly-siox}} = 1.89 \times 10^{-20} \text{ J}$ and $A_{\text{air-poly-si}} = -4.92 \times 10^{-20} \text{ J}$.³⁸ On the basis of these values, the curvature of the effective interface potential is negative ($\partial^2\Phi/\partial h^2 < 0$). This negative curvature indicates that there is an attraction between the external interfaces what would lead to destabilization (dewetting) of the film, provided it is sufficiently thin. Because both components are nonwetting on the substrate (negative spreading coefficient, $S < 0$) and the effective Hamaker constant is positive, the final state of the original film would be droplets, as observed.

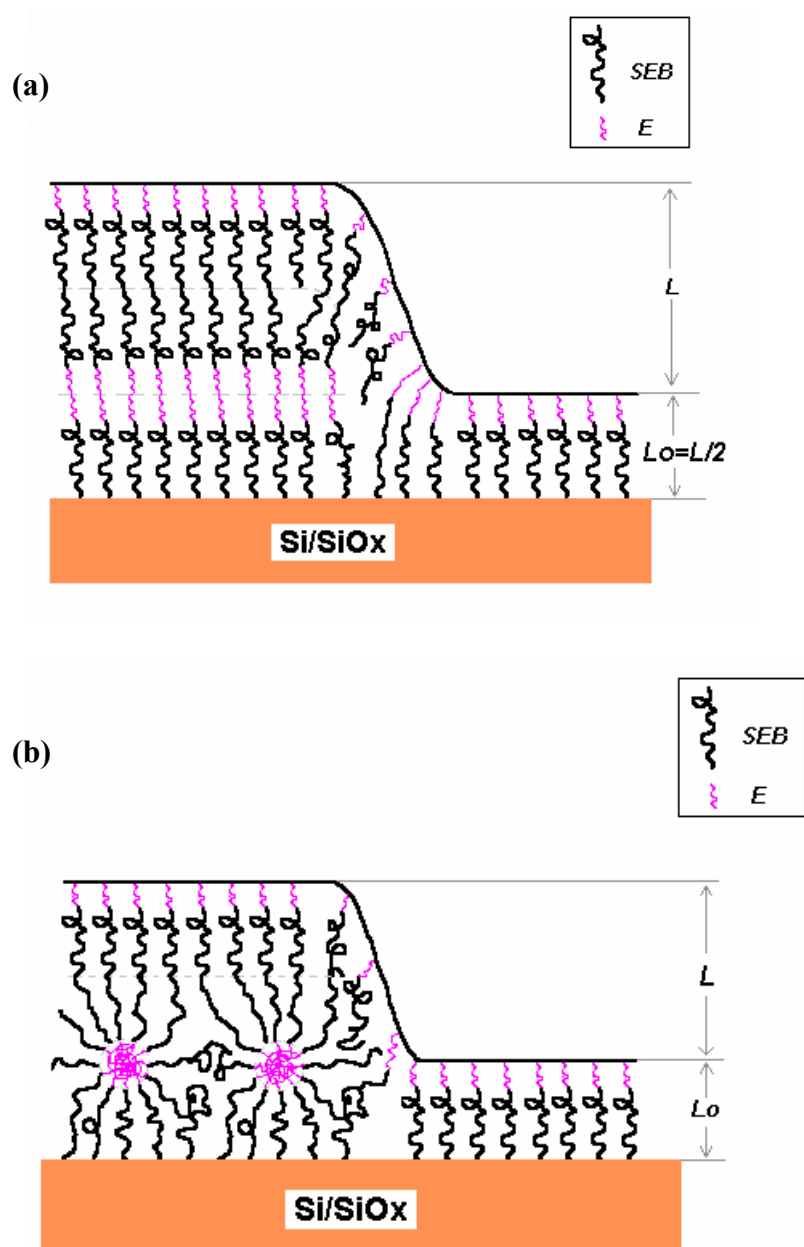


FIGURE 2.4: (a) Schematic of the case where a lamellar structure is formed at the surface.
(b) Schematic of the case where a spherical layer is formed next to the substrate.

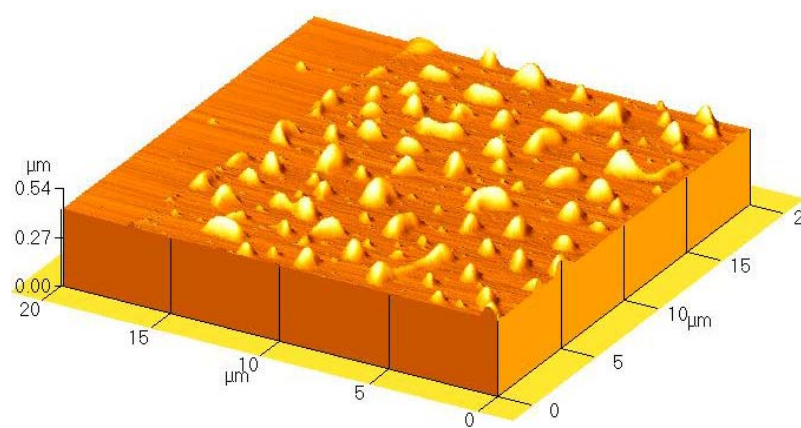


FIGURE 2.5: Topographical structure of a sample with $h = 8 \text{ nm}$ ($< L_0$), annealed at 170°C .

The oscillatory profile associated with the effective interface potential for the copolymer was not considered explicitly for this calculation. However, it suffices to mention that the first minimum of the potential, corresponding to a stable film thickness, would be at the brush height, 12 nm. The stability of the film would in principle be due to the competition between the destabilizing van der Waals forces and the stability associated with block connectivity that favors a stable film of thickness L_0 . If the ordering associated with block connectivity dominated, then the film would have to thicken, and this would happen only if holes developed in the film, as observed in the polystyrene-b-poly(methyl methacrylate) (PS-b-PMMA) systems.¹ The PS-b-PMMA copolymer films in the thickness range $h < 12$ nm are relatively more stable because the effective interface potential for this system is different. Specifically, $S > 0$ and the minimum in the potential corresponding to the stable film thickness is 7 nm for the copolymer examined in that study.¹

In summary, in the temperature range $T_m < T < T_{ODT}$, the morphology of films of $h \geq L_0$ is determined by structural forces associated with chain connectivity, leading to long-range order. For films of h thinner than L_0 , the dominance of the destabilizing influence of the van der Waals forces is evident. The minimum of the interface potential of the copolymer denoting a stable film thickness is $L_0 = 12$ nm, and coupled with the fact that in this system, $S < 0$, the films form droplets on the Si/SiO_x substrate. A quantitative assessment of the relative interactions would have to await computer simulations of the entire potential for this system.

2.3.2 Effect of Crystallization on the Structure

To understand the effect of forces associated with crystallization, two types of experiments were performed. In the first, films in the thickness range $7 \text{ nm} < h < 100 \text{ nm}$ were isothermally annealed at 76 ± 1 °C; this temperature is above the glass transition of

the amorphous component of the copolymer but below the melting temperature of the E block. The samples were subsequently quenched to room temperature and analyzed using SFM. Crystallization is evident in all films. A second series of films was first isothermally annealed at 170 °C to allow sufficient time for ordering and was subsequently quenched to 76 ± 1 °C. At this temperature, crystallization was shown to destroy the topographies associated with copolymer ordering in thicker films. These findings are discussed in parts 2.3.2a and 2.3.2b below.

2.3.2a Morphology of Films Annealed in the Temperature Range $T_g < T < T_m$

The samples discussed in this section were annealed at 76 ± 1 °C and allowed to undergo crystallization for various time intervals. Figure 2.6 shows SFM images of two films, one of thickness $h = 8.5$ nm and the other $h = 11$ nm, that were annealed at 77 °C for 5 hours. Both films remain structurally stable with no dewetting. Holes developed throughout the $h = 8.5$ nm sample and appear to be the result of an attempt by the system to decrease its free energy by adjusting its thickness (locally) to L_0 , the stable film thickness. This behavior contrasts with that at 170 °C, where droplets developed on the substrate. The thicker $h = 11$ nm film, on the other hand, did not contain holes because its thickness is approximately $h = L_0$. The topographies of both films are indicative of crystallization. The stabilization effect on the structure of the film due to crystallization is evident. Morphological stability should not be particularly surprising because energies associated with crystallization are much larger than those attributable to interfacial energies, van der Waals forces, or attributable to phase separation. The energy associated with crystallization is about 100 J/g^{17,39} and for phase separation, it is about 1 J/g.^{17,40} An estimate of the crystallization energy per unit volume for a polymer with density 1 g/cm³ is $\sim 10^8$ J/m³. Considering that the Hamaker constant is $\sim 10^{-20}$ J and the energy per unit area of interaction for a film of thickness 10 nm is $\sim 10^{-5}$ J/m², then it should be clear

that the film would be stable at this temperature largely because of the stabilizing effects of crystallization. We are unable to predict the structure of the film because the relative kinetics of these forces is not well-known. Nevertheless, the topography of the film reveals evidence of some degree of crystallization; the holes in the film suggest evidence of the attempt of the system to form a complete brush layer at the substrate. The stability of the film at this temperature and the absence of stability above T_m are clear indications of the influence of crystallization.

The influence of crystallization on the final morphology of the film increases with increasing film thickness. Three images of the same general region of a film with $h = 33$ nm that was annealed for 23 hours at 77 °C are shown in Figure 2.7. The optical micrograph (Figure 2.7a) and the SFM image (Figure 2.7b) indicate that locally one region is flat, whereas the other region consists of a spherulite structure within a hole. Figure 2.7c reveals further details about the structure of the film near a region where a scratch exposes the substrate. These measurements show that a brush layer appears close to the edge and its height is h_1 . The flat layer on top is of thickness h_2 and the maximum height of the spherulite structure is h_3 . We took more than 20 images of samples with average thickness of 27-40 nm and for each image, 3 or 4 line-scans were chosen. The average values of h_1 , h_2 , h_3 obtained from these measurements were compared with L and L_0 . It is clear that h_1 (11.2 nm) $\sim L$ and h_2 (33.7 nm) $\sim L_0 + L$. The height h_3 (61.0 nm) bears no relation to any intrinsic morphological features. These results indicate that the microdomain structure is retained near the substrate whereas the topography reflects evidence of crystallinity at the free surface.

Optical microscope and SFM images of thicker films, with $h = 94$ nm and $h = 67$ nm, annealed for 3 h at 75 °C, are shown in Figure 2.8. The topography of 94 nm film reflects complete crystallization whereas the topography of the 67 nm film shows

evidence of flat regions, indicating incomplete crystallization. The influence of the substrate on crystallization of the film is consistent with observations reported by others. For example, Frank et al. showed that, because of the polymer-substrate interfacial interactions, crystallization of polymers is substantially hindered in thin PEO films with thickness below a critical thickness of 15 nm.^{41, 42}

2.3.2b Morphology of Films Annealed in Temperature Range $T_m < T_1 < T_{ODT}$ and Subsequently in the Range $T_g < T_2 < T_m$

Further insight into the relative contributions of crystallization and microdomain formation to the structure of the film may be obtained by first allowing a sample to form an ordered structure at temperatures above T_m and quenching it below T_m , where it would crystallize. Figure 2.9a shows image of a film with thickness $h = 41$ nm annealed at 170 °C for a sufficiently long time (24 h) to develop a stable phase-separated morphology. The image in Figure 2.9b is of a sample with identical thickness. However, this sample underwent an additional heat treatment; it was quenched to $T = 76$ °C, where it was allowed to crystallize. It is evident from the images that nucleation at the surface occurs preferentially at the edges of the islands and alters the topography appreciably. This is not surprising because, as mentioned earlier, the crystallization energy is usually larger than the energy associated with microphase separation.

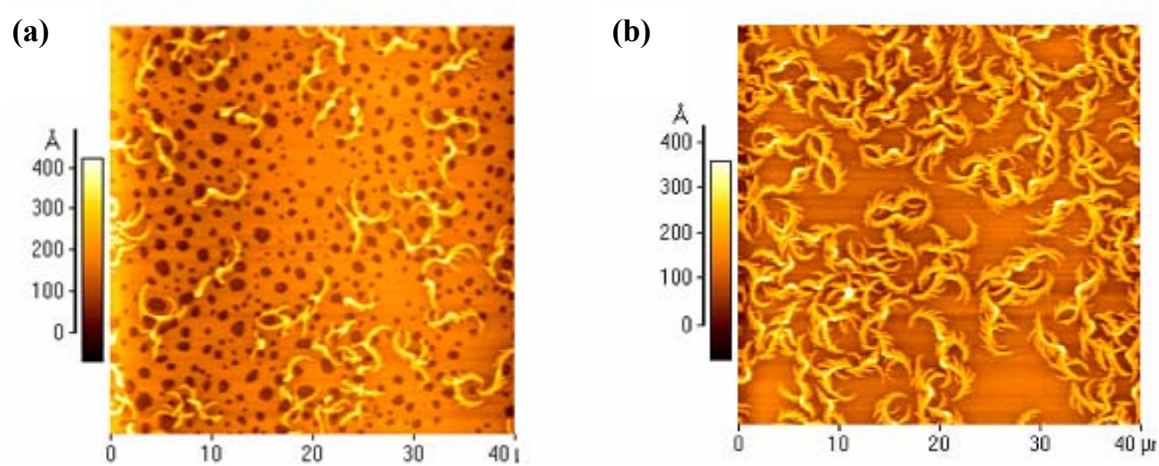


FIGURE 2.6: SFM images of (a) an $h = 8.5$ nm E/SEB film crystallized at 77°C for 5 h and (b) an $h = 11$ nm E/SEB film crystallized at 77°C for 5 h.

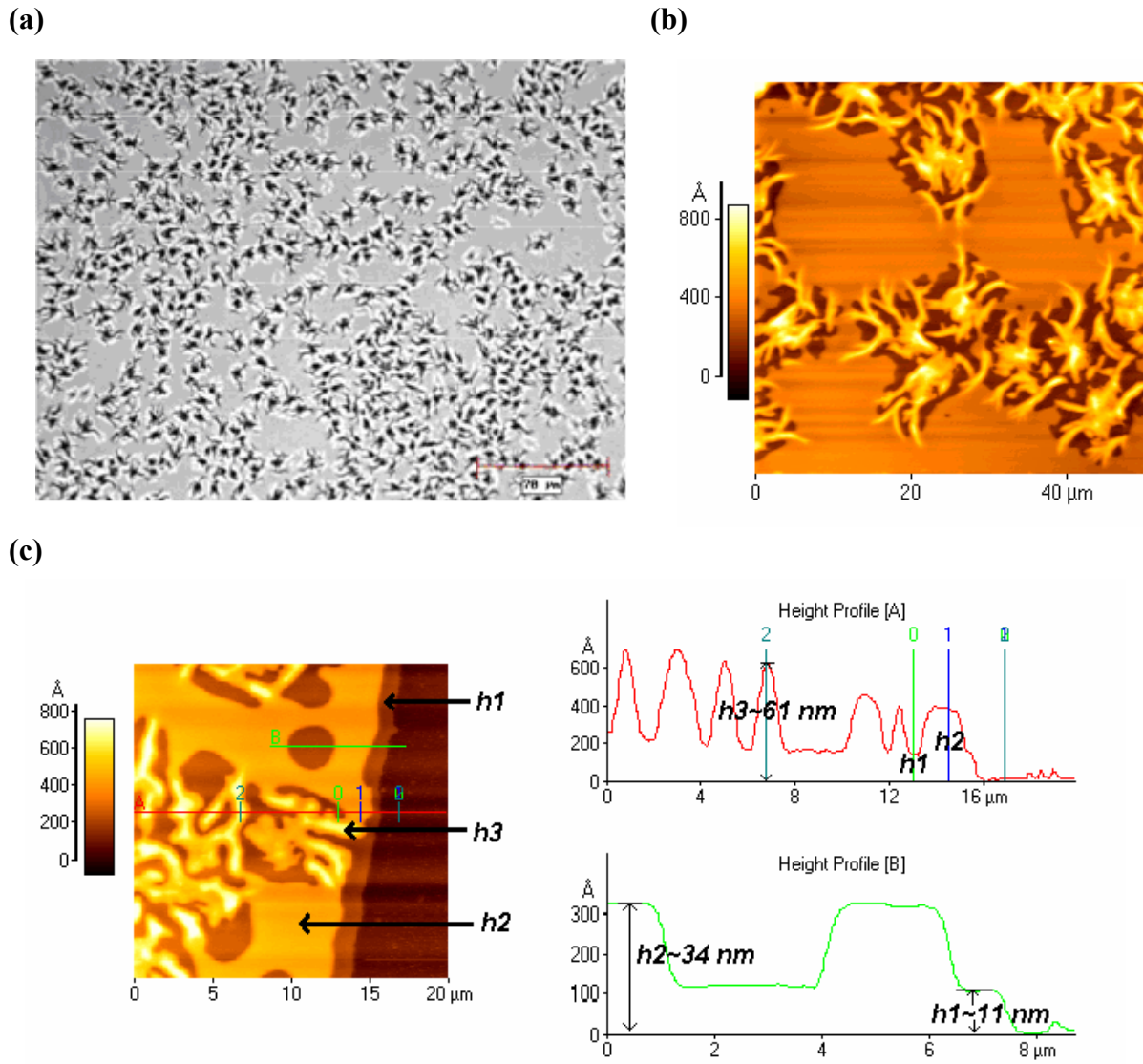


FIGURE 2.7: Optical microscopy (a), scanning force topographies (b), and line scans (c) of a film of thickness $h = 33 \text{ nm}$ annealed (crystallized) at 77°C for 23 h. The parameters identified in the diagram are $h_1 = 11.2 \pm 1.5 \text{ nm}$ ($\sim L_0$), $h_2 = 33.7 \pm 2.4 \text{ nm}$ ($\sim L + L_0$) and $h_3 = 61.0 \pm 3.0 \text{ nm}$. The scale bar in (a) is $70 \mu\text{m}$.

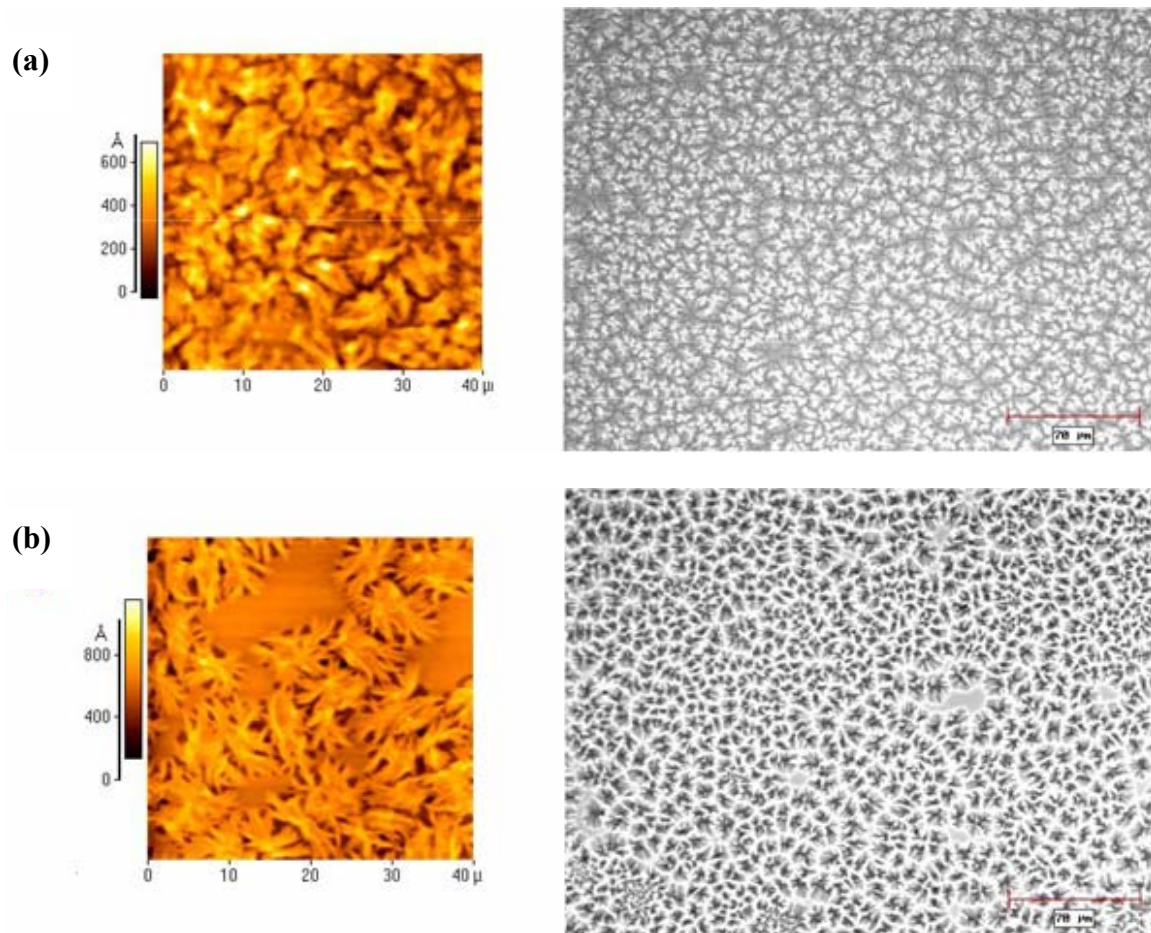


FIGURE 2.8: Optical microscopy (right) and SFM images (left) of samples crystallized at 76-77 °C: (a) an $h = 94$ nm film crystallized at 75 °C for 3 h; (b) an $h = 67$ nm film crystallized at 75 °C for 3 h. The scale bars in both optical microscopy images are 70 μm.

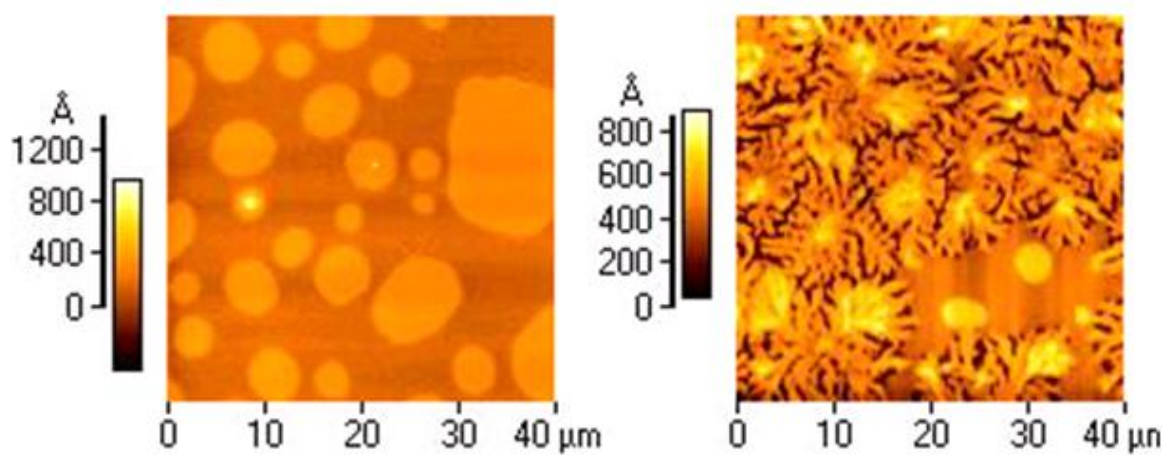


FIGURE 2.9: SFM images of (a) an $h = 41$ nm E-b-SEB film annealed at $170\text{ }^{\circ}\text{C}$ for 24 h and (b) an $h = 41$ nm E-b-SEB film annealed at $170\text{ }^{\circ}\text{C}$ for 3 h and then crystallized at $75\text{ }^{\circ}\text{C}$ for 3 h.

2.4 CONCLUDING REMARKS

The influence of interfacial constraints and temperature on the self-organization of an asymmetric E-b-SEB diblock copolymer, in which the E-component is crystallizable, was examined. In the bulk, the equilibrium morphology of this copolymer exhibits bcc symmetry, with E spheres embedded in the SEB matrix. Throughout the temperature range $T_m < T < T_{ODT}$, in thin films ($h > 12$ nm), supported by SiO_x/Si substrates, an ordered, terraced structure is observed, indicating the dominance of the driving forces for ordering as in a typical block copolymer. Films thinner than 12 nm were structurally unstable; they dewet, and formed droplets on the substrate. This instability was due to long-range van der Waals forces. All films annealed within the temperature range $T_g < T < T_m$, remained structurally stable, and the stability is largely associated with crystallization (films of $h < 12$ nm were also stable). Crystallization destroyed the microdomain morphology; this was particularly evident in thicker films, where the influence of the substrate is smaller than that for thinner films. Specifically, the layered structure, steps, was evident in films of thickness below or about 33 nm. In thicker films they were completely eradicated by crystallization. A more quantitative assessment of the relative influence of the interfacial forces on the structure of thin films awaits simulations.

2.5 REFERENCES

1. Green, P. F. *J. Polym. Sci., Part B: Polym. Phys.* **2003**, 41, 2219.
2. Brochard-Wyart, F.; Debregeas, G.; Fondecave, R.; Martin, P. *Macromolecules* **1997**, 30, 1211.
3. Reiter, G. *Langmuir* **1993**, 9, 1344.
4. Seemann, R.; Herminghaus, S.; Jacobs, K. *Phys. Rev. Lett*, **2001**, 86, 5534.
5. Sharma, A.; Reiter, G. *J. Colloid and Interface Sci.* **1996**, 178, 383.
6. Hamley, I. W. *The Physics of Block Copolymers*; Oxford University Press: New York, **1998**.
7. Bates, F. S.; Fredrickson, G. H. *Annu. Rev. Phys. Chem.* **1990**, 41, 525.
8. Hamley, I. W. *Adv. Polym. Sci.* **1999**, 148, 113.
9. Fasolka, M. J.; Mayes, A. M. *Annu. Rev. Mater. Res.* **2001**, 31, 323.
10. De Rosa, C.; Park C.; Thomas, E. L.; Lotz B. *Nature* **2000**, 405, 433.
11. Volkmuth, W. D.; Austin, R. H. *Nature* **1992**, 358, 600.
12. Chou, S. Y.; Wei, M. S.; Krauss, P. R.; Fischer, P. B. *J. Appl. Phys.* **1994**, 76, 6673.
13. Fink, Y.; Winn, J. N.; Fan, S.; Chen, C.; Michel, J.; Joannopoulos, J. D.; Thomas, E. L. *Science* **1998**, 282, 1679.
14. Park, M.; Harrison, C.; Chaikin, P. M.; Register, R. A.; Adamson, D. H. *Science* **1997**, 276, 1401.
15. Flory, P. G. *Scaling Concepts in Polymer Physics*; Cornell University Press: Ithaca, New York, **1979**.
16. Shull, K. R. *Macromolecules* **1996**, 29, 8487.
17. Loo, Y. L. Templating Polymer Crystal Growth on a Nanoscale Using Phase-Separated Block Copolymers. In *The Encyclopedia of Nanoscience and Nanotechnology*; Marcel Dekker: New York, **2002**.
18. Reiter, G. *J. Polym Sci., Polym. Phys.* **2003**, 41, 1869.

19. Reiter, G.; Castelein, G.; Sommer J. U. *Phys. Rev. Lett.* **2001**, 87, 226101.
20. Reiter, G.; Castelein, G.; Hoerner, P.; Riess. G.; Bluman, A.; Sommer J. U. *Phys. Rev. Lett.* **1999**, 83, 3844.
21. Reiter, G.; Castelein, G.; Hoerner, P.; Riess. G; Sommer, J. U.; Floudas, G. *Eur. Phys. J. E* **2000**, 2, 319.
22. Opitz, R.; Lambreva, D.M.; de Jeu, W. H. *Macromolecules* **2002**, 35, 6930.
23. Hong, S.; Macknight, W. J.; Russell, T. P.; Gido, S. P. *Macromolecules* **2001**, 34, 2876.
24. Hamley, I. W.; Wallwork, M. L.; Smith D. A.; Fairclough L. P. A.; Ryan A. J.; Mai S. M.; Yang Y. W.; Booth C. *Polymer* **1998**, 39, 3321.
25. Zhang, F.; Chen, Y.; Huang, H.; Hu, Z.; He, T. *Langmuir* **2003**, 19, 5563.
26. Zhang, F.; Huang, H.; Hu, Z.; Chen, Y.; He, T. *Langmuir* **2003**, 19, 10100.
27. Loo, Y. L.; Register, R. A.; Ryan, A. J. *Phys. Rev. Lett.* **2000**, 84, 4120.
28. Loo, Y. L.; Register, R. A.; Ryan, A. J. *Macromolecules* **2002**, 35, 2365.
29. Russell, T. P. *Curr. Opin. Colloid Interface Sci.* **1996**, 1, 107.
30. Orso, K. A.; Green, P. F. *Macromolecules* **1999**, 32, 1087.
31. Van Krevelen, D. W. *Properties of polymers*; Elsevier Science: New York, **1976**.
32. On the basis of ref 31, we estimate the surface tension using an additive function, $\gamma = (\text{Ps}/V)^4$, in which Ps is molar parachor and V is molar volume. The values of Ps and V are calculated using group contribution. For example, for polybutylene $\text{Ps(PB)} = 39(\text{CH}_2) \times 2 + 56.1(\text{CH}_3) + 17.1(\text{C}) + 4.8(\text{H}) = 156.0 \text{ (cm}^3/\text{mol)} \times (\text{mJ/m}^2)^{1/4}$, $V(\text{PB}) = 9.45(\text{CH}) + 15.85(\text{CH}_2) \times 2 + 23.9(\text{CH}_3) = 65.05 \text{ cm}^3/\text{mol}$, so $\gamma = (156/65.05)^4 = 33.1 \text{ mJ/m}^2$. All these calculated values agree with Table 5 in comprehensive tables section of ref 31.
33. Harrison, C.; Park, M.; Chaikin, P. M.; Register, R. A.; Adamson, D. H.; Yao, N. *Polymer* **1998**, 39, 2733.
34. Turner, M. S.; Rubinstein, M.; Marques, C. M. *Macromolecules* **1994**, 27, 4986.
35. Chen X.; Gardella, Jr. J. A.; Kumler P. A. *Macromolecules* **1992**, 25, 6631.
36. Wu, S. *Polymer Interface and Adhesion*; Marcel Dekker: New York, **1982**.

37. From eq 8.12 in ref 31, $\gamma_{AB} \approx \gamma_A + \gamma_B - 2\phi_{AB}(\gamma_A\gamma_B)^{1/2}$, $\Phi_{AB} = \frac{4(V_A V_B)^{1/3}}{(V_A^{1/3} + V_B^{1/3})^2}$,
 $V_{SEB} = 83.45 \text{ cm}^3/\text{mol}$, and $V_E = 34.37 \text{ cm}^3/\text{mol}$, so $\phi_{E-SEB} = 0.978$ and $\gamma_{E-SEB} = 1.7 \text{ mJ/m}^2$. Table 3.14 of ref 36 shows that the value of interfacial energy between polystyrene and polyethylene is 5.1 mJ/m^2 at 180°C , significantly larger than the result of $\gamma_{E-SEB} = 1.7 \text{ mJ/m}^2$. This deviation can be understood by the fact that the polyethylene chains in SEB block can stay in contact with E block to minimize the unfavorable chain interaction between polystyrene and polyethylene. Thus a smaller interfacial energy is expected for E-SEB than for polystyrene-polyethylene. In fact, using the same method as above, the estimated γ_{S-E} value between polystyrene-polyethylene is 3.1 mJ/m^2 , which is much larger than 1.7 mJ/m^2 .
38. $A_{132} = (\sqrt{A_{11}} - \sqrt{A_{33}})(\sqrt{A_{22}} - \sqrt{A_{33}})$, $A_{\text{Si-Si}} = 21.1 \times 10^{-20} \text{ J}$, $A_{\text{SiOx-SiOx}} = 5 \times 10^{-20} \text{ J}$.
The Hamaker constant of polymers can be estimated by

$$A = \frac{3}{4} kT \left(\frac{\epsilon_1 - 1}{\epsilon_1 + 1} \right)^2 + \frac{3h\nu_e}{16\sqrt{2}} \frac{(n_1^2 - 1)^2}{(n_1^2 - 1)^{3/2}}$$
Here n is the refractive index of the polymer, ϵ is the dielectric permittivity of the polymer, and ν_e is the main electric absorption frequency in the UV, typically around $3 \times 10^{15} \text{ s}^{-1}$. From ref 31, $n_{\text{PS}} = 1.591$, $n_{\text{PE}} = 1.49$, $n_{\text{PB}} = 1.5125$, $\epsilon_{\text{PS}} = 2.55$, $\epsilon_{\text{PE}} = 2.3$, and $\epsilon_{\text{PB}} = 2.2$. According to the Lorentz–Lorenz ideal mixing rule, $\frac{(n_{\text{mix}}^2 - 1)}{(n_{\text{mix}}^2 + 2)} = \sum \Phi_i \frac{(n_i^2 - 1)}{(n_i^2 + 2)}$ and

$$\frac{(\epsilon_{\text{mix}}^{1/2} - 1)^2}{(\epsilon_{\text{mix}}^{1/2} + 2)^2} = \sum \Phi_i \frac{(\epsilon_i^{1/2} - 1)^2}{(\epsilon_i^{1/2} + 2)^2}$$
Here, Φ_i is the volume fraction of each component. Thus $n_{\text{E/SEB}} = 1.55$ and $\epsilon_{\text{E/SEB}} = 2.42$, so $A_{\text{poly-poly}} = 8.34 \times 10^{-20} \text{ J}$, $A_{\text{air-poly-SiOx}} = 1.89 \times 10^{-20} \text{ J}$ and $A_{\text{air-poly-Si}} = 4.92 \times 10^{-20} \text{ J}$. More information about this calculation can be found in (a) Meli, L.; Pham, J. Q.; Johnston, K. P.; Green, P. F. *Phys. Rev. E* **2004**, 69, 051601; (b) Abramowitz, H.; Shah, P. S.; Green, P. F.; Johnston, K. P. *Macromolecules* **2004**, 37, 7316.
39. Brandrup, J.; Immergut, E. H.; *Polymer Handbook*. JohnWiley & Sons: **1989**.
40. Stuhn B. *J. Polym. Sci., Part B: Polym. Phys.* **1992**, 30, 1013.
41. Frank, C. W.; Rao, V.; Despotopoulou, M. M.; Pease, R. F. W.; Hinsberg, W. D.; Miller, R. D.; Rabolt, J. F. *Science* **1996**, 273, 912.
42. Despotopoulou, M. M.; Frank, C. W.; Miller, R. D.; Rabolt, J. F. *Macromolecules* **1996**, 29, 5797.

Chapter 3: Ordering in Asymmetric Block Copolymer Films by a Compressible Fluid

We examine the morphological structures of asymmetric poly(ethylene oxide)-b-poly(1,1'-dihydroperfluorooctyl methacrylate) (PEO-b-PFOMA) thin films upon annealing in a compressible fluid, supercritical CO₂ (Sc-CO₂). The strong affinity between PFOMA and CO₂ is found to induce phase segregation when annealing PEO-b-PFOMA films at the same temperature as compared with vacuum. In vacuum, PEO-b-PFOMA films remain disordered from 80-180 °C, whereas in Sc-CO₂ at 13.9 MPa, an upper order-disorder transition (UODT) between 116 and 145 °C is found. In Sc-CO₂, the observed ordered structure is layers of PEO spheres embedded in the matrix of PFOMA, followed by a brush layer, in which PEO wets the substrate. The swelling isotherms of PFOMA and PEO in CO₂ are correlated with the Sanchez-Lacombe Equation of State (SLEOS) to estimate the interaction parameters, $\chi_{\text{PFOMA-CO}_2}$ and $\chi_{\text{PEO-CO}_2}$. The phase segregation (order) induced by CO₂ relative to vacuum at a given temperature is explained in terms of two factors: (1) copolymer volume fraction upon dilution with CO₂, Φ , and (2) the relative interaction parameter, $\Delta\chi = |\chi_{\text{PEO-CO}_2} - \chi_{\text{PFOMA-CO}_2}|$. The latter factor favors order and is dominant at low temperatures over the Φ factor, which always favors disorder. At high temperatures (above the T_{ODT}), the preferential swelling of PFOMA by CO₂ is less pronounced ($\Delta\chi$ decreases), and the copolymer is disordered.

3.1 INTRODUCTION

In recent years, rapid progress has been reported toward exploiting microphase segregation in block copolymer (BCP) thin films to create periodically ordered nano-patterned substrates for potential applications such as nanolithography and “bottom up” microelectronic device fabrication.^{1, 2} Efforts have been largely devoted to the control of the orientation and lateral ordering of microphase segregated domains using external and internal forces.¹⁻⁷ Compressible fluids, such as supercritical CO₂ (Sc-CO₂), have been widely used in many polymer related processes and provide certain advantages.^{8, 9} Unlike conventional liquid solvents, the density and hence the “solvent strength” of Sc-CO₂, can be tuned by small variations in pressure, temperature or both. This tunability, along with the low interfacial tension and high diffusion coefficient makes Sc-CO₂ a strategic solvent to pattern BCP templates at relatively low temperatures. For example, Pai et al. used Sc-CO₂ as a processing medium for the infusion and condensation of silicon alkoxides in mesophase separated BCP templates.¹⁰ Li et al. demonstrated that the core-shell structure of BCP micelles in thin films can be inverted by Sc-CO₂ and that the size of micellar cores can be finely tuned by modifying CO₂ activities.⁷ This inversion was utilized to guide the segregation of pre-synthesized Au nanoparticles in one of the domains, and thus inorganic nanocrystals were sequestered into multilayered BCP templates.¹¹

The effects of Sc-CO₂ on the compatibility of bulk BCPs and polymer blends have been investigated.¹²⁻¹⁴ Both enthalpic driven upper order-disorder transition (UODT) and entropic driven lower disorder-order transition (LDOT) temperatures were found to decrease in Sc-CO₂.¹²⁻¹⁴ The presence of Sc-CO₂ on the free surface of thin BCP films can strongly influence the interfacial interactions, effectively modify the

kinetics of phase segregation and substantially affect the wetting behavior. RamachandraRao et al. showed that sorption of Sc-CO₂ highly enhanced the ordering kinetics of high molecular weight, symmetric, polystyrene-b-polymethylmethacrylate (PS-b-PMMA) films (~0.3 μm) and that the wetting symmetry was reversed in Sc-CO₂ compared with vacuum.¹⁵ Arceo et al. examined much thinner, symmetric, PS-b-PMMA films, (~30 nm) and showed that Sc-CO₂ decreased the order-disorder transition temperature, T_{ODT} and favored microphase segregation.¹⁶ Specifically, the ordering transition shifts from $(\chi N)_{ODT} > 10.5$ in the bulk, where N is the degree of polymerization and χ is the Flory-Huggins interaction parameter, to $(\chi N)_{ODT} = 7.94$ for films thinner than 30 nm on silicon oxide. Theoretical work by Shah et al. indicates that the solvent compressibility and selectivity toward one block can significantly affect the ordering of copolymer thin films.¹⁷

In this study we examine the influence of Sc-CO₂ on the ordering of highly asymmetric bulk and thin film poly(ethylene oxide)-b-poly(1,1'-dihydroperfluorooctyl methacrylate) (PEO-b-PFOMA) copolymers. We show that in vacuum, PEO-b-PFOMA films are disordered in the temperature range of 80-180 °C and in Sc-CO₂, at a pressure of 13.9 MPa, PEO-b-PFOMA films undergo an ODT between 116 and 145 °C. The ordered structure is composed of layers of PEO spheres embedded in the matrix of PFOMA. This structure resides on a brush layer of PEO chains in contact with substrate. The phase segregation (order) induced by CO₂ is explained in terms of two factors: (1) copolymer volume fraction upon dilution with CO₂, Φ and (2) the relative interaction parameter, $\Delta\chi = |\chi_{PEO-CO_2} - \chi_{PFOMA-CO_2}|$. The Sanchez-Lacombe Equation of State (SLEOS) is used to fit the swelling isotherms of PFOMA and PEO in CO₂ and to estimate quantitatively the two interaction parameters, $\chi_{PFOMA-CO_2}$ and χ_{PEO-CO_2} .

3.2 EXPERIMENTAL SECTIONS

3.2.1 Materials and Thin Film Preparation

Poly(ethylene oxide)-b-poly(1,1'-dihydroperfluorooctyl methacrylate) (PEO-b-PFOMA) was synthesized by Dr. Lim and the synthesis procedure has been described elsewhere.¹⁷ The molar weight of PEO block is 5 kg/mole and that of the PFOMA block is 52 kg/mole as determined by ¹H NMR. Other properties of this copolymer are summarized in Table 3.1.^{18, 19} Since the volume fraction of PEO block is 0.12, the equilibrium microphase segregated structure is expected to be spheres of PEO embedded in a continuous matrix of PFOMA.^{20, 21}

Small Angle X-ray Scattering (SAXS) measurement was performed on bulk PEO-b-PFOMA, and the experimental procedure is described as the following. Sufficient material to fill a 3 mm × 10 mm × 1 mm deep cavity was sealed in a stainless steel sample holder using a pair of 0.001" thick Kapton windows. Kapton windows do not contribute significantly to the scattering in the region of interest. The prepared sample was then loaded into a temperature controlled heating block and placed under the X-ray beam (Cu K α) of a Molecular Metrology SAXS instrument. The geometry of the experimentally afforded sampling d-spacing is from about 3.5 nm to 70 nm.

To prepare thin film samples, the diblock was first dissolved using a co-solvent mixture of 1, 1, 2-trichlorotrifluoroethane (Freon 113) and chloroform. The resulting transparent solutions had a concentration of 0.5-1 wt% polymer and 15-25 wt% chloroform. Thin films were prepared by spin casting the solutions onto silicon wafers (Wafer World Inc.) with a thin native oxide layer. The thicknesses of the films were measured by spectroscopic ellipsometry (J. A. Woollam Co., Inc.). Different thicknesses (30-80 nm) were obtained by controlling the spin rate and modifying the solution concentrations. The samples were then annealed in either vacuum ovens or Sc-CO₂

Table 3.1: Characteristic Properties of PEO and PFOMA in the Diblock

Parameters	PEO	PFOMA
M_n (kg/mole)	5	52
T_g ($^{\circ}\text{C}$)	< RT	50^{18}
T_m ($^{\circ}\text{C}$)	63^{19}	NA
M_o (g/mole)	44	468
N	114	111
γ (dyne/cm)	43	$< 11^{18}$
f (volume fraction)	0.12	0.88

environments. Topography analyses of the resulting films were performed in contact mode using an Autoprobe CP Scanning Force Microscopy (SFM) from Park Instruments. For some samples, SFM height and phase images were obtained simultaneously in tapping mode using a Nanoscope IV/Dimension 3100 (Digital Instruments).

3.2.2 Supercritical CO₂ Annealing

The samples were loaded into a fixed volume cell, which was subsequently sealed and pressurized with carbon dioxide (Air Products, > 99.999%) using a manual pressure generator (High-Pressure Equipment Co.). The pressure was controlled with a strain gauge pressure transducer (Sensotec) calibrated to within $\pm 7 \times 10^{-3}$ MPa. Typically, the temperature was controlled to ± 0.1 °C by immersing the pressure cell into a water bath equipped with a temperature controller (Julabo, Inc.). For high temperature (above 100 °C) experiments, the pressure cell was wrapped with a heating tape connected to a temperature controller (Omega Engineering, Inc). The glass transition temperature (T_g) of PFOMA is 50 °C¹⁸ and the melting temperature (T_m) of PEO is about 63 °C¹⁹ (T_g for PEO is below room temperature) in vacuum. Since all transition temperatures should be even more depressed in CO₂, the diblock was in a rubbery state at all conditions studied (60-145 °C and at the Sc-CO₂ pressure of 13.9 MPa). After an annealing period (varying from 10 hours to 10 days), the cell was cooled to approximately 25 °C and depressurized by venting Sc-CO₂ as a vapor from the top. In the process of depressurization and cooling, the films return to the glassy state and the morphology was frozen.

3.2.3 *In-situ* Swelling Experiments

Spectroscopic ellipsometry (J. A. Woollam Co., Inc.) was used to measure in-situ swelling of PFOMA ($M_n = 100$ kg/mole) homopolymer films (thicknesses between 100-

120 nm) in Sc-CO₂. The detailed experimental apparatus and procedures are described elsewhere.²² The swelling percentage was determined by assuming uniaxial swelling

$$S_w\% = \frac{\Delta V}{V_0}(\%) = \frac{h - h_0}{h_0} \times 100\% \quad (3.1).$$

Here V_0 is the initial volume of the film, h is the thickness of the swollen film, and h_0 is the initial thickness of the polymer films determined by spectroscopic ellipsometry at 0 psig.

3.3 RESULTS

3.3.1 The Absence of Order in Vacuum vs. an Order-Disorder Transition in Sc-CO₂ at the Same Temperature Range

In BCP thin films, phase segregated domains typically align parallel to the surfaces due to the preferential interactions between one block and the interfaces (both free surface and the substrate).²³⁻²⁸ For symmetric BCP films, if L is the size of the periodic spacing, then the thickness of the brush layer, L_0 , in contact with the substrate, is normally L or $L/2$ for symmetric and asymmetric wetting cases, respectively.²³ If the initial film thickness deviates from the $nL + L_0$ criterion,²³ then the excess material will form a discontinuous layer with either holes or islands, of height L . This so-called terrace structure has been widely used to identify the ordering of both symmetric and asymmetric BCP films.²³⁻²⁶

The eventual structure of the film is allowed to develop after spin-casting from solution onto the substrate and subsequently annealing under either vacuum or Sc-CO₂ conditions. Figure 3.1 compares the topography of PEO-b-PFOMA films under different annealing conditions. In the first set of experiments, the films (30-80 nm) were annealed in vacuum ovens at various temperatures (in the range of 80-180 °C) and representative

images are shown in Figures 3.1a and 3.1b. The absence of any terrace structure in the height image (Figure 3.1a) indicates that the diblock is in a disordered state. The phase image (Figure 3.1b) does not show any particular nanoscopic structure, further supporting the observation of the height image that the PEO-b-PFOMA films are phase miscible under the experimental vacuum conditions. It's noteworthy that no dewetting droplets associated structural instability was observed for PEO-b-PFOMA films after extensive annealing period in vacuum ovens. This stability is not surprising since both PEO and the carbonyl group in PFOMA are known to have strong interactions with the polar Si/SiOx substrate.^{27, 29}

In the second set of experiments, the PEO-b-PFOMA films were annealed under Sc-CO₂ conditions at 13.9 MPa, over a temperature range of 60-145 °C. This range was chosen so that Sc-CO₂ annealing temperatures were kept above the melting temperature of PEO block,¹⁹ given complications that may arise from crystallization. The film shown in Figures 3.1c and 3.1d was annealed at 145 °C for 48 hours. The absence of either a mesoscopic terrace-like or nanoscopic spherical structures indicates that PEO-b-PFOMA films are also disordered under this condition. However, as the Sc-CO₂ annealing temperature decreases, the films start to become ordered. Figures 3.1e and 3.1f are the topography of a PEO-b-PFOMA film after annealing at 75 °C, and 13.9 MPa for 76 hours. Evidently, Figure 3.1e shows a discontinuous layer with holes, suggesting the diblock is in an ordered state. In addition, random arrays of PEO spheres embedded in the matrix of PFOMA were observed in Figure 3.1f. Consistent with previous studies^{30, 31}, the PEO block appears in a darker color in the phase contrast SFM images, owing to its much lower glass transition temperature compared with PFOMA. Finally it is noteworthy that similar images as Figures 3.1e and 3.1f were obtained for samples annealed in Sc-CO₂ at the temperature range of 60-116 °C at 13.9 MPa.

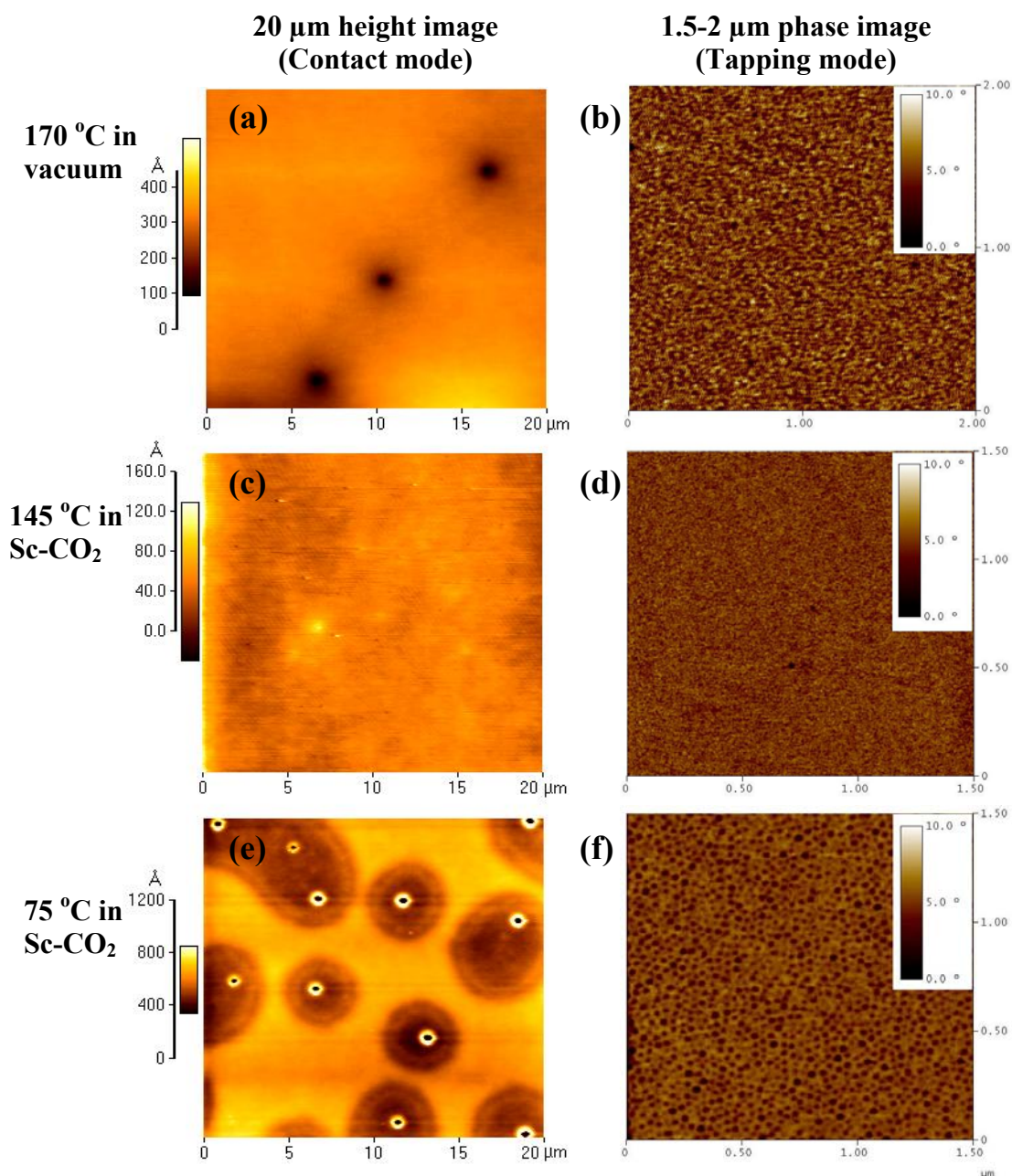


FIGURE 3.1: SFM images of PEO-b-PFOMA films with (a, b) $h = 67\text{nm}$ after annealing in vacuum ovens at 170 $^{\circ}\text{C}$ for 240 hours; (c, d) $h = 57\text{ nm}$ after annealing at CO_2 , 145 $^{\circ}\text{C}$, 13.9 MPa for 48 hours; (e, f) $h = 55\text{ nm}$ after annealing at CO_2 , 75 $^{\circ}\text{C}$, 13.9 MPa for 76 hours. Left column shows 20 μm height images from contact mode SFM, whereas right column shows 1.5-2 μm phase images from tapping mode SFM.

To further prove the absence of order after vacuum annealing, SAXS measurements were performed on bulk PEO-b-PFOMA samples to explore any potential ODT over a broader temperature range (100-280 °C in 30-40 °C increments). However, as shown by a representative spectrum (Figure 3.2), no scattering peak can be found from the intensity vs. scattering angle profile. The scattering intensity contrast between PEO and PFOMA blocks is expected to be strong due to the large difference in the X-ray atomic scattering factors for H and F atoms.³² Therefore, this absence of scattering peak suggests that no ordering could be identified over the experimental temperature range.

In summary, in vacuum, SAXS shows bulk PEO-b-PFOMA diblock remains disordered at 100-280 °C and consistently, SFM shows PEO-b-PFOMA thin films is disordered at 80-180 °C. On the other hand, upon annealing in Sc-CO₂ at 13.9 MPa, an ODT was found between 116 °C and 145 °C.

Before ending this section, it is noteworthy that in Figure 3.1f, the PEO spheres appear to only have a short-range liquid-like order. The absence of any long-range order is an intrinsic property associated with asymmetric BCP systems. Unlike symmetric BCPs, which go directly from a disordered state to an ordered lamellar state, asymmetric BCPs was found to follow the path from a disordered state, to liquid-like array of spheres, and to a perfectly aligned crystal structure of spheres.^{28, 33} Therefore two first-order phase transitions are believed to exist in asymmetric BCPs, one being the conventional ODT and the other being the “spatial disordering”³³ or lattice disorder-order transition²⁸. Given the lack of perfectly aligned spheres, the experimental temperature range of 60-116 °C in Sc-CO₂ at 13.9 MPa is below the T_{ODT} while above the corresponding “spatial disorder” transition temperature.

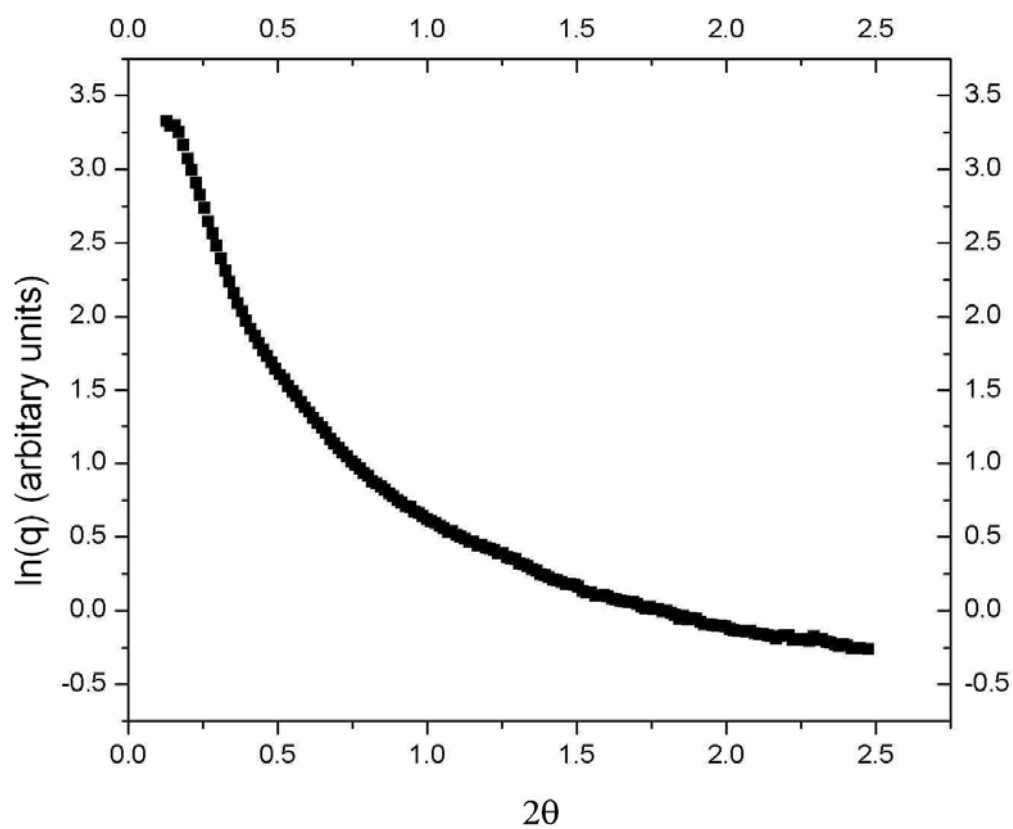


FIGURE 3.2: A representative small angle X-ray scattering (SAXS) spectrum of bulk PEO-b-PFOMA at 135 °C.

3.3.2 The Periodic Spacing of Ordered PEO-b-PFOMA Films in Sc-CO₂

To obtain a height profile of the PEO-b-PFOMA films in the z direction, films were scratched prior to annealing to expose the underlying substrate, and numerous line scans were taken near the scratch. However, as has been observed by Reiter et al.^{29, 34}, the PEO chains have a strong affinity with the polar Si/SiO_x substrate. As a consequence, the scratch made prior to annealing will be covered by a thin brush layer once the polymer chains are given mobility to move under annealing conditions.

Figures 3.3a-c show the representative SFM images and the corresponding line-scans on the edge of the scratches on PEO-b-PFOMA samples after annealing at different Sc-CO₂ temperatures at 13.9 MPa. Figure 3.3a shows a film after annealing at 145 °C for 48 hours, where no steps are observed near the scratch, further proving that the film is disordered. In Figures 3.3b-c, two steps can be clearly identified on the edge and the heights of each layer, L_1 and L_2 , are measured based on the average of numerous line-scans as listed in Table 3.2. Moreover, several white spots, which are actually small holes with rims, are observed throughout Figures 3.3b-c as well as in Figure 3.1e. These white spots (0.5-1 μm in diameter) are the result of fast CO₂ diffusion from the interface between the films and substrate when the samples were abruptly depressurized to ambient condition. Decreasing depressurization rate reduces the number of depressions, or holes. Since CO₂ is expected to partially absorb on the substrate,³⁵ the bottom of each depression is found to expose the underlying substrate. Therefore the height difference between brush layer covering the scratch and bottom of these holes is used to determine the height of the brush layer, L_0 (also shown in Table 3.2).

Figure 3.3d shows a schematic drawing of the layered structure in phase segregated PEO-b-PFOMA films, where spheres of PEO are embedded in the matrix of

PFOMA, consistent with Figure 3.1f. PFOMA block, owing to its substantially lower surface tension, resides on the free surface. To determine which block remains contact with the substrate, it is instructive to compare the size of L_0 with L_1 and L_2 . If PFOMA, the majority block, wets the substrate, then the spherical phase structure can remain intact. Consequently, L_0 should be equivalent to L_1 and L_2 .²⁴ On the other hand, if PEO, the minority block wets the substrate, then the diblock has to form a half-lamellar layer on the substrate; hence the value of L_0 is approximately half of L_1 and L_2 .²⁴ Based on the above discussion and Table 3.2, it is evident that PEO resides on the substrate.

To prove the validity of our height measurement for each layer, the $nL + L_0$ criteria is used to justify the formation of islands or holes in films that were annealed at 75 °C, 13.9 MPa for 76 hours (Figure 3.4). As shown in Table 3.2, at 75 °C, the corresponding values for measured L_0 , L_1 and L_2 are 12 nm, 24 nm and 23 nm respectively. Accordingly, a stable layer would have a thickness of $12 + 24 + 23 = 59$ nm. Thus an $h = 63$ nm film (Figure 3.4a) can minimize its free energy by forming a 59 nm layer and then another discontinuous layer of islands on top. In the same fashion, for an $h = 55$ nm film (Figure 3.4b), the free energy of the system is minimized by forming a discontinuous layer, which is 59 nm in height and contains holes. Therefore good agreement is found between the measured layer heights and the $nL + L_0$ criterion.

It is noteworthy that the flower-like patterns observed in Figure 3.4 (indicated by the circles) are due to partial crystallization of PEO block when quenching to room temperature. PEO is a semicrystalline polymer and the crystallization of PEO films as well as PEO containing copolymer films has been examined.^{29, 31, 34} The melting temperature depression for bulk PEO in supercritical CO₂ has also been explored.¹⁹ In our study, to avoid the complication between crystallization and phase separation, the experimental CO₂ annealing temperatures are always kept above the melting temperature

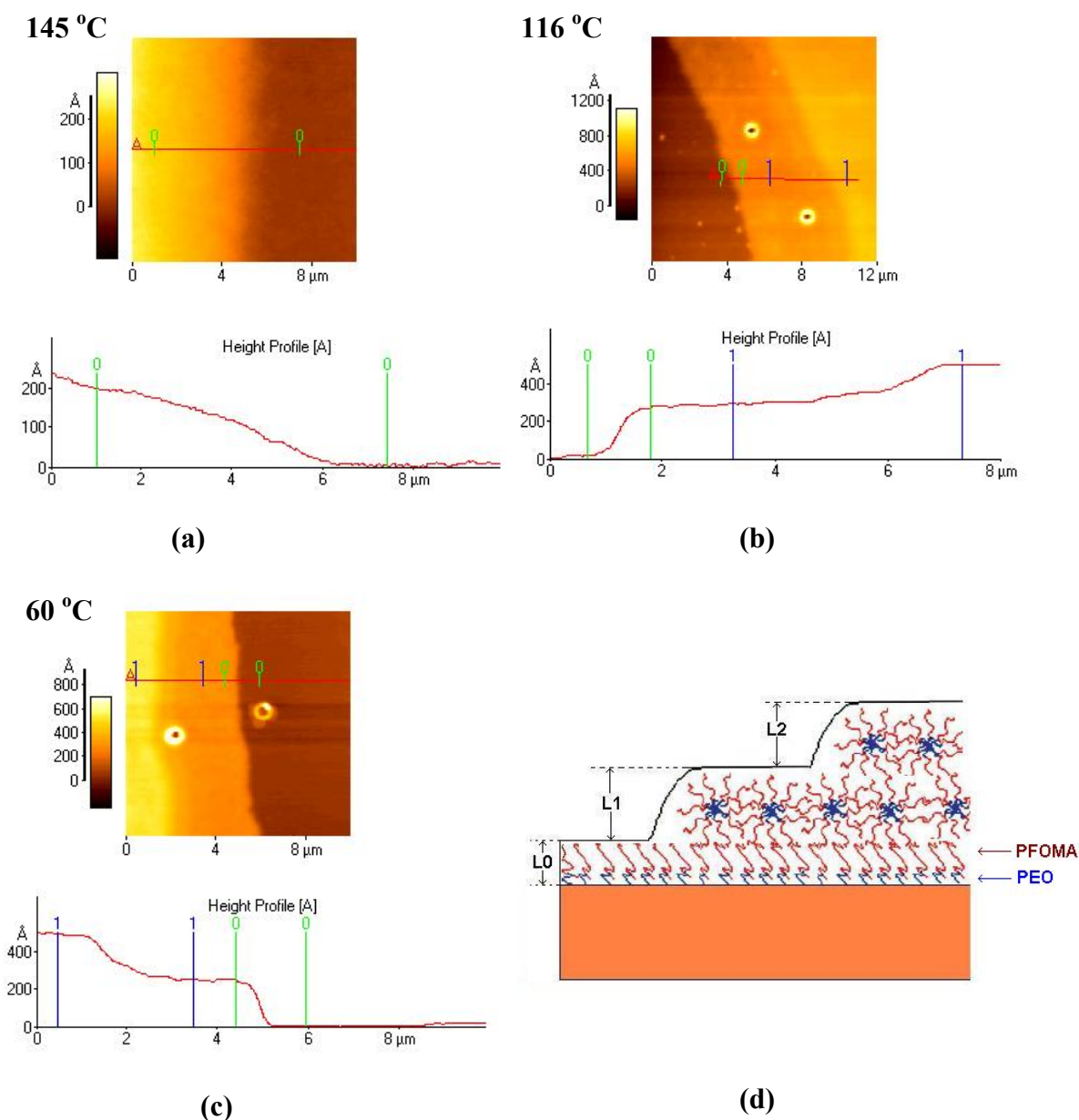


FIGURE 3.3: SFM images and the corresponding line scans for PEO-b-PFOMA films annealed in Sc-CO₂: (a) an $h = 46$ nm film after annealing at CO₂, 145 °C, 13.9 MPa for 48 hours; (b) an $h = 57$ nm film after annealing at CO₂, 116 °C, 13.9 MPa for 48 hours; (c) an $h = 47$ nm film after annealing at CO₂, 60 °C, 13.9 MPa for 30 hours. Notice that except (a), both (b) and (c) show formation of terrace near the scratch. (d) Schematic drawing of the layered structure in phase segregated PEO-b-PFOMA films.

Table 3.2: Measured layer heights for PEO-b-PFOMA Films after Sc-CO₂ Annealing

Condition	L ₀ (nm)	L ₁ (nm)	L ₂ (nm)
60 °C, 13.9 MPa	10.3 ± 1.1	24.2 ± 1.8	23.0 ± 2.0
75 °C, 13.9 MPa	11.7 ± 1.2	23.8 ± 2.1	22.7 ± 3.7
116 °C, 13.9 MPa	11.3 ± 2.2	22.6 ± 3.1	19.1 ± 3.3

Note: L₀ is the brush layer thickness; L₁ and L₂ are the next two layers above the brush layer.

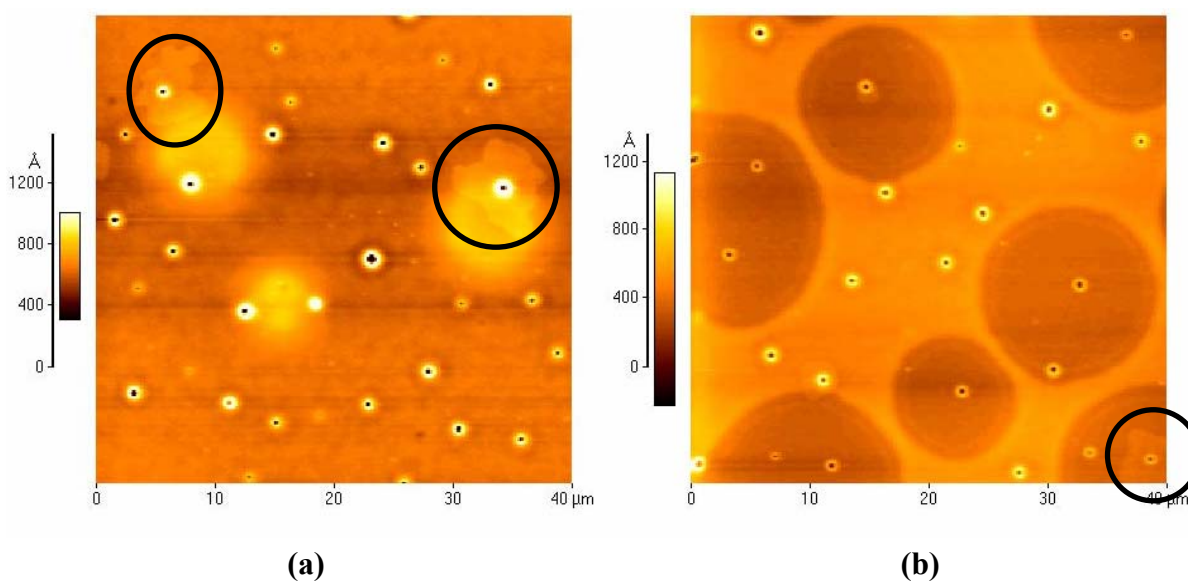


FIGURE 3.4: SFM topography of PEO-b-PFOMA films with thicknesses (a) $h = 63$ nm and (b) $h = 55$ nm after annealing at CO₂, 75 °C, 13.9 MPa for 76 hours. Notice that the flower-like patterns in both images (marked by the circles) are the results of PEO chains crystallization when subsequently quenching to ambient condition from Sc-CO₂ annealing.

of PEO. However, after CO₂ annealing, the PEO-b-PFOMA films are subsequently quenched to room temperature for SFM imaging. During this abrupt quenching, PEO-b-PFOMA films can partially crystallize, forming the observed flower-like patterns.

3.3.3 Sanchez-Lacombe Equation of State (SLEOS) Fitting of Swelling Isotherms for PFOMA and PEO in CO₂

In-situ sorption measurements were performed using spectroscopic ellipsometry for PFOMA films as shown in Figure 3.5a, where swelling isotherms of PFOMA are plotted against Sc-CO₂ activity to combine the effects of temperature and pressure. As has been discussed in our previous work³⁶, swelling of a rubbery polymer in Sc-CO₂ only depends on CO₂ activity. Because the T_g of PFOMA is only 50 °C¹⁸ under ambient conditions and is depressed under Sc-CO₂, the difference between the two PFOMA isotherms is within experimental error range. This superposed swelling vs. CO₂ activity also suggests that one can estimate the corresponding % swelling at higher temperatures, given the corresponding CO₂ activities (shown in Figure 3.5b).

To estimate the change of $\Delta\chi = |\chi_{\text{PEO-CO}_2} - \chi_{\text{PFOMA-CO}_2}|$ with temperature, the Sanchez-Lacombe equation of state (SLEOS)^{37, 38} is used to fit the swelling isotherms using nonlinear least square method. Following the mixing rule proposed by Sanchez et al.³⁷ and commonly used by many SLEOS modeling papers^{13, 39-41}, we employ the following equations for the mixture of CO₂ (phase 1) and polymer (phase 2),

$$P^* = \phi_1^2 P_1^* + \phi_2^2 P_2^* + 2\phi_1\phi_2 P_{12}^*, \quad P_{12}^* = (1 - k_{12})(P_1^* P_2^*)^{1/2} \quad (3.2a),$$

$$\nu_1^* = \frac{RT_1^*}{P_1^*}, \nu_2^* = \frac{RT_2^*}{P_2^*}, \nu^* = \phi_1^0 \nu_1^* + \phi_2^0 \nu_2^* \quad (3.2b),$$

$$T^* = \frac{P^* \nu^*}{R} \quad (3.2c),$$

$$\frac{1}{r} = \frac{\phi_1^0}{r_1^0} + \frac{\phi_2^0}{r_2^0} \quad (3.2d).$$

Here Φ_1 and Φ_2 are the closed-packed volume fractions of the components and v^* is the close-packed volume. Φ_1^0 and Φ_2^0 are given by

$$\phi_1^0 = \frac{\phi_1}{\phi_1 + \frac{v_1^*}{v_2^*} \phi_2} \quad (3.3).$$

The essence of the above mixing rules is that a temperature dependent binary parameter, k_{12} is introduced to correct the deviation of the characteristic pressure, P_{12}^* from the geometric mean. In addition, the size parameters of two components, r_1 and r_2 in the mixture can be related to those of pure phases as

$$r_1^0 = \frac{r_1 v^*}{v_1^*}, \quad r_2^0 = \frac{r_2 v^*}{v_2^*} \quad (3.4).$$

Then the chemical potential of CO₂ in the polymer-CO₂ mixture can be calculated by

$$\frac{\mu_1^P}{RT} = \ln \phi_1 + \left(1 - \frac{r_1}{r_2}\right) \phi_2 + r_1^0 \tilde{\rho} X_1 \phi_2^2 + r_1^0 \left\{ -\frac{\tilde{\rho}}{\tilde{T}_1} + \frac{\tilde{P}_1}{\tilde{T}_1 \tilde{\rho}} + \frac{1}{\tilde{\rho}} \left[(1 - \tilde{\rho}) \ln(1 - \tilde{\rho}) + \frac{\tilde{\rho}}{r_1^0} \ln \tilde{\rho} \right] \right\} \quad (3.5a),$$

$$X_1 = \frac{[P_1^* + P_2^* - 2(P_1^* P_2^*)^{1/2} (1 - k_{12})] v_1^*}{RT} \quad (3.5b).$$

The chemical potential of CO₂ in the pure CO₂ phase is

$$\frac{\mu_1^0}{RT} = r_1^0 \left\{ -\frac{\tilde{\rho}_1}{\tilde{T}_1} + \frac{\tilde{P}_1}{\tilde{T}_1 \tilde{\rho}_1} + \frac{1}{\tilde{\rho}_1} \left[(1 - \tilde{\rho}_1) \ln(1 - \tilde{\rho}_1) + \frac{\tilde{\rho}_1}{r_1^0} \ln \tilde{\rho}_1 \right] \right\} \quad (3.6).$$

Once the temperature dependent binary interaction parameter k_{12} is given, the corresponding Φ_1 , Φ_2 , Φ_1^0 and Φ_2^0 can be solved by letting $\mu_{CO_2}^P = \mu_{CO_2}^0$. Then the degree of swelling (sw %) or the mass fraction (m_1 , m_2) can be calculated, respectively, by

$$Sw\% = \frac{\Delta V}{V_0} = \frac{V^* / \tilde{\rho}}{V_2^* \phi_2^0 / \tilde{\rho}_2} - 1 \quad (3.7a),$$

and

$$m_1 = \frac{\phi_1 \rho_1^*}{\phi_1 \rho_1^* + \phi_2 \rho_2^*} \quad (3.7b).$$

Sanchez and Lacombe³⁷ derived a concentration dependent interaction parameter χ , which can be expressed as

$$\chi = \chi_1 + \chi_2 \phi_2 + \chi_2 \phi_2^2 + \dots \quad (3.8).$$

In the infinite dilution region ($\Phi_2 \sim 0$), $\chi = \chi_1$, which can be expressed as

$$\chi_1 = r_1^0 (\tilde{\rho}_1 X_1 + \tilde{\rho}_1 \psi_1^2 \tilde{T}_1 P_1^* \beta_1) \quad (3.9a),$$

$$\psi = \rho \frac{d(1/\tilde{T})}{d\phi_1} - \frac{d(1/r)}{d\phi_1} + \tilde{v} \frac{d(\tilde{P}/\tilde{T})}{d\phi_1} \quad (3.9b),$$

$$\tilde{T} P^* \beta = \tilde{v} \left[1/(\tilde{v} - 1) + 1/r - 2/\tilde{v} \tilde{T} \right]^{-1} \quad (3.9c).$$

Here ψ is a dimensionless function and β is the isothermal compressibility of the mixture; ψ_1 and β_1 are the corresponding values at infinite dilution. In eq 3.9a, χ_1 is comparable to the interaction parameter in classic Flory-Huggins theory, χ_{FH} , which simply assumes that interaction parameter is inversely proportional to temperature and is independent of concentration. However, since we are interested in the absorption of CO₂ into polymer, infinite dilution is not reasonable. Therefore we use the concentration dependent χ to evaluate the interactions between CO₂ and polymers:

$$\chi = \chi_H + \chi_S \quad (3.10a),$$

$$\chi_H = \frac{r_1^0}{\phi_2^2} \left\{ (\tilde{\rho}_1 - \tilde{\rho})/\tilde{T}_1 + P_1(\tilde{v} - \tilde{v}_1)/\tilde{T}_1 + \tilde{\rho} X_1 \phi_2^2 \right\} - \frac{r_1 \tilde{\rho}^2 \psi P^* \beta}{\phi_2} \quad (3.10b)^{37},$$

$$\chi_S = \frac{r_1^0}{\phi_2^2} \left\{ (\tilde{v} - 1) \ln(1 - \tilde{\rho}) - (\tilde{v}_1 - 1) \ln(1 - \tilde{\rho}_1) + \frac{1}{r_1^0} \ln(\tilde{\rho}/\tilde{\rho}_1) \right\} + \frac{r_1 \tilde{\rho}^2 \psi P^* \beta}{\phi_2} \quad (3.10c)^{37}.$$

Another advantage of our calculation is that χ may be determined as a function of temperature and pressure, which influence the reduced density. Since the reduced density term is included in both eqs 3.10a and 3.10b, the effects of CO₂ as a compressible

solvent, which are distinctly different from that of a relatively incompressible liquid solvent, are addressed.

Table 3.3 shows characteristic SLEOS parameters used in our fitting.⁴²⁻⁴⁴ It is noteworthy that several sets EOS parameters for CO₂ are available⁴⁵. We choose the one that gives a critical CO₂ temperature (T_c) close to 31 °C. Additionally, P* is known to related to the cohesive energy density (CED). Both CO₂ and CO₂-philic polymers possess inherently low CED⁴⁶; however, Table 3.3 shows P* for CO₂ is fairly large and even exceeds that of PEO. This discrepancy can be explained by Table 3.4, which estimates the CED values based on the equation of state approach as derived by Panayiotou⁴⁷

$$CED = \delta^2 = \tilde{\rho}^2 P^* \quad (3.11).$$

Here δ is the solubility parameter. From Table 3.4, it is clear than even though CO₂ has a relatively large P*, it also has a much lower reduced density ($\tilde{\rho}$) than those of the polymers. Thus, the estimated CED for CO₂ is small as expected.

Figure 3.5b shows that SLEOS fits the PFOMA swelling isotherms in CO₂ at temperatures of from 50 °C to 100 °C with good accuracy. Phase equilibrium of the PEO-CO₂ system has been examined by many groups.^{40, 48-50} Weidner et al. measured the mass fraction of CO₂ in PEO (4 kg/mole) at 55, 60, 80, 100 °C and suggested that the solubility of CO₂ in PEO is almost independent on PEO molar weight.⁴⁸ Similar results were obtained by Gourgouillon and co-workers.⁴⁰ We fit Weidner et al.'s data⁴⁸ for the four available temperatures, as shown in Figure 3.5c. It is noteworthy that Gourgouillon et al.⁴⁰ also modeled Weidner et al.'s data with the SLEOS, but with a different set of CO₂ EOS parameters.

Table 3.5 summarizes the values of k_{12} fitted from the swelling isotherms and the corresponding χ values (eq 3.10) calculated at all temperatures. Firstly, as expected, the

Table 3.3: Sanchez-Lacombe Pure Component Characteristic Parameters

Component	T* (K)	P* (atm)	ρ^* (g/cm ³)	Ref
CO ₂	283	6504	1.62	42
PFOMA	540.01	4399	1.677	43
PEO	658	4787	1.182	44

Table 3.4: Estimated Cohesive Energy Density (CED) from the Parameters in Table 3.3

Component	60 °C, 13.9 MPa		145 °C, 13.9 MPa	
	$\tilde{\rho}$	CED (MPa)	$\tilde{\rho}$	CED (MPa)
CO ₂	0.262	45.2	0.134	10.1
PFOMA	0.893	356	0.826	304
PEO	0.933	423	0.885	380

Table 3.5: SLEOS Fitting Results for PFOMA and PEO in Sc-CO₂

T (°C)	PFOMA		PEO		$\Delta\chi$
	k ₁₂	χ	k ₁₂	χ	
50	-0.0739	0.82			
55*	-0.0765	0.86	-0.0247	1.39	0.53
60*	-0.0758	0.90	-0.0237	1.46	0.56
80*	-0.0580	1.17	-0.0300	1.61	0.44
100*	-0.0461	1.40	-0.0386	1.80	0.40
145*,**	-0.0331	1.77	-0.0498	2.00	0.23

* Swelling isotherm estimated based on % swelling vs. CO₂ activity curve for PFOMA films. The estimated and calculated isotherm for 145 °C is not shown in Figure 3.5b.

** Swelling isotherm estimated based on % swelling vs. CO₂ activity curve for PEO films. Similarly to PFOMA, a superposed isotherm curve for PEO can be produced (plot not shown), if one plots Weidner et al.'s sorption data at all four temperatures versus CO₂ activity.

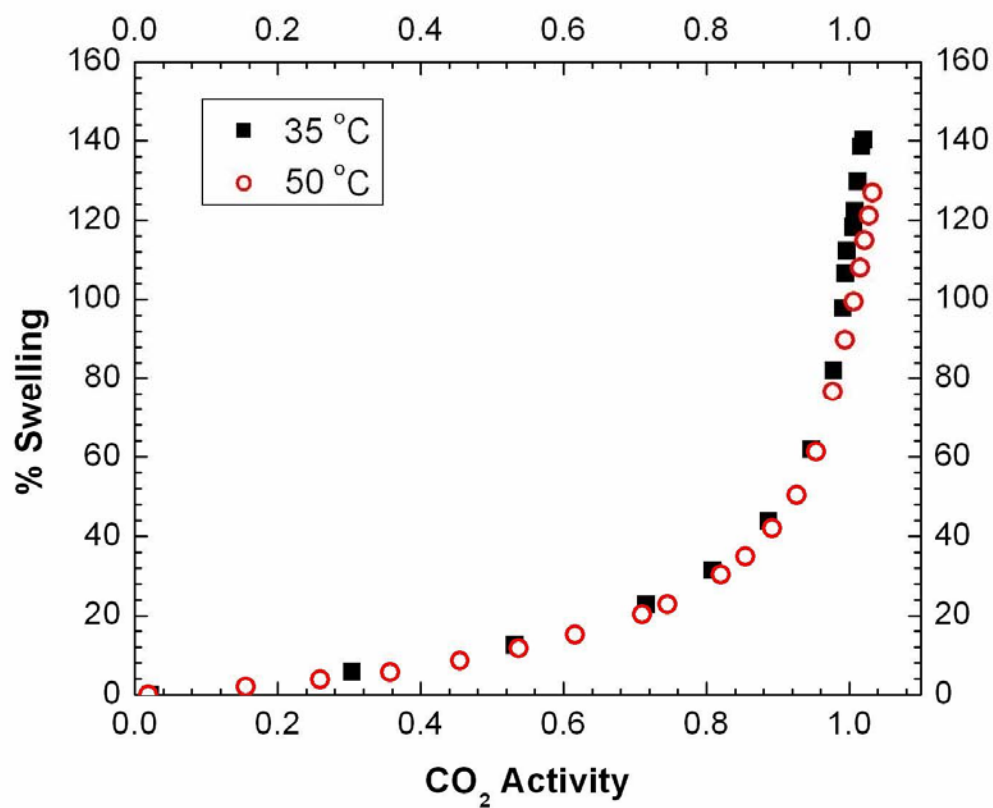


FIGURE 3.5: (a) Experimentally measured % swelling as the function of CO₂ activity for PFOMA films ($h \sim 110$ nm).

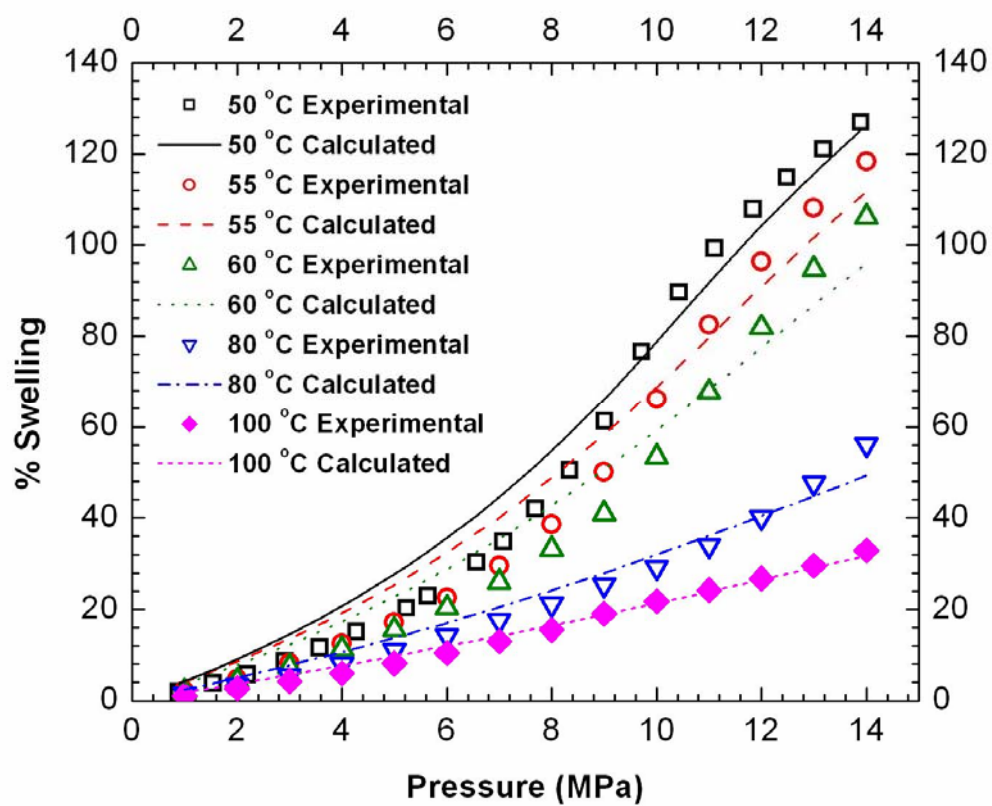


FIGURE 3.5: (b) SLEOS fitting of the experimental and extrapolated swelling isotherms for PFOMA films in Sc-CO₂.

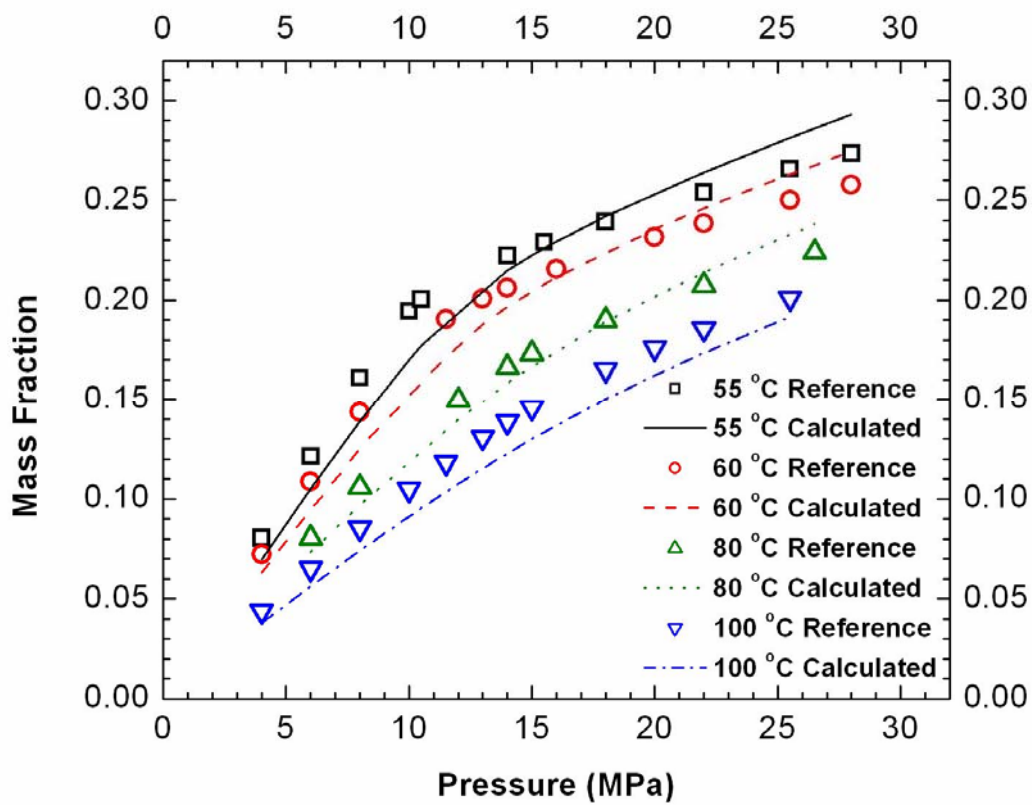


FIGURE 3.5: (c) SLEOS fitting of the mass fraction of CO₂ in PEO based on the work by Weidner et al.⁴⁸.

SLEOS calculated values for $\chi_{\text{PFOMA-CO}_2}$ are always lower than those for $\chi_{\text{PEO-CO}_2}$, suggesting that the interaction between PFOMA and CO₂ is more favorable. Secondly, the observed increase in χ with increasing temperature indicates that the interaction between polymers and CO₂ becomes less favorable, consistent with the decreasing CO₂ solubility in polymers with increasing temperature. This trend is opposite to the temperature dependence of classic χ_{FH} , and is the reason why the simplified Flory-Huggins theory does not explain the commonly observed LCST behavior in polymer-solvent systems. Thirdly, as CO₂ temperature increases, the value of $\Delta\chi = |\chi_{\text{PEO-CO}_2} - \chi_{\text{PFOMA-CO}_2}|$ decreases, suggesting that CO₂ becomes less of a selective solvent towards PFOMA. In Figure 3.6, the calculated χ values for both PFOMA-CO₂ and PEO-CO₂ are plotted versus $1/T$ and the trend of decreasing difference in χ as increasing temperature is clearly demonstrated.

3.4 DISCUSSION

It is well known that the phase diagram of a diblock copolymer (A-b-B) is typically determined by the interaction parameter, χ_{AB} , the total number of monomers that compose the chain, N and the volume fraction of one block, f .^{20, 51} At a given f , when $\chi_{\text{AB}}N$ exceeds the corresponding critical value, the diblock can change from a disordered state to an ordered state. For example, the critical $\chi_{\text{AB}}N$ is 10.5 for $f = 0.5$. Figure 3.7a illustrates schematically the effects of adding a neutral or selective solvent on the $\chi_{\text{AB}}N$ versus f_{A} phase diagram of a diblock copolymer. Generally speaking, adding a neutral solvent is equivalent to a vertical trajectory, whereas adding a selective solvent is equivalent to a diagonal trajectory.⁵² These effects will be examined into detail next.

When an A-b-B copolymer is diluted in a solvent, the effective interaction parameter will change to^{52, 53}

$$\chi_{\text{eff}} \sim \phi(\chi_{AB} + \Delta\chi) = \phi(\chi_{AB} + |\chi_{A-S} - \chi_{B-S}|) \quad (3.12).$$

Here Φ is the volume concentration of the copolymer in the solvent and $\Delta\chi$ is the difference between A-solvent and B-solvent interaction parameters. For the case of a neutral solvent, $\Delta\chi \sim 0$, and consequently,

$$\chi_{\text{eff}}N \sim \phi\chi_{AB}N \quad (3.13).$$

Thus when adding a neutral solvent into a BCP system ($\Phi < 1$), $\chi_{\text{eff}}N$ decreases and the system may change from an ordered state to a disordered one. In other words, neutral solvent can effectively screen the unfavorable segmental contacts between A and B blocks, and can enhance phase compatibility. Because CO_2 can be considered as a neutral solvent for the two systems examined by Vogt and co-workers^{12, 13}, it is not surprising that CO_2 induces phase compatibility relative to vacuum. For example, for the diblock of PS-b-PIP¹³, Vogt et al. showed the degrees of swelling for PS and PIP at 35°C are very similar, indicating that CO_2 interacts almost equally with both blocks.

However, the effects of a selective solvent on the compatibility of BCP systems can be complicated due to the interplay between Φ and $\Delta\chi$. If we assume that the selective solvent preferentially swells B block, then the volume fraction of A block and effective interaction parameter will change, accordingly^{52, 53}

$$f_A' \sim f_A\phi \quad (3.14),$$

$$\chi_{\text{eff}}N \sim \phi(\chi_{AB} + \Delta\chi)N \sim \phi(\chi_{AB} + |\chi_{AS} - \chi_{BS}|)N \quad (3.15).$$

In many cases, the presence of a large difference between the two polymer-solvent interaction parameters ($\Delta\chi$ is large and positive) raises $\chi_{\text{eff}}N$ from a disordered state into an ordered state. In other words, if the $\Delta\chi$ effect dominates the contribution resulting from Φ less than unity, then phase segregation can be induced by adding selective solvents. In addition, according to eq 3.14, adding a selective solvent for block B can lead to a significant decrease in the volume fraction of the A block, f_A . As a

consequence, the decrease in f_A can cause a change in the equilibrium phase structure. For instance, Hanley et al. observed a sequence of phase changes from lamella (L) to perforated layer (PL) to gyroid (G) to cylinder (C) as the dilation of a slightly selective solvent to poly(styrene-*b*-isoprene).⁵²

Now we can apply the above discussion on PEO-*b*-PFOMA system annealed in Sc-CO₂ conditions. Based on eq 3.14, selective swelling of PFOMA by CO₂ decreases the effective volume fraction of PEO block (f_{PEO}' decreases). However, since f_{PEO} already lies in the spherical phase region in vacuum, further decreasing it will not change the equilibrium phase structure. In addition, according to eq 3.15, CO₂ annealing introduces two competing terms to $\chi_{eff}N$: the overall copolymer volume fraction in the presence of CO₂, Φ , which is less than 1 and a positive $\Delta\chi$, due to the preferential interaction between PFOMA and CO₂.⁴⁶ The observed CO₂ induced phase segregation relative to vacuum annealing at the same temperature suggests that the $\Delta\chi$ effect is dominant, therefore $(\chi_{eff}N)_{CO_2} > (\chi N)_{VAC}$. This induced phase separation by the dominating $\Delta\chi$ effect has been observed in other systems, where a large disparity in the strength of polymer-solvent interactions exists.^{39, 54}

Next, we will discuss how changing CO₂ temperature affects the phase diagram of PEO-*b*-PFOMA. Here we will focus on the $\Delta\chi$ effect since that of Φ is expected to be minor. Figure 3.7b illustrates schematically the effects of CO₂ as a selective solvent on the phase diagram of PEO-*b*-PFOMA. In vacuum, the diblock films are in disordered states at both temperatures ($T_1 < T_2$); in Sc-CO₂ and at 13.9 MPa, the diblock is ordered at T_1 and disordered at T_2 . As shown in Figure 3.7b, adding a selective solvent is equivalent to a diagonal trajectory⁵² in the χN versus f phase diagram. At lower temperature T_1 , the higher degree of CO₂ swelling reduces f_{PEO} more and thus the

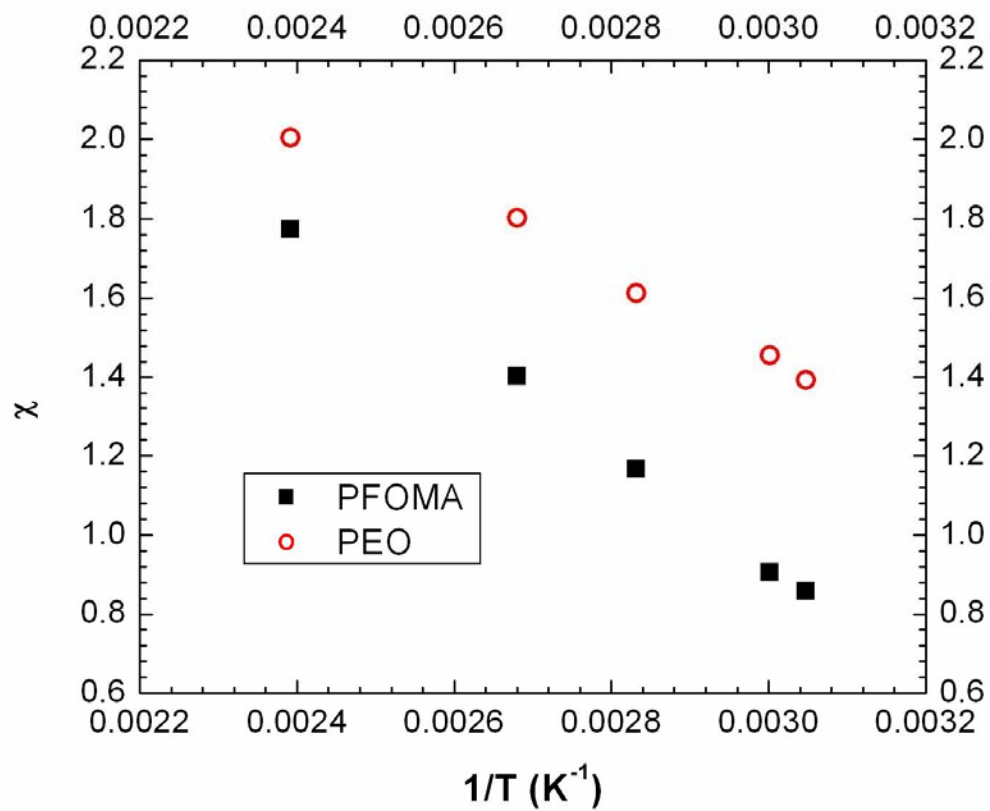


FIGURE 3.6: Calculated interaction parameters, $\chi_{\text{PFOMA-CO}_2}$ and $\chi_{\text{PEO-CO}_2}$, vs. temperature ($1/T$).

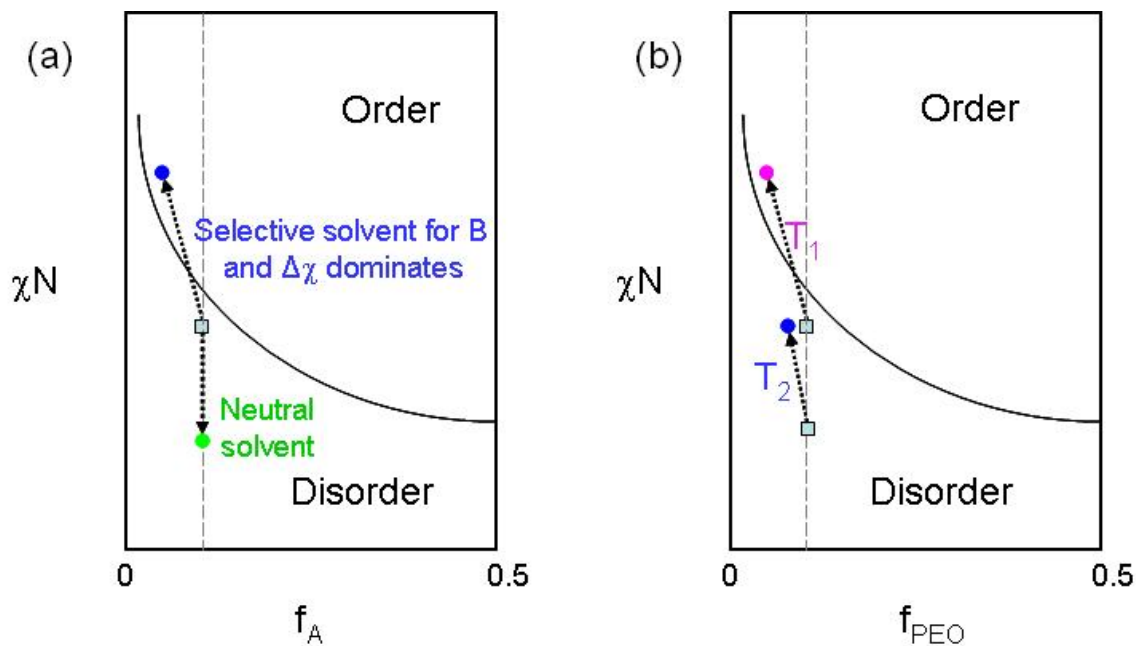


FIGURE 3.7: (a) Schematic phase diagrams for a typical diblock copolymer to show the effects of both neutral and selective solvents. (b) Schematic phase diagrams for PEO-b-PFOMA diblock copolymer ($T_1 < T_2$). Squares represent the case in vacuum while dots represent the case in CO_2 . At lower temperature T_1 (such as 116 °C), the diblock is disordered in vacuum and ordered in CO_2 , 13.9 MPa; while at higher temperature T_2 (such as 145 °C), the diblock is disordered in both vacuum and CO_2 , 13.9 MPa.

trajectory is steeper (the horizontal distance between the two ending points along the trajectory is larger). In addition, from Table 3.5, since $\Delta\chi$ decreases with increasing temperature, the increase in $\chi_{\text{eff}}N$ is more distinct at lower temperature T_1 (the vertical distance between the two ending points along the trajectory is larger). As a result, only at T_1 , the change in $\chi_{\text{eff}}N$ is large enough to shift the diblock from a disordered state in vacuum to an ordered state in CO_2 .

Finally, we would like to point out that in order to calculate the T_{ODT} of PEO-b-PFOMA in Sc-CO_2 , one must consider the phase stability of a ternary system. In the case of a diblock copolymer in CO_2 , the corresponding phase stability calculation of the ternary system is not available and thus will not be examined further. It is also evident that if χ_{eff} decreases with increasing temperature (because $\Delta\chi$ decreases), then since the characteristic spacing of phase segregated BCP domains, L , is proportional to χ_{AB}^α (for example, α is 1/6 for strongly segregated systems),^{20, 51} one would expect L to decrease with increasing temperature. From Table 3.2, as CO_2 annealing temperature increases from 60 to 116 °C, the values of both L_1 and L_2 slightly decrease. However, this decrease is within the experimental error range and is therefore inconclusive.

3.5 CONCLUSIONS

We demonstrate that supercritical CO_2 induces phase segregation in PEO-b-PFOMA (5k/52k) diblock copolymer thin films. The diblock films remain disordered in vacuum within the temperature range of 80-180 °C. In supercritical CO_2 at 13.9 MPa, between 60-116 °C, the diblock films are ordered, with an equilibrium structure of PEO spheres embedded in the matrix of PFOMA. However at 145 °C the diblock films are disordered. This change of morphology suggests a T_{ODT} between 116 °C and 145 °C. Regression of the swelling isotherms of PFOMA and PEO homopolymers in CO_2 with

the Sanchez-Lacombe equation of state proves that as temperature increases, $\Delta\chi = |\chi_{\text{PEO-CO}_2} - \chi_{\text{PFOMA-CO}_2}|$ decreases significantly. The CO₂ induced phase segregation is due to the selectivity of CO₂ toward PFOMA block (large $\Delta\chi$), whereas the effect of dilution Φ must be minor, as it is in the opposite direction of the experimental observations. At high temperatures, the preferential swelling becomes small enough ($\Delta\chi$ becomes small) that CO₂ no longer induces a transition to the ordered state.

3.6 REFERENCES

1. Segalman, R. A. *Materials Science and Engineering R* **2005**, 48, 191.
2. Fasolka, M. J.; Mayes, A. M. *Annu. Rev. Phys. Chem.* **2001**, 31, 323.
3. Thurn-Albrecht, T.; Schotter, J.; Kastle, G. A.; Emley, N.; Shibauchi, T.; Krusin-Elbaum, L.; Guarini, K.; Black, C. T.; Tuominen, M. T.; Russell, T. P. *Science* **2000**, 290, 2126.
4. Sundrani, D.; Darling, S. B.; Sibener, S. J. *Langmuir* **2004**, 20, 5091.
5. Bodycomb, J.; Funaki, Y.; Kimishima, K.; Hashimoto, T. *Macromolecules* **1999**, 32, 2075.
6. Albalak, R. J.; Thomas, E. L.; Capel, M. S. *Polymer* **1997**, 38, 3819.
7. Li, Y.; Meli, L.; Lim, K. T.; Green, P. F.; Johnston, K. P. *Macromolecules* **2006**, 39, 7044.
8. DeSimone, J. M. *Science* **2002**, 297, 799.
9. Kazarian, S. G. *Polymer Science, Ser. C* **2000**, 42, 78.
10. Pai, R. A.; Humayun, R.; Schulberg, M. T.; Sengupta, A.; Sun, J. N.; Watkins, J. J. *Science* **2004**, 303, 507.
11. Meli, L.; Li, Y.; Lim, K. T.; Johnston, K. P.; Green, P. F. *Manuscript in preparation* **2006**.
12. Vogt, B. D.; Brown, G. D.; RamachandraRao, V. S.; Gupta, R. R.; Lavery, K. A.; Francis, T. J.; Russell, T. P.; Watkins, J. J. *Macromolecules* **2003**, 36, 4029.

13. Vogt, B. D.; Brown, G. D.; RamachandraRao, V. S.; Watkins, J. J. *Macromolecules* **1999**, 32, 7907.
14. Watkins, J. J.; Brown, G. D.; RamachandraRao, V. S.; Pollard, M. A.; Russell, T. P. *Macromolecules* **1999**, 32, 7737.
15. RamachandraRao, V. S.; Gupta, R. R.; Russell, T. P.; Watkins, J. J. *Macromolecules* **2001**, 34, 7923.
16. Arceo, A.; Green, P. F. *J. Phys. Chem. B* **2005**, 109, 6958.
17. Lim, K. T.; Lee, M. Y.; Moon, M. J.; Lee, G. D.; Hong, S. S.; Dickson, J. L.; Johnston, K. P. *Polymer* **2002**, 43, 7043.
18. Arnold, M. E.; Nagai, K.; Freeman, B. D.; Spontak, R. J.; E., B. D.; DeSimone, J. M.; Pinnau, I. *Macromolecules* **2001**, 34, 5611.
19. Madsen, L. A. *Macromolecules* **2006**, 39, 1483.
20. Bates, F. S.; Fredrickson, G. H. *Annu. Rev. Phys. Chem.* **1990**, 41, 525.
21. Loo, Y. L.; Register, R. A.; J., R. A. *Phys. Rev. Lett.* **2000**, 84, 4120.
22. Sirard, S. M.; Green, P. F.; Johnston, K. P. *J. Phys. Chem. B* **2001**, 105, 766.
23. Green, P. F. *J. Polym. Sci. B: Polym. Phys.* **2003**, 41, 2219.
24. Li, Y.; Loo, Y.-L.; Register, R. A.; Green, P. F. *Macromolecules* **2005**, 38, 7745.
25. Limary, R.; Green, P. F. *Macromolecules* **2002**, 35, 2535.
26. Shull, K. R. *Macromolecules* **1996**, 29, 8487.
27. Xu, T.; Hawker, C. J.; Russell, T. P. *Macromolecules* **2005**, 38, 2802.
28. Segalman, R. A.; Hexemer, A.; Hayward, R.; Kramer, E. J. *Macromolecules* **2003**, 36, 3272.
29. Reiter, G.; Sommer, J. U. *Phys. Rev. Lett.* **1998**, 80, 3771.
30. Lin, Z.; Kim, D. H.; Wu, X.; Boosahda, L.; Stone, D.; LaRose, L.; Russell, T. P. *Adv. Mater.* **2002**, 14, 1373.
31. Reiter, G.; Castelein, G.; Sommer, J. U. *Phys. Rev. Lett.* **2001**, 87, 226101.
32. Ibers, J. A.; Hamilton, W. C., *International Tables for X-Ray Crystallography*. The Kynoch Press: Birmingham, England, **1974**.

33. Shibayama, M.; Hashimoto, T.; Kawai, H. *Macromolecules* **1983**, 16, 16.
34. Reiter, G. *J. Polym. Sci. B: Polym. Phys.* **2003**, 41, 1869.
35. Pham, J. Q.; Johnston, K. P.; Green, P. F. *J. Phys. Chem. B* **2004**, 108, 3457.
36. Sirard, S. M.; Ziegler, K. J.; Sanchez, I. C.; Green, P. F.; Johnston, K. P. *Macromolecules* **2002**, 35, 1928.
37. Sanchez, I. C.; Lacombe, R. H. *Macromolecules* **1978**, 11, 1145.
38. Sanchez, I. C.; Lacombe, R. H. *J. Phys. Chem.* **1976**, 80, 2352.
39. RamachandraRao, V. S.; Watkins, J. J. *Macromolecules* **2000**, 33, 5143.
40. Gourgouillon, D.; da Ponte, M. N. *Phys. Chem. Chem. Phys.* **1999**, 1, 5369.
41. Liu, D.; Li, H.; Noon, M. S.; Tomasko, D. *Macromolecules* **2005**, 38, 4416.
42. Sanchez, I. C.; Stone, M. T., Statistical Thermodynamics of Polymer Solutions and Blends. In *Polymer Blends Volume I: Formulation*, Paul, D. R.; Bucknall, C. B., Eds. John Wiley & Sons, Inc: **2000**.
43. *From Dr. Gabriel Luna Barcenas, to be published.*
44. Harrison, K. L.; Johnston, K. P.; Sanchez, I. C. *Langmuir* **1996**, 12, 2637.
45. Condo, P. D.; Sumpter, S. R.; Lee, M. L.; Johnston, K. P. *Ind. Eng. Chem. Res.* **1996**, 35, 1115.
46. O'Neill, M. L.; Cao, Q.; Fang, M.; Johnston, K. P.; Wilkinson, S. P.; D., S. C.; Kerschner, J. L.; Jureller, S. H. *Ind. Eng. Chem. Res.* **1998**, 37, 3067.
47. Panayiotou, C. G. *Fluid Phase Equilibria* **1997**, 131, 21.
48. Weidner, E.; Wiesmet, V.; Knez, Z.; Skerget, M. *J. Supercritical Fluids* **1997**, 10, 139.
49. Guadagno, T.; Kazarian, S. G. *J. Phys. Chem. B* **2004**, 108, 13995.
50. Daneshvar, M.; Kim, S.; Gulari, E. *J. Phys. Chem.* **1990**, 94, 2124.
51. Matsen, M. W.; Bates, F. S. *Macromolecules* **1996**, 29, 1091.
52. Hanley, K. J.; Lodge, T. P. *J. Poly. Sci., Part B: Poly. Phys.* **1998**, 36, 3101.
53. Helfand, E.; Tagami, Y. *J. Chem. Phys.* **1972**, 56, 3592.

54. Robard, A.; Patterson, D.; Delmas, G. *Macromolecules* **1977**, 10, 706.

Chapter 4: Structural Inversion of Micellar Block Copolymer Thin Films

Polystyrene-*b*-poly(1,1',2,2'-tetrahydroperfluorooctyl methacrylate) (PS-*b*-PFOMA) thin films, cast from a cosolvent mixture of Freon 113 and toluene onto Si/SiO_x substrates, form spherical micelles; the cores are composed of PFOMA chains with a PS corona. Upon exposing the films to supercritical CO₂ (Sc-CO₂), the morphology inverts, wherein the core is composed of PS chains and the PFOMA chains constitute the corona. In each case, the free surface and polymer/substrate layers are enriched with PFOMA. The size of the PS cores is found to increase with decreasing Sc-CO₂ activity. This size variation is discussed in light of recent theoretical developments that account for the effect of Sc-CO₂ activity on PS-CO₂ interfacial tension and chain stretching of the corona versus the core.

Reprinted with permission from Li, Y.; Meli L.; Lim K. T.; Johnston, K. P.; Green P. F. *Macromolecules* **2006**, 39, 7044-7054. Copyright © 2006 American Chemical Society.

4.1 INTRODUCTION

Block copolymers are exploited for a diverse range of applications, which include templates to create periodic patterns for nanolithography and for “bottom up” fabrication in microelectronics.¹⁻¹¹ Important challenges are typically associated with processing to control the long-range orientation and lateral ordering of the nanometer-scale domains. Strategies that use external fields are employed, such as electric fields,^{6, 12} graphoepitaxy,^{11, 13} chemical patterned substrates,¹⁴⁻¹⁷ for thin films, and shear^{18, 19} and temperature gradients,²⁰ for bulk.

Liquid and supercritical CO₂ have been shown to be attractive alternatives to organic solvents in many polymer processes.²¹⁻²⁴ Sorption of CO₂ into polymers can cause significant swelling and plasticization, lowering the glass transition temperature T_g of amorphous polymers, inducing crystallization in crystalline polymers,^{22, 25-28} and influencing order-disorder transition (ODT) temperatures and ordering kinetics of block copolymers.²⁹⁻³² Aside from the environmentally benign properties and easily accessible critical conditions ($T_c = 31\text{ }^\circ\text{C}$ and $P_c = 73.8\text{ bar}$) of CO₂, the solvent strength of CO₂ can be tuned markedly with pressure and temperature. While most research has focused on bulk polymer systems in supercritical CO₂ (Sc-CO₂),²² the effects of Sc-CO₂ on thin polymer films have received far less attention. Studies in our laboratories have suggested a strong influence of Sc-CO₂ on the sorption, on the glass transition temperatures (T_g), on the morphological instability of homopolymer thin films and on the ordering transition of block copolymer thin films.^{29, 33-37}

In this study we show that polystyrene-*b*-poly(1,1',2,2'-tetrahydroperfluorooctyl methacrylate) (PS-*b*-PFOMA) thin films spin cast, using a cosolvent of Freon 113 and toluene, onto Si/SiO_x substrates, form micelles with a PFOMA core and PS corona. We

show that, upon annealing in a compressed solvent, Sc-CO₂, the structure is inverted and the PS chains, which formally constituted the continuous phase (corona), now form the core phase and the PFOMA chains form the continuous phase. The sizes of PS cores increase with increasing Sc-CO₂ annealing temperatures at a constant pressure. These observations are rationalized based on the change of interfacial tension between PS and CO₂ as well as the relative stretching of PS and PFOMA chains as Sc-CO₂ activity varies.

4.2 EXPERIMENTAL SECTIONS

In this section, the synthetic procedures used to prepare the polymers and the processing strategies, involving Sc-CO₂ annealing used to prepare the films, are described. In addition, the characterization techniques, scanning transmission electron microscopy (STEM) and scanning force microscopy (SFM), used for morphological analysis, X-ray photoelectron spectroscopy (XPS) for surface compositional analysis, and spectroscopic ellipsometry for analyzing the swelling of the films in Sc-CO₂ are described.

4.2.1 Synthesis of Materials

4.2.1a Preparation of PSt-Br Macroinitiator

A Florence (round-bottom) flask containing a Teflon coated magnetic stir bar was charged with CuBr and bipy(2,2'-dipyridyl) (Bpy). Prior to use, the flask was vacuumed and back-filled with dry nitrogen several times. Ethyl-2-bromoisobutyrate (EtBr) and styrene (St) were then added under nitrogen atmosphere with the ratio of [St]/[EtBr]/[CuBr]/[Bpy] as 19.2:1:1:3. The flask was subsequently placed in an oil bath and heated to 110 °C with continuous stirring for 24 h. After polymerization, the reaction mixture was diluted with tetrahydrofuran (THF) and passed through a neutral Al₂O₃

column to remove the catalyst. The solution was then precipitated into methanol, and the polystyrene (PSt-Br) product was filtered and dried in a vacuum. The molecular weight of polystyrene (PSt-Br) was determined to be 27,000 g/mol by ^1H NMR, with the polydispersity of 1.12 determined by gel permeation chromatography (GPC).

4.2.1b Synthesis of PSt-b-PFOMA Block Copolymer

PSt-Br macroinitiator, CuCl, and Bpy were placed in a Florence flask with Teflon coated magnetic stir bar. After the flask was vacuumed and back-filled with dry nitrogen several times, trifluorotoluene (TFT) was added into the flask. The solution was degassed with dry nitrogen, and then 1,1',2,2'-tetrahydroperfluorooctyl methyl methacrylate (FOMA) was introduced to the solution with the ratio of [FOMA]/[PSt-Br]/[CuCl]/[Bpy] as 198:1:1:3. Polymerization was performed at 110 °C in nitrogen blanket for 37 h. After polymerization, the mixture was diluted with TFT and passed through the Al_2O_3 column. Then the reaction solution was precipitated into heptane, and the resulting product was filtered and dried in vacuum for 12 h. After extraction with cyclohexane to remove unreacted macroinitiator, the polymer was filtered and dried in a vacuum. The molecular weight of the resulting polystyrene-b-poly(1,1',2,2'-tetrahydroperfluorooctyl methacrylate) (PS-b-PFOMA) block polymer was determined to be 154,000 g/mol by comparing the signal of PSt and PFOMA block in ^1H NMR spectrum.

Table 4.1: Characteristic Properties of PS and PFOMA in the Copolymer

Parameters	PS	PFOMA
Molecular weight, M_n (kg/mole)	27	127
Glass transition temperature, T_g ($^{\circ}\text{C}$)	100	50 ³⁸
Density, ρ (g/cm^3)	1.06	1.53 ^a
Monomer molecular weight, M_o (g/mole)	104	432
Number of monomers, N	260	294
Surface tension, γ (dyn/cm)	41	< 11 ⁴⁰
Volume fraction, f	0.25 ^b	0.75 ^b
Volume per monomer, V (nm^3)	0.167 ³⁹	0.389 ^c
End-to-end distance in unperturbed state, l_e (nm)	10.5 ³⁹	14.5 ^c
Maximum stretching length, l_m (nm)	80.1 ^d	90.5 ^d

^a Data provided by Dr. Gabriel Luna-Barcenas, to be published.

$$^b f = \frac{M_{PS} / \rho_{PS}}{M_{PS} / \rho_{PS} + M_{PFOMA} / \rho_{PFOMA}}.$$

$$^c \text{Based on: } \frac{V_{PFOMA}}{V_{PS}} = \left(\frac{l_{ePFOMA}}{l_{ePS}} \right)^3 = \frac{Mo_{PFOMA} / \rho_{PFOMA}}{Mo_{PS} / \rho_{PS}}.$$

$$^d l_m = 2N \times 1.54 \text{ \AA}.$$

4.2.2 Thin Film Preparation and Characterization

The block copolymer of PS-*b*-PFOMA (properties listed in Table 4.1³⁸⁻⁴⁰) was dissolved using a cosolvent of 1,1,2-trichlorotrifluoroethane (Freon 113) and toluene. The resulting transparent solutions have weight concentrations of 0.5-1% polymer and 15-25% toluene. Dynamic light scattering (DLS) measurements were performed using a Brookhaven laser light scattering instrument (Brookhaven Instruments Corp.), with a diode laser (24 mV) at a wavelength of 659 nm at 20 °C.

Thin films were prepared by spin casting the solutions onto silicon wafers with a native oxide layer (Wafer World Inc.), and the thicknesses of the films were measured by spectroscopic ellipsometry (J. A. Wollam Co., Inc.). Different thicknesses were obtained by controlling the spin rate and concentration of the copolymer solutions. Samples for STEM imaging were prepared by floating as-cast films into water and picking up with electron transparent silicon nitride windows (SPI supplies) to achieve film uniformity.

4.2.3 Supercritical CO₂ Annealing

The samples (supported by either Si/SiO_x or silicon nitride windows) were loaded into a fixed volume cell, which was subsequently sealed and pressurized with carbon dioxide (Air Products, > 99.999%) using a manual pressure generator (High-Pressure Equipment Co.). The pressure was controlled with a strain gauge pressure transducer (Sensotec) calibrated to within $\pm 7 \times 10^{-3}$ MPa. Typically, the temperature was controlled to ± 0.1 °C by immersing the pressure cell into a water bath equipped with a temperature controller (Julabo, Inc.). For high-temperature (above 100 °C) experiments, the pressure cell was wrapped by heating tapes connected to a temperature controller (Omega Engineering, Inc.). The diblock was in a rubbery state under all conditions studied (35, 50, 75, 140 °C and at the Sc-CO₂ pressure of 13.8 MPa). After a certain annealing period

(varying from 10 hours to 10 days), the cell was cooled to approximately 25 °C and depressurized by venting Sc-CO₂ as a vapor from the top of the cell. In the process of depressurization and cooling, the films returned to glassy state and the morphology of the films was frozen.

4.2.4 Morphological Analysis Using Scanning Force Microscopy (SFM) and Scanning Transmission Electron Microscopy (STEM)

Morphological characterization of the films was achieved by a combination of scanning force microscopy (SFM) and scanning transmission electron microscopy (STEM). SFM measurements were performed in tapping mode using a Nanoscope IV/Dimension 3100 (Digital Instruments). Identical morphology was observed by SFM for samples supported by Si/SiO_x wafers or silicon nitride windows. Figure 4.1 is indicative of the micellar structure of the films formed from the solution; the images are discussed in further detail in the next section.

Considerable more detail of the morphological structure of the film can be obtained using STEM. STEM imaging was performed using a JEOL 2010F transmission electron microscope operating at an accelerating voltage 200 kV in scanning mode, using a high angle annular dark field (HAADF) detector. HAADF imaging, also called Z-contrast imaging, enabled observation of the species present based on differences in atomic numbers (Z), densities, and sample thicknesses. Thus, for copolymer samples without vapor staining, contrast was provided by the difference between the densities of the two constituent blocks; the denser PFOMA regions appear brighter than the PS domains. In some cases, samples were exposed to the vapor of an aqueous RuO₄ solution (SPI supplies) for 5 minutes to selectively stain the PS-rich domains. In this case, the selectively adsorbed ruthenium compound provides brighter contrast to the PS phase.

Figure 4.2 shows typical images of as-cast films with the circular PFOMA cores and the PS corona (continuous phase). This will be discussed in further detail later.

4.2.5 X-Ray Photoelectron Spectroscopy (XPS)

XPS measurements were performed on PS-b-PFOMA films with thicknesses on the order of 100 nm using a Physical Electronics (PHI) model 5700 spectrometer employing a monochromatic Al $K\alpha_{1,2}$ source. XPS spectra of PS ($M_n = 30$ kg/mole, from Pressure Chemical) and poly(1,1'-dihydroperfluorooctyl methacrylate) (PDHFOMA) ($M_n = 100$ kg/mole, synthesis procedure was described elsewhere⁴¹) homopolymer films were taken as references. The binding energy of the instrument was calibrated by using Au $4f_{7/2}$, Cu $1p_{3/2}$ and Ag $3d_{5/2}$. Typical operating conditions were the following: 1×10^{-9} Torr chamber pressure; 14 kV; 250W for the Al X-ray source. Survey scans from 0 to 1000 eV were taken with the pass energy of 93.9 eV. High-resolution elemental scans of the C $1s$, F $1s$ regions were collected with the pass energy of 11.75 eV at takeoff angles of 45 and 75° between the sample and analyzer, where the sampling depth was estimated to be 5.7 and 7.8 nm respectively.⁴⁰ The atomic percentages of C and F were determined using XPS peak areas and the appropriate instrumental sensitivity factors. To ensure that the samples were not damaged by long-time X-ray exposure, three high-resolution elemental scans were carried out subsequently, where the resulting C and F atomic percentages were in good agreement within experimental error ranges. In some experiments, the topmost part of the samples were etched by Argon (Ar⁺) ion sputtering at 2 kV voltage and 1 μ A beam current (2 mm \times 2 mm area) for 5 s, and high-resolution elemental scans of C $1s$ and F $1s$ regions were then carried out.

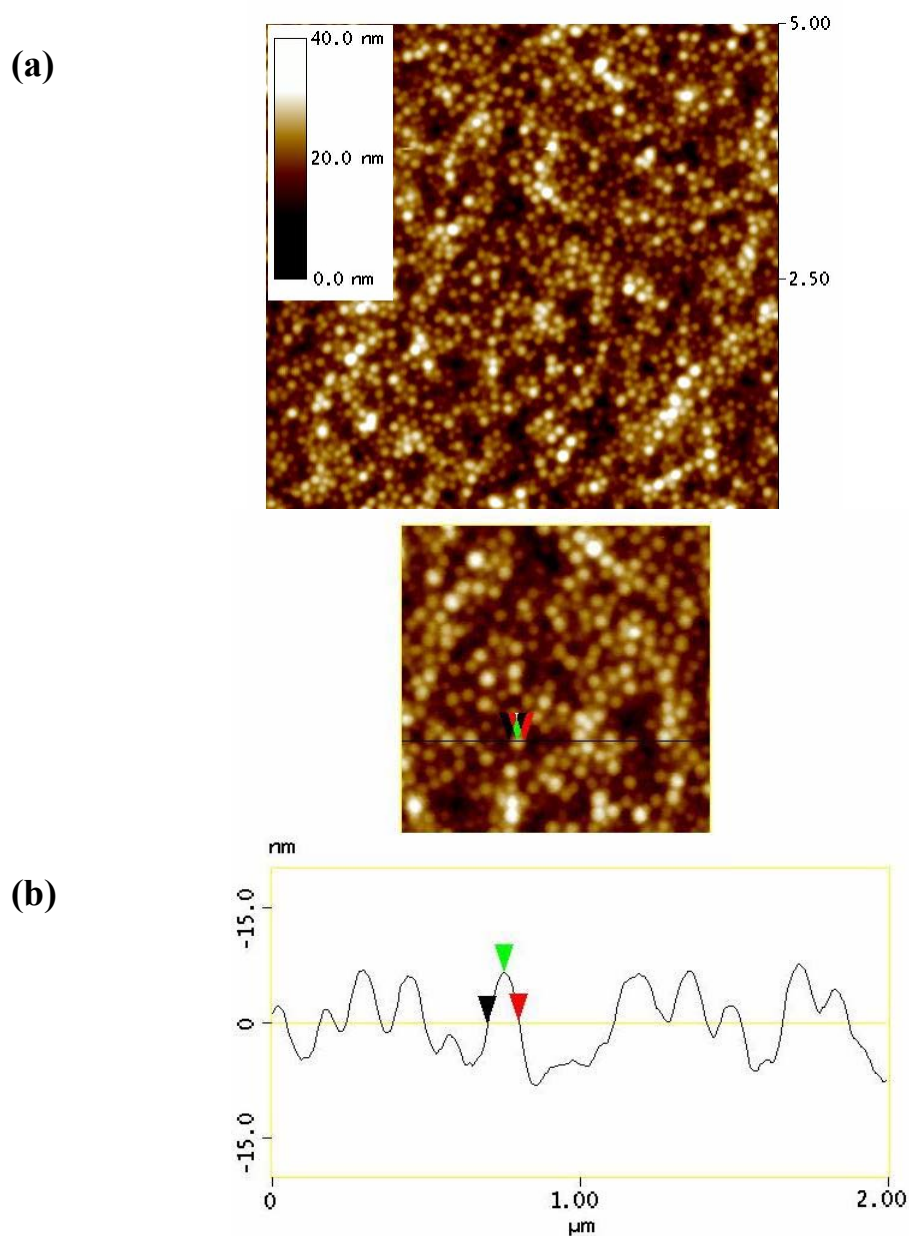
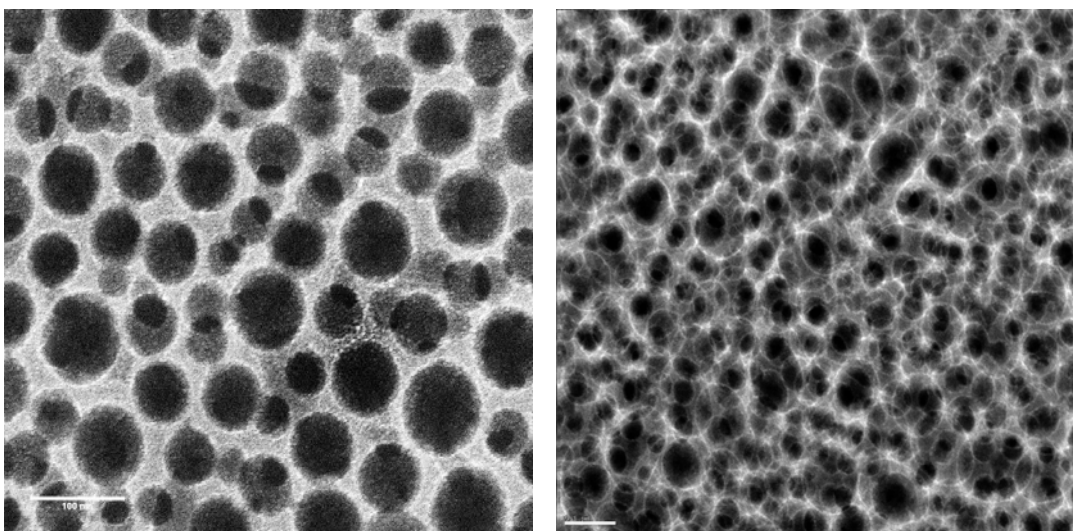


FIGURE 4.1: SFM topography (a) and the corresponding line scan (b) of a PS-b-PFOMA film ($h = 90$ nm) after spin-casting from solution onto Si/SiO_x substrate. The scan sizes are $5\text{ }\mu\text{m}$ in (a) and $2\text{ }\mu\text{m}$ in (b). The colored triangles in the topography (b) are corresponding to those in the line scan. This particular circular feature has a diameter of 101.56 nm (between leftmost and rightmost triangles) and a height of 7.3 nm (between leftmost and middle triangles).



(a)

(b)

FIGURE 4.2: HAADF-STEM images of RuO_4 stained PS-b-PFOMA films after spin casting: (a) a 72 nm film presenting two layers of micellar aggregates; (b) an even thicker film with more layers of micellar aggregates. The scale bars in both images are 100 nm.

4.2.6 *In-Situ* Swelling Experiments

Spectroscopic ellipsometry (J. A. Wollam Co., Inc.) was used to measure *in-situ* swelling of PS ($M_n = 30$ kg/mole), PDHFOMA ($M_n = 100$ kg/mole) homopolymers, and PS-*b*-PFOMA copolymer films (thicknesses between 100 and 120 nm) in Sc-CO₂. Detailed experimental setup and analysis procedures had been described elsewhere³⁷. The swelling percentage was determined by the following equation assuming uniaxial swelling

$$Sw\% = \frac{\Delta V}{V_0}(\%) = \frac{h - h_0}{h_0} \times 100\% \quad (4.1).$$

Here V_0 is the initial volume of the film, h is the thickness of the swollen film, and h_0 is the initial thickness of the polymer films determined by spectroscopic ellipsometry at 0 psig.

4.3 RESULTS AND DISCUSSION

This section is divided into three parts. The morphology of the as-cast films, which form a micellar structure (PFOMA core and PS corona), is first discussed. In the section that follows, the evolution of the structure during Sc-CO₂ annealing is discussed; it is shown that the structure inverts, wherein the PS segments constitute the cores of the micelles and PFOMA segments form the corona. Finally, experiments and theory describing the variation of the size of the micelles with Sc-CO₂ activity are discussed.

4.3.1 Self-Assembly of PS-*b*-PFOMA Diblock into Micelle-like Aggregates in Thin Films after Spin-Casting

Typical SFM image of the topography of a PS-*b*-PFOMA thin film supported by the Si/SiO_x substrate is shown in Figure 4.1a. Figure 4.1b shows a small region of the image in Figure 4.1a and an accompanying line scan. The observed circular regions

possess an average feature height of 6.7 ± 1.5 nm and an average diameter of 105 ± 18 nm. Figure 4.2a shows an STEM image of a stained 72 nm thick as-cast sample. It is evident from this figure that the micelles are composed of PFOMA cores embedded in a continuous PS (corona) matrix; the overlapping circular features reveal the presence of two layers of micellar aggregates across the film thickness. The existence of multiple layers of micelles is evident from Figure 4.2b, the image of a much thicker film.

Having described the internal structure of the as-cast films, the free surface structure is now described. Table 4.2 shows the XPS results for as-cast PDHFOMA and PS-*b*-PFOMA films; three observations can be made. First, as the takeoff angle increases from 45 to 75°, the experimental F/C ratio for PS-*b*-PFOMA thin films decreases from 0.81 to 0.68. This decrease indicates that, as expected, PFOMA chains are more segregated to the free surface than PS chains due to their lower surface energy (< 11 dyn/cm). Second, the F/C ratios for both takeoff angles are either comparable or slightly larger than the theoretical value for PS-*b*-PFOMA. They are, however, smaller than the theoretical values for PFOMA. One would anticipate that the surface of PS-*b*-PFOMA films is composed entirely of PFOMA because the surface tension of PFOMA is substantially lower than that of PS. However, our XPS data suggests that the top 8 nm of copolymer films consist predominantly, but not entirely, of PFOMA. This is not surprising in light of the nonequilibrium nature of the spinning process. Third, the last XPS experiment shows that the F/C ratio drops dramatically after sputter etching of the topmost layer of the film. This large decrease also suggests that surface PFOMA segregated layer is very thin and that there is a PS-rich domain below this topmost thin layer. Our results are consistent with the work by Arnord et al.,⁴⁰ where they observed the surface of PDMAEMA-*b*-PFOMA films consisted primarily of PFOMA and that as the XPS takeoff angle increased, the surface concentration of PFOMA decreased rapidly.

Because PFOMA chains form the core of the aggregates, the surface segregated PFOMA layer can be either a half-lamella-like structure^{42, 43} or a thin layer with the fluorinated side chains aligned towards the surface. However, the thickness of this layer (less than 8 nm) is too small for a half-lamella layer (see Table 4.1). Therefore we conclude that a few nanometer thin PFOMA layer, with the fluorinated side groups facing outward, resides at the free surface.

The micellar formation process is now discussed. Amphiphilic block copolymers are known to self-organize into aggregates in water or in selective organic solvents. The adsorption or covalent attachment of block copolymer micelles to solid surfaces has attracted appreciable attention experimentally, during the past decade.⁴⁴⁻⁵³ Theoretical work has been rare, and the effects of interfaces and confinement on the structure of spherical micelles are not well understood. Work by Liquore shows that, unlike micelles in solution, the structures of surface micelles can be strongly affected by an absorbing solid surface, and that the critical surface micelle concentration (CSMC) can be different from the value for bulk micelles.⁵⁰ It is found that if the contact angle between the core-block and the surface is less than a universal value of $\theta_o^C \sim 51^\circ$, then surface micelles appear at a CSMC much lower than the critical micelle concentration (CMC) in bulk solution.⁵⁰

It is evident that micelles do not exist in solution; instead they form during the spin-casting process. Our DLS measurements of the PS-b-PFOMA solutions showed no evidence of particles within a reasonable size-range. Furthermore, solubility tests were performed to examine the solubility of PS and PDHFOMA in the cosolvent mixture. Specifically, a saturated solution of PS in the cosolvent was prepared so that adding one drop of Freon 113 would make the solution turbid and another drop of toluene would make the solution clear. We found that the solubility of PS and PDHFOMA in the

Table 4.2: Atomic Ratio between Fluorine and Carbon from XPS Data for As-Cast Films

Samples	Angle (°)	Sputter time (s)	C (%)	F (%)	F/C Expt.	F/C Cal.
PS	45	0	99.95	0.05	0	0
PDHFOMA [*]	45	0	43.29	56.71	1.31	1.25
PTHFOMA ^{**}						1.08
PS-b-PFOMA	45	0	55.31	44.69	0.81	0.68
PS-b-PFOMA	75	0	59.40	40.60	0.68	0.68
PS-b-PFOMA	75	5	77.93	22.07	0.28	0.68

^{*} PDHFOMA: Poly(1,1'-dihydroperfluorooctyl methacrylate).

^{**} PTHFOMA: Poly(1,1',2,2'-tetrahydroperfluorooctyl methacrylate).

cosolvent is definitely higher than the concentration of the solutions used to spin cast films, suggesting that the surface aggregates were formed upon spin casting. In addition, because the majority of the solvent used was Freon 113, a good solvent for PFOMA, it is expected that any possible aggregates in the solution would possess a PFOMA shell, in contrast to the STEM observations. Therefore, we believe that the surface PS-b-PFOMA aggregates were formed upon spin casting due to the fast evaporation of Freon 113.

The block copolymers form micelles only during the spin coating process; similar results has been observed in other systems.^{54, 55} Lin et al. found that polystyrene-b-poly(ethylene oxide) (PS-b-PEO) formed ordered arrays of cylindrical domains perpendicular to the substrate after spin-casting from a benzene solution.⁵⁵ This ordering of PS-b-PEO after spin-casting can be attributed to two factors. First, benzene is good solvent for both blocks, hence the diblock was phase mixed in the solution. Second, the interfacial tension between PS and PEO blocks increases abruptly as benzene evaporates during the spin-casting process, leading to the formation of phase-separated domains. For the PS-b-PFOMA system, upon spin-casting, Freon 113, which possesses a larger vapor pressure (285 mm Hg at 20 °C) evaporates at much faster rates than toluene, with a vapor pressure of 22 mm Hg at 20 °C. Hence, with the evaporation of Freon 113, the quality of the solvent becomes progressively poorer for the PFOMA block and the effective concentration of the copolymer increases above the critical micelle concentration (CMC), leading to micellar formation.

In summary, the combination of SFM and STEM images indicates PS-b-PFOMA films self-organize into spherical micelle-like aggregates with PFOMA composing the core after spin-casting. The XPS data revealed the existence of PS-rich domains below a thin PFOMA-rich surface layer, with thickness much less than one half of the domain spacing.

4.3.2 Effects of Supercritical CO₂ Annealing on the Morphologies of PS-*b*-PFOMA Thin Films

4.3.2a Inversion of the Core-Shell Composition of PS-*b*-PFOMA Aggregates in Sc-CO₂

Upon Sc-CO₂ annealing the as-cast film, the structure underwent an inversion; the PS chains now constitute the cores. Figure 4.3 shows both the SFM and STEM images of PS-*b*-PFOMA samples annealed in Sc-CO₂ at 75 °C, 13.8 MPa. The SFM image (Figure 4.3a) of the Sc-CO₂ annealed film shows topography of random arrays of circular features, very similar to those before Sc-CO₂ annealing. However, the RuO₄ stained Z-contrast image (Figure 4.3b) reveals that the darker PFOMA domain forms the matrix (corona) of the film, whereas the brighter stained PS chains form the cores of the spheres in this multilayered structure. This reversal in core-shell composition is not surprising due to the fact that Sc-CO₂ is a selective solvent for fluoropolymers.⁵⁶

The structure of the film was confirmed by STEM images of unstained films (without RuO₄ staining, the contrast between PS and PFOMA is only strong enough to show one layer of micellar aggregates), as shown by Figures 4.4a and 4.4b. The denser (higher Z) PFOMA regions (1.53 g/mL) of the film should appear brighter than the PS regions (1.06 g/mL). Figure 4.4a clearly shows black circular features in a bright, hazy matrix, further confirming that PS constitutes the cores after Sc-CO₂ annealing. It is evident that CO₂ annealing is also responsible for an increased degree of lateral ordering, as shown by the ring that appears in the fast Fourier Transform (FFT) of the image (the inset in Figure 4.4a). Detailed size measurements (size distribution shown in Figure 4.4c) of Figure 4.4a gave an average diameter of PS core and center-to-center distance between two cores as $D = 85 \pm 12$ nm, and $L = 115 \pm 15$ nm, respectively, and the nearest neighbor distance obtained from FFT was $l = 110$ nm.

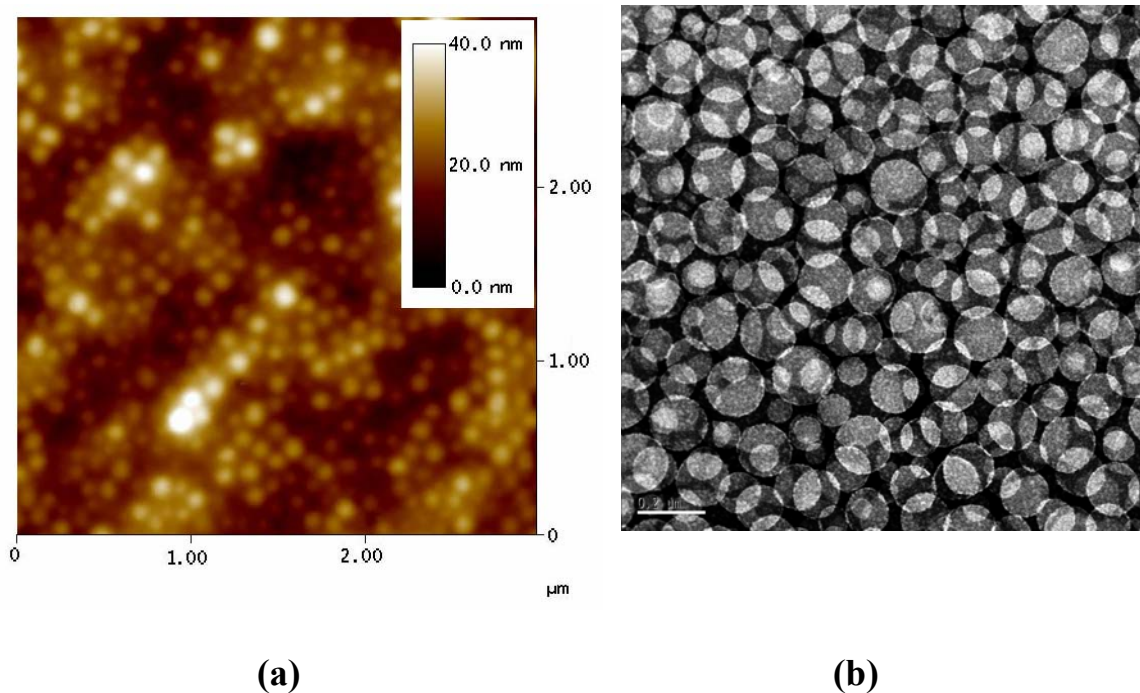


FIGURE 4.3: (a) SFM topography of a PS-b-PFOMA film ($h = 88$ nm) after annealing at Sc-CO₂, 75 °C, 13.8 MPa for 3 days. (b) HAADF-STEM image of a RuO₄ stained PS-b-PFOMA thin film sample supported on SiN grid after annealing at Sc-CO₂, 75 °C, 13.8 MPa for 3 days. The scale bar represents 200 nm.

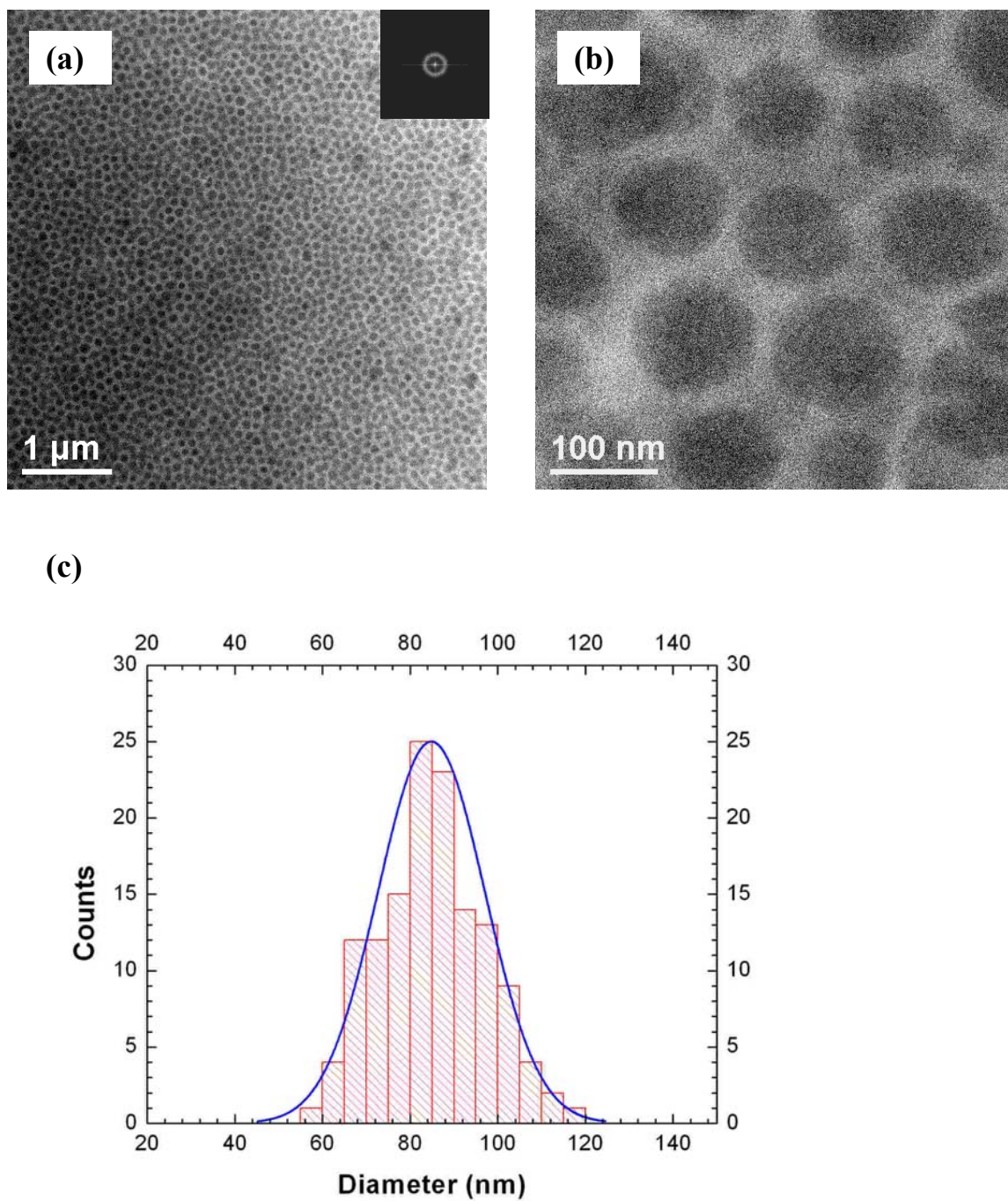


FIGURE 4.4: (a) (b) HAADF-STEM images of a PS-b-PFOMA thin film sample supported on SiN grid after annealing at Sc-CO₂, 75 °C, 13.8 MPa for 3 days. (c) The size distribution of PS cores in (a).

Table 4.3: Atomic Ratio between Fluorine and Carbon from XPS Data for PS-b-PFOMA Films after Sc-CO₂ Annealing at 35 °C and 13.8 MPa

XPS takeoff Angle (°)	F/C ratio			
	After spin-casting	After CO2 annealing	Cal. for the diblock	Cal. for PFOMA
45	0.81	1.13	0.68	1.08
75	0.68	1.31		

Table 4.3 compares the XPS results of Sc-CO₂ annealed PS-*b*-PFOMA films with those after spin casting. It is clear that the F/C ratios at both takeoff angles increase upon Sc-CO₂ annealing, suggesting that the surface of the Sc-CO₂ annealed films is pure PFOMA. In addition, the F/C ratios for Sc-CO₂ annealed films were even larger than the calculated F/C ratio for PFOMA homopolymer, indicating that the perfluorocarbon side chains are more biased toward the free surface due to the strong affinity between PFOMA and CO₂.

We conclude this section by first pointing out that in addition to the free surface, a layer of PFOMA resides at the PS-*b*-PFOMA/SiO_xSi interface due to the carbonyl groups. This is the same reason the PMMA component of a PS-*b*-PMMA diblock preferentially wets SiO_x/Si.^{29, 57, 58} Second, the strong affinity between PFOMA and the Sc-CO₂ leads to a reversal of the internal core-shell composition of the micelles. The schematics in parts a and b of Figures 4.5 summarize the structures of the as-cast and the Sc-CO₂ annealed films, respectively.

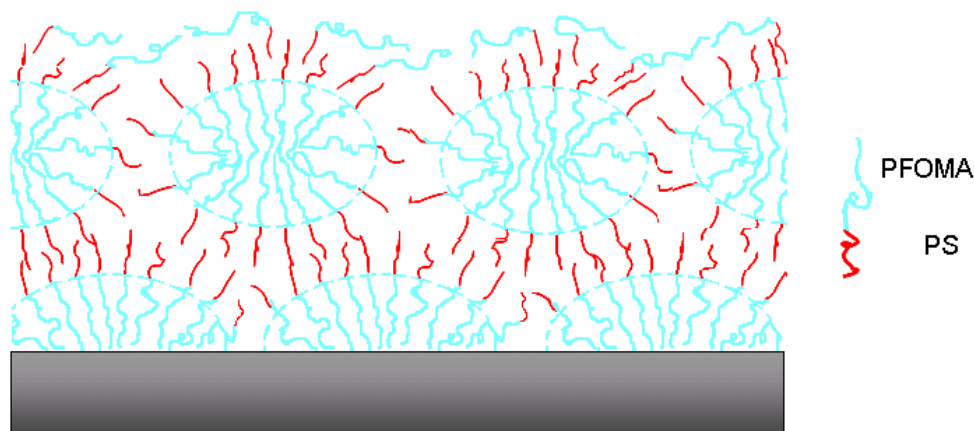
4.3.2b Shape of the PS-*b*-PFOMA Micellar Aggregates

The micellar size and shape are now discussed. Following the work by Eisenberg and coworkers³⁹, the size of a typical block copolymer micelle can be estimated from the degree of stretching, S_c , of the core block and is specified by

$$S_c = \frac{D}{2l_e} \quad (4.2).$$

Here D is the diameter of the micelle cores. For the micelles with PS cores in Figure 4.5b, l_e denotes the end-to-end distance of PS block in unperturbed state and is listed in Table 4.1. For most block copolymer micelles, S_c is found in the range of 0.7-1.5.³⁹ Thus a maximum value of D of $2 \times 1.5 \times 11 = 33$ nm is expected for PS cores. However,

(a)



(b)

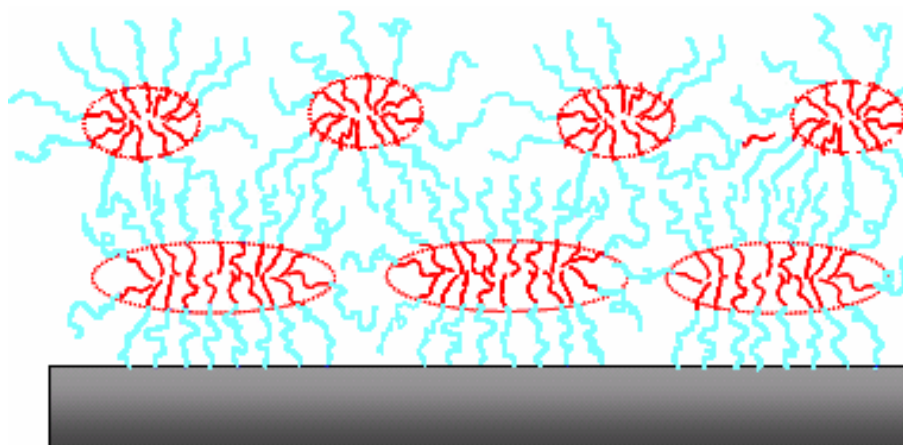


FIGURE 4.5: Schematic representations of the PS-b-PFOMA surface aggregates after spin-casting from the solution onto Si/SiO_x substrate (a) and annealing under Sc-CO₂ (b). Light blue chains are PFOMA; red chains are PS. Note in (a) an ultrathin layer of PFOMA segregated layer (with the fluorinated side groups aligned towards the outer face) is drawn on free surface. On the substrate interface, a layer of highly deformed PFOMA cored hemimicelles is drawn due to the strong interaction between the carbonyl group and SiO₂.

the experimentally determined values of the PS core diameter in Figure 4.4a is 85 nm, more than twice the calculated value. This discrepancy can be explained by the deformation of spherical micelles confined on a solid substrate.⁵⁹ This increase in size can be understood by the fact that the carbonyl groups of the PFOMA chains at the substrate have a strong affinity to the polar Si/SiO_x.^{29, 57, 58} Consequently, the micellar cores develop an ellipsoid-like shape, wherein the height of the ellipsoid is smaller than its radius on the plane parallel to the substrate (the core radius measured from the Z-contrast images is the major axis of the ellipsoid-like aggregates, which is highly extended due to this confinement effect). The minor axis, only observable from cross-section imaging (not performed in this study), should be approximately equal to l_e . It is noteworthy that this deformation of the spherical micelle cores is analogous to the phenomena that the volume pervaded by a polymer chain changes from a spherical to ellipsoidal shape when confined in ultrathin films.⁶⁰

Before concluding this section, the effect of rapid CO₂ desorption on the aggregate size is discussed. *Ex-situ* ellipsometry measurements of PS-b-PFOMA films showed a thickness increase of about 12-18% after annealing at 75 °C in Sc-CO₂. Although this degree of swelling is measurable, it is much lower than the swelling ratio of 47% determined by *in-situ* ellipsometry on PS-b-PFOMA films under the same condition. We expect that, upon desorption of CO₂, the diblock films rapidly cross the glass transition and become “frozen”. The “frozen” PS core would, therefore, have a size somewhere between the pure unswollen PS and the CO₂ swollen PS. For PS, *in-situ* ellipsometry experiments at 75 °C and 13.8 MPa gives a swelling ratio of about ~9.3%, which corresponds to an increase of 3% in the diameter of PS core. Thus the effect of CO₂ swelling on the measured PS core sizes after CO₂ desorption is negligible and within

experimental errors. On the other hand, PFOMA swells substantially more in CO₂, and the length of the corona is highly underestimated from the ex-situ STEM measurements.

4.3.3 Effects of Supercritical CO₂ Annealing Temperature on the Core Sizes of PS-b-PFOMA Aggregates

In this section, the effects of Sc-CO₂ annealing temperature on the morphologies of the copolymer films are examined, experimentally and theoretically. Parts a-d of Figure 4.6 show STEM images of unstained PS-b-PFOMA films, after annealing under Sc-CO₂ at four temperatures while the pressure was fixed at 13.8MPa. It is clear that, as the Sc-CO₂ annealing temperature increases from 35 to 140 °C, the sizes of the PS cores increase continuously, as seen in the increase of D, L, and l (Figure 4.6e).

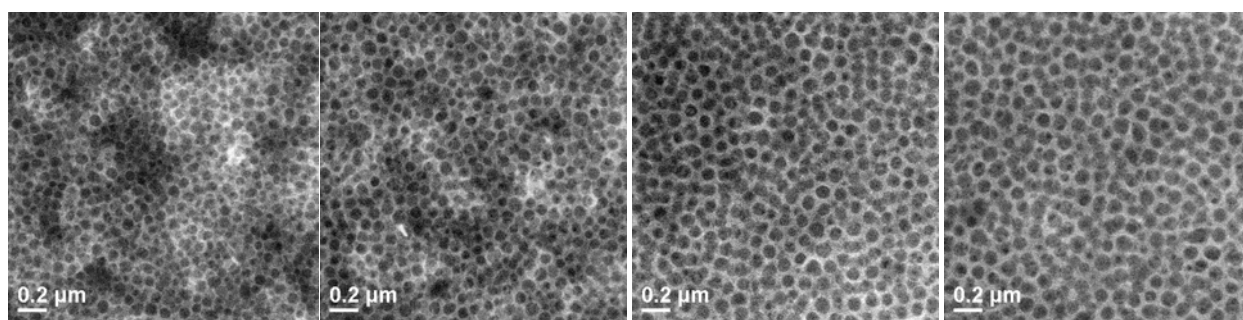
To further understand the effect of Sc-CO₂ temperature on relative swelling of the two blocks, the swelling isotherm for PS, PDHFOMA homopolymer thin films in Sc-CO₂ at 35 and 50 °C was measured by *in-situ* ellipsometry (Figure 4.7a). At a constant pressure, as temperature increases from 35 to 50 °C, the swelling for PDHFOMA decreases appreciably. On the other hand, the change in swelling of PS films with temperature is very small. It is noteworthy that both curves at 35 °C show anomalous swelling peaks in the regions where the compressibility of Sc-CO₂ is at maximum. These unique anomalous swelling maximum of polymer thin films in Sc-CO₂ was discovered by Sirard et al.³⁶ and will be examined into further detail in a subsequent paper.

The swelling isotherms can be plotted against Sc-CO₂ activity to combine the effect of both temperature and pressure (Figure 4.7b). As has been discussed in our previous work, the swelling of a rubbery polymer in Sc-CO₂ is only dependent on CO₂ activity.³⁶ Because the T_g of PFOMA is only 50 °C at ambient conditions and is even more depressed under Sc-CO₂, the difference between the two isotherms of PDHFOMA films is, within experimental errors, not observable. Regarding the PS phase, the

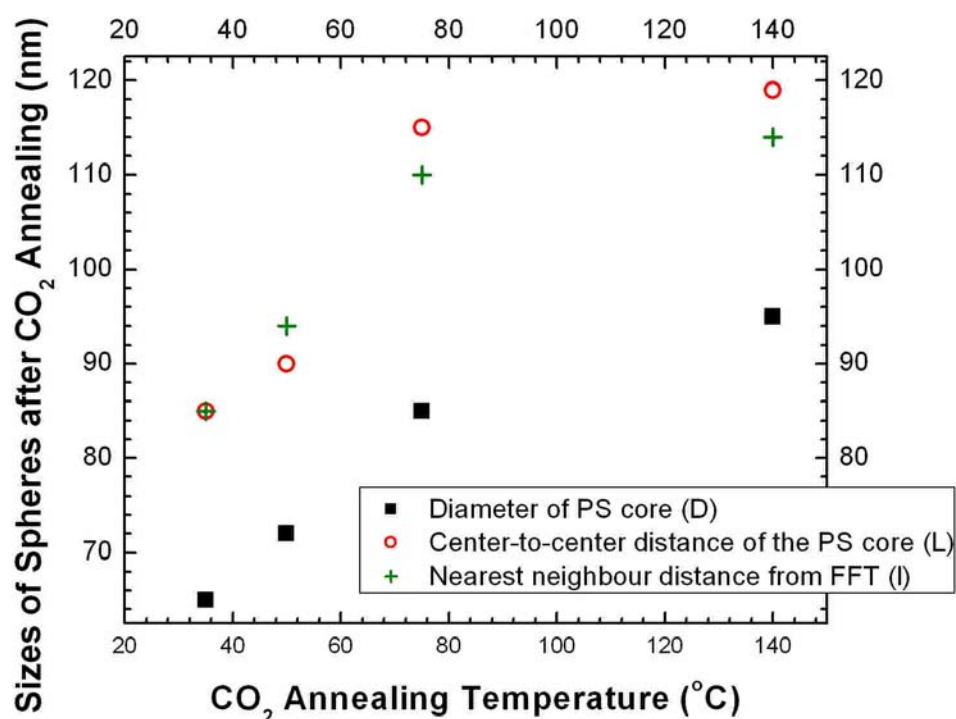
differences between the two isotherms below the respective P_g values³³ are also not obvious due the relatively large normal axis scale. On the basis of the experimental conditions in Figure 4.6a-d, both blocks are expected to be rubbery³³, and the swelling of each block may be estimated from the corresponding CO_2 activities, listed in Table 4.4. It is evident that the sorption difference between PS and PFOMA in CO_2 decreases with increasing temperature, at constant pressure.

Thus far, we have shown that both the size of PS cores and the relative swelling ratio of PS versus PFOMA increase gradually with increasing CO_2 annealing temperature at constant pressure. Next, we will explain these results based on the classical scaling theory for the formation of block copolymer micelles in a selective solvent. It is well-known that the growth of the micelles is driven by the high surface tension between the core block and the solvent. As micelles grow, the corona chains will become highly stretched and the repulsion of the swollen corona chains will increase. An entropy loss will thus arise as an opposing effect against the micelle growth. For star-like micelles, it is the balance of the two dominant contributions to the free energy of a micelle (the elastic energy of corona and the surface energy of the core) that governs the equilibrium micelle size as well as the aggregation number, whereas the elastic energy of the core is often omitted.⁶¹

Most theoretical models for micellization of block copolymer can be divided into two categories: “mean field”⁶² and “scaling”⁶¹ theories.^{63, 64} We will follow the “scaling” model developed by Zhulina et al.⁶¹ to examine the contribution of each energy term in the total free energy of the micelles, especially the effects of core and corona chain stretching on the micelles sizes. This “scaling” model developed by Zhulina et al.⁶¹ is constructed so that we can redefine part of the contribution to core size dependence into a new term that characterizes the relative stretching between corona and core chains. It is



(a) (b) (c) (d)



(e)

FIGURE 4.6: HAADF-STEM images of PS-b-PFOMA samples ($h \sim 150$ -200 nm) after annealing under various Sc-CO₂ conditions. The annealing conditions are as the following: (a) 35 °C, 6 days; (b) 50 °C, 3 days; (c) 75 °C, 3 days; (d) 140 °C, 25 h; the CO₂ pressure was fixed at 13.8 MPa (2000 psig) for all temperatures. (e) The sizes of PS cores measured from (a-d) as increasing CO₂ annealing temperature. Typical error bars for the diameter of PS cores are 11-13 nm and those for the center-to-center distance of the PS cores are 12-15 nm.

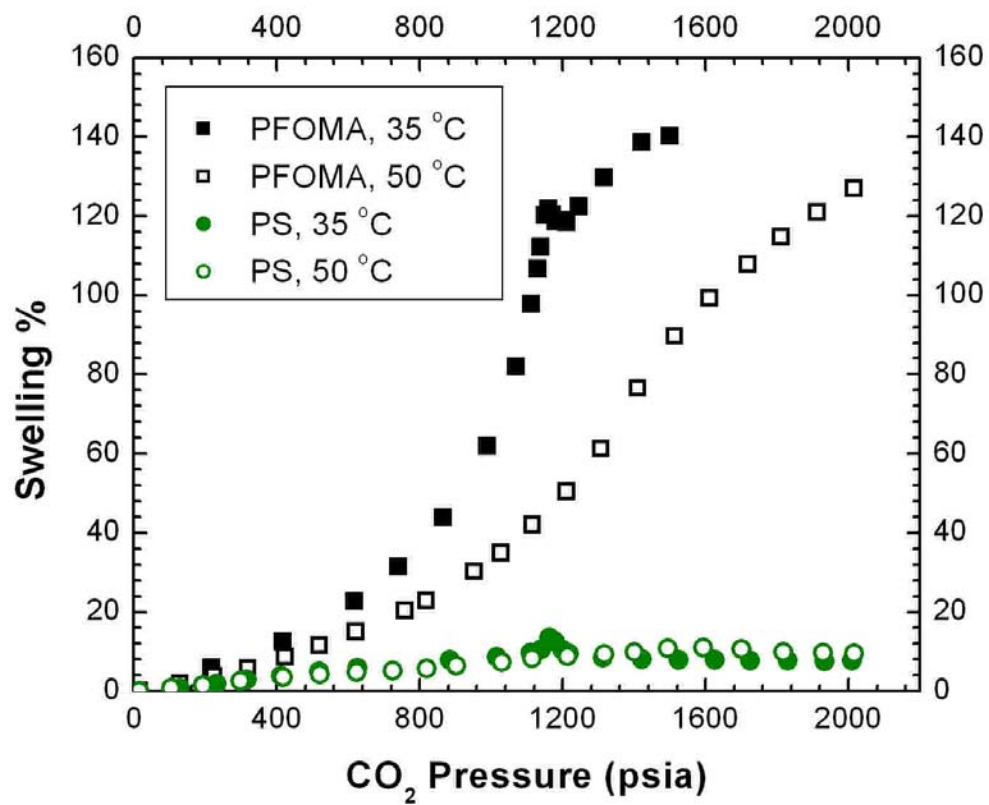


FIGURE 4.7: (a) Swelling isotherm for PS and PDHFOMA (for simplicity, indicated by PFOMA on the plot legends) films in Sc-CO₂.

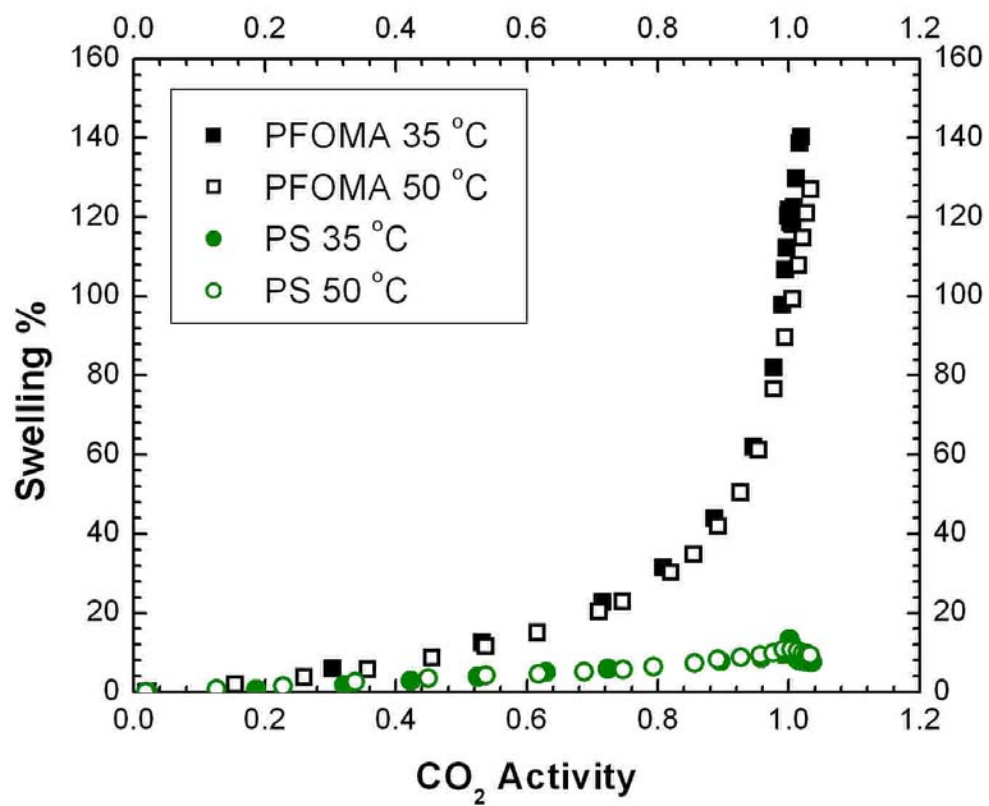


FIGURE 4.7: (b) Swelling vs. CO₂ activity for PS and PDHFOMA films.

Table 4.4: The Swelling % of PS and PFOMA in CO₂ under Four Conditions

T (K)	P (Mpa)	CO₂ Activity	% Swelling PS	% Swelling PFOMA	$K = (Sw \%_{PFOMA} + 100\%) / (Sw \%_{PS} + 100\%)$	$K^{1/3}$
308	13.79	1.036	7.6	138*	2.21	1.30
323	13.79	1.032	9.4	127	2.07	1.27
348	13.79	0.957	9.3*	63*	1.49	1.14
413	13.79	0.701	5.3*	21*	1.15	1.05

* These swelling ratios are based on the estimation from Figure 4.7b.

particularly instructive to examine the dependence of core sizes on this new term, given the effect of Sc-CO₂ on chain stretching.

We consider a flexible A-b-B diblock copolymer with $N_A, N_B \gg 1$ and with respective monomers sizes of a_A and a_B , selectively, dissolved in a good solvent for A. The free energy of a block copolymer A-b-B spherical micelle in the solution is

$$F = F_A + F_S + F_B \quad (4.3).$$

Here F_B , F_S , and F_A are the free energy per chain of the micellar core (composed by B), of its surface and of the corona (composed by A). The elastic free energy per chain for the micellar core due to the stretching of B chains compared with their unperturbed state is

$$F_B/kT = 3\pi^2 r^2 / 80 p_B N_B \quad (4.4)^{61}.$$

Here, $r = R/a_B$ is the dimensionless radius of the core, R is the radius of the spherical core, and p_B is the ratio between the Kuhn segment l_B and the monomer size a_B ($p_B = l_B/a_B$).

The following two assumptions are made: (1) the micellar core composed of B block is partially swollen by the poor solvent; (2) the volume fraction of B block in the micellar core is denoted by Φ , which does not depend on the distance d from its center.⁶¹ Then Φ can be represented by the following equation,

$$\Phi = 3N_B a_B^3 / (Rs) \quad (4.5)^{61},$$

where s is the surface area per chain. Thus surface free energy per chain is

$$\frac{F_S}{kT} = \tilde{\gamma}s = \gamma(s/a_B^2) = \gamma \frac{3N_B a_B}{\phi R} \quad (4.6)^{61}.$$

Here, $\tilde{\gamma}$ is the surface free energy per unit area and $\gamma = \tilde{\gamma}a_B^2$ is the surface free energy per area a_B^2 , both divided by kT .

The equilibrium structure of the corona is determined by the balance between the elastic stretching and the repulsive interaction of the A block. Here, the corona of the

micelles can be regarded as a melt of correction blobs (region of nonoverlapping chains), which has a thermal energy of kT . Then free energy of the corona may be given by

$$\frac{F_A}{kT} = \nu \hat{C}_F r^{3/2} \left(\frac{\Phi}{3N_B} \right)^{1/2} \ln \left[1 + \frac{1}{\nu} \left(\frac{a_A}{a_B} \right)^{1/\nu} \hat{C}_H N_A r^{(1-3\nu)/(2\nu)} \left(\frac{3N_B}{\Phi} \right)^{(v-1)/(2\nu)} \right] \quad (4.7).^{61}$$

Here, ν is the scaling exponent and is equals to $3/5$ in a good solvent. \hat{C}_F and \hat{C}_H are solvent dependent coefficients. The thickness, H , of the corona is given by

$$H = R \left\{ \left[1 + \frac{1}{\nu} \left(\frac{a_A}{a_B} \right)^{1/\nu} \hat{C}_H N_A r^{(1-3\nu)/(2\nu)} \left(\frac{3N_B}{\Phi} \right)^{(v-1)/(2\nu)} \right]^\nu - 1 \right\} \quad (4.8).^{61}$$

Combining eqs 4.7 and 4.8, one obtains

$$\frac{F_A}{kT} = \hat{C}_F r^{3/2} \left(\frac{\Phi}{3N_B} \right)^{1/2} \ln \left(\frac{H}{R} + 1 \right) \quad (4.9),$$

Hence, the total free energy of block copolymer micelles is

$$\frac{F}{kT} = \frac{3\pi^2 r^2}{80 p_B N_B} + \frac{3N_B \gamma}{\Phi r} + \hat{C}_F r^{3/2} \left(\frac{\Phi}{3N_B} \right)^{1/2} \ln \left(\frac{H}{R} + 1 \right) \quad (4.10).$$

If we assume that $\xi = H/R$, which is the ratio between corona thickness and core radius, then ξ can be related to r by

$$\xi = \left[1 + \frac{1}{\nu} \left(\frac{a_A}{a_B} \right)^{1/\nu} \hat{C}_H N_A r^{(1-3\nu)/(2\nu)} \left(\frac{3N_B}{\Phi} \right)^{(v-1)/(2\nu)} \right]^\nu - 1 \quad (4.11).$$

ξ is, alternatively, proportional to the ratio between the degree of stretching for the corona and core chains. Recalling that $Sw\% = (\Delta V/V_0)\%$, we have

$$\xi = \frac{H}{R} = \left(\frac{H/H_0}{R/R_0} \right) \times \frac{H_0}{R_0} = \frac{(V/V_0)_{corona}^{1/3}}{(V/V_0)_{core}^{1/3}} \times \frac{H_0}{R_0} = \left(\frac{Sw\%_{corona} + 100\%}{Sw\%_{core} + 100\%} \right)^{1/3} \times \frac{H_0}{R_0} \quad (4.12).$$

Here, H_0/R_0 can be calculated from the ratio between PFOMA and PS's end-to-end distance in unperturbed states (Table 4.1). By minimizing the free energy per chain with respect to the dimensionless radius of the core r (eq 4.10), we can obtain

$$\frac{\delta F}{\delta r} = \frac{3\pi^2 r}{40 p_B N_B} - \frac{3N_B \gamma}{\Phi r^2} + \frac{3}{2} \hat{C}_F r^{1/2} \left(\frac{\Phi}{3N_B} \right)^{1/2} \ln(\xi + 1) + \hat{C}_F r^{3/2} \left(\frac{\Phi}{3N_B} \right)^{1/2} \frac{1}{(\xi + 1)} \frac{\delta(\xi + 1)}{\delta r} = 0 \quad (4.13).$$

If we assume that $\xi \gg 1$ ($H \gg R$), then (reference 61 made the same assumption in the Appendix II.1 section)

$$\frac{\delta(\xi + 1)}{\delta r} \sim \frac{(1 - 3\nu)}{2} \frac{\xi}{r} \quad (4.14).$$

For star-like micelles, the stretching free energy F_B of the core block can often be neglected. Thus eq 4.13 can be further simplified as

$$\frac{\delta F}{\delta r} = -\frac{3N_B \gamma}{\Phi r^2} + \frac{3}{2} \hat{C}_F r^{1/2} \left(\frac{\Phi}{3N_B}\right)^{1/2} \ln(\xi) + \hat{C}_F r^{1/2} \left(\frac{\Phi}{3N_B}\right)^{1/2} \left(\frac{1 - 3\nu}{2}\right) = 0 \quad (4.15).$$

Hence

$$r \sim \left(\frac{2\gamma}{\hat{C}_F}\right)^{2/5} \left(\frac{3N_B}{\Phi}\right)^{3/5} \left(\frac{1}{3\ln \xi + (1 - 3\nu)}\right)^{2/5} \sim \left(\frac{\gamma}{\ln \xi}\right)^{2/5} \left(\frac{N_B}{\Phi}\right)^{3/5} \quad (4.16).$$

Please note here that eq 4.16 is equivalent to eq AII.2 in reference 61, except that we indicate explicitly how r varies with the relative stretching between corona and core chains by introducing the new term, ξ . The aggregation number (total number of chains per micelle) Q is given by

$$Q = \frac{4\pi r^3 \Phi}{3N_B} \sim \left(\frac{\gamma}{\ln(\xi)}\right)^{6/5} \left(\frac{N_B}{\Phi}\right)^{4/5} \quad (4.17).$$

Eq 4.16 indicates that the micelle core will grow under one of these three conditions: (1) as the interfacial tension between the core and solvent, γ , increases; (2) as the volume fraction of B block in the swollen core, Φ , decreases, or equivalently as the swelling of core block by the solvent increases; (3) as the relative degree of stretching between corona and core, ξ , decreases. Although the first two conclusions seem quite intuitive, the last one, which shows that the size of micelles is strongly dependent on the relative stretching of corona and core chains, has not been discussed in previous studies.

To compare the above prediction with our experimental results, we first estimated the interfacial tension between PS (27 kg/mole) and CO₂, γ . Different values of γ

associated with different molecular weights of PS have been reported,^{65, 66} and interfacial tension is strongly dependent on molecular weight such that

$$\gamma = \gamma_{\infty} - \frac{K_e}{M^{2/3}} \quad (4.18).^{67}$$

Here K_e is a constant and γ_{∞} is the interfacial tension at infinite molecular weight. Based on eq 4.18, we estimated the values of γ from two reported PS-CO₂ interfacial tensions, as shown in Table 4.5. Here the reference values of γ for PS (158 kg/mole) and PS (1.85 kg/mole) at the four CO₂ densities were estimated from Figure 9 in ref 66 and Figure 4 in ref 65, respectively. Consistent with both references, Table 4.5 shows that the interfacial tension between PS and CO₂, γ , increases with decreasing CO₂ activity. This trend can be understood by considering that the cohesive energy density of CO₂ is much smaller than that of PS. As the CO₂ activity decreases, the difference in cohesive energy densities of CO₂ and PS grows, and consequently γ increases.

Table 4.6 summaries the values for ξ , Φ (obtained from Table 4.4) and γ . Because Φ does not change significantly with CO₂ annealing temperature, its effect on r can be neglected. From Table 4.6, it is clear that as the CO₂ annealing temperature increases, or as CO₂ activity decreases, γ increases while the relative stretching between corona and core chains (ξ) decreases. From eq 4.16, both factors will cause the size of PS cores to increase, consistent with the STEM images. In Figure 4.8, the measured diameters of the PS core, D , are plotted versus the estimated values of $\gamma/\ln(\xi)$.

The data can be reasonably well described by a power law with an exponent of 0.31. A line with a slope of 2/5, as predicted by eq 4.16, appears to work equally well, although the following is worth mentioning. First, the scaling model assumes a dilute solution of polymer, whereas the PS-b-PFOMA films in CO₂ should be considered as quite concentrated. Second, the size of PS core is large compared with the measured center-to-center distance between the aggregates, partially as a consequence of the

Table 4.5: Estimation of the Interfacial Tension between PS (27k) and CO₂

T (K)	P (Mpa)	CO₂ Density	γ (PS 158k) (dyne/cm)	γ (PS 1.85k) (dyne/cm)	K_e[*]	γ (PS 27k) (dyne/cm)
308	13.79	0.799	8.6	2.5	9.7	7.9
323	13.79	0.666	9.4	3.1	10.1	8.6
348	13.79	0.406	12.1	5.3	10.8	11
413	13.79	0.223	16.6	10.5	9.6	16

* Based on $\gamma = \gamma_{\infty} - \frac{K_e}{M^{2/3}}$, $K_e = \frac{\gamma_2 - \gamma_1}{M_1^{-2/3} - M_2^{-2/3}}$.

Table 4.6: Effects of CO₂ Annealing Temperature on the Sizes of Micelles Cores

T (K)	P (Mpa)	D (nm)	γ (PS 27k) (dyne/cm)	ξ = K^{1/3} × (H₀/R₀)[*]	Φ	γ / (ln ξ) (dyne/cm)
308	13.79	65	7.9	1.79	0.93	14
323	13.79	72	8.6	1.77	0.91	15
348	13.79	85	11	1.57	0.92	24
413	13.79	95	16	1.44	0.95	44

* H₀/R₀ = 1.38, from the ratio between PFOMA and PS's end-to-end distance in unperturbed states.

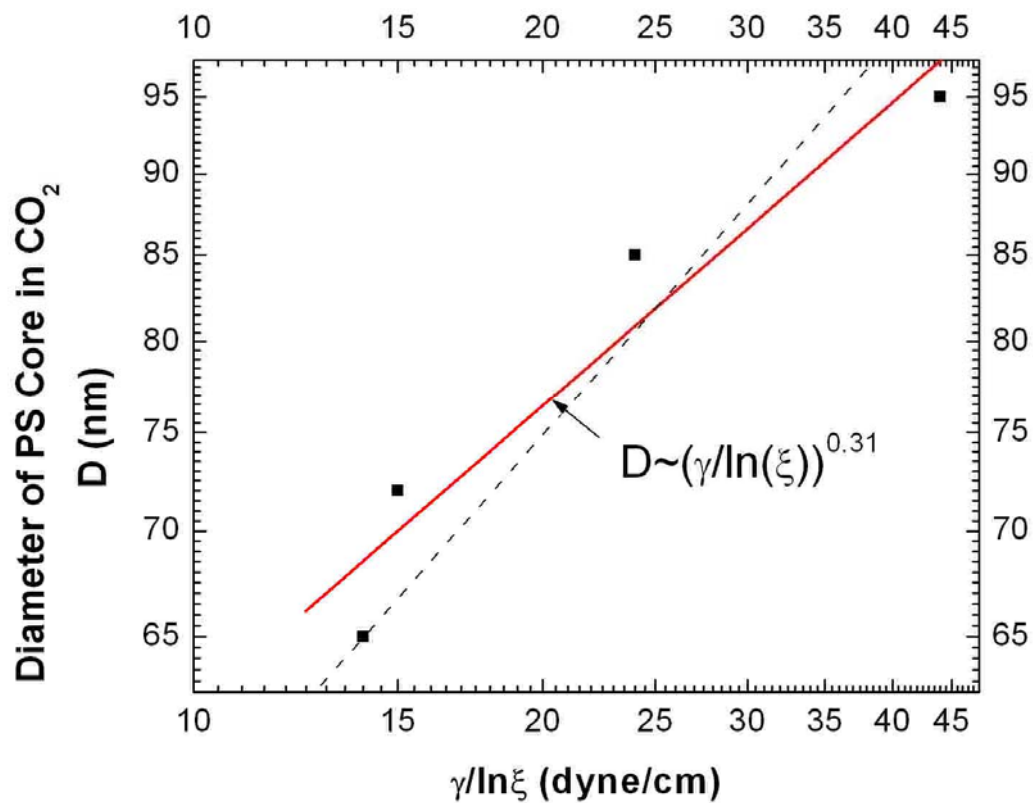


FIGURE 4.8: The diameters of PS cores after Sc-CO₂ annealing measured from STEM images vs. $\gamma/\ln(\xi)$, where γ is the interfacial tension between PS and CO₂, and $\xi = H/R$ is the relative stretching between corona and core chains. The broken line has a slope of 2/5. The solid line, a fit to the data, has a slope of 0.31.

ellipsoidal shape. Other scaling models showed that for micelles with relatively large cores, the dependence of core sizes on γ is weaker.⁶⁴ Third, $\xi \gg 1$ is assumed, while the values of ξ obtained from the swelling isotherms are not necessarily much larger than unity (Table 4.6). Finally, γ is only estimated through reported values for other PS molecular weights and the swelling of PDHFOMA homopolymer could be different from that of PFOMA block in the diblock. Nevertheless, the key finding is that the scaling model qualitatively predicts that size of PS cores increases with increasing CO₂ annealing temperature, and the observed exponential dependence of D on $\gamma/\ln(\xi)$ agrees, nearly quantitatively, with the model.

It is noteworthy that this trend of increasing micelles size with decreasing CO₂ density is in agreement with related studies on bulk block copolymer micelles dissolved in Sc-CO₂.⁶⁸⁻⁷¹ This agreement further suggests that the size dependence of PS-*b*-PFOMA micelles in thin films on CO₂ solvent properties is similar to that of block copolymer micelles dissolved in Sc-CO₂.

4.4 CONCLUSIONS

PS-*b*-PFOMA cast from a cosolvent mixture of toluene and Freon 113 formed a micellar structure, with a PFOMA core and PS corona, on SiO_x/Si substrates. The free surface and polymer/substrate layers were enriched with PFOMA. Upon annealing in Sc-CO₂, the structure underwent an inversion, wherein the PS chain segments formed the core and the PFOMA segments formed the corona. This inversion is associated with the strong affinity of PFOMA with Sc-CO₂. In addition, the sizes of the PS cores were found to increase with decreasing CO₂ activity. A “scaling” model showed that the increasing interfacial tension between PS and CO₂, as well as the decreasing relative stretching between the corona and core chains, lead to the increasing aggregates sizes with

decreasing Sc-CO₂ activity. The ability to tune the morphology of self-assembled copolymer films with Sc-CO₂ is of practical interest for templating inorganic nanocrystals in block copolymer scaffolds. In a companion study,⁵⁹ Au nanocrystals with low PS oligomers as ligands premixed with the copolymer in solution were found to sequester within the PS domains of PS-*b*-PFOMA films and to follow the structural inversion when annealed in Sc-CO₂. The unique electronic, photonic, magnetic and mechanical properties of such inorganic nanoparticles can add functionalities to the copolymer/nanoparticle composites, which are very desirable in applications such as the synthesis of photonic crystals and the fabrication of flash memory devices.

4.5 REFERENCES

1. Segalman, R. A. *Materials Science and Engineering R* **2005**, 48, 191.
2. Volkmuth, W. D.; Austin, R. H. *Nature* **1992**, 358, 600.
3. Park, M.; Harrison, C.; Chaikin, P. M.; Register, R. A.; Adamson, D. H. *Science* **1997**, 276, 1401.
4. Fink, Y.; Winn, J. N.; Fan, S.; Michel, J.; Joannopoulos, J. D.; Thomas, E. L. *Science* **1998**, 282, 1679.
5. Chou, S. Y.; Wei, M. S.; Krauss, P. R.; Fischer, P. B. *J. Appl. Phys.* **1994**, 76, 6673.
6. Thurn-Albrecht, T.; Schotter, J.; Kastle, G. A.; Emley, N.; Shibauchi, T.; Krusin-Elbaum, L.; Guarini, K.; Black, C. T.; Tuominen, M. T.; Russell, T. P. *Science* **2000**, 290, 2126.
7. Pai, R. A.; Humayun, R.; Schulberg, M. T.; Sengupta, A.; Sun, J. N.; Watkins, J. J. *Science* **2004**, 303, 507.
8. Zhu, L.; Cheng, S. Z. D.; Calhoun, B. H.; Ge, Q.; Quirk, R. P.; Thomas, E. L.; Hsiao, B. S.; Yeh, F.; Lotz, B. *Polymer* **2001**, 42, 5829.
9. Kim, D. H.; Jia, X.; Lin, Z.; Guarini, K. W.; Russell, T. P. *Adv. Mater.* **2004**, 16, 702.

10. Kim, D. H.; Kim, S. H.; Lavery, K.; Russell, T. P. *Nano Lett.* **2004**, 4, 1841.
11. Sundrani, D.; Darling, S. B.; Sibener, S. J. *Langmuir* **2004**, 20, 5091.
12. Morkved, T. L.; Lu, M.; Urbas, A. M.; Ehrichs, E. E.; Jaeger, H. M.; Mansky, P.; Russell, T. P. *Science* **1996**, 273, 931.
13. Segalman, R. A.; Yokoyama, H.; Kramer, E. J. *Adv. Mater.* **2001**, 15, 1152.
14. Fasolka, M. J.; Harris, D. J.; Mayes, A. M.; Yoon, M.; Mochrie, S. G. J. *Phys. Rev. Lett.* **1997**, 79, 3018.
15. Kim, S. O.; Solak, H. H.; Stoykovich, M. P.; Ferrier, N. J.; dePablo, J. J.; Nealey, P. F. *Nature* **2003**, 424, 411.
16. Rockford, L.; Liu, Y.; Mansky, P.; Russell, T. P.; Yoon, M.; Mochrie, S. G. J. *Phys. Rev. Lett.* **1999**, 88, 2602.
17. Rockford, L.; Russell, T. P.; Yoon, M.; Mochrie, S. G. J. *Macromolecules* **2001**, 34, 1487.
18. Albalak, R. J.; Thomas, E. L.; Capel, M. S. *Polymer* **1997**, 38, 3819.
19. Villar, M. A.; Rueda, D. R.; Ania, F.; Thomas, E. L. *Polymer* **2002**, 43, 5139.
20. Bodycomb, J.; Funaki, Y.; Kimishima, K.; Hashimoto, T. *Macromolecules* **1999**, 32, 2075.
21. DeSimone, J. M. *Science* **2002**, 297, 799.
22. Kazarian, S. G. *Polymer Science, Ser. C* **2000**, 42, 78.
23. Zhang, Y.; Gangwani, K. K.; M., L. R. *J. Supercritical Fluids* **1997**, 11, 115.
24. Zhang, Z.; Handa, P. Y. *Macromolecules* **1997**, 30, 8505.
25. Liao, X.; Wang, J.; Li, G.; He, J. *J. Polym. Sci.: B* **2004**, 42, 280.
26. Gross, S.; Roberts, G. W.; Kiserow, D.; DeSimone, J. M. *Macromolecules* **2000**, 33, 40.
27. Lambert, S. M.; E., P. M. *J. Supercritical Fluids* **1991**, 4, 15.
28. Beckman, E.; Porter, R. *J. Polym. Sci.: B* **1987**, 25, 1511.
29. Arceo, A.; Green, P. F. *J. Phys. Chem. B* **2005**, 109, 6958.

30. Vogt, B. D.; Brown, G. D.; RamachandraRao, V. S.; Gupta, R. R.; Lavery, K. A.; Francis, T. J.; Russell, T. P.; Watkins, J. J. *Macromolecules* **2003**, 36, 4029.
31. Vogt, B. D.; Brown, G. D.; RamachandraRao, V. S.; Watkins, J. J. *Macromolecules* **1999**, 32, 7907.
32. Watkins, J. J.; Brown, G. D.; RamachandraRao, V. S.; Pollard, M. A.; Russell, T. P. *Macromolecules* **1999**, 32, 7737.
33. Pham, J. Q.; Johnston, K. P.; Green, P. F. *J. Phys. Chem. B* **2004**, 108, 3457.
34. Meli, L.; Pham, J. Q.; Johnston, K. P.; Green, P. F. *Phys. Rev. E* **2004**, 69, 051601.
35. Pham, J. Q.; Sirard, S. M.; Johnston, K. P.; Green, P. F. *Phys. Rev. Lett.* **2003**, 91, 175503.
36. Sirard, S. M.; Ziegler, K. J.; Sanchez, I. C.; Green, P. F.; Johnston, K. P. *Macromolecules* **2002**, 35, 1928.
37. Sirard, S. M.; Green, P. F.; Johnston, K. P. *J. Phys. Chem. B* **2001**, 105, 766.
38. Arnold, M. E.; Nagai, K.; Freeman, B. D.; Spontak, R. J.; E., B. D.; DeSimone, J. M.; Pinnau, I. *Macromolecules* **2001**, 34, 5611.
39. Zhang, L.; Eisenberg, A. *J. Am. Chem. Soc.* **1996**, 118, 3168.
40. Arnold, M. E.; Nagai, K.; Spontak, R. J.; Freeman, B. D.; Leroux, D.; Betts, D. E.; DeSimone, J. M.; DiGiano, F. A.; Stebbins, C. K.; Linton, R. W. *Macromolecules* **2002**, 35, 3697.
41. Sirard, S. M.; Castellanos, H. J.; Hwang, H. S.; Lim, K. T.; Johnston, K. P. *Ing. Eng. Chem. Res.* **2004**, 43, 525.
42. Li, Y.; Loo, Y.-L.; Register, R. A.; Green, P. F. *Macromolecules* **2005**, 38, 7745.
43. Turner, M. S.; Rubinstein, M.; Marques, C. M. *Macromolecules* **1994**, 27, 4986.
44. Webber, S. E. *J. Phys. Chem. B* **1998**, 102, 2618.
45. Webber, G. B.; Wanless, E. J.; Butun, V.; Armes, S. P.; Biggs, S. *Nano Letters* **2002**, 2, 1307.
46. Webber, G. B.; Wanless, E. J.; Armes, S. P.; Baines, F. L.; Biggs, S. *Langmuir* **2001**, 17, 5551.

47. Spatz, J. P.; Sheiko, S.; Moller, M. *Macromolecules* **1996**, 29, 3220.
48. Regenbrecht, M.; Akari, S.; Forster, S.; Mohwald, H. *J. Phys. Chem. B* **1999**, 103, 6669.
49. Meiners, J. C.; Quintel-Ritzi, A.; Mlynek, J.; Elbs, H.; Krausch, G. *Macromolecules* **1997**, 30, 4945.
50. Ligoure, C. *Macromolecules* **1991**, 24, 2968.
51. Li, Z.; Zhao, W.; Liu, Y.; Rafailovich, M. H.; Sokolov, J.; Khougaz, K.; Eisenberg, A.; Lennx, R. B.; Krausch, G. *J. Am. Chem. Soc.* **1996**, 118, 10892.
52. Connell, S. D.; Collins, S.; Fundin, J.; Yang, Z.; Hamley, I. W. *Langmuir* **2003**, 19, 10449.
53. Breulmann, M.; Forster, S.; Antonietti, M. *Macromol. Chem. Phys.* **2000**, 201, 204.
54. Kim, S. H.; Misner, M. J.; Russell, T. P. *Adv. Mater.* **2004**, 16, 2119.
55. Lin, Z.; Kim, D. H.; Wu, X.; Boosahda, L.; Stone, D.; LaRose, L.; Russell, T. P. *Adv. Mater.* **2002**, 19, 1373.
56. O'Neill, M. L.; Cao, Q.; Fang, M.; Johnston, K. P.; Wilkinson, S. P.; D., S. C.; Kerschner, J. L.; Jureller, S. H. *Ind. Eng. Chem. Res.* **1998**, 37, 3067.
57. RamachandraRao, V. S.; Gupta, R. R.; Russell, T. P.; Watkins, J. J. *Macromolecules* **2001**, 34, 7923.
58. Xu, T.; Hawker, C. J.; Russell, T. P. *Macromolecules* **2005**, 38, 2802.
59. Meli, L.; Li, Y.; Lim, K. T.; Johnston, K. P.; Green, P. F. *Manuscript in preparation* **2006**.
60. Brown, H. R.; Russell, T. R. *Macromolecules* **1996**, 29, 798.
61. Zhulina, E. B.; Adam, M.; LaRue, I.; Sheiko, S. S.; Rubinstein, M. *Macromolecules* **2005**, 38, 5330.
62. Nagarajan, R.; Ganesh, K. *J. Chem. Phys.* **1989**, 90, 1989.
63. Lund, R.; Willner, L.; Stellbrink, J.; Radulescu, A.; Richter, D. *Macromolecules* **2004**, 37, 9984.

64. Linse, P., Modelling of the self-assembly of block copolymer in selective solvent. In *Amphiphilic Block Copolymers*, Alexandridis, P.; Lindman, B., Eds. Elsevier: Amsterdam, the Netherlands, **2000**.
65. Harrison, K. L.; da Rocha, S. R. P.; Yates, M. Z.; Johnston, K. P. *Langmuir* **1998**, 14, 6855.
66. Jaeger, P. T.; Eggers, R.; Baumgartl, H. *Journal of Supercritical Fluids* **2002**, 24, 203.
67. Wu, S., *Polymer Interface and adhesion*. Marcel Dekker: New York, **1982**.
68. Johnston, K. P.; McFann, G.; Lemert, R. M. *Am. Chem. Soc. Symp. Ser.* **1989**, 406, 140.
69. Fulton, J. L.; Pfund, D. M.; McClain, J. B.; Romack, T. J.; Maury, E. E.; Combes, J. R.; Samulski, E. T.; Desimone, J. M.; Capel, M. *Langmuir* **1995**, 11, 4241.
70. McClain, J. B.; Betts, D. E.; Canelas, D. A.; Samulski, E. T.; DeSimone, J. M.; Londono, D.; Cochran, H. D.; Wignall, G. D.; Chillura-Martino, D.; Triolo, R. *Science* **1996**, 274, 2049.
71. McClain, J. B.; Londono, D.; Combes, J. R.; Romack, T. J.; Canelas, D. A.; Betts, D. E.; Wignall, G. D.; Samulski, E. T.; DeSimone, J. M. *J. Am. Chem. Soc.* **1996**, 118, 917.

Chapter 5: Role of Interfacial Interactions on the Anomalous Swelling of Polymer Thin Films in Supercritical Carbon Dioxide

In this study, we use *in-situ* spectroscopic ellipsometry to investigate the effects of film thickness, polymer-substrate interaction and polymer-CO₂ interaction on anomalous swelling maximum of polymer thin films exposed to Sc-CO₂. We examine a range of polymers: poly(1, 1'-dihydroperfluorooctyl methacrylate) (PFOMA), polystyrene (PS), poly(ethylene oxide) (PEO) and the diblock copolymer of PS-b-PFOMA. A three-layer model is proposed to understand the role of excess CO₂ adsorption at the free and substrate interfaces on the total swelling % of polymer thin films. In this model, three swelling coefficients associated with the CO₂/polymer interfacial layer, the middle layer and the polymer/substrate interfacial layer were taken into consideration. While the model reveals that the relative interactions between polymer-substrate and polymer-CO₂ affect the swelling coefficients of all three layers, thus strongly influencing anomalous maximum, it further indicates that the anomalous swelling maximum cannot be solely explained by the excess absorption of CO₂ at interfaces, as was previously believed.

5.1 INTRODUCTION

Extensive attention has been paid to the use of supercritical CO₂ (Sc-CO₂) as an alternative to water or organic solvents in many polymer processes.¹⁻⁴ In addition to the environmentally benign character of CO₂, the tunable property of this supercritical fluid, through varying the pressure or temperature, enables control of its properties as a solvent. Recently, several studies of block copolymer thin films used CO₂ to induce the ordering of copolymer templates⁵⁻⁸, to control the spatial distribution of metal nanoparticles in copolymer matrices⁹, and to diffuse precursors in copolymers for the synthesis of nanoporous materials¹⁰. In addition to polymer processing, supercritical CO₂ has been investigated as a potential medium in many microelectronic thin film processes.¹¹⁻¹⁸ For example, it has been shown that CO₂ promotes penetration and removal of aqueous surfactant cleaning solutions in methylsilsesquioxane (MSQ) low dielectric constant (k) films.¹⁵ Moreover, the cleaning and drying steps may be integrated with silylation in CO₂ to convert the hydrophilic surface after etching and ashing to a hydrophobic surface in order to restore the k-value.¹⁵

In this paper we are particularly interested in Sc-CO₂ processing of polymer thin films. Polymer thin films exhibit film thickness dependent properties. Properties that include the glass transition temperatures, wetting and phase equilibria are of scientific and technological interests for a range of thin film based technologies, from microelectronics to sensors. There have been a few investigations on the effects of Sc-CO₂ on the properties of thin polymer.^{5-8, 19-25} Pham et al. found a Sc-CO₂ induced devitrification transition in PMMA and PS thin films.^{21, 22} Meli et al. showed that the kinetics of the morphological destabilization of PS thin films in Sc-CO₂ are suppressed.²⁰ Studies have also shown that the order-disorder transition (ODT) temperature of A-b-B diblock

copolymer films in Sc-CO₂ are increased appreciably compared to the case in vacuum; on the other hand, for bulk copolymers, the effect is opposite.^{5, 7, 8}

With regard to the behavior of CO₂ in the vicinity of its critical point, an anomalous maximum is known to occur, first observed in the adsorption isotherm of CO₂ on carbon black²⁶ and on silica surfaces^{27, 28}. Similar observations were made for other adsorbents,²⁹⁻³² including porous Zeolite,³¹ and activated carbon.^{29, 32} Anomalous adsorption has been rationalized by the fact that long-range density fluctuations of CO₂, affects the Gibbs excess adsorption of CO₂ under critical conditions.³³ The swelling of polymer thin films in CO₂ also exhibits anomalous maximum in the vicinity of the critical point.^{25, 34-37} Specifically, Sirard et al. first discovered the anomalous maxima in the swelling isotherms of PMMA thin films in CO₂ by *in-situ* spectroscopic ellipsometry.²⁵ Koga et al. then used neutron reflectivity to further explore the anomalous swelling of polymer thin films with thickness h less than 10 R_g in Sc-CO₂.^{34, 35} The effect of CO₂ on the swelling kinetics of colloidal crystals of PS was examined by *in-situ* measurement of Bragg diffraction and by scanning electron microscopy.³⁸ An anomalous excess in the swelling rate was observed in the region where CO₂ is highly compressible.³⁸ Additional studies have shed further insight into thin film swelling in CO₂^{36, 37}; however, the role of interfaces on the anomalous maximum remains unclear.

This work investigates the effects of film thicknesses (h) and polymer-substrate, polymer-CO₂ interactions on the swelling of a variety of polymer thin films exposed in Sc-CO₂. Most polymers that have been examined so far are hydrocarbons, in which the solubility of CO₂ in polymer is small, indicating unfavorable polymer-CO₂ interactions.^{25, 34, 35, 37, 39, 40} Therefore, we focus on a highly CO₂-philic polymer, poly(1,1'-dihydroperfluorooctyl methacrylate) (PDFFOMA, or abbreviated as PFOMA). Other polymer systems we examine include polystyrene (PS), poly(ethylene oxide) (PEO) and

the diblock copolymer of polystyrene-*b*-poly(1,1',2,2'-tetrahydroperfluorooctyl methacrylate) (PS-*b*-PTHFOMA). We are interested in a larger thickness regime (100-300 nm) than the previously examined thickness range (below 50 nm)^{34, 35}. We show that even within this thicker regime, amorphous polymer thin films (such as PS) swell more than their bulk analogues.

The anomalous swelling is characterized by analysis of the maximum swelling % and the maximum excess swelling thickness. We demonstrate that our data, and those of others^{25, 34, 35} can be rationalized by considering the contribution of three layers in the total swelling % of the film: the CO₂/polymer interfacial layer, the middle layer, and the polymer/substrate interfacial layer. We conclude that the anomalous swelling maximum cannot be solely explained by the excess absorption of CO₂ at interfaces, as had previously suggested.²⁵

5.2 EXPERIMENTAL SECTIONS

5.2.1 Materials

Three homopolymers, poly(1,1'-dihydroperfluorooctyl methacrylate) (PDFFOMA, or abbreviated as PFOMA), polystyrene (PS) and poly(ethylene oxide) (PEO) and the diblock copolymer of polystyrene-*b*-poly(1,1',2,2'-tetrahydroperfluorooctyl methacrylate) (PS-*b*-PTHFOMA) are studied in this work. Their molecular weights, dissolving solvents and sources are listed in Table 5.1.^{6, 41} Thin films were prepared by dissolving each polymer in its corresponding solvent (polymer concentration about 1-2 wt%) and then spin-casting the solution onto silicon wafers with a native oxide layer (Wafer World Inc.). Different thicknesses (100-300 nm) were obtained by controlling the spin rate and concentration of polymer solutions. Prior to swelling experiments, PS and PS-*b*-

PTHFOMA films were annealed in vacuum ovens at 120 °C for 3 hours while PEO and PFOMA films were annealed in vacuum ovens at 70 °C for 3 hours to remove any residue solvent.

5.2.2 *In-situ* Swelling Experiments

Spectroscopic ellipsometry (J. A. Wollam Co., Inc.) and a customer-built high pressure cell were used to measure *in-situ* swelling of polymer films in Sc-CO₂. The design of the cell and the experimental setup had been described elsewhere.²³ The ellipsometry angle of incidence of 70° was used for all samples. CO₂ pressure was controlled by a strain gauge pressure transducer (Sensotec). The cell was heated using four cartridge heaters (Omega) that were inserted at the top and a PID temperature controller (Omega) was used to control temperature within an accuracy of ± 0.2 °C.

The experimental procedure can be described as the following. Once a sample was loaded into the high pressure cell and subsequently sealed, at least 1 hour was allowed for thermal equilibration at the desired experimental temperatures (35 or 50 °C). Then CO₂ (Air Products, > 99.999%) was charged into the cell using a manual pressure generator (High-Pressure Equipment Co.). At each pressure point, 5-10 minutes were allowed for the swollen films to reach equilibrium, and then ellipsometry angles ψ and Δ were measured.

A four-layer model (from top to bottom, a bulk CO₂ ambient layer, a swollen polymer layer, a native silicon oxide layer and a silicon substrate layer) was used to fit the swelling data. Detailed fitting procedures can be found elsewhere.²³ The swelling percentage was determined by the following equation assuming uniaxial swelling

$$S(\%) = \frac{\Delta V}{V_0}(\%) = \frac{h - h_0}{h_0} \times 100\% \quad (5.1).$$

Table 5.1: Molecular Weights and Sources of Polymers

Polymer	M_n (kg/mole)	Casting solvent	Source
PDHFOMA	100	1,1,2-trichlorotrifluoroethane (Freon 113)	Synthesized by Dr. Lim ⁴¹
PS-b-PTHFOMA	27/127	Co-solvent mixture of Freon 113 (~ 80 wt%) and toluene (~ 20 wt%)	Synthesized by Dr. Lim ⁶
PS	30	Toluene	Purchased from Pressure Chemical
PEO	8.6	Chloroform	Purchased from Polymer source

Here V_0 is the initial volume of the film, h is the thickness of the swollen film, and h_0 is the initial thickness of the polymer film determined by spectroscopic ellipsometry at 0 psig.

5.2.3 Ellipsometry Fitting

It is well known that the results of spectroscopic ellipsometry can be model dependent. Therefore a model that closely describes the composition of a film is crucial to assure the accuracy of measured thickness and optical constant.⁴² Previous attempts have been made to model an adsorbed CO_2 layer between the swollen polymer layer and the CO_2 environment.^{21, 25} However, this model of a CO_2 absorbed layer proved to be unreliable, producing correlations in the fitting parameters and destroyed the uniqueness of the fitting results.^{21, 25} In the case of soft materials interfaces, such a layer is extremely thin compared to the film, and is not measurable with ellipsometry. The effect would be apparent in very thin films where the overall percent swelling is larger than the initial thickness.^{21, 25}

Data from all of the swelling measurements and the corresponding mean squared error (MSE) values are presented in tabular form in Appendix A of this dissertation.

5.3 RESULTS

The results of experiments performed at 35 °C are first discussed. The swelling experiments were conducted by performing alternating pressurization/depressurization runs, where both film thickness and average reflective index of the CO_2 -swollen film were recorded.^{23, 25} Figure 5.1 shows a representative isotherm as well as the changes in average refractive indices at 35 °C for an $h_0 = 109$ nm PFOMA film. Several observations may be made. First, the swelling isotherm exhibits an anomalous

maximum, which also corresponds to a sharp minimum in the refractive index curves. The pressure at which this anomalous swelling shows, 8.0 MPa, is in excellent agreement with the location of the maximum in the compressibility of CO₂, i.e.: density fluctuation, $(\partial\rho/\partial P)_T$, at 35 °C.^{25, 34, 35} Secondly, the swelling isotherms for PFOMA at low pressures possess positive curvature (concaved up), suggesting that PFOMA films reside in a rubbery state.^{23, 25} Because the glass transition temperature of bulk PFOMA is 50 °C at ambient conditions, and can be highly depressed in Sc-CO₂, it is not surprising that PFOMA films are rubbery at 35 °C in CO₂. Thirdly, hysteresis between sorption and desorption runs was observed in both the swelling isotherm and the change in average reflective index. Hysteresis is often due to the nonequilibrium state of the initial sorption run for glassy polymers.²⁵ However, since PFOMA is believed to be in rubbery state, this discrepancy between sorption and desorption is more likely to be the result of PFOMA dissolution in CO₂. Dissolution rates of fluorinated polymer films in CO₂ are found to decrease significantly with decreasing films thicknesses.⁴³ This might be due to the more dominant role of the polymer/substrate interaction.⁴³ Although some dissolution is expected and evident in PFOMA films with thickness below 300 nm, its effect on the sorption isotherms is not obvious. Multiple swelling experiments of PFOMA films show consistent results at 35 and 50 °C. (These results will be shown next.) The influence of dissolution will not be discussed in this paper.

Figure 5.2a shows the swelling isotherms for four PFOMA films with various thicknesses at 35 °C. The four isotherms for these films of different thicknesses are consistent. At low pressures, the percent swelling increases slightly with decreasing film thickness. This small swelling enhancement for thinner films in Sc-CO₂ is reasonable because strong enhancement in swelling of polymer thin films was only found when the thickness of film is below 10 R_g ($h_0 < 10 R_g$).³⁵ On the other hand, the influence of film

thickness on the anomalous swelling maximum is distinct. From Figure 5.2a, it is evident that the two thinner films ($h_0 = 109$ nm and $h_0 = 153$ nm) have smaller swelling maxima (S_{\max}) than the two thicker ones ($h_0 = 179$ nm and $h_0 = 282$ nm). The biggest S_{\max} was observed for the $h_0 = 179$ nm film.

To place the results for the anomalous swelling maxima in perspective, a baseline can be constructed by interpolating the data on either side of the anomalous maxima as shown by the solid lines in Figures 5.2b and 5.2c.²⁵ An effective excess swelling thickness (h_{exc}) at the maxima can be defined by

$$h_{\text{exc}} = h_0 \times (S_{\max} - S_{\text{base}}) \quad (5.2).$$

Here S_{base} is the interpolated swelling % from the baseline at the pressure where S_{\max} is observed. Table 5.2 lists the values of S_{\max} , h_{exc} and the proportional excess swelling, Δ_{exc} for each sample. It is clear that h_{exc} increases as increasing film thickness, consistent with the results of Sirard et al. on the swelling PMMA films in Sc-CO₂.²⁵

It is noteworthy that Koga et al. used the absolute values of S_{\max} to examine the effect of film thickness on anomalous swelling.^{34, 35} They found that S_{\max} decreases as increasing film thickness and levels off when h_0 approaches $8 R_g$.^{34, 35} Here we focus on a much thicker regime, and we examine both S_{\max} and h_{exc} with different film thicknesses. Because h_{exc} is strongly depended on the initial film thickness ($h_{\text{exc}} = h_0 \times (S_{\max} - S_{\text{base}})$), as film thickness increases (h_0 increases), even if S_{\max} decreases (as shown by Koga et al.^{34, 35}), h_{exc} would still increase (as Table 5.2 shows).

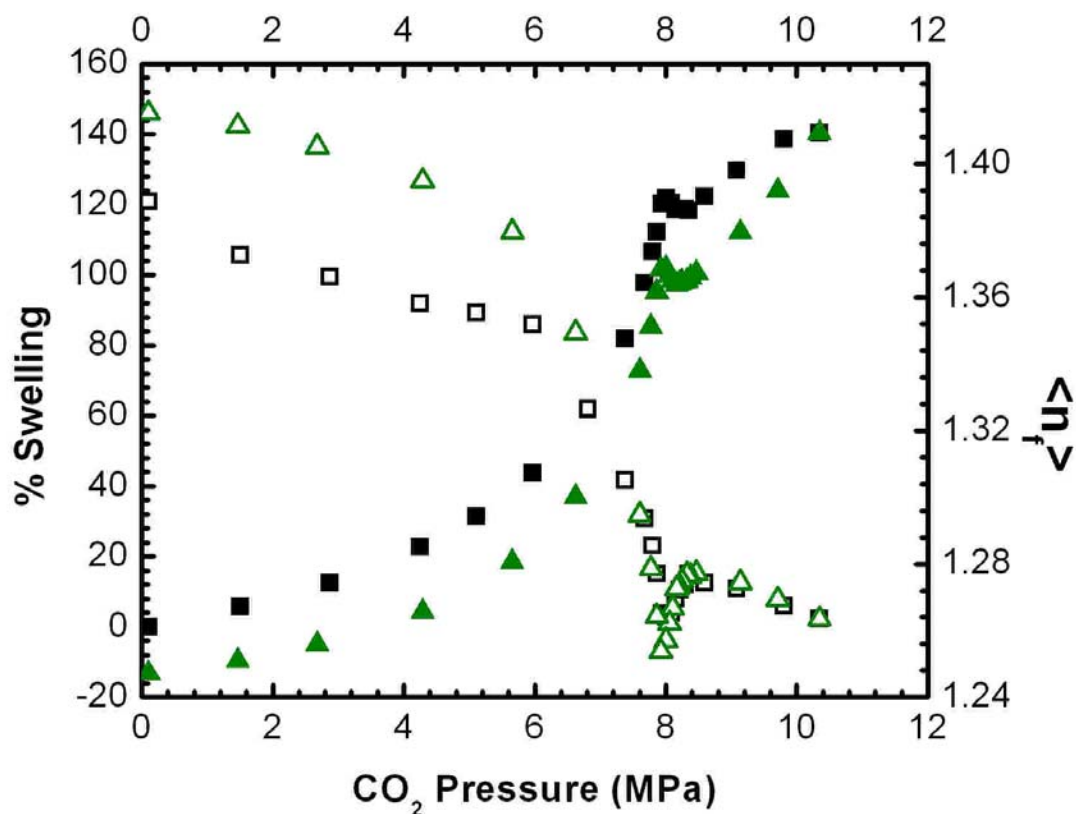


FIGURE 5.1: Representative swelling isotherm and the change in average refractive indices at 35 °C for an $h_0 = 109$ nm PFOMA film. Filled symbols (\blacksquare , \blacktriangle) represent % swelling and open symbols (\square , \triangle) represent the change in average refractive indices. Squares (\blacksquare , \square) represent data obtained during the pressurization run and triangles (\blacktriangle , \triangle) represent data obtained during the depressurization run.

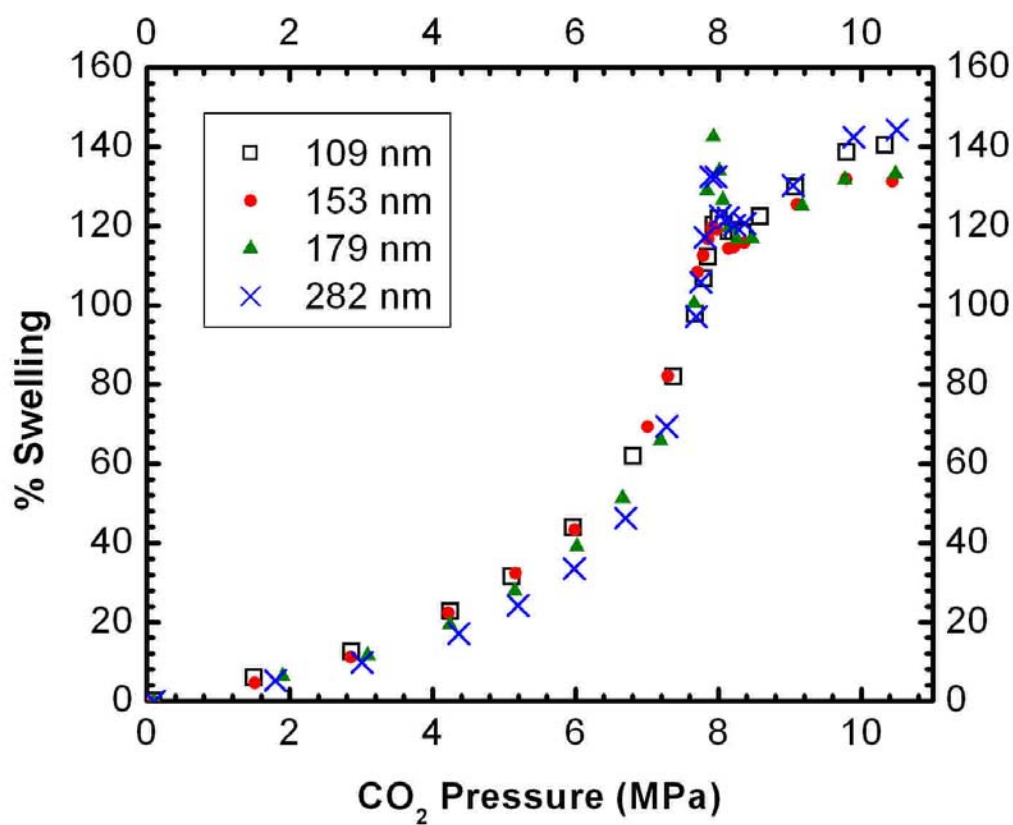


FIGURE 5.2: (a) Swelling isotherms for PFOMA films with various thicknesses at 35 °C.

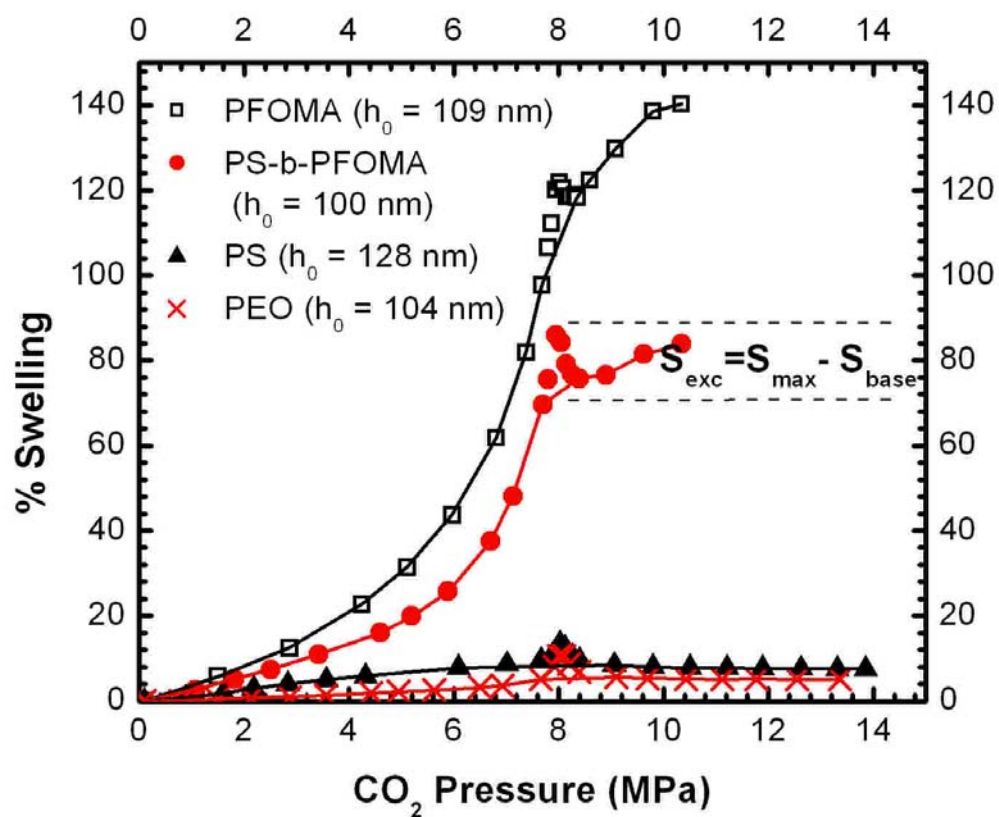


FIGURE 5.2: (b) Swelling isotherms at 35 °C for various polymer films with thickness around 100 nm. The solid line in each isotherm represents the interpolated baseline, which is used to estimate the excess % swelling at the anomalous peak.

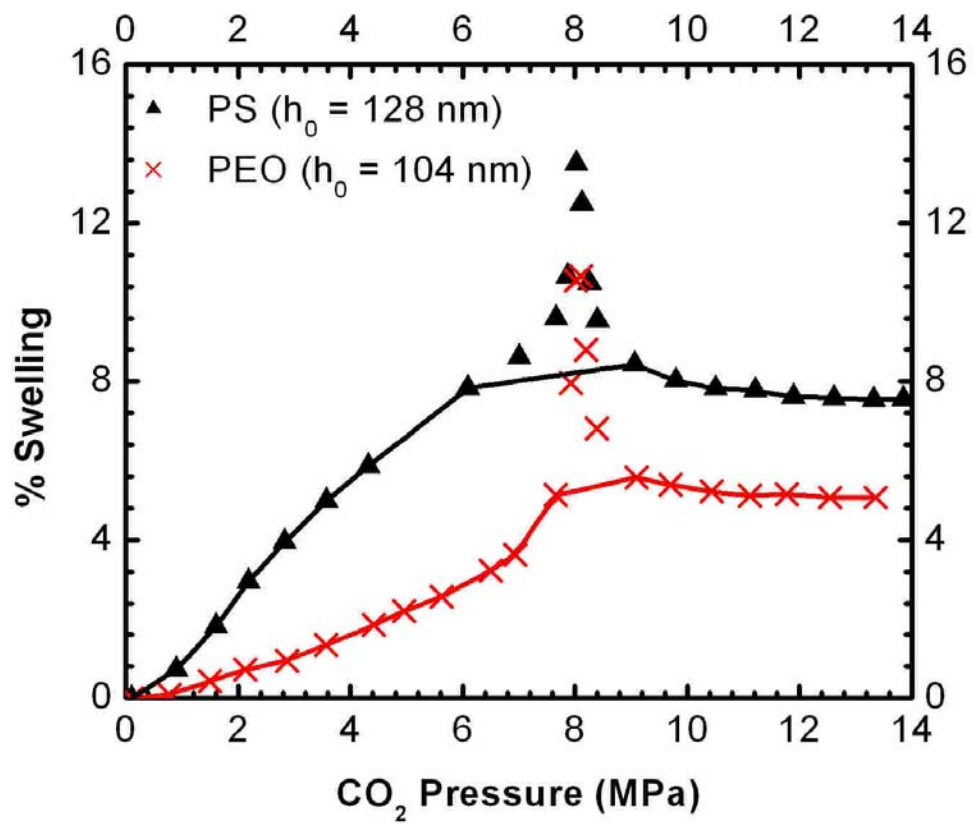


FIGURE 5.2: (c) Swelling isotherms of PS and PEO films with magnified normal axis.

Table 5.2: Analysis of Anomalous Swelling Maximum for Polymer Films at 35 °C

Polymer	Initial film thickness h (nm)	Press. at max. swelling (MPa)	Max. % swelling S_{\max}	Max. excess % swelling S_{exc}^a	Max. excess thickness h_{exc}^b (nm)	Proportional max. swelling Δ_{exc}^c
PDHFOMA	109	8.0	122	14	15	0.11
	153	7.9	120	18	28	0.15
	179	7.9	143	37	65	0.26
	282	7.9	133	28	80	0.21
PS-b-PTHFOMA	100	8.0	86.0	14	14	0.17
PS	128	7.9	13.5	5.0	6.4	0.37
PEO	104	8.1	10.7	5.4	5.6	0.51
PMMA ²⁵	88	8.0	23	3	2.5	0.13
	321	8.0	25	5	16	0.2

$$^a S_{\text{exc}} = S_{\max} - S_{\text{base}}$$

$$^b h_{\text{exc}} = h_0 \times S_{\text{exc}}$$

$$^c \Delta_{\text{exc}} = S_{\text{exc}} / S_{\max}$$

To examine the effect of polymer-substrate and polymer-CO₂ interactions on anomalous swelling maxima, we studied two other homopolymers, PS and PEO as well as the diblock copolymer of PS-b-PTHFOMA. Figure 5.2b compares the swelling isotherm for all four polymers at 35 °C, from which h_{exc} and Δ_{exc} are estimated and listed in Table 5.2. All four isotherms show the characteristic sigmoidal shape as seen in other polymer-CO₂ systems.⁴⁴ As expected, the isotherm for the diblock PS-b-PTHFOMA lies in between that of PS and PFOMA. The curvatures of the swelling isotherms for PFOMA and PS-b-PTHFOMA at low pressure values are positive (concaved up), indicating that both films reside in the rubbery state. On the other hand, the swelling isotherm for PS (Figure 5.2c) at low pressure values are slight negative (concaved down), which is consistent with the fact that the plasticization pressure (P_g) at 35 °C for $h_0 = 90$ nm PS was found to be 5.2 MPa^{9, 21}. However, with regard to PEO, another dimension of complexity needs to be considered and will be discussed next.

It is well known that PEO is a crystalline polymer and crystallization of PEO or copolymers with PEO as a constituent has been widely studied.⁴⁵⁻⁴⁸ Sc-CO₂ can depress the glass transition temperature of glassy polymers significantly; similarly, it has been found that both the crystallization temperature (T_{cr}) and the melting temperature (T_m) of crystalline polymers decrease with increasing CO₂ pressure.⁴⁸⁻⁵⁰ Recently, Madsen employed NMR spectroscopy to study bulk PEO exposed to Sc-CO₂ and found T_m (PEO) is depressed from 63 °C at atmospheric pressure to 43 °C at Sc-CO₂, 8.1 MPa.⁴⁸ The coupling between crystallization and sorption had also been explored, and it was found that the extent of crystallization can affect Sc-CO₂ sorption by reducing both the equilibrium solubility and the diffusivity of Sc-CO₂ in the polymer.⁴⁹

In our study, the PEO films remain in a partially crystalline state throughout the entire pressure range, leading to an extremely small degree of sorption. For example, as

shown in Figure 5.2c, at the highest pressure, 13.8 MPa, PEO film swells 5% at 35 °C. Interestingly, Weidner et al. reported that the solubility of CO₂ in amorphous PEO (4 kg/mole) is as high as 22 wt% at 55 °C and 15 MPa.⁵¹ Because the degree of CO₂ swelling in most polymers increases with decreasing temperature,⁵² the small degree of swelling reported in our study is the result of crystalline PEO films. Further evidence that T_m (PEO) is above 35 °C at 13.8 MPa is that the swelling isotherm levels off at high pressures (P > 10 MPa) in the absence of a distinct change in slope; this indicates the absence of a phase transformation at high pressures. Despite of the crystalline state of our PEO films and the associated unusually small degree of swelling, our key finding is, nevertheless, that anomalous swelling maximum is evident in crystalline polymer films.

Table 5.2 summarizes the results of the anomalous swelling maximum experiments for all polymer films; for comparison, the results by Sirard et al. on PMMA²⁵ are included as well. It is clear that the pressure at which anomalous swelling maxima are observed for all films resides in the pressure regime of 7.9-8.1 MPa. Among the polymer films with h₀ ~ 100 ± 10 nm (for PS film, h₀ = 128 nm) examined in this paper, the trend for both the absolute degree of swelling (S_{max}) and for the effective excess swelling thickness (h_{exc}) in CO₂ is PFOMA > PS-b-PTHFOMA > PS ~ PEO. However, if we consider Sirard's data on PMMA²⁵, then PMMA swelling % is between those for PS and PS-b-PTHFOMA, while it possesses the smallest h_{exc} of all polymers. Consistently, Koga et al. also found that PMMA has an enormously smaller anomalous swelling maximum than PS and PB, while PMMA swells the most among the three at other pressures.^{34, 35} It is also instructive to compare the proportional excess swelling at the anomalous maximum, Δ_{exc}, for different polymers in Table 5.2. It is evident that the trend for Δ_{exc} is PFOMA < PS-b-PTHFOMA < PS < PEO, just opposite that of S_{max} and h_{exc}. All these results will be discussed into detail later.

The results obtained at 50 °C are now discussed. Figure 5.3 shows the swelling isotherm for three PFOMA films, of different thicknesses, at 50 °C. The shapes of the isotherms are relatively independent of film thickness. The anomalous maxima are suppressed at this temperature, compared to those at 35 °C, but they do exist. They occur at a higher pressure than at 35 °C and extend over a broader range of pressure; this was identified in an earlier publication.²⁵ The swelling isotherms of PFOMA films at 35 °C and 50 °C are plotted versus CO₂ activity in Figure 5.4a. The swelling vs. activity curves of all seven isotherms representing the PFOMA films superpose into a single curve. These data indicate that the PFOMA films reside in the rubbery state at both temperatures. Additional swelling vs. CO₂ activity plots for PS-*b*-PTHFOMA and PS films are shown in Figures 5.4b and 5.4c, respectively. In the case of PS (Figure 5.4c), at lower activities, a small discrepancy between the two isotherms is apparent. This is because PS undergoes a glassy state to a rubbery state transition. The anomalous swelling maxima are clear for PS films at both temperatures.

The swelling isotherms of PS thin film are compared with those of bulk PS from other groups in Figures 5.5a and 5.5b.^{44, 53} It is evident that below the anomalous maximum, PS films with thickness $h_0 \sim 130$ nm swell approximately 1 % more than the bulk analogues. While this slight swelling enhancement in PS films compared with bulk is consistent with the data from Koga³⁵ and Sirard²³ at lower pressures, the difference between bulk and thin films is significant in the vicinity of the critical point.

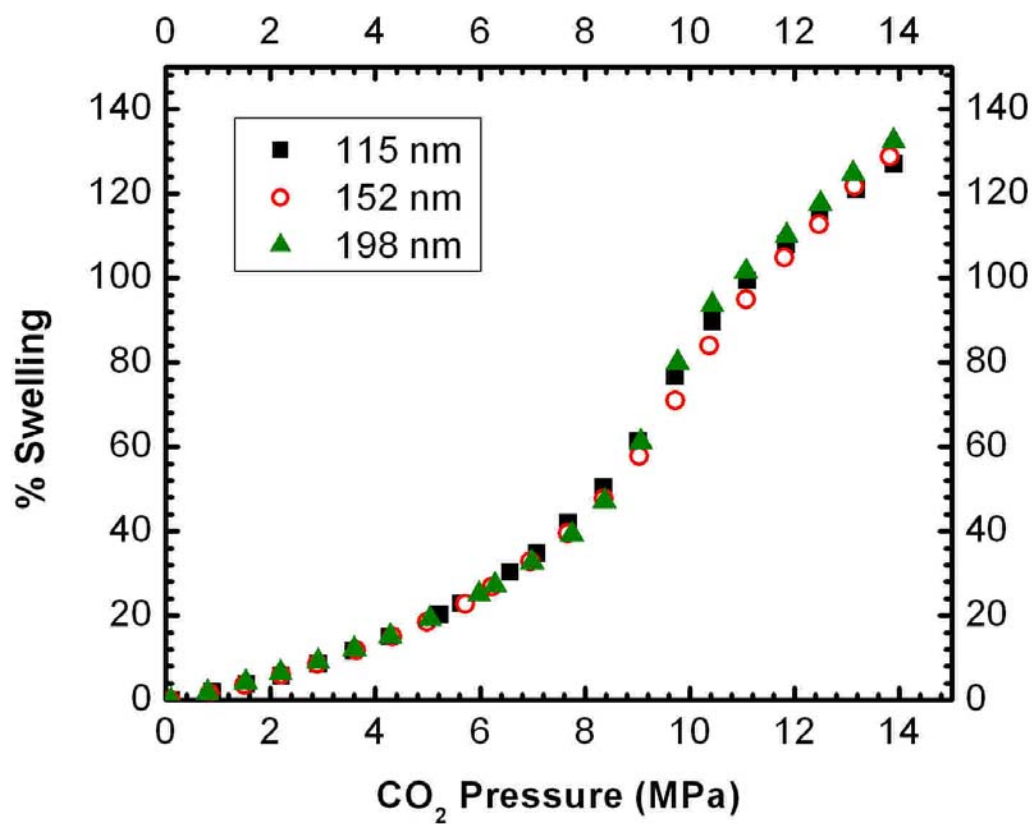


FIGURE 5.3: Swelling isotherms for PFOMA films with various thicknesses at 50 °C.

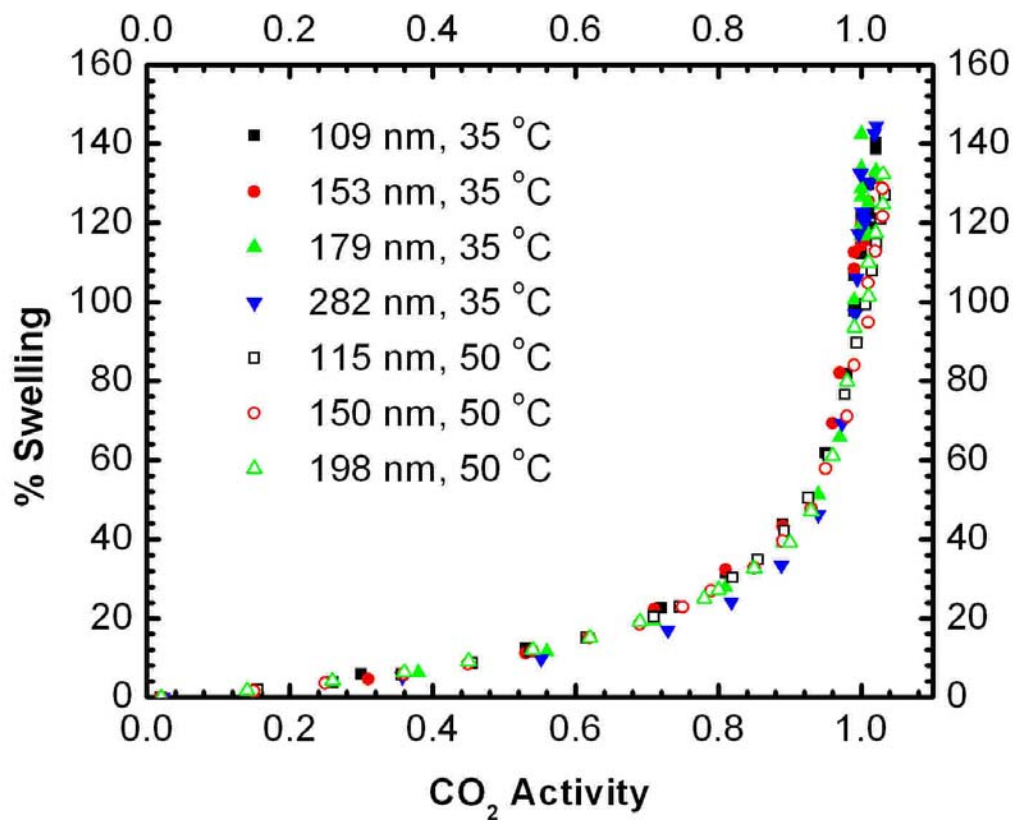


FIGURE 5.4: (a) Swelling of PFOMA films with various thicknesses at both 35 °C and 50 °C plotted against CO₂ activity.

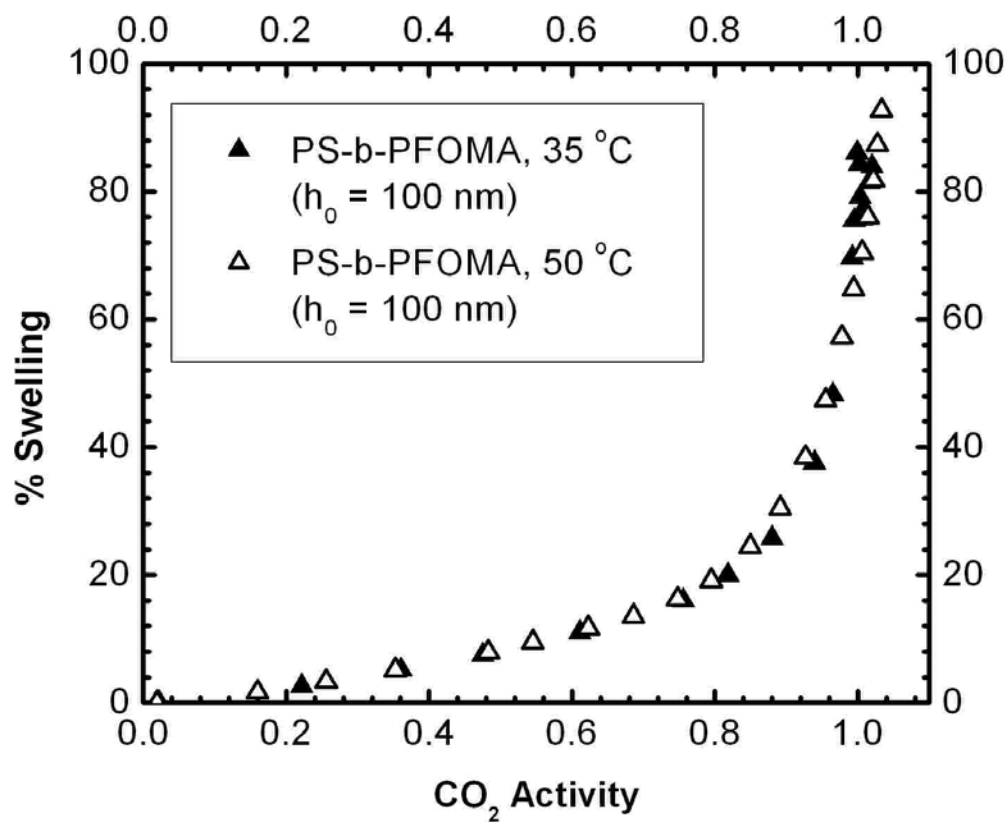


FIGURE 5.4: (b) Swelling of PS-b-PFOMA films plotted against CO₂ activity.

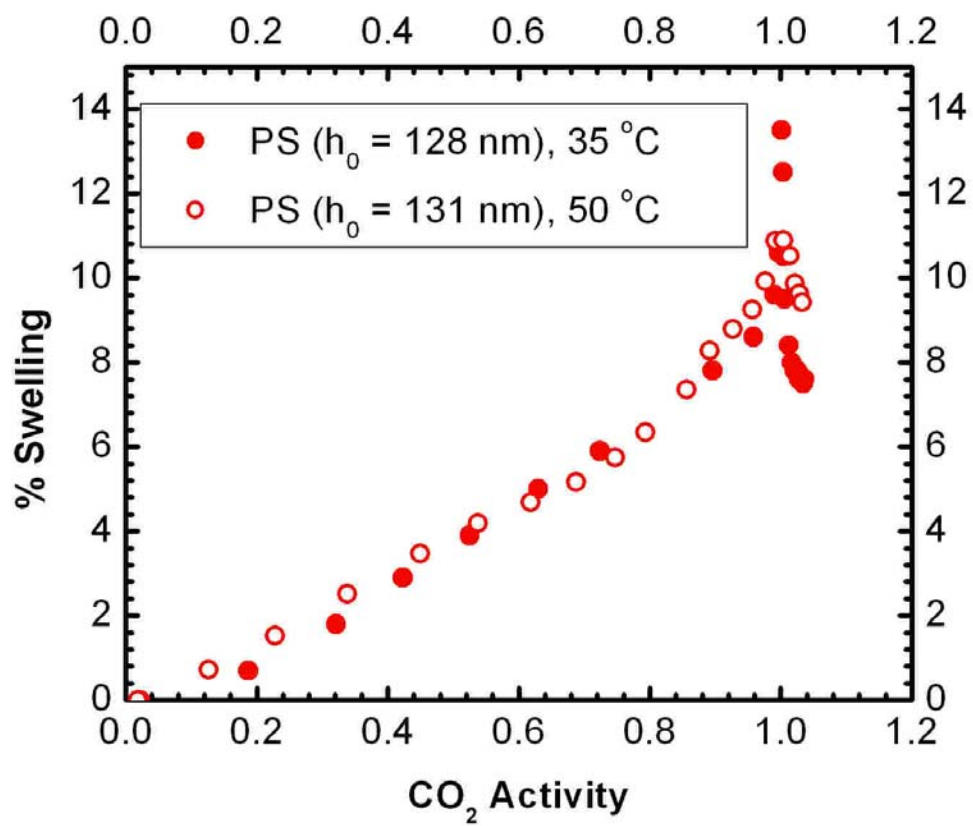
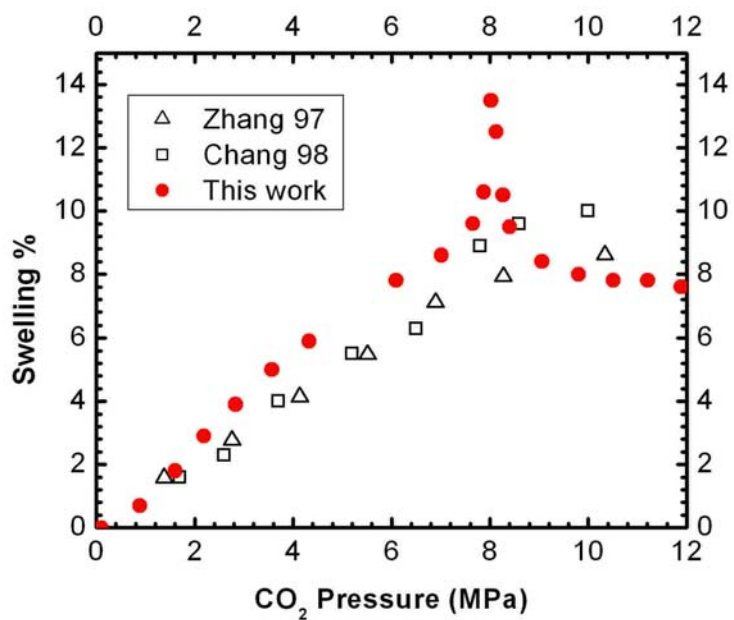


FIGURE 5.4: (c) Swelling of PS films plotted against CO₂ activity.

(a)



(b)

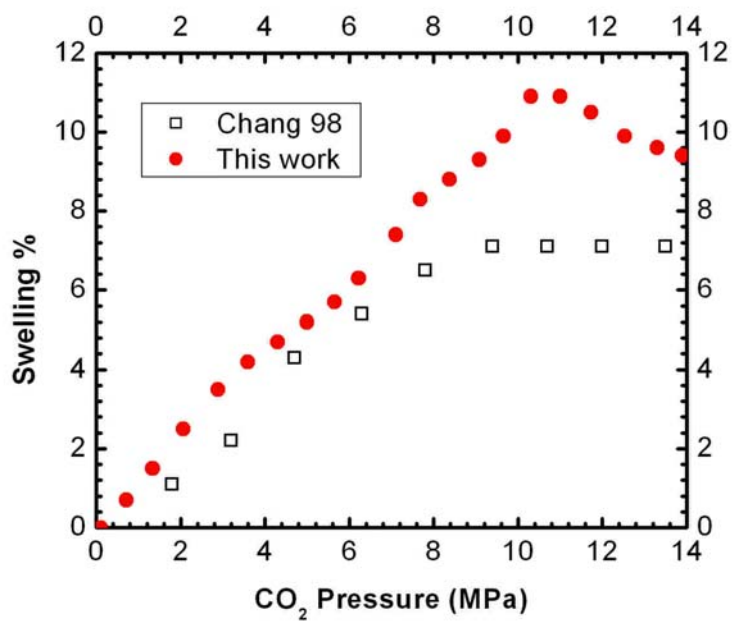


FIGURE 5.5: Comparison between our PS swelling isotherms at 35 °C (a) and 50 °C (b) with two reference works.^{44, 53}

5.4 DISCUSSION: INTERFACIAL EFFECTS ON THE ANOMALOUS SWELLING OF POLYMER THIN FILMS.

The role of interfaces on the anomalous swelling of polymer thin films remains an open question, and there is not much agreement among different groups.^{25, 37, 54-56} Some attribute the anomalous swelling to the surface excess adsorption of CO₂,

$$\Gamma_{ex} = \int_0^{\infty} (\rho(z) - \rho_{bulk}) dz \quad (5.3).$$

We briefly alluded to this in the experimental section. In this equation, z is the distance from the substrate ($z = 0$ represents the substrate interface), $\rho(z)$ is the local density of CO₂ at distance z and ρ_{bulk} is the density of the bulk CO₂. Because CO₂ has low cohesive energy density, the interaction between CO₂ and the surface may be expected to exceed the intermolecular attraction between pure CO₂ molecules. Consistently, there is a difference between $\rho(z)$ and ρ_{bulk} ($\rho(z) > \rho_{bulk}$), which leads to excesses of CO₂ at the surface. However, if the anomalous swelling maximum is solely caused by this surface excess CO₂ wetting layer, then h_{exc} should be relatively independent on the initial film thickness. On the contrary, Table 5.2 indicates that the excess swelling thickness increases with increasing film thickness; clearly the observed excess swelling cannot be explained by the surface excess CO₂ absorption alone. A theoretical study by Wang et al.⁵⁶ determined the thickness of the surface excess CO₂ absorption layer to be 2 nm, which is much less than the observed h_{exc} . It turns out that this 2 nm thick surface excess CO₂ layer is too thin to be accurately determined by ellipsometry, particularly with the small contrast. Attempts to add CO₂ adsorption layer into the ellipsometry-fitting model only produce larger uncertainty and compromised the uniqueness of the fitting results.

Another factor that may contribute to anomalous swelling maximum is the excess CO₂ absorption on the substrate interface. Recent studies^{54, 55} on moisture absorption in photoresist films have pointed out that the attractive interaction between water and

hydrophilic surfaces cause an accumulation of water on the polymer/silicon interface. As a result, the swelling of photoresist films by moisture increases as decreasing film thickness.^{54, 55} However, similar to the approach relying on surface CO₂ wetting layer, attempts to explain the anomalous swelling maximum solely by CO₂ absorption on polymer/substrate interface cannot count the observed thickness dependence of h_{exc} .

The information discussed in the foregoing paragraph (the thickness dependence) indicates that the anomalous swelling observed in polymer thin films cannot be solely due to interfaces. However, it is true that there would be excess CO₂ in thin films compared to the bulk, because the entropy would lead to excess molecules at the interfaces. The comparison between PS films and bulk PS, Figure 5.5, reveals a slight swelling enhancement in thin films compared to the bulk. Moreover, the proportional maximum excess swelling, Δ_{exc} , exhibits the following trend with the polymers from Table 5.2: PFOMA < PS-b-PTHFOMA < PS < PEO. This trend is opposite to that of S_{max} , which be understood by considering the fact that enhanced swelling at interfaces can be more dominant for polymer films that do not have a strong affinity with CO₂.

For a more quantitative assessment of interfacial effects on the anomalous swelling maximum, a simple model is now proposed. Let's simply assume that a polymer film with thickness h_0 is composed, from top to bottom, of a CO₂/polymer interfacial layer h_0^{free} , a middle layer h_0^m and a polymer/substrate interfacial layer h_0^{sub} . By defining a swelling coefficient (α) for each layer, the initial thickness (h_0) and the thickness after swelling (h) can be expressed by

$$h_0 = h_0^{free} + h_0^m + h_0^{sub} \quad (5.4),$$

and

$$h = h^{free} + h^m + h^{sub} = (1 + \alpha_{free})h_0^{free} + (1 + \alpha_m)h_0^m + (1 + \alpha_{sub})h_0^{sub} \quad (5.5).$$

Combining (5.4) and (5.5),

$$h = (1 + \alpha_m)h_0 + (\alpha_{free} - \alpha_m)h_0^{free} + (\alpha_{sub} - \alpha_m)h_0^{sub} = Ah_0 + B,$$

where $A = 1 + \alpha_m$, $B = (\alpha_{free} - \alpha_m)h_0^{free} + (\alpha_{sub} - \alpha_m)h_0^{sub}$ (5.6).

Eq 5.6 shows that at a certain pressure, a linear relationship between the swollen film thickness, h , and the initial film thickness, h_0 , exists. The slope of this linear relationship is directly related to the swelling coefficient of the middle layer (α_m), while the intercept is dependent on the interfacial interactions (α_{free} and α_{sub}). Our model is similar to the two layer model (bulk film layer and polymer/substrate interfacial layer) proposed by Beck Tan and coworkers⁵⁴ to explain the interfacial effect on moisture absorption in thin films. We also want to point out that in order to quantitatively calculate α_{sub} and α_{free} , one must first estimate the values for h_{sub} and h_{free} , which are not directly known.

Alternatively, we first collect all the available experimental data for the thickness dependence of anomalous swelling of various polymer films (10-300 nm) in CO₂ at 35 °C, as listed in Table 5.3.^{25, 34, 35} The swollen film thickness (h) at the anomalous maxima is plotted as a function of the initial film thickness (h_0) in Figure 5.6. It is evident that for all four types of polymer films, h varies linearly as h_0 . The resulting slopes and intercepts are summarized in Table 5.4, where the values of α_m are also listed. PFOMA has higher α_m than all the polymers, while PS processes the lowest α_m , which are expected based on the polymer/solvent interactions.

Table 5.3: Summary of the Initial and Swollen Film Thicknesses at the Anomalous Maximum for Various Polymer Films in CO₂, 35 °C

Polymer	Data Source	Initial film thickness, h_0 (nm)	Swollen film thickness, h (nm)
PFOMA	This study	109	242
		153	327
		179	435
		282	657
PMMA	Koga et al. ³⁵	9.8	14.2
	Sirard et al. ²⁵	88	108
		321	402
PS	This study	128	145
	Koga et al. ³⁴	14	19
		17	22
		29	34
		60	66
		80	87
		107	117
		120	130
		44.5	51
PB	Koga et al. ³⁵	18	30
		32	51
		62	96
		99	153
		17	28
		31	49

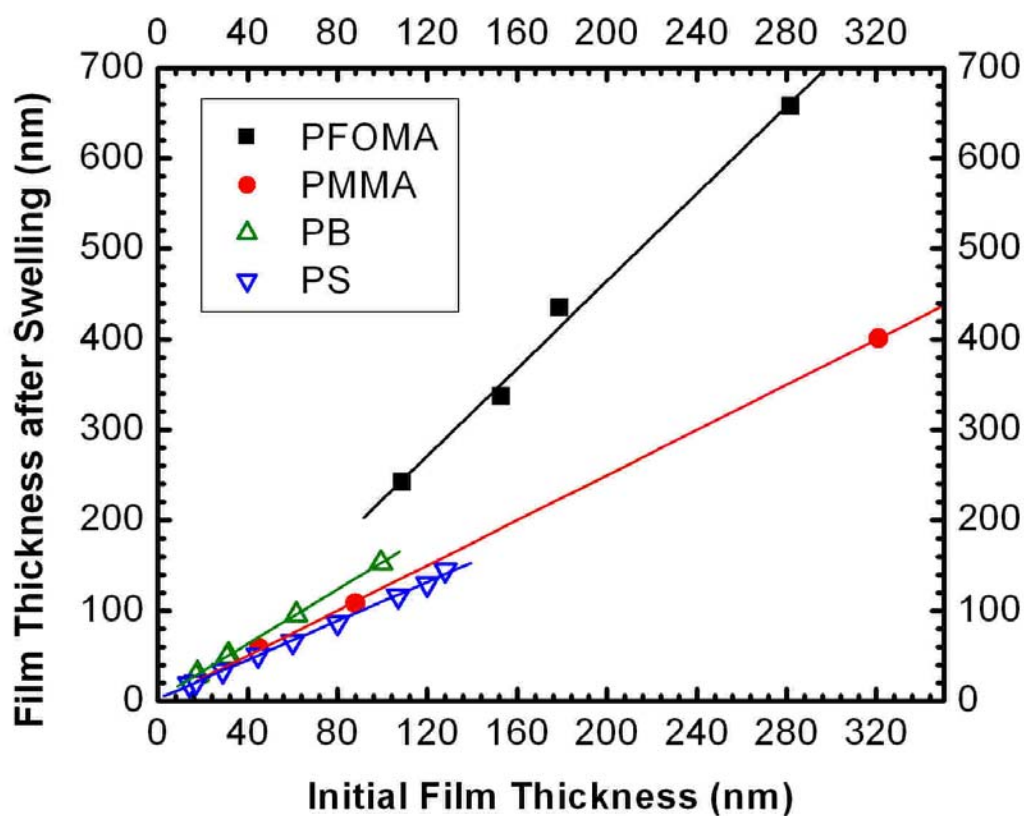


FIGURE 5.6: Film thicknesses for the swollen films at the anomalous maximum (7.9-8.0 MPa) vs. the initial film thicknesses for a variety of polymer films at 35 °C. Linear lines are the fit from the experimental data.

Table 5.4: Summary of the Fitting Results Obtained from Figure 5.6

Polymer	Slope $1 + \alpha_m$	α_m	Intercept	Linearity R^2
PFOMA	2.42	1.42	-18.9	0.993
PMMA	1.25	0.25	0.602	0.999
PS	1.08	0.08	2.80	0.998
PB	1.51	0.51	3.35	0.999

The intercept for each polymer as listed in Table 5.4 is also informative. On the basis of eq 5.6, there are three cases. Case 1: if the middle layer swells more than the other layers ($\alpha_m > \alpha_{\text{free}}$ or $\alpha_m > \alpha_{\text{sub}}$), then B is negative. This case might arise if the interaction between polymer and substrate is more favorable than that between CO₂ and the substrate. For instance, this might occur if there exists a strong attractive short-range interaction between the polymer segments and the substrate. Table 5.4 shows that PFOMA has a negative B value at the anomalous maximum, suggesting that PFOMA chains at interfaces swell less than bulk PFOMA. This may be explained by considering the interaction between the carbonyl group in PFOMA and the native SiO₂ layer at the substrate.^{5, 6, 8} Sirard et al.²⁴ examined the structure of ultra thin ($h < 10$ nm) grafted PDMS films in CO₂ by neutron reflectivity and observed a polymer-concentrated region on the SiO_x interface. They showed that at elevated CO₂ pressures, the thickness of this polymer-concentrated region remains relatively constant while the thickness of the outer solvated region increases, which means $\alpha_m > \alpha_{\text{sub}}$. Case 2: if the middle layer swells less than the polymer chains in interfacial regions ($\alpha_m < \alpha_{\text{free}}$ or $\alpha_m < \alpha_{\text{sub}}$), then B is positive. This means that CO₂ is more favorably segregated into the interfaces. Both PS and PB films (see Table 5.4) belong to this case, which can be explained by the absence of strong interactions between both PS and PB segments and Si/SiO_x substrate. Case 3: if α_m is comparable to α_{free} and α_{sub} , then B can be close to zero. Table 5.4 shows that this is the case for PMMA. PMMA also has a favorable interaction with the substrate, similarly to PFOMA (we can assume the corresponding values of α_{sub} for PMMA and PFOMA are comparable). However, PFOMA has an extremely large α_m and as the result, B for PFOMA is negative while that for PMMA is close to zero.

From the foregoing discussion, it is clear that by applying this simple three-layer model to the existing polymer thin films swelling data in CO₂, the thickness dependence

of anomalous maximum can be explained. It is also shown that depending on the polymer-CO₂ and polymer-substrate interactions, the swelling coefficients for interfaces (α_{free} and α_{sub}) can be either above or below the swelling coefficient of the middle layer (α_{m}). Further insight can be obtained by applying the same analysis for PFOMA films with various thicknesses at pressures different from the anomalous swelling maximum. Figure 5.7 shows the fitted curves at eleven pressures distinct from the anomalous maximum. Figure 5.8 summarizes the results of α_{m} from fitting the data in Figure 5.7. It is clear that α_{m} increases with increasing CO₂ pressure and exhibits a maximum at a pressure ~ 8.0 MPa. This observed maximum in α_{m} further confirms that the swelling of the middle layer also exhibits an anomalous behavior, which can be understood as follows. Because the phase stability of a binary mixture decreases with its compressibility^{25, 57}, the solubility of CO₂ in the polymer film decreases abruptly near the region where the compressibility of CO₂ is at maximum. As a result, CO₂-rich phase and polymer-rich phase may coexist in the film, leading to the observed anomalous maximum in α_{m} . Clearly, the anomalous maximum in α_{m} further confirms that anomalous swelling is not solely due to the excess absorption of CO₂ at interfaces.

5.5 CONCLUSIONS

In-situ spectroscopic ellipsometry was employed to examine the swelling of PFOMA, PS, PEO and PS-b-PFOMA thin films in Sc-CO₂ with the goal to further understand the role of interfaces on anomalous swelling maximum. The anomalous excess swelling thickness (h_{exc}) was found to be dependent on the initial film thickness, on polymer-substrate interaction and on polymer-CO₂ interaction. The experimental data of the dependence of anomalous maximum on polymers and film thicknesses from this study and several references^{25, 34, 35} can be rationalized by considering a three-layer model, which indicates that the anomalous swelling maximum cannot solely be explained by the excess absorption of CO₂ at interfaces (α_{free} , α_{sub}). Instead, the swelling coefficient of middle layer (α_m) also plays an important role and exhibits the anomalous maximum. In addition, the relative interactions between polymer-substrate and polymer-CO₂ were found to affect the magnitudes of α_{free} , α_m and α_{sub} , and therefore influence the anomalous swelling maximum. Clearly, this study further clarifies the role of interfacial interactions on the anomalous swelling maxima exhibited by polymer thin films exposed to compressible fluids.

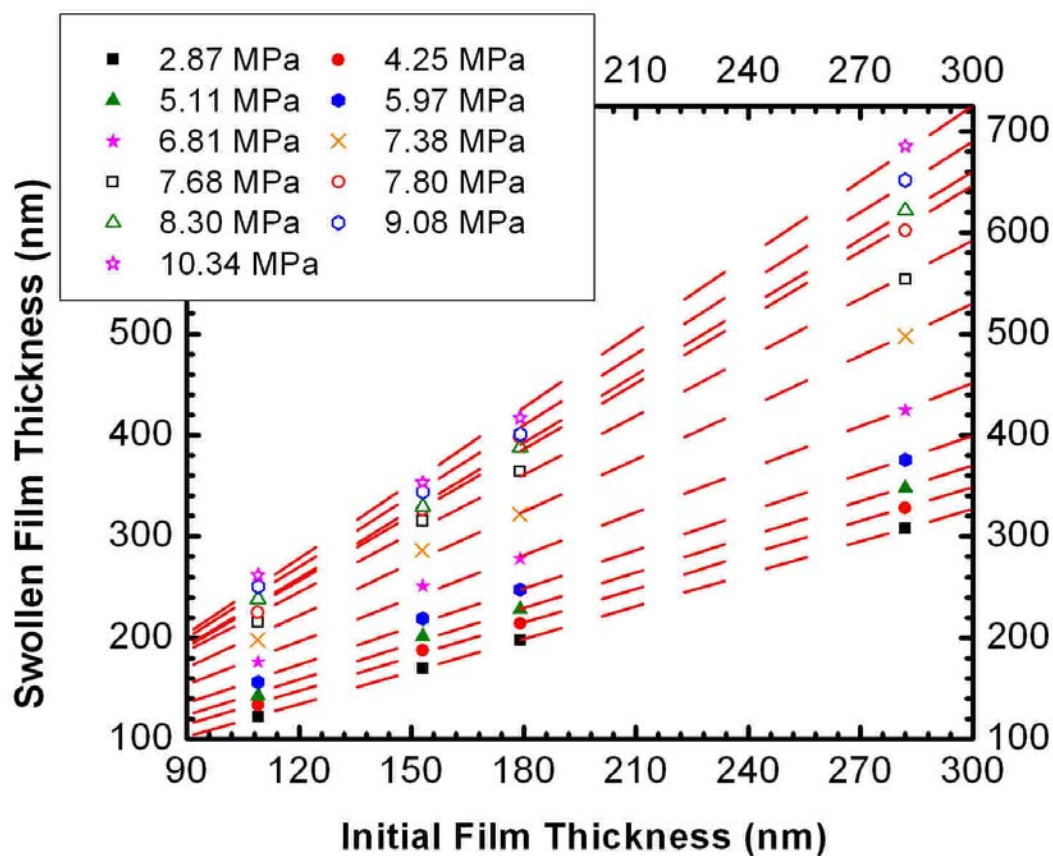


FIGURE 5.7: Film thicknesses for the swollen films vs. the initial film thicknesses at pressure points other than the anomalous maximum for PFOMA films at 35 °C. Linear lines are the fit from the experimental data.

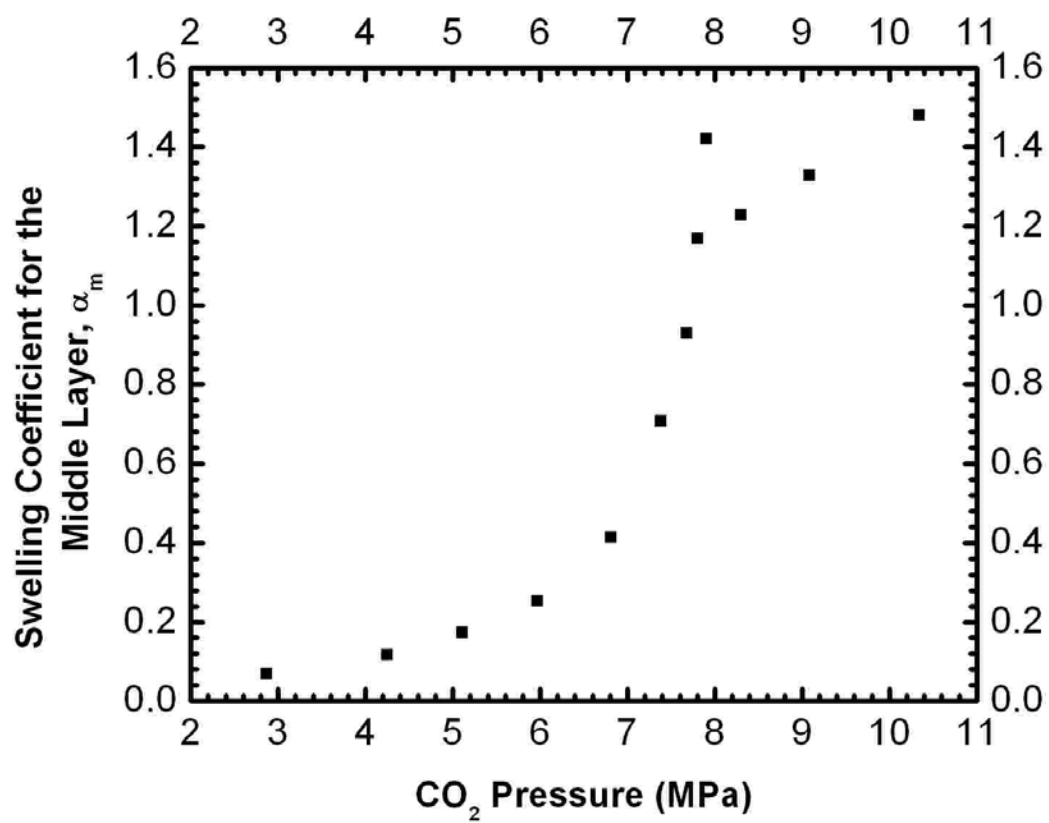


FIGURE 5.8: The swelling coefficients for the middle layer, α_m , vs. CO₂ pressure for PFOMA films at 35 °C.

5.6 REFERENCES

1. Cooper, A. I. *J. Mater. Chem.* **2000**, 10, 207.
2. DeSimone, J. M. *Science* **2002**, 297, 799.
3. Kazarian, S. G. *Polymer Science, Ser. C* **2000**, 42, 78.
4. Yeo, S. D.; Erdogan, K. *Journal of Supercritical Fluids* **2005**, 34, 287.
5. Arceo, A.; Green, P. F. *J. Phys. Chem. B* **2005**, 109, 6958.
6. Li, Y.; Meli, L.; Lim, K. T.; Green, P. F.; Johnston, K. P. *Macromolecules* **2006**, 39, 7044.
7. Li, Y.; Wang, X.; Sanchez, I. C.; Green, P. F.; Johnston, K. P. *Submitted to J. Phys. Chem. B* **2006**.
8. RamachandraRao, V. S.; Gupta, R. R.; Russell, T. P.; Watkins, J. J. *Macromolecules* **2001**, 34, 7923.
9. Meli, L.; Li, Y.; Lim, K. T.; Johnston, K. P.; Green, P. F. *Manuscript in preparation* **2006**.
10. Pai, R. A.; Humayun, R.; Schulberg, M. T.; Sengupta, A.; Sun, J. N.; Watkins, J. *J. Science* **2004**, 303, 507.
11. Zhang, X.; Pham, J. Q.; Ryza, N.; Green, P. F.; Johnston, K. P. *J. Vac. Sci. Technol. B* **2004**, 22, 818.
12. Zhang, X.; Pham, J. Q.; Martinez, H. J.; Wolf, J.; Green, P. F.; Johnston, K. P. *J. Vac. Sci. Technol. B* **2003**, 21, 2569.
13. O'Neill, A.; Watkins, J. J. *MRS Bulletin* **2005**, 30, 967.
14. Keagy, J. A.; Zhang, X.; Busch, E.; Weber, F.; Wolf, P. J.; Rhoad, T.; Martinez, H. J.; Johnston, K. P. *J. Supercritical Fluids* **2006**, in press.
15. Keagy, J. A.; Li, Y.; Green, P. F.; Johnston, K. P.; Weber, F.; Rhoad, J. T.; Busch, E. L.; Wolf, P. J. *Submitted to J. Supercritical Fluids* **2006**.
16. Jones, C.; Zweber, A.; DeYoung, J.; McClain, J.; Carbonell, R.; DeSimone, J. *Critical Reviews in Solid State and Materials Science* **2004**, 29, 97.
17. Gorman, B. P.; Orozco-Teran, R. A.; Zhang, Z.; Matz, P. D.; W., M. D.; Reidy, R. *J. Vac. Sci. Technol. B* **2004**, 22, 1210.

18. Xie, B.; Muscat, A. J. *Microelectronic Engineering* **2004**, 76, 52.
19. Cao, T.; Johnston, K. P.; Webber, S. E. *Macromolecules* **2005**, 38, 1335-1340.
20. Meli, L.; Pham, J. Q.; Johnston, K. P.; Green, P. F. *Phys. Rev. E* **2004**, 69, 051601.
21. Pham, J. Q.; Johnston, K. P.; Green, P. F. *J. Phys. Chem. B* **2004**, 108, 3457.
22. Pham, J. Q.; Sirard, S. M.; Johnston, K. P.; Green, P. F. *Phys. Rev. Lett.* **2003**, 91, 175503.
23. Sirard, S. M.; Green, P. F.; Johnston, K. P. *J. Phys. Chem. B* **2001**, 105, 766.
24. Sirard, S. M.; Gupta, R. R.; Russell, T. P.; Watkins, J. J.; Green, P. F.; Johnston, K. P. *Macromolecules* **2003**, 36, 3365.
25. Sirard, S. M.; Ziegler, K. J.; Sanchez, I. C.; Green, P. F.; Johnston, K. P. *Macromolecules* **2002**, 35, 1928.
26. Findenegg, G. H., In *Fundamentals of Adsorption*, Myers, A. L.; Belfort, G., Eds. Engineering Foundation: New York, **1984**.
27. Strubinger, J. R.; Song, H.; Parcher, J. F. *Anal. Chem.* **1991**, 63, 98.
28. Strubinger, J. R.; Parcher, J. F. *Anal. Chem.* **1989**, 61, 951.
29. Zhou, L.; Bai, S.; Su, W.; Yang, J.; Zhou, Y. *Langmuir* **2003**, 19, 2683.
30. Giovanni, O. D.; Dorfler, W.; Mazzotti, M.; Morbidelli, M. *Langmuir* **2001**, 17, 4316.
31. Gao, W.; Butler, D.; Tomasko, D. L. *Langmuir* **2004**, 20, 8083.
32. Chen, J. H.; Wong, D. S. H.; Tan, C. S.; Subramanian, R.; Lira, C. T.; Orth, M. *Ind. Eng. Chem. Res.* **1997**, 36, 2808.
33. Kiselev, S. B.; Ely, J. F.; Belyakov, M. Y. *J. Chem. Phys.* **2000**, 112, 3370.
34. Koga, T.; Seo, Y. S.; Zhang, Y.; Shin, K.; Kusano, K.; Nishikawa, K.; Rafailovich, M. H.; Sokolov, J. C.; Chu, B.; Peiffer, D.; Occhiogrosso, R.; Satija, S. K. *Phys. Rev. Lett.* **2002**, 89, 125506.
35. Koga, T.; Seo, Y. S.; Shin, K.; Zhang, Y.; Rafailovich, M. H.; Sokolov, J. C.; Chu, B.; Satija, S. K. *Macromolecules* **2003**, 36, 5236.

36. Koga, T.; Akashige, E.; Reinstein, A.; Bronner, M.; Seo, Y. S.; Shin, K.; Rafailovich, M. H.; Sokolov, J. C.; Chu, B.; Satija, S. K. *Physica B* **2005**, 357, 73.
37. Carbonell, R. G.; Carla, V.; Hussain, Y.; Doghieri, F. In *The Role of Gibbs Excess Adsorption on Submerged Surface in Explaining the Complex Swelling Behavior of Supported Polymeric Thin Films in Supercritical Carbon Dioxide*, Eighth Conference on Supercritical Fluids and Their Applications, Ischia, Italy, 28-31 May, **2006**.
38. Abramowitz, H.; Shah, P. S.; Green, P. F.; Johnston, K. P. *Macromolecules* **2004**, 37, 7316.
39. Koga, T.; Seo, Y. S.; Hu, X.; Shin, K.; Zhang, Y.; Rafailovich, M. H.; Sokolov, J. C.; Chu, B.; Satija, S. K. *Europhysics Letters* **2002**, 60, 559.
40. Koga, T.; Y., J.; Seo, Y. S.; Gordon, C.; Qu, F.; Rafailovich, M. H.; Sokolov, J. C.; Satija, S. K. *J. Poly. Sci. B: Polym. Phys.* **2004**, 42, 3282.
41. Sirard, S. M.; Castellanos, H.; Hwang, H. S.; Lim, K. T.; Johnston, K. P. *Ind Eng. Chem. Res.* **2004**, 43, 525.
42. Tompkins, H. G.; McGahan, W. A., *Spectroscopic ellipsometry and reflectometry*. Wiley: New York, **1999**.
43. Pham, V. Q.; Rao, N.; Ober, C. K. *J. Supercritical Fluids* **2004**, 31, 323.
44. Chang, S. H.; Park, S. C.; Shim, J. J. *J. Supercritical Fluids* **1998**, 13, 113.
45. Reiter, G.; Sommer, J. U. *Phys. Rev. Lett.* **1998**, 80, 3771.
46. Reiter, G.; Castelein, G.; Sommer, J. U. *Phys. Rev. Lett.* **2001**, 87, 226101.
47. Reiter, G. *J. Polym. Sci. B: Polym. Phys.* **2003**, 41, 1869.
48. Madsen, L. A. *Macromolecules* **2006**, 39, 1483.
49. Lambert, S. M.; Paulaitis, M. E. *J. Supercritical Fluids* **1991**, 4, 15.
50. Beckman, E.; Porter, R. S. *J. Poly. Sci. B: Polym. Phys.* **1987**, 25, 1511.
51. Weidner, E.; Wiesmet, V.; Knez, Z.; Skerget, M. *J. Supercritical Fluids* **1997**, 10, 139.
52. Wissinger, R. G.; Paulaitis, M. E. *J. Poly. Sci. B: Polym. Phys.* **1987**, 25, 2497.
53. Zhang, Y.; Gangwani, K. K.; Lemert, R. M. *J. Supercritical Fluids* **1997**, 11, 115.

- 54. Beck Tan, N. C.; Wu, W. L.; Wallace, W. E.; Davis, G. T. *J. Poly. Sci. B: Polym. Phys.* **1998**, 36, 155.
- 55. Vogt, B. D.; Soles, C. L.; Jones, R. L.; Wang, C. Y.; Lin, E. K.; Wu, W. L.; Satija, S. K. *Langmuir* **2004**, 20, 5285.
- 56. Wang, X.; Sanchez, I. C. *Submitted to Langmuir* **2006**.
- 57. Sanchez, I. C.; Stone, M. T., Statistical Thermodynamics of Polymer Solutions and Blends. In *Polymer Blends*, Paul, D. R.; Bucknall, C. B., Eds. John Wiley & Sons: New York, **2000**.

Chapter 6: Contact Angle of Water on Polystyrene Thin Films: Effects of CO₂ Environment and Film Thickness

We examine the contact angle of water droplets on polystyrene (PS) thin films supported by silicon wafers under both air and pressurized carbon dioxide (CO₂) environments. At 23 °C, the contact angle is found to increase upon increasing CO₂ pressure in the vapor regime and then levels off in the liquid regime. A macroscopic model based on Young's equation and the geometric-mean method for interfacial tensions correctly predicts the contact angle behavior, although some deviation is observed at higher CO₂ activities. Interestingly, film thickness, h , is also found to affect contact angle, especially when h is comparable with the radius of gyration (R_g). Herein the contact angle decreases, indicating that the apparent surface energy increases with decreasing PS film thickness. This behavior is described by a microscopic model that considers the effect of film thickness on long-range van der Waals forces. In addition, this microscopic model, combined with the PS swelling data in CO₂, well predicts the observed effects of CO₂ pressure on contact angles.

6.1 INTRODUCTION

Extensive research has been devoted to the use of liquid and supercritical carbon dioxide as alternatives to conventional solvents in many polymer and semiconductor processes.¹⁻⁵ CO₂ is an appealing solvent as it is inexpensive, non-toxic, environmentally benign and has an easily accessible critical temperature and pressure. Moreover, the low viscosity and surface tension of CO₂ enable its applications in photoresist cleaning and drying to enhance solvent penetration and to avoid capillary collapse.^{6, 7} However, developing applications of CO₂ in these thin film processes⁶⁻¹⁵ requires a fundamental understanding of the effects of CO₂ environment on properties such as the swelling and wettability of thin films.¹⁶⁻¹⁸ For example, it is found that polystyrene latex particles swell to a greater degree than bulk PS in the presence of CO₂.¹⁸

Polymer thin films have received a lot of attention as the result of their emerging applications.¹⁹⁻²⁷ A thin polymer film may be used as coating to provide a physical/chemical barrier or to improve desirable properties, for instance, antireflective and superhydrophobic coatings.^{27, 28} Consequently, studies on the wettability of polymer films are of technical importance. Other applications of polymer films include photoresists in lithography²⁶, thin film transistors²³ and optical display materials²⁷. In addition, differences in the properties of polymer thin films relative to their bulk analogies are scientifically intriguing. Many studies have shed light on the glass transition,²⁹⁻³³ stabilities,³⁴⁻³⁷ dynamics of polymer thin films^{38, 39} as well as the phase segregation behavior of copolymer thin films.^{34, 40-42} It is known that as the film thickness becomes comparable with the radius of gyration (R_g) of polymer chains, significant deviation from bulk behavior occurs. This deviation is strongly dependent on the interfacial interactions with the substrate as well the free surface.

In this study, we are interested in controlling the wettability of polymer films by employing a CO₂ environment and by varying the film thickness. A high-pressure apparatus and technique had been previously developed by Dickson et al. to examine the wetting phenomena at the CO₂/water/silica interface.¹⁶ To our knowledge, this phenomenon has not been investigated previously for the CO₂/water/polymer interface, where polymer surface is swollen by CO₂. Thus we examine the contact angle of water droplets, θ , placed on polystyrene (PS) thin films supported by silicon wafers with a native oxide layer, under both air and CO₂ environments. Firstly, we show that at a temperature of 23 °C, θ increases upon increasing CO₂ pressure in the vapor regime (from 0 to 61 bar) and then levels off in the liquid regime (above 61 bar). A macroscopic model based on Young's equation and geometric-mean method for the interfacial tensions correctly predicts the trend of θ in CO₂, although some deviation is observed at higher CO₂ activities. Secondly, film thickness, h , is also found to affect the wettability of water on thin films, especially when h is less than 10 R_g; θ is found to decrease with decreasing PS film thickness. A microscopic model that considers the effects of film thickness and CO₂ pressure on the long range van der Waals potential of the system is proposed. It is found that the calculated Hamaker constant of PS film from θ increases with decreasing film thickness, consistent with a decrease in the refractive index of PS films, as measured by ellipsometry. In addition, this microscopic model, combined with the PS swelling data in CO₂, well predicts the observed effects of CO₂ pressure on contact angles.

6.2 EXPERIMENTAL SECTIONS

6.2.1 Thin Film Preparation

Polystyrene (PS) with a molecular weight of 30 kg/mol (purchased from Pressure Chemical) was first dissolved in toluene. Thin films were prepared by spin casting the solutions (typical concentration of 1-2 wt%) onto silicon wafers with a native oxide layer (Wafer World Inc.). Different thicknesses (20-700 nm) were obtained by controlling the spin rate as well as the concentration of solutions. Film thickness and refractive index were measured simultaneously by spectroscopic ellipsometry (J. A. Wollam Co., Inc.). Prior to contact angle measurements, PS films were annealed in vacuum ovens at 120 °C for 3 hours to remove any residue solvent and to relax polymer chains. The radius of gyration (R_g) for PS (30 kg/mole) is calculated to be approximately 4.6 nm.⁴³

To examine the sorption of CO₂ into PS films, spectroscopic ellipsometry was used to measure *in-situ* swelling of a thick PS film ($h = 172$ nm) in Sc-CO₂ at 25 °C. Detailed procedures of the swelling measurements have been described in Chapter 5 and results are presented in Sec. B.1 of Appendix B.

6.2.2 High-Pressure Contact-Angle Measurements

A custom-made high pressure cell was used for the *in-situ* contact angle measurements. The detailed experimental apparatus has been described elsewhere.¹⁶ Before loading the sample, about 5 mL DI-water was first placed in the rear of the high-pressure cell to ensure the saturation of water in the CO₂ phase. PS films were then loaded onto the sample stage and a DI-water drop with the volume of 6-8 μ L was subsequently placed on top of the film using a 10 μ L syringe. Figure 6.1a shows a schematic drawing of water contact angle, θ , for the air/water/PS/SiO_x/Si system. The image of the water drop was then recorded by a CCD camera and analyzed using a

software package from KSV Instruments Ltd.. This software package uses the Young-Laplace method to estimate θ by fitting the complete contour of the sessile drop as a function of interfacial and gravity forces. The pure component densities of water and CO₂ were also used to estimate θ .

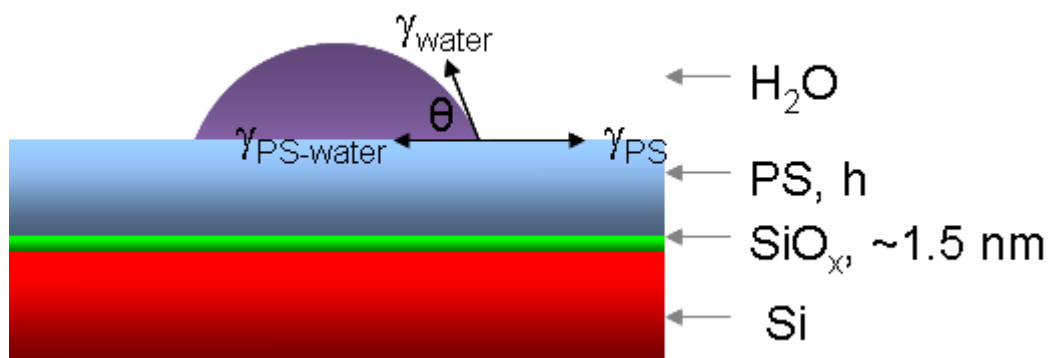
Once the image of the water drop in air was recorded and analyzed, the cell was sealed and CO₂ vapor was subsequently introduced into the viewing cell using a computer-controlled syringe pump (ISCO 260D). Figure 6.1b illustrates of the measurement of θ for the CO₂/water/PS/SiO_x/Si system. All experiments were conducted at room temperature, 23 ± 1 °C. The system pressure was increased gradually from atmospheric pressure and the drop contour was recorded and analyzed at each desired pressure. To examine any hysteresis effects, θ was also measured upon depressurizing the system by using a micrometering valve (Autoclave Engineer, 10B-5896) and slowly venting CO₂ from the cell. All θ measurements were repeated at least three times on multiple films with the same thickness and the reproducibility was $\pm 2^\circ$. For a given droplet measured multiple times, the reproducibility in θ was $\pm 1^\circ$. All of the measured θ values are presented in tabular form in Sec. B.2 of Appendix B.

6.3 RESULTS AND DISCUSSION

6.3.1 Effects of CO₂ Pressure on the Contact Angle: Experimental Results and the Macroscopic Model

The water contact angle, θ on top of PS films was observed to change significantly upon the addition of CO₂ into the high pressure cell. Figure 6.2 shows the representative photographs of a water droplet on a PS film with initial thickness $h = 120$ nm at 23 °C under various CO₂ pressures. Clearly, θ increases with increasing CO₂ pressure. Figure 6.3 shows that θ increases monotonically from $86^\circ \pm 2^\circ$ to $111^\circ \pm 2^\circ$ as

(a)



(b)

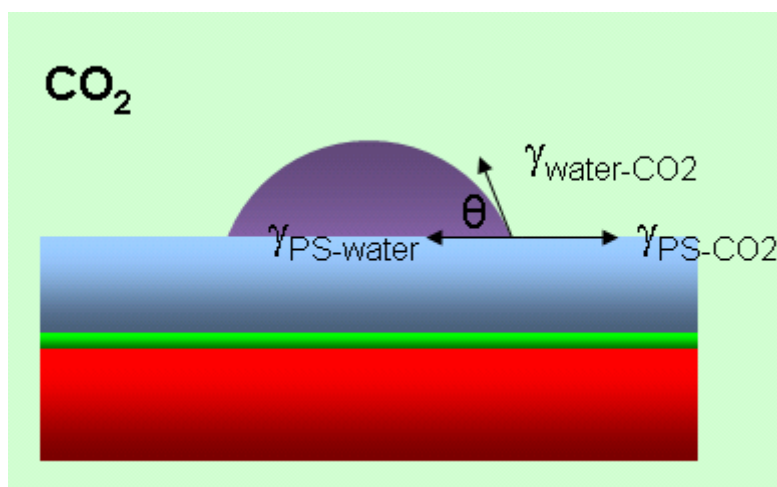


FIGURE 6.1: Schematic of the water contact angle measurements in (a) air/water/PS/SiO_x/Si and (b) CO₂/water/PS/SiO_x/Si systems.

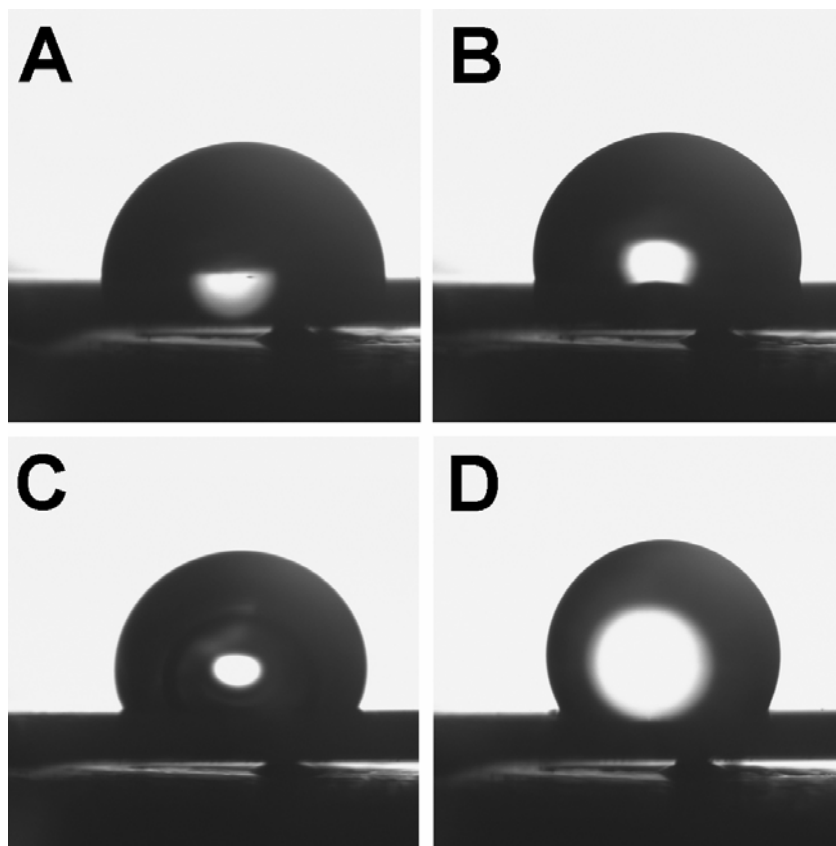


FIGURE 6.2: Photographs of the water contact angle for an $h = 120$ nm PS film at $23\text{ }^{\circ}\text{C}$: (a) in air; (b) 41 bar, vapor CO_2 ; (c) 59 bar, vapor CO_2 ; (d) 138 bar, liquid CO_2 .

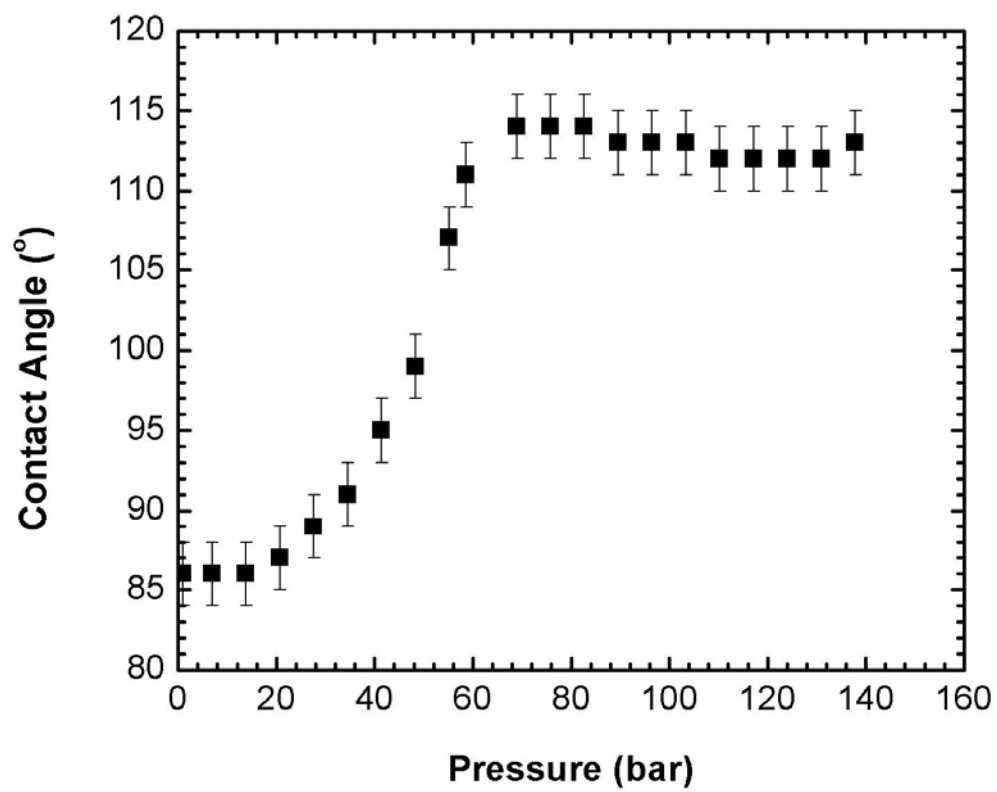


FIGURE 6.3: Effects of CO₂ pressure on the contact angle of water on an $h = 120$ nm PS film at 23 °C.

CO₂ pressure increases to the vapor pressure (61.2 bar at 23 °C). Further increasing CO₂ pressure to 138 bar only increases θ to $113^\circ \pm 2^\circ$, indicating that θ remains relatively constant once CO₂ is in the liquid regime. This observed effect of CO₂ pressure on θ is very similar to the experimental results by Dickson et al.¹⁶ on CO₂/water/silica systems. It is also noteworthy that the measured θ of water drops on PS film in air is $86^\circ \pm 2^\circ$, consistent with the reported value of $88.41^\circ \pm 0.28^\circ$ by Kwok et al.⁴⁴ In addition, as shown by the red triangles in Figure 6.4, θ can be plotted as a function of CO₂ activity, which is a more relevant thermodynamic parameter than pressure.

On the basis of Young's equation, the contact angle of a water droplet on a glassy polymer surface in air, θ , can be related to the surface energy of glassy PS, γ_{PS} , the surface tension of water, γ_w , and the interfacial tension between PS and water, γ_{PS-W} by (also see Figure 6.1a)

$$\cos \theta = \frac{\gamma_{PS} - \gamma_{PS-W}}{\gamma_w} \quad (6.1).$$

Similarly, in a CO₂ environment, θ is dependent on three binary interfacial tensions, γ_{PS-W} , γ_{PS-CO_2} and γ_{W-CO_2} by (see Figure 6.1b)

$$\cos \theta = \frac{\gamma_{PS-CO_2} - \gamma_{PS-W}}{\gamma_{W-CO_2}} \quad (6.2).$$

To model the observed trend of θ with CO₂ pressure, the first step is to calculate the surface energy of glassy PS films in air, γ_{PS} . Typically, to estimate the surface energy of a solid surface, the contact angles of multiple liquids with known surface tensions are measured on the solid. The surface tension of both liquid and solid can be divided into two components,^{16, 45} the dispersive (non-polar) part, γ^d and the polar one, γ^p

$$\gamma = \gamma^d + \gamma^p \quad (6.3).$$

The interfacial tension between two phases, α and β , may be calculated by using a geometric-mean combining rule^{16, 46}

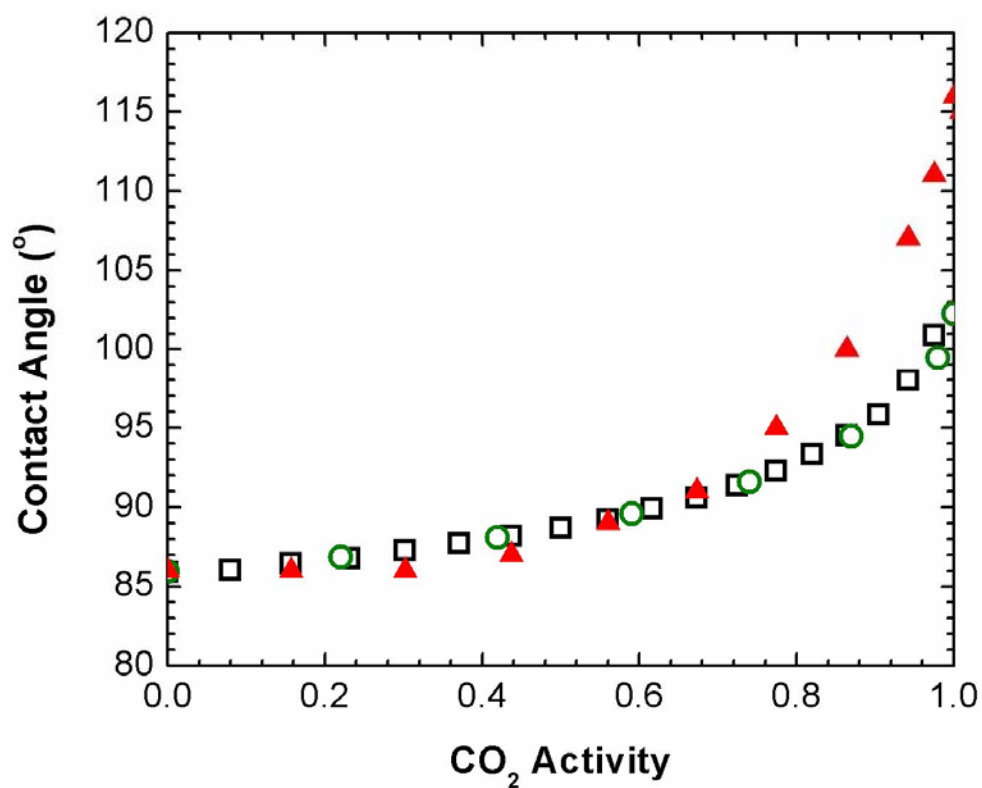


FIGURE 6.4: Comparison between experimentally measured contact angles of water on an $h = 120$ PS film in CO_2 at 23°C and the predicted values by a macroscopic model. The filled triangles (▲) are experimental data; the empty squares (□) are predicted on the basis of water- CO_2 interfacial tension from ref 16; the empty circles (○) are predicted using water- CO_2 interfacial tension from ref 48.

Table 6.1: The Polar and Dispersion Components of Surface Tension for Water, PS and CO₂

Substance	$\gamma = \gamma^d + \gamma^p$ (mN/m)	γ^d (mN/m)	γ^p (mN/m)	$x^p = \gamma^p / \gamma$
Water	71.9 ¹⁶	21.5 ¹⁶	50.4 ¹⁶	0.700
PS	29.1	24.2	4.9	0.168 ⁴⁷
CO ₂	-	-	-	0.06 [*]

* Estimated from the fact that quadrupole-quadrupole interactions count for about 20% of CO₂'s solubility parameter and the remaining 80% is from dispersive interactions.¹⁶
Therefore, $x^p = 0.2^2 / (0.8^2 + 0.2^2) = 0.06$.

$$\gamma_{\alpha\beta} = \gamma_{\alpha}^d + \gamma_{\alpha}^p + \gamma_{\beta}^d + \gamma_{\beta}^p - 2\sqrt{\gamma_{\alpha}^d \gamma_{\beta}^d} - 2\sqrt{\gamma_{\alpha}^p \gamma_{\beta}^p} \quad (6.4).$$

Therefore, if the contact angles of two liquids with known γ_L^p , γ_L^d on a solid are measured, then the surface energies of the solid, γ_s^p and γ_s^d , can be calculated by substituting eq 6.4 into Young's equation (eq 6.1).

The liquids that are commonly used include water and an organic solvent, such as heptane. However, an important criterion in choosing liquids is that the surface tension of the liquids has to be higher than that of the solid.⁴⁴ This criterion is challenging for solids that process a high surface energy because most organic liquids have low surface tensions. Alternatively, it is convenient to introduce the polarity of a solid surface, which is defined by⁴⁷

$$x_s^p = \gamma_s^p / (\gamma_s^p + \gamma_s^d) \quad (6.5).$$

Thus once the polarity of a solid, x_s^p , is known, γ_s^p , γ_s^d can be solved by knowing the contact angle of only one liquid.

As shown in Table 6.1, the polar and dispersive components for the surface tension of water are known, and the polarity of PS, x_{PS}^p , is 0.168.^{16, 47} Substitute eq 6.4 into Young's equation and set $\theta = 86^\circ \pm 2^\circ$, we can obtain an equation that relates γ_{PS}^p and γ_{PS}^d , which can be combined with eq 6.5 to solve γ_{PS}^p and γ_{PS}^d . The calculated values for γ_{PS}^p and γ_{PS}^d are 4.9 and 24.2 mN/m, respectively. Thus the surface tension of the $h = 120$ nm PS film ($\gamma_{PS} = \gamma_{PS}^p + \gamma_{PS}^d$) is calculated to be 29.1 mN/m, consistently with the value of 29.8 ± 0.5 mN/m obtained by Kwok et al.⁴⁴

Next, the effect of CO₂ pressure on the contact angle of water on PS films will be modeled on the basis of eqs 6.2 and 6.4. Because air is miscible with CO₂ in the vapor phase, the surface tension of vapor CO₂ in air, γ_{CO_2} , is not measurable. Following the work by Dickson et al.,¹⁶ the solubility of CO₂ is calculated as a function of CO₂ activity at 23 °C and is used to estimate the corresponding γ_{CO_2} . (Detailed description and values

can be found in ref 16.) The polarity of CO₂ is estimated on the basis of the contribution of the quadrupole-quadrupole interaction in the solubility parameter of CO₂ and is listed in Table 6.1.¹⁶

Having obtained the values of $\gamma_{\text{CO}_2}^{\text{p}}$, $\gamma_{\text{CO}_2}^{\text{d}}$, $\gamma_{\text{PS}}^{\text{p}}$, $\gamma_{\text{PS}}^{\text{d}}$, $\gamma_{\text{W}}^{\text{p}}$ and $\gamma_{\text{W}}^{\text{d}}$, we are now in the position to model the effect of CO₂ pressure on θ . The interfacial tension between PS and water, $\gamma_{\text{PS-W}}$, is estimated to be 24.0 mN/m at 23 °C from eq 6.4. This value of $\gamma_{\text{PS-W}}$ is simply assumed to be fixed upon varying CO₂ pressure (shown by the dashed line in Figure 6.5). Estimated values of $\gamma_{\text{PS-CO}_2}$ (from eq 6.4) and experimental data of $\gamma_{\text{W-CO}_2}$ by Dickson et al.¹⁶ at 23 °C are also plotted as a function of CO₂ activity as shown in Figure 6.5. It is noteworthy we choose to use experimental values for $\gamma_{\text{W-CO}_2}$ rather than estimating it from eq 6.4, because the strong polar contribution in γ_{W} would cause the true value of $\gamma_{\text{W-CO}_2}$ to deviate from eq 6.4. Finally, θ is calculated from eq 6.2 as a function of CO₂ activity and is shown by the empty squares in Figure 6.4.

From Figure 6.4, it is evident that the predicted and experimental θ values agree reasonably well, especially at lower CO₂ activities. However, at CO₂ activities above 0.6, experimental θ increases more rapidly than the model prediction and the deviation increases with increasing CO₂ activity. This deviation is not likely caused by the inaccuracy in $\gamma_{\text{W-CO}_2}$, because another set of reference $\gamma_{\text{W-CO}_2}$ values from Hebach et al.⁴⁸ at 25 °C (shown by empty squares in Figure 6.4) produced similar results. In addition, predicted $\gamma_{\text{PS-CO}_2}$ values from the geometric-mean model are compared with the estimation by Li et al.⁴² (see Figure B.2 in Appendix B) and good agreement is obtained. However, at higher CO₂ activities, a “liquid like” excess CO₂ layer^{32, 49} can reside on the top of PS film, lowering the apparent PS-CO₂ interfacial tension. In other words, $\gamma_{\text{PS-CO}_2}$ at higher CO₂ activities could be overestimated by the model, and as the result, the actual water contact angle θ is higher than the model prediction. It is noteworthy that the

assumption of γ_{PS-W} being independent on CO_2 pressure can also lead to some discrepancy between model prediction and experimental results. The reason is at higher CO_2 activities, CO_2 can strongly absorb into both water and PS phases and can modify γ_{PS-W} .

The effect of CO_2 pressure on the contact angle of water on PS films is reasoned next. It is well known that CO_2 possesses an unusually small cohesive energy density (CED) and consequently, the surface tension of CO_2 is very low. As CO_2 activity increases, the CED of CO_2 increases and becomes closer to the CED of water or PS. Accordingly, both γ_{PS-CO_2} and γ_{W-CO_2} decrease as shown in Figure 6.5. At lower CO_2 activities, θ is less than 90° and $\cos\theta > 0$, indicating that $\gamma_{PS-CO_2} > \gamma_{W-CO_2}$. Hereby the decrease in γ_{PS-CO_2} dominates over that in γ_{W-CO_2} and consequently, θ increases as increasing CO_2 activity. At higher CO_2 activities, θ is large than 90° ($\cos(\theta) < 0$), indicating that $\gamma_{PS-CO_2} < \gamma_{W-CO_2}$, and thus the increase in θ is the result of both decreasing γ_{PS-CO_2} and γ_{W-CO_2} . In summary, the experimentally observed increasing hydrophobicity for PS films with increasing CO_2 activity is due to the interplay among several factors, namely γ_{PS-CO_2} , γ_{W-CO_2} and the sign of $\gamma_{PS-CO_2} - \gamma_{W-CO_2}$.

6.3.2 Contact-Angle Hysteresis in CO_2

Interesting results were obtained by recording contact angles during both pressurization and depressurization. This novel type of contact angle hysteresis in CO_2 was first proposed and investigated by Dickson et al. on CO_2 /water/silica systems in our laboratory.¹⁶ Figure 6.6 demonstrates the change of θ for the CO_2 /water/PS ($h = 120$ nm)/ SiO_x /Si system as the function of CO_2 pressure upon pressurization and depressurization. Because θ does not change significantly in liquid CO_2 regime, the cell was only pressurized in the vapor regime of CO_2 at $23^\circ C$ before being depressurized as shown in Figure 6.6. As expected, θ decreases monotonically with decreasing CO_2

pressure during depressurization. However, it is evident that at each pressure, the value of θ during depressurization is slightly higher ($4-5^\circ$) than the corresponding values during pressurization.

Dickson et al.¹⁶ examined the same hysteresis phenomenon in CO₂ on two CO₂/water/silica systems, where the hydrophilicity of the silica surfaces was different. They found that for silica that had a low surface silanol (SiOH) coverage of 17%, there is no hysteresis between pressurization and depressurization.¹⁶ On the other hand, for silica that had a high surface silanol (SiOH) coverage of 37%, the measured values of θ during depressurization are noticeably higher ($10-20^\circ$) than those during pressurization.¹⁶ This distinct difference between two surfaces was explained by the strong physisorption of CO₂ onto the surface with higher SiOH coverage.¹⁶ As CO₂ physisorbs into the exposed silanol groups and partially remains bound upon rapid depressurization, the surface of 37% SiOH glass becomes more hydrophobic during depressurization as compared with pressurization.¹⁶ Therefore, the contact angle of water, θ , possesses higher values during depressurization as compared with pressurization.¹⁶

With regard to PS thin films, the excess CO₂ on the free surface^{43, 49} may partially remain upon rapid depressurization and cause the depressurization θ to be slightly higher than the pressurization values. However, because there is no strong short-range interaction between PS and CO₂, this excess CO₂ layer is not as robust as the physisorbed CO₂. Once a subsequent run of pressurization and depressurization is complete, a new water drop can be put on the same PS film and measured contact angle of this second drop agrees with the initial measurement very well (unlike the case for hydrophilic silica¹⁶), indicating that there is no strong CO₂ physisorption on the PS surfaces.

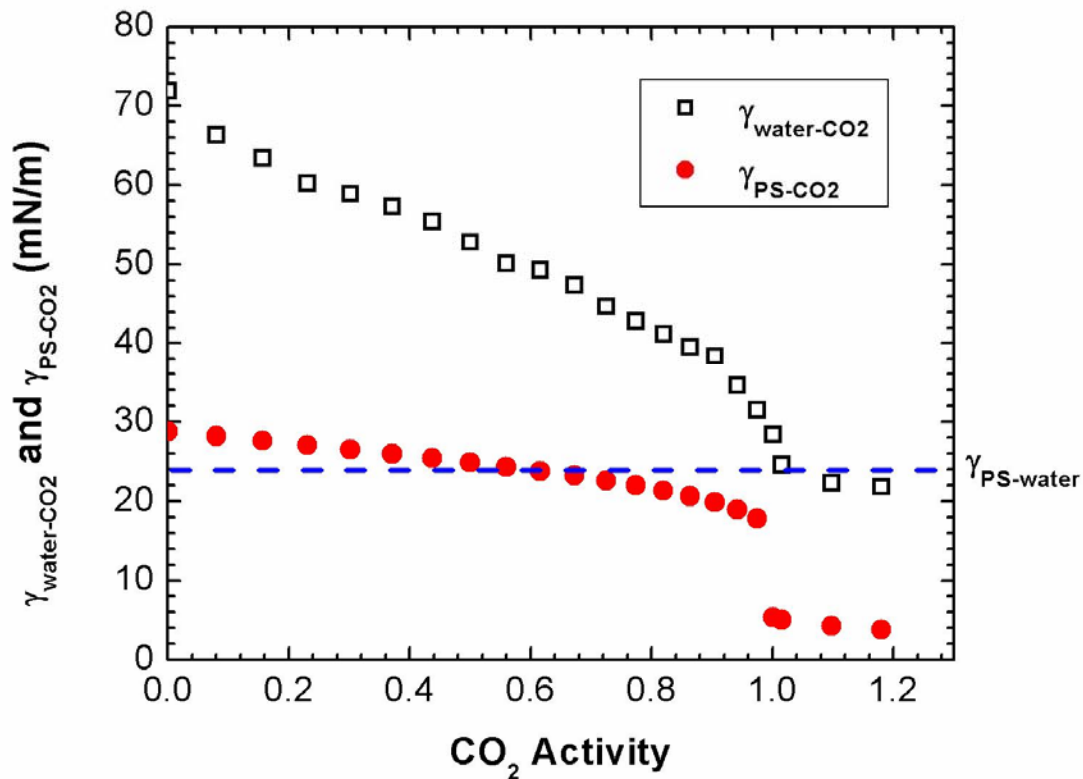


FIGURE 6.5: Estimated interfacial tension between PS and CO₂, $\gamma_{\text{PS-CO}_2}$ from geometric-mean combining rule at 23 °C and experimental measured interfacial tension between water and CO₂, $\gamma_{\text{water-CO}_2}$ at 23 °C by Dickson et al.¹⁶ Dashed line shows the interfacial tension between PS and water, $\gamma_{\text{PS-water}}$, which is assumed to be fixed at a certain temperature.

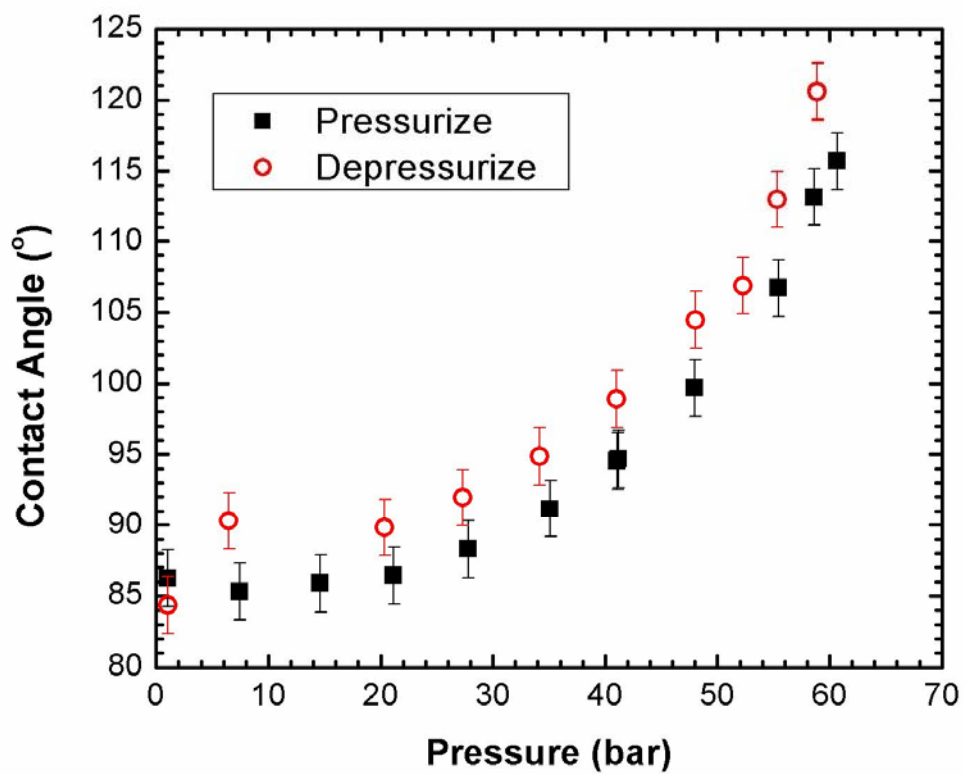


FIGURE 6.6: Contact angle of water on an $h = 120$ nm PS film at 23°C during both pressurization and depressurization.

6.3.3 Effects of Film Thickness on the Contact Angle: Experimental Results and the Microscopic Model

The effect of PS film thickness on θ was also examined. Five samples with thicknesses ranging from 21 nm to 625 nm were investigated and the results are plotted in Figure 6.7. All samples consistently show that θ increases with increasing CO₂ pressure. More importantly, Figure 6.7 shows that at a certain pressure, θ increases with increasing film thickness. This increase is extremely distinct for film thickness below 48 nm ($h < 10 R_g$). Figure 6.8 shows the values of θ in air (corresponding to atmospheric pressure in Figure 6.7) as a function of PS film thicknesses, wherein θ increases significantly from 81 ° for $h = 21$ nm to 86 ° for $h = 120$ nm and then levels off as h increases further. Following our previous discussion, the apparent surface energy of PS films with different thicknesses can be calculated from the values of θ in air by assuming a constant PS polarity of 0.168 as shown in Figure 6.8. Consistent with the trend in contact angle, the apparent surface energy of PS films decreases significantly as h increases from 21 to 120 nm and then levels off.

This strong influence of film thickness, h , on the water contact angle on top of polymer thin films, θ , especially with $h < 10 R_g$ is very interesting. Two factors could be present: (1) as polymer films become ultra thin, the long-range van der Waals forces with the underlying substrate are strongly film thickness dependent, and thus affect the observed contact angle; (2) as the film thickness becomes comparable to R_g , the finite size effect can strongly affect the conformation of polymer segments in thin films as well as the chain mobility, and as a result, the surface energy of PS may be a strong function of film thickness. To this end, a microscopic model will be proposed to evaluate which factor is dominant.

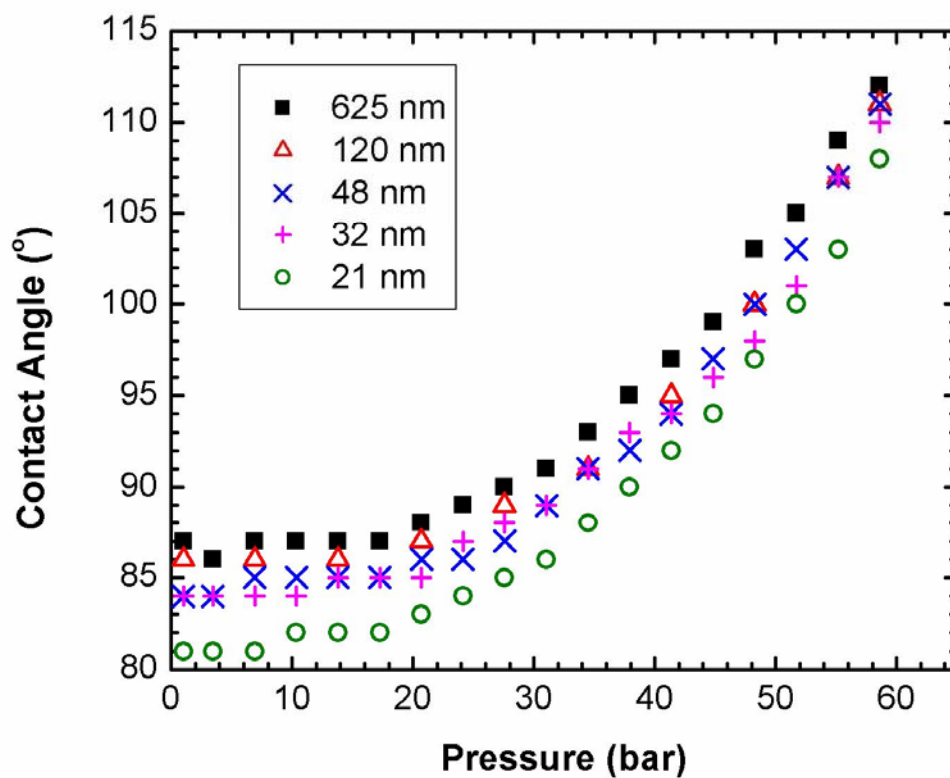


FIGURE 6.7: Effect of film thicknesses on the contact angle of water on PS films at 23 °C. Typical error bars for contact angle (not shown for figure clarity) are $\pm 2^\circ$.

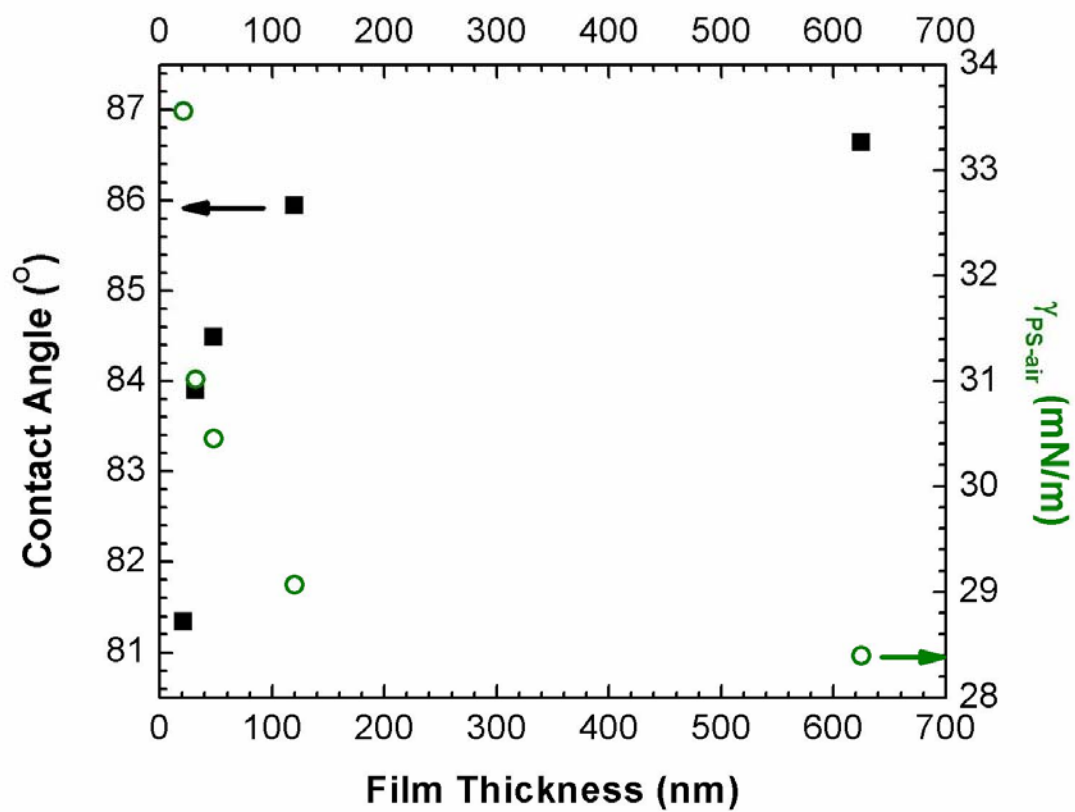


FIGURE 6.8: The contact angle of water and the calculated surface energy for PS films with different thicknesses in air at 23 °C.

6.3.3a The Microscopic Model in Air

The case in air will be examined first. The spreading coefficient that determines whether water spreads on the PS surface or forms a droplet with a finite angle of contact in air is defined by

$$S = \gamma_{PS} - (\gamma_W + \gamma_{PS-W}) \quad (6.6).$$

Positive spreading coefficient ($S > 0$) means complete wetting whereas negative spreading coefficient ($S < 0$) means partial wetting with a contact angle, θ . Combining eq 6.1 and eq 6.6 yields

$$S = \gamma_W (\cos \theta - 1) \quad (6.7).$$

Just like surface tension, it is also convenient to define the spreading coefficient into two terms: the contribution from short range polar interactions, S^P and that from long-range van der Waals dispersive forces, S^{vdw} ,

$$S = S^{vdw} + S^P \quad (6.8).$$

For simplicity, the short-range polar interaction is assumed to be thickness independent, or $S^P \neq S^P(h)$. On the other hand, the thickness dependent S^{vdw} is equivalent to the effective van der Waals potential of a five-layer system (as illustrated in Figure 6.1a) as³⁶

$$S^{vdw}(h) = -\frac{A_{air-water-PS}}{12\pi d_0^2} + \frac{A_{air-water-PS} - A_{air-water-SiOx}}{12\pi(d_0 + h)^2} + \frac{A_{air-water-SiOx} - A_{air-water-Si}}{12\pi(d_0 + h + h_{SiOx})^2} \quad (6.9).$$

Here, A_{132} is the effective Hamaker constant for components 1 and 2 interacting across component 3 and can be related to the Hamaker constants of pure substances by⁵⁰

$$A_{132} = (\sqrt{A_{11}} - \sqrt{A_{33}})(\sqrt{A_{22}} - \sqrt{A_{33}}) \quad (6.10).$$

In addition, $d_0 \sim 0.165 \text{ nm}$ ⁵⁰ is the separation distance between materials in van der Waals contact, h is the thickness of PS film and $h_{SiOx} = 1.5 \text{ nm}$ is the thickness of the native oxide layer.

The Hamaker constant of a pure substance can be calculated from the corresponding refractive index, n , and dielectric constant, ϵ , from Lifshitz theory⁵⁰

$$A_{11} = 3/4kT\left(\frac{\epsilon_1 - 1}{\epsilon_1 + 1}\right)^2 + \frac{3h\nu_e}{16\sqrt{2}} \frac{(n_1^2 - 1)^2}{(n_1^2 + 1)^{3/2}} \quad (6.11).$$

Here ν_e is the mean ionization frequency of the material, typically 3×10^{15} Hz.⁵⁰ Table 6.2 lists the calculated Hamaker constants of water, PS, SiOx and Si, wherein all values are consistent with several literatures.^{35, 50, 51} On the basis of Table 6.2 and eq 6.10, the Hamaker constants can be calculated as $A_{\text{air-water-PS}} = -1.9 \times 10^{-20}$ J, $A_{\text{air-water-SiOx}} = -1.1 \times 10^{-20}$ J and $A_{\text{air-water-Si}} = -5.1 \times 10^{-20}$ J.

Next, we can estimate the value of thickness independent S^P from the thickest, or the most bulk-like film. On the basis of eq 6.7-6.10, using the value of $\theta = 86.6^\circ$ when $h = 625$ nm, we calculate $S^P = -86.3$ mJ. Then θ can be calculated as a function of film thickness (Figure 6.9). It is evident from Figure 6.9 that long range van der Waals forces only affects θ for ultra thin films, namely those with $h < 10$ nm. In addition, although θ increases with increasing h in the range from $10 < h < 100$ nm, this increase is almost negligible (less than 0.05°). In other words, the observed trend of θ with varying PS film thickness cannot be explained by the thickness dependent van der Waals forces. Thus the effects of film thickness on the surface energy of PS films will be examined next.

It is well known that when polymer chains are confined into thin film geometry, especially when the film thickness is comparable with R_g of the chain, properties such as glass transition temperature can become strongly dependent on film thickness.^{29, 30, 33} However, not many studies have focused on the effects of film thickness on the surface energy of polymer films. Consequently, most work that explored the stability or the wetting-dewetting behavior of polymer thin films relied on the bulk polymer surface energy values. To the best of our knowledge, only two studies have examined the change of surface energy of polymer thin films with varying film thickness.^{17, 52} Ashley et al.¹⁷

reported that the surface energy of PS films supported by silicon wafer increases with decreasing film thickness, whereas Shin et al.⁵² showed that the surface energy of free standing PS films decreases with decreasing film thickness.

To examine whether the change of surface energy, and consequently, the change in Hamaker constant of PS films with film thickness can explain the observed trend in contact angle, we fit the Hamaker constant of PS, A_{PS} from the measured θ vs. h data. In eq 6.9, varying PS Hamaker constant only affects $A_{\text{air-water-PS}}$, while the values of $A_{\text{air-water-SiO}_2}$ and $A_{\text{air-water-Si}}$ remain the same. Recalling that $S^P = -86.3$ mJ, we can calculate the corresponding $A_{\text{air-water-PS}}$ for each thickness on the basis of eqs 6.7-6.9 and then the values of A_{PS} can be obtained accordingly. Table 6.3 lists the calculated values of S^{vdw} , $A_{\text{air-water-PS}}$ and A_{PS} , where it is clear that the Hamaker constant of PS increases significantly with decreasing film thickness.

To further verify this proposed thickness dependence of Hamaker constant, it is instructive to revisit eq 6.11. It is well known that in eq 6.11, the second term or the one that is related to the refractive index, n , is dominating. Therefore, it is intuitive to examine the effects of film thickness on the refractive indices of PS films. We first calculated the values of refractive index as a function of h from the fitted Hamaker constants (Table 6.3) as shown in Figure 6.10. It is clear that to be consistent with the trend of A_{PS} vs. h , refractive indices have to increase with decreasing film thickness. Next, we measured the refractive indices of PS films with two different molecular weights from spectroscopic ellipsometry as also shown in Figure 6.10.⁵³ Excellent agreement is found between fitted and experimentally measured refractive indices, proving that it is the change of refractive index with film thickness that affects the Hamaker constant and thus influences the surface energy of the films.

Table 6.2: The Hamaker Constants of Pure Substances

Substance	n	ϵ	A ($\times 10^{-20}$ J)
Water ⁵⁰	1.333	80	3.7
PS ⁵⁰	1.557	2.55	8.5
SiOx ⁵¹	1.46	3.82	6.2
Si ³⁵	-	-	21.1

Table 6.3: The Fitted Hamaker Constants for PS films as a Function of Film Thickness

Thickness h (nm)	h/R _g [*]	θ (°)	S ^{vdw} (mJ)	S ^p (mJ)	A _{air-w-ps} ($\times 10^{-20}$ J)	A _{ps} ($\times 10^{-20}$ J)
625	136	86.6	18.6	-86.3	-1.91	8.5
120	26	85.9	19.5	-86.3	-2.00	8.8
48	10	84.5	21.3	-86.3	-2.18	9.4
32	7.0	83.9	22.0	-86.3	-2.26	9.6
21	4.6	81.3	25.2	-86.3	-2.59	10.7

* $R_g = \sqrt{N/6} \times 0.67 \text{ nm}$, from ref 43.

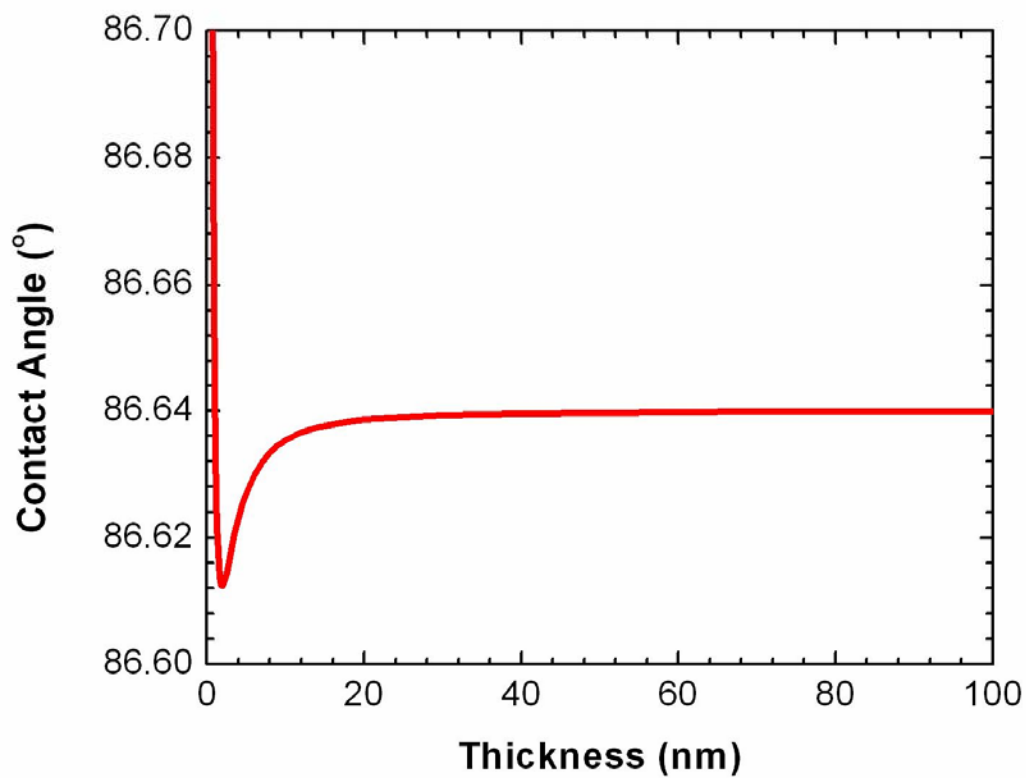


FIGURE 6.9: Calculated contact angle of water on PS films as a function of PS film thickness from the microscopic model at 23 °C.

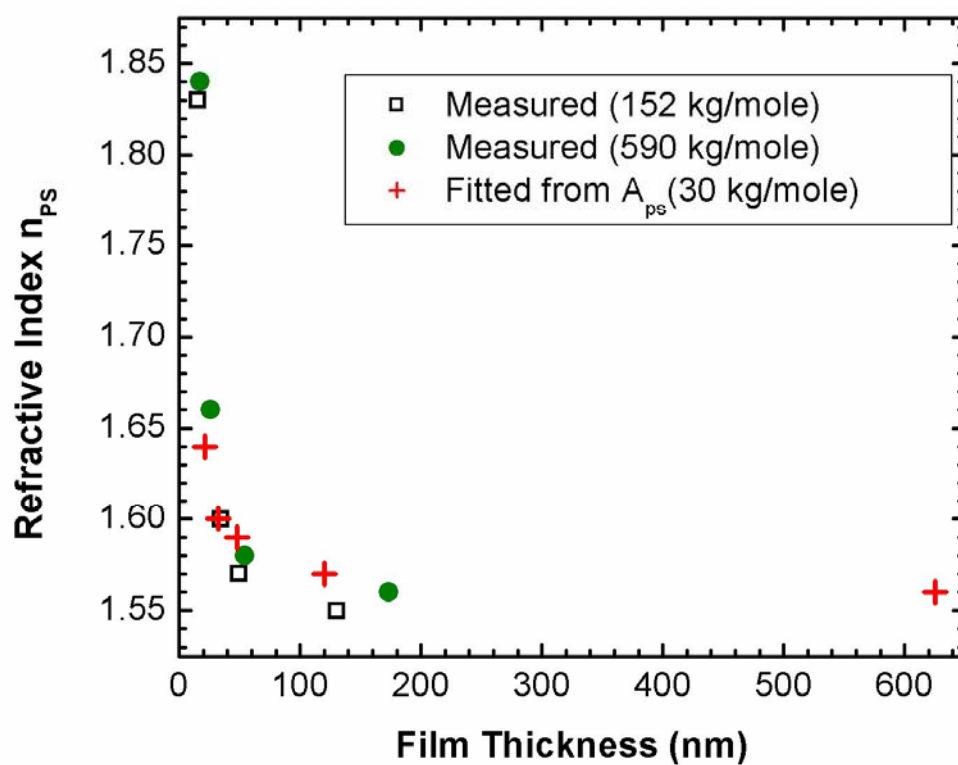


FIGURE 6.10: Comparison between experimentally measured and fitted refractive index of PS films vs. film thickness at 23 °C.

The change of refractive index with film thickness, which have also been observed by other studies⁵⁴, gives more insight into the mechanism of thickness dependent surface energy of polymer thin films. The Clausius-Mossotti equation relates the refractive index of a substance, n , with the number density of molecules, N , molecular electronic polarizability, α , and the vacuum permittivity, ϵ_0 , by,

$$\frac{n^2 - 1}{n^2 + 2} = \frac{N\alpha}{3\epsilon_0} \quad (6.12).^{55}$$

Accordingly, the refractive index increases with increasing molecular density. Soles et al. employed incoherent neutral scattering to study the dynamics of thin polymer films.³⁹ They found that thin film confinement always leads to a reduction in the mean square displacement of polymer chain, $\langle u^2 \rangle$, above the glass transition temperature, T_g and for polymers with strong sub- T_g segmental mobility, $\langle u^2 \rangle$ is also suppressed below T_g .³⁹ Therefore, when film thickness is comparable with R_g , the suppression in $\langle u^2 \rangle$ would result in enhanced molecular density and subsequently cause refractive index to increase. It is noteworthy that alternatively, Ashley et al. used the reduction in $\langle u^2 \rangle$ to directly explain the observed increase in surface energy of thinner PS films.¹⁷

6.3.3b The Microscopic Model in CO₂

The microscopic model will be extended to examine the observed effect of CO₂ pressure on the contact angle. In CO₂, eqs 6.6-6.9 can be rewritten as

$$S = \gamma_{PS-CO_2} - (\gamma_{W-CO_2} + \gamma_{PS-W}) = \gamma_{W-CO_2} (\cos \theta - 1) = S_{CO_2}^{vdw} + S_{CO_2}^P \quad (6.13),$$

and

$$S_{CO_2}^{vdw}(h) = -\frac{A_{CO_2-water-PS'}}{12\pi d_0^2} + \frac{A_{CO_2-water-PS'} - A_{CO_2-water-SiOx}}{12\pi(d_0 + h)^2} + \frac{A_{CO_2-water-SiOx} - A_{CO_2-water-Si}}{12\pi(d_0 + h + h_{SiOx})^2} \quad (6.14).$$

Here we use PS' to denote the CO₂ swollen PS films. The Hamaker constant, A_{PS'} can be calculated from the corresponding refractive index and dielectric constant of the PS-CO₂ mixture, n_{PS'} and ε_{PS'}, on the basis of Lorentz-Lorenz mixing rule

$$\frac{(n_{PS'}^2 - 1)}{(n_{PS'}^2 + 2)} = \Phi_{PS} \frac{(n_{PS}^2 - 1)}{(n_{PS}^2 + 2)} + \Phi_{CO_2} \frac{(n_{CO_2}^2 - 1)}{(n_{CO_2}^2 + 2)} \quad (6.15a),$$

$$\frac{(\epsilon_{PS'}^{1/2} - 1)^2}{(\epsilon_{PS'}^{1/2} + 2)^2} = \Phi_{PS} \frac{(\epsilon_{PS}^{1/2} - 1)^2}{(\epsilon_{PS}^{1/2} + 2)^2} + \Phi_{CO_2} \frac{(\epsilon_{CO_2}^{1/2} - 1)^2}{(\epsilon_{CO_2}^{1/2} + 2)^2} \quad (6.15b)$$

Φ_{PS} and Φ_{CO₂} are the volume fraction of PS and CO₂, respectively and can be obtained from *in-situ* ellipsometric swelling measurements as shown in Sec. B.1 in Appendix B. It is also noteworthy that the swelling of polymer films is found to be thickness dependent^{43, 49} However, for the purpose of this study, we simply use the measured swelling % of an h = 172 nm film. The refractive index of CO₂ can be generated using CO₂-PAC software and the dielectric constant of CO₂ can be calculated from the literature.⁵⁶ Tables B.3 and B.4 in Appendix B list detailed calculation of A_{CO₂}, A_{PS'} and S_{CO₂}^{vdw}.

Unlike the case in air where we can assume that S_{air}^P is independent of film thickness, the value of S_{CO₂}^P varies with changing CO₂ pressure. This variation must be considered in a model for S_{CO₂}^P. To this end, the polar contribution to the spreading coefficient of CO₂/water/PS system is

$$S_{CO_2}^P = \gamma_{PS-CO_2}^P - (\gamma_{W-CO_2}^P + \gamma_{PS-W}^P) \quad (6.16).$$

Because both PS and CO₂ have small γ^P, γ_{PS-CO₂}^P may be estimated from the geometric-mean method by

$$\gamma_{PS-CO_2}^P = \gamma_{PS}^P + \gamma_{CO_2}^P - 2\sqrt{\gamma_{PS}^P \gamma_{CO_2}^P} \quad (6.17).$$

Next, γ_{PS-W}^P can be calculated from the fitted polar spreading coefficient in air ($S_{air}^P = -86.3$ mJ) and the known γ_{PS}^P and γ_W^P (Table 6.1) using

$$S_{air}^P = \gamma_{PS}^P - (\gamma_W^P + \gamma_{PS-W}^P) \quad (6.18).$$

And then $\gamma_{W-CO_2}^P$ can be calculated from the measured water-CO₂ interfacial tension, γ_{W-CO_2} by

$$\gamma_{W-CO_2} = \gamma_{W-CO_2}^P + (\gamma_W^d + \gamma_{CO_2}^d - 2\sqrt{\gamma_W^d \gamma_{CO_2}^d}) \quad (6.19).$$

Therefore, $S_{CO_2}^P$ at each pressure can be calculated from eqs 6.16-6.19 (detailed calculation is shown in Table B.5 in Appendix B) and accordingly, the contact angle of water in the CO₂/water/PS/SiOx/Si system can be estimated as a function of CO₂ pressure (Table B.6 in Appendix B). For comparison, the same calculation is also performed without considering the sorption of CO₂ into PS phase (PS films in CO₂ are treated as pure PS).

Figure 6.11 shows the prediction of θ from this microscopic model (both with and without considering CO₂ sorption into the PS films), as well as the experimental data and the prediction from the macroscopic model. It is clear that the calculated contact angle values from the microscopic model, after considering CO₂ sorption in PS films, agree more closely with the experimental data than the other two models. The same microscopic model, but without considering CO₂ sorption in PS films, only does a slightly better job than the macroscopic model, indicating that CO₂ sorption is the key in the deviation between the macroscopic model and the experimental data. This observation is consistent with our previous discussion in section 6.3.1.

Figure 6.12 compares the microscopic model prediction, after considering of CO₂ sorption, with experimental data for four PS films. Interestingly, the deviation between model prediction and experimental data increases as the film thickness decreases. This increased deviation at thinner films is probably due to a greater enhancement in CO₂

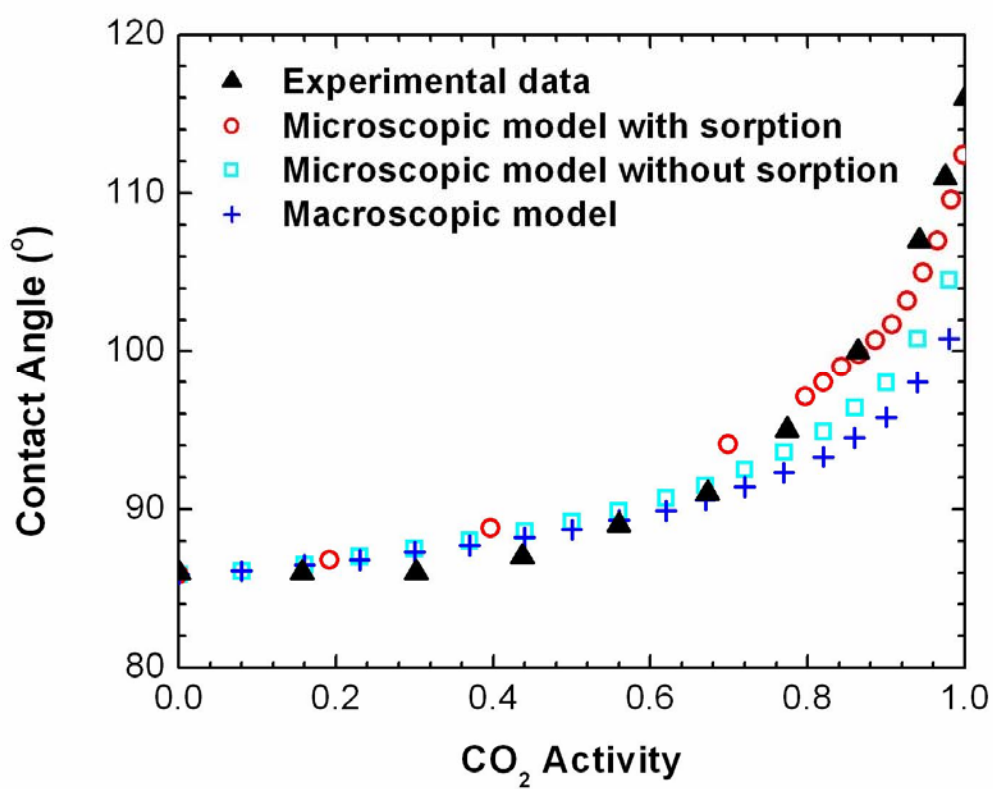


FIGURE 6.11: Comparison between the microscopic model prediction and the experimentally measured water contact angle of an $h = 120$ nm PS film in CO₂ at 23 °C.

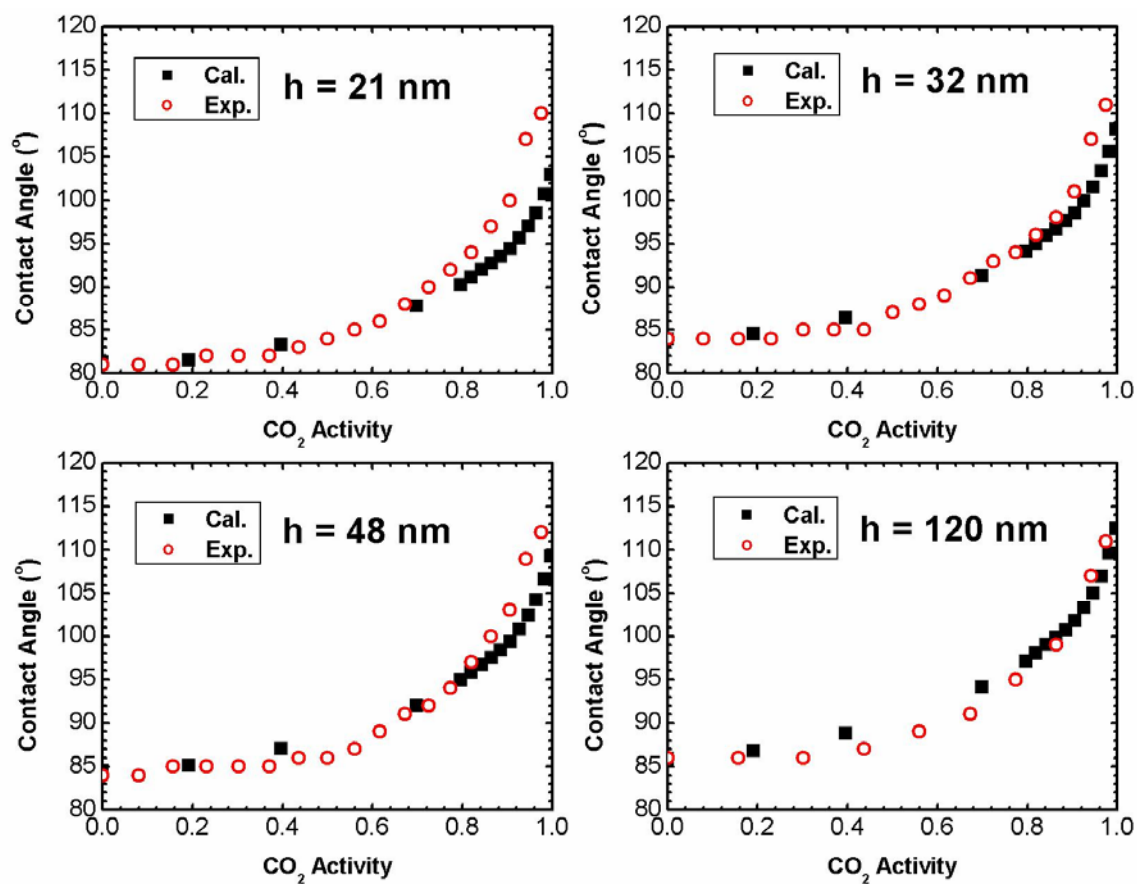


FIGURE 6.12: Comparison between the microscopic model prediction and the experimentally measured water contact angle of PS films with different thicknesses in CO_2 at 23 °C.

sorption for thinner films. The PS swelling % was measured for an $h = 172$ nm film and it can be highly underestimated for films thinner than 50 nm. Therefore, $A_{\text{CO}_2\text{-W-PS}}$ is underestimated and consequently, the calculated $S_{\text{CO}_2}^{\text{vdw}}$ values are higher than the true values. Likewise, calculated values of θ are lower than the experimental values.

In summary, a microscopic model is proposed to calculate the contact angle of water on PS films from the effective van der Waals potential of the system. This microscopic reflects the dependence of PS Hamaker constants on both film thickness and CO_2 pressure, and hence well explains the experimental results.

6.4 CONCLUSIONS

The influence of CO_2 environment and film thickness on the contact angle of water on PS thin films has been investigated both experimentally and theoretically.

Firstly, we show that at the temperature of 23 °C, the contact angle of water increases upon increasing CO_2 pressure in the vapor regime (from 0 to 61 bar) and then levels off as CO_2 enters the liquid regime (above 61 bar). A macroscopic model on the basis of Young's equation and geometric-mean method for the interfacial tensions correctly predicts the trend of contact angle in CO_2 , although some deviation is observed at higher CO_2 activities.

Secondly, the contact angle of water on PS films is found to decrease with decreasing PS film thickness, especially when the films thickness is below 10 R_g . A microscopic model that considers the effects of film thickness as well as CO_2 pressure on the long rang van der Waals potential of the system is proposed. The Hamaker constant of PS films, fitted from the contact angle data, is found to increase with decreasing film thickness, consistent with the measured change of refractive index with film thickness.

In addition, this microscopic model, combined with the PS swelling data in CO₂, well predicts the observed effects of CO₂ pressure on contact angles.

6.5 REFERENCES

1. Cooper, A. I. *J. Mater. Chem.* **2000**, 10, 207.
2. DeSimone, J. M. *Science* **2002**, 297, 799.
3. Kazarian, S. G. *Polymer Science, Ser. C* **2000**, 42, 78.
4. Yeo, S. D.; Erdogan, K. *Journal of Supercritical Fluids* **2005**, 34, 287.
5. Efimenko, K.; Novick, B.; Carbonell, R. G.; DeSimone, J. M.; Genzer, J. *Langmuir* **2002**, 18, 6170.
6. Namatsu, H. *J. Vac. Sci. Technol. B* **2000**, 18, 3308.
7. Namatsu, H.; Yamazaki, K.; Kurihara, K. *J. Vac. Sci. Technol. B* **2000**, 18, 780.
8. Jones, C.; Zweber, A.; DeYoung, J.; McClain, J.; Carbonell, R.; DeSimone, J. *Critical Reviews in Solid State and Materials Science* **2004**, 29, 97.
9. Keagy, J. A.; Zhang, X.; Busch, E.; Weber, F.; Wolf, P. J.; Rhoad, T.; Martinez, H. J.; Johnston, K. P. *J. Supercritical Fluids* **2006**, in press.
10. Mount, D. J.; Rothman, L. B.; Robey, R. J.; Ali, M. K. *Solid State Technol* **2002**, 45, 103.
11. O'Neill, A.; Watkins, J. J. *MRS Bulletin* **2005**, 30, 967.
12. Xie, B.; Muscat, A. J. *Microelectronic Engineering* **2004**, 76, 52.
13. Zhang, X.; Pham, J. Q.; Martinez, H. J.; Wolf, J.; Green, P. F.; Johnston, K. P. *J. Vac. Sci. Technol. B.* **2003**, 21, 2569.
14. Zhang, X.; Pham, J. Q.; Ryza, N.; Green, P. F.; Johnston, K. P. *J. Vac. Sci. Technol. B.* **2004**, 22, 818.
15. Gorman, B. P.; Orozco-Teran, R. A.; Zhang, Z.; Matz, P. D.; W., M. D.; Reidy, R. F. *J. Vac. Sci. Technol. B* **2004**, 22, 1210.
16. Dickson, J. L.; Gupta, G.; Horozov, T. S.; Binks, B. P.; Johnston, K. P. *Langmuir* **2006**, 22, 2161.

17. Ashley, K. M.; Raghavan, D.; Douglas, J. F.; Karim, A. *Langmuir* **2005**, 21, 9518.
18. Otake, K.; Webber, S. E.; Munk, P.; Johnston, K. P. *Langmuir* **1997**, 3047.
19. Black, C. T.; Bezencenet, O. *IEEE Transactions on Nanotechnology* **2004**, 3, 412.
20. Cintavey, L. A.; Clarson, S. J.; Husband, D. M.; Brabander, G. N.; Boyd, J. T. *J. Appl. Polym. Sci.* **2000**, 76, 1448.
21. Dimitrakopoulos, C. D.; Mascaro, D. J. *IBM Journal of Research and Development* **2001**, 45, 11.
22. Guarini, K. W.; Black, C. T.; Milkove, K. R.; Sandstrom, R. L. *J. Vac. Sci. Technol. B* **2001**, 19, 2874.
23. Ziemelis, K. *Nature* **1998**, 393, 619.
24. Black, C. T.; Guarini, K. W.; Milkove, K. R.; Baker, S. M.; Russell, T. P.; Tuominen, M. T. *Appl. Phys. Lett.* **2001**, 79, 409.
25. Pai, R. A.; Humayun, R.; Schulberg, M. T.; Sengupta, A.; Sun, J. N.; Watkins, J. *J. Science* **2004**, 303, 507.
26. Frank, C. W.; Rao, V.; Despotopoulou, M. M.; Pease, R. F.; Hinsberg, W. D.; Miller, R. D.; Rabolt, J. F. *Science* **1996**, 273, 912.
27. Ibn-Elhaj, M.; Schadt, M. *Nature* **2001**, 410, 796.
28. Zhao, N.; Xie, Q.; Weng, L.; Wang, S.; Zhang, X.; Xu, J. *Macromolecules* **2005**, 38, 8996.
29. Besancon, B. M.; Soles, C. L.; Green, P. F. *Phys. Rev. Lett.* **2006**, 97, 057801.
30. Pham, J. Q.; Green, P. F. *Macromolecules* **2003**, 36, 1665.
31. Pham, J. Q.; Johnston, K. P.; Green, P. F. *J. Phys. Chem. B* **2004**, 108, 3457.
32. Pham, J. Q.; Sirard, S. M.; Johnston, K. P.; Green, P. F. *Phys. Rev. Lett.* **2003**, 91, 175503.
33. Soles, C. L.; Douglas, J. F.; Wu, W.-L. *Macromolecules* **2004**, 37, 2901.
34. Green, P. F. *J. Polym. Sci. B: Polym. Phys.* **2003**, 41, 2219.
35. Meli, L.; Pham, J. Q.; Johnston, K. P.; Green, P. F. *Phys. Rev. E* **2004**, 69, 051601.

36. Seemann, R.; Herminghaus, S.; Jacobs, K. *J. Phys.: Condens. Matter* **2001**, 13, 4925.
37. Kropka, J. M.; Green, P. F. *Macromolecules* **2006**, in press.
38. Inoue, R.; Kanaya, T.; Nishida, K.; Tsukushi, I.; Shibata, K. *Phys. Rev. Lett.* **2005**, 95, 056102.
39. Soles, C. L.; Douglas, J. F.; Wu, W.-L. *J. Polym. Sci. B: Polym. Phys.* **2004**, 42, 3218.
40. Arceo, A.; Green, P. F. *J. Phys. Chem. B* **2005**, 109, 6958.
41. Li, Y.; Loo, Y.-L.; Register, R. A.; Green, P. F. *Macromolecules* **2005**, 38, 7745.
42. Li, Y.; Meli, L.; Lim, K. T.; Green, P. F.; Johnston, K. P. *Macromolecules* **2006**, 39, 7044.
43. Koga, T.; Seo, Y. S.; Shin, K.; Zhang, Y.; Rafailovich, M. H.; Sokolov, J. C.; Chu, B.; Satija, S. K. *Macromolecules* **2003**, 36, 5236.
44. Kowk, D. Y.; Lam, C. N. C.; Li, A.; Zhu, K.; Wu, R.; Neumann, A. W. *Polym. Eng. Sci.* **1998**, 38, 1675.
45. Fowkes, F. M. *J. Phys. Chem.* **1963**, 67, 2538.
46. Binks, B. P.; Clint, J. H. *Langmuir* **2002**, 18, 1270.
47. Brandrup, J.; Immergut, E. H., *Polymer Handbook*. John Wiley & Sons: **1989**.
48. Hebach, A.; Oberhof, A.; Dahmen, N.; Kogel, A.; Ederer, H.; Dinjus, E. *J. Chem. Eng. Data* **2002**, 47, 1540.
49. Li, Y.; Park, E. J.; Lim, K. T.; Johnston, K. P.; Green, P. F. *Submitted to J. Polym. Sci. B* **2006**.
50. Israelachvili, J. N., *Intermolecular and Surface Forces*. 2 ed.; Academic Press: **1992**.
51. Butt, H.-J.; Graf, K.; Kappl, M., *Physics and Chemistry of Interfaces*. Wiley-Vch GmbH & Co. : **2003**.
52. Shin, K.; Pu, Y.; Rafailovich, M. H.; Sokolov, J.; Seech, O. H.; Sinha, S. K.; Tolan, M.; Kolb, R. *Macromolecules* **2001**, 34, 5620.

53. The experimental refractive index data was measured on PS films with higher molecular weights than those used for the contact angle measurements. This is because PS with higher M_w has larger R_g , so the change of refractive index with film thickness is experimentally more distinct.
54. Kim, H., K.; Shi, F. G. *Journal of Materials Science: Materials in Electronics* **2001**, 12, 361.
55. Mark, J.; Ngai, K.; Graessley, W.; Mandelkern, L.; Samulski, E.; Koenig, J.; Wignall, G., *Physical Properties of Polymers*. 3 ed.; Cambridge University Press: **2004**.
56. Hourri, A.; St-Arnaud, J. M.; Bose, T. K. *J. Chem. Phys.* **1997**, 106, 1780.

Chapter 7: Conclusions and Recommendations for Future Work

This dissertation showed that compressible fluids, such as supercritical CO₂, can significantly influence the self-assembly in block copolymer thin films. We demonstrated that desirable morphologies in block copolymer films can be obtained by manipulating interfacial interactions through varying film thickness, annealing conditions (such as temperature and pressure) and materials properties. In this final chapter, key findings in this dissertation are highlighted and recommendations for future research are proposed.

7.1 CONCLUSIONS

7.1.1 Crystalline-Amorphous Block Copolymer Thin Films

Through control of temperature, T , and film thickness, h , the relative influence of molecular forces associated with crystallization, with long-range van der Waals forces, and with block-copolymer ordering can be manipulated to control the structure of crystalline-amorphous diblock copolymers thin films. In the temperature range of $T_m < T < T_{ODT}$, where T_m is the melting temperature of the crystalline block and T_{ODT} is the order-disorder transition (ODT) temperature, the driving forces for ordering dominate for films with thickness $h > L_0$. The thickness of this brush layer, L_0 , in contact with the substrate, is about one-half of the intersphere spacing of the bulk copolymer. Films equal or thinner than L_0 dewet, forming droplets on the substrate, because of the long-range van der Waals forces. However, at temperatures of $T_g < T < T_m$, wherein T_g is the glass transition temperature of the amorphous block, all films, regardless of the thickness

range, are structurally stable. This stability is due to the dominance of driving forces for crystallization over the long-range destabilizing van der Waals forces. We found that crystallization has a significant effect on the topography of these films, particularly as the film thickness increases.

7.1.2 Self-Assembly of Asymmetric Block copolymer Thin Films in CO₂

Supercritical CO₂ has shown great potential as an annealing medium to induce ordered structures and to tune feature sizes in block copolymer thin films.

First, we demonstrated that supercritical CO₂ induced phase segregation into spherical structures in PEO-b-PFOMA (5k/52k) diblock copolymer thin films by comparing the morphologies after CO₂ annealing with those after vacuum annealing. The ordered structure is composed of layers of PEO spheres embedded in the matrix of PFOMA. The phase segregation (order) induced by CO₂ was explained in terms of two factors: (1) copolymer volume fraction upon dilution with CO₂, Φ and (2) the relative interaction parameter, $\chi = |\chi_{\text{PEO-CO}_2} - \chi_{\text{PFOMA-CO}_2}|$. The Sanchez-Lacombe Equation of State (SLEOS) was used to fit the swelling isotherms of PFOMA and PEO in CO₂ and to estimate quantitatively the two interaction parameters, $\chi_{\text{PFOMA-CO}_2}$ and $\chi_{\text{PEO-CO}_2}$.

Secondly, the selectivity of supercritical CO₂ towards fluorinated block was exploited to control the formation of surface micellar structure. PS-b-PFOMA cast from a cosolvent mixture of toluene and Freon forms a micellar structure, with a PFOMA core and PS corona, on SiO_x/Si substrates. Upon annealing in supercritical CO₂, the structure undergoes an inversion, wherein the PS chain segments forms the core and the PFOMA segments forms the corona. In addition, the sizes of the PS cores were found to increase with decreasing CO₂ activity. This size variation was explained by considering the effects of Sc-CO₂ activity on PS-CO₂ interfacial tension and on chain stretching of the corona versus the core.

The ability to tune the morphology of self-assembled copolymer films with Sc-CO₂ is of practical interest for templating inorganic nanocrystals in block copolymer scaffolds.

7.1.3 Swelling and Wetting Properties of Polymer Films in CO₂

The swelling of polymer thin films in CO₂ exhibit an anomalous maximum in the vicinity of the critical point of CO₂. The anomalous excess swelling thickness was found to be dependent on the initial film thickness, on polymer-substrate interaction and on polymer-CO₂ interaction. The existing experimental data¹⁻³ on the dependence of anomalous maximum on polymers and film thicknesses can be rationalized by considering a three-layer model, which indicates that the anomalous swelling maximum cannot be solely explained by the excess absorption of CO₂ at interfaces. This study further clarified the role of interfacial interactions on the anomalous swelling maxima exhibited by polymer thin films exposed to compressible fluids.

Both pressured CO₂ environment and film thickness were found to affect the contact angle of water on PS thin films. At 23 °C, the contact angle was found to increase upon increasing CO₂ pressure in the vapor regime and then level off in the liquid regime. In addition, the contact angle decreases with decreasing PS film thickness, especially when PS film thickness is comparable with the radius of gyration. All the experimental results were well explained by a microscopic model that considers the effects of film thickness as well as CO₂ pressure on the long range van der Waals potential of the system.

7.2 RECOMMENDATIONS FOR FUTURE WORK

7.2.1 Nanopatterning Using Block Copolymer Films in CO₂

In Chapter 3, only one molecular weight of PEO-b-PFOMA diblock copolymer was examined. Extending this study on the same diblock but with different molecular weights and symmetries can further explore the effects of CO₂ on the phase diagram of this system. However, one needs to be careful with the choice of molecular weights. PEO-b-PFOMA with small molecular weights may have extremely low order-disorder transition temperatures and the films may be in the phase-mixed state under both accessible CO₂ and vacuum/air conditions. Instead of using PEO-b-PFOMA (5k/52k) in which the phase structure is spheres of PEO embedded in the matrix of PFOMA, systems with PFOMA as the spherical domain, or those with cylindrical phase structure can also be interesting. It is noteworthy that for PEO-b-PFOMA diblock with PFOMA as the minor component, the substantial swelling of PFOMA by CO₂ may significantly increase the volume fraction of PFOMA and thus induce a distinct change in phase structure. The same strategy of changing molecular weights and symmetries can be also applied to the PS-b-PFOMA system examined in Chapter 4. In addition, the effects of film thickness on the structures of micelles are worthy studying. As PS-b-PFOMA films get thinner, the shape of micelles can become more distorted and can evolve from spheres to ellipsoids.

The choice of the right materials is the key in designing future experiments to develop block copolymer templates with ordered features in supercritical CO₂. Other than the copolymers that contain PFOMA as the block that possesses preferential interaction with CO₂, systems that containing poly(dimethyl siloxane) (PDMS) would also be a good choice. With regard to diblock copolymers that lack preferential interactions with CO₂ (both blocks are equally “CO₂-phobic”), CO₂ can be used to lower the T_{ODT} and to increase the kinetics of phase segregation. For systems in which the T_{ODT}

are substantially high under air/vacuum conditions, ordered structures can be obtained at accessible temperatures in supercritical CO₂.

In addition, the self-assembly of nanoparticles on diblock copolymer scaffolds has attracted a lot of research interests, because the ease and control offered by the copolymer can be combined with the electronic, magnetic or photonic properties of the inorganic component.⁴⁻¹² Once the self-assembly behavior of a particular block copolymer in supercritical CO₂ is well understood, more effort can be put into using CO₂ to selectively sequester nanoparticles into one block domain to make functional materials. The low processing temperature of CO₂ can be an asset here, because it can prevent ligand detachment and particle fusion. One promising strategy is to immerse preformed block copolymer template in CO₂, which is premixed with inorganic precursors.¹³ The dilation effects and the high-diffusivity of CO₂ can be utilized to infuse inorganic precursors into one domain. In another possible approach, nanoparticles can be mixed with block copolymer upon depositing the films, and then CO₂ annealing can be used to induce ordering in the nanoparticle/copolymer composite.

7.2.2 Interfacial Phenomena of Polymer Films in CO₂

Chapter 5 showed that *in-situ* spectroscopic ellipsometry may have reached its limitation in examining the anomalous swelling maximum of polymer thin films in CO₂. More advanced technique is required to differentiate between the excess absorption of CO₂ at the free surface and the swelling of CO₂ into the bulk-like internal part of the film. In addition, a more quantitative assessment of the roles of interfaces on the anomalous swelling maximum awaits further progress in theoretical studies.

In Chapter 6, the contact angle of water on polystyrene films as a function of CO₂ pressure and polymer thickness at 23 °C was studied. Further investigations can be taken under three directions. First, more processing temperatures in CO₂ can be examined.

Because 23 °C is below the critical temperature of CO₂, 31 °C, studies at higher temperatures are needed to explore the effects of supercritical CO₂ processing on the wetting properties of polymer thin films. These measurements will provide great fundamental insights and have important implication for extending the applications of supercritical CO₂ in thin film processes in microelectronics.^{14, 15} Contact angles can be measured near the critical condition of CO₂ to investigate any anomalous behavior near the critical point of CO₂ as a compensatory study for the swelling experiments in Chapter 5. Second, various polymers such as PFOMA, PMMA or even block copolymer films can be examined. Preliminary study has been conducted on PFOMA films under similar conditions as those shown in Chapter 6. It was found that the part of a PFOMA film underneath the water droplet becomes unstable and dewets on the silicon wafer at 23 °C and CO₂ pressure around 4 MPa, whereas the rest of the film remains stable. This instability of some polymer films under humid CO₂ environments can be used to selectively delaminate photoresist films.¹⁶⁻¹⁸ Third, the hydrophobicity of polymer films that possess high surface non-uniformity can be an interesting topic. For example, one possible project is to explore the potential of using block copolymer films with surface terrace or micellar structures (as shown in Figures 2.2 and 4.1, respectively) as superhydrophobic coating materials.¹⁹

7.3 REFERENCES

1. Koga, T.; Seo, Y. S.; Shin, K.; Zhang, Y.; Rafailovich, M. H.; Sokolov, J. C.; Chu, B.; Satija, S. K. *Macromolecules* **2003**, 36, 5236.
2. Koga, T.; Seo, Y. S.; Zhang, Y.; Shin, K.; Kusano, K.; Nishikawa, K.; Rafailovich, M. H.; Sokolov, J. C.; Chu, B.; Peiffer, D.; Occhiogrosso, R.; Satija, S. K. *Phys. Rev. Lett.* **2002**, 89, 125506.
3. Sirard, S. M.; Ziegler, K. J.; Sanchez, I. C.; Green, P. F.; Johnston, K. P. *Macromolecules* **2002**, 35, 1928.

4. Bockstaller, M.; Lapetnikov, Y.; Margel, S.; Thomas, E. L. *J. Am. Chem. Soc.* **2003**, 125, 5276.
5. Bockstaller, M.; Thomas, E. L. *J. Phys. Chem. B* **2003**, 107, 10017.
6. Chiu, J. J.; Lim, B. J.; Kramer, E. J.; Pine, D. J. *J. Am. Chem. Soc.* **2005**, 127, 5036.
7. Kim, S. H.; Misner, M. J.; Xu, T.; M., K.; Russell, T. P. *Adv. Mater.* **2004**, 16, 226.
8. Kim, D. H.; Jia, X.; Lin, Z.; Guarini, K. W.; Russell, T. P. *Adv. Mater.* **2004**, 16, 702.
9. Lin, Y.; Boker, A.; He, J.; Sill, K.; Xiang, H.; Abetz, C.; Li, X.; Wang, J.; Emrick, T.; Long, S.; Wang, Q.; Balazs, A.; Russell, T. P. *Nature* **2005**, 434, 55.
10. Lopes, W. A.; Jaeger, H. M. *Nature* **2001**, 414, 735.
11. Yoon, J.; Lee, W.; Thomas, E. L. *MRS Bulletin* **2005**, 30, 721.
12. Thurn-Albrecht, T.; Schotter, J.; Kastle, G. A.; Emley, N.; Shibauchi, T.; Krusin-Elbaum, L.; Guarini, K.; Black, C. T.; Tuominen, M. T.; Russell, T. P. *Science* **2000**, 290, 2126.
13. Pai, R. A.; Humayun, R.; Schulberg, M. T.; Sengupta, A.; Sun, J. N.; Watkins, J. J. *Science* **2004**, 303, 507.
14. Namatsu, H. *J. Vac. Sci. Technol. B* **2000**, 18, 3308.
15. Namatsu, H.; Yamazaki, K.; Kurihara, K. *J. Vac. Sci. Technol. B* **2000**, 18, 780.
16. Otake, K.; Webber, S. E.; Munk, P.; Johnston, K. P. *Langmuir* **1997**, 3047.
17. Gulari, E.; Serhatkulu, G. K. Method of delaminating a graphite structure with a coating agent in a supercritical fluid and its use in polymer nanocomposites. **2005**.
18. Xie, B.; Finstad, C. C.; Muscat, A. J. *Chem. Mater.* **2005**, 17, 1753.
19. Zhao, N.; Xie, Q.; Weng, L.; Wang, S.; Zhang, X.; Xu, J. *Macromolecules* **2005**, 38, 8996.

Appendix A: Tabular Data for the Swelling Experiments in Chapter 5

Table A.1a: Swelling data for a PFOMA film with $h_0 = 109$ nm during pressurization at 35 °C in CO₂

Pressure (psig)	CO ₂ Activity	Thickness (nm)	Swelling %	Reflective index	MSE
0	0.022	109.36	0.0	1.3922	1.134
203	0.304	115.71	5.8	1.3756	1.437
402	0.532	123.03	12.5	1.3636	1.673
602	0.716	134.18	22.7	1.3429	1.467
727	0.809	143.70	31.4	1.3301	1.468
852	0.887	157.16	43.7	1.3154	1.204
974	0.947	176.98	61.8	1.3045	1.308
1056	0.978	198.98	81.9	1.2909	1.925
1099	0.991	216.27	97.8	1.2786	2.379
1117	0.995	225.96	106.6	1.2685	2.049
1125	0.997	232.07	112.2	1.2599	1.687
1137	0.999	240.77	120.2	1.2486	1.428
1147	1.001	242.61	121.8	1.2504	1.390
1157	1.002	241.03	120.4	1.2551	1.277
1167	1.003	238.94	118.5	1.2618	1.233
1178	1.004	238.93	118.5	1.2658	1.226
1189	1.005	239.39	118.9	1.2679	1.199
1197	1.006	238.70	118.3	1.2710	1.187
1231	1.008	243.18	122.4	1.2702	1.157
1302	1.012	251.25	129.7	1.2685	1.088
1407	1.017	260.91	138.6	1.2644	0.933
1486	1.020	262.79	140.3	1.2605	0.724

Table A.1b: Swelling data for a PFOMA film with $h_0 = 109$ nm during depressurization at 35 °C in CO₂ (continued from Table A.1a)

Pressure (psig)	Thickness (nm)	Swelling %	Reflective index	MSE
1486	262.79	140.3	1.2605	0.724
1394	244.85	123.9	1.2642	0.685
1311	231.98	112.1	1.2674	0.706
1214	219.23	100.5	1.2689	0.875
1200	217.92	99.3	1.2684	0.946
1193	216.85	98.3	1.2683	0.959
1182	216.50	98.0	1.2664	1.059
1176	216.15	97.6	1.2653	1.168
1170	215.68	97.2	1.2640	1.241
1161	216.83	98.3	1.2575	1.322
1154	218.58	99.9	1.2533	1.351
1146	220.81	101.9	1.2473	1.465
1135	220.52	101.6	1.2447	1.900
1126	213.50	95.2	1.2570	2.385
1113	202.77	85.4	1.2757	2.508
1088	188.95	72.8	1.2942	2.573
946	149.76	36.9	1.3314	1.463
806	129.48	18.4	1.3591	0.635
607	114.03	4.3	1.3923	0.934
374	103.86	-5.0	1.4195	0.976
198	98.91	-9.6	1.4324	0.911
0	94.94	-13.2	1.4419	0.793

Table A.2: Swelling data for a PS-b-PFOMA film with $h_0 = 100$ nm at 35 °C in CO₂

Pressure (psig)	CO ₂ Activity	Thickness (nm)	Swelling %	MSE
0	0.022	99.72	0.0	0.726
140	0.222	102.29	2.6	0.656
249	0.361	104.85	5.1	0.661
349	0.475	107.12	7.4	0.630
483	0.611	110.65	11.0	0.642
653	0.756	115.64	16.0	0.739
740	0.818	119.58	19.9	0.904
840	0.88	125.36	25.7	1.245
957	0.939	137.13	37.5	1.930
1020	0.965	147.73	48.2	2.239
1103	0.992	169.17	69.7	2.841
1117	0.995	174.98	75.5	2.966
1138	0.999	185.47	86.0	2.867
1153	1.002	183.77	84.3	2.379
1167	1.003	178.55	79.1	2.149
1183	1.005	176.18	76.7	2.005
1203	1.006	175.26	75.8	1.859
1277	1.011	176.13	76.6	1.608
1383	1.016	180.94	81.5	1.434
1486	1.020	183.34	83.9	1.130

Table A.3: Swelling data for a PS film with $h_0 = 128$ nm at 35 °C in CO₂

Pressure (psig)	CO₂ Activity	Thickness (nm)	Swelling %	MSE
0	0.022	128.39	0.00	0.799
114	0.187	129.31	0.72	0.840
217	0.321	130.71	1.81	0.924
302	0.423	132.16	2.94	0.953
396	0.525	133.46	3.95	1.016
503	0.630	134.79	4.98	1.108
612	0.724	135.91	5.86	1.166
869	0.896	138.44	7.83	1.261
1002	0.958	139.44	8.61	1.320
1096	0.990	140.71	9.60	1.394
1127	0.997	142.06	10.65	1.132
1149	1.001	145.72	13.50	1.148
1164	1.003	144.44	12.50	1.172
1184	1.005	141.86	10.49	1.199
1204	1.006	140.64	9.54	1.251
1299	1.012	139.21	8.43	1.644
1407	1.017	138.69	8.02	1.812
1510	1.021	138.43	7.82	1.801
1611	1.025	138.37	7.77	1.842
1710	1.028	138.16	7.61	1.913
1816	1.031	138.12	7.58	1.930
1918	1.034	138.07	7.54	1.874
1995	1.036	138.10	7.56	1.856

Table A.4: Swelling data for a PEO film with $h_0 = 104$ nm at 35 °C in CO₂

Pressure (psig)	Thickness (nm)	Swelling %
0	103.77	0.00
98	103.86	0.09
201	104.22	0.43
294	104.52	0.72
402	104.76	0.95
502	105.16	1.34
626	105.69	1.85
704	106.05	2.20
800	106.43	2.56
929	107.11	3.22
990	107.54	3.63
1097	109.09	5.13
1134	112.03	7.96
1148	114.71	10.54
1160	114.82	10.65
1175	112.90	8.80
1202	110.84	6.81
1306	109.56	5.58
1392	109.36	5.39
1499	109.19	5.22
1598	109.08	5.12
1693	109.11	5.15
1804	109.03	5.07
1924	109.03	5.07

Table A.5: Swelling data for a PFOMA film with $h_0 = 153$ nm at 35 °C in CO₂

Pressure (psig)	CO₂ Activity	Thickness (nm)	Swelling %	MSE
0	0.022	153.22	0.0	0.555
204	0.305	160.33	4.6	0.989
400	0.530	170.40	11.2	1.397
597	0.712	187.38	22.3	2.216
734	0.814	202.61	32.2	2.311
854	0.888	219.49	43.2	1.959
1003	0.959	259.33	69.3	1.047
1045	0.974	279.00	82.1	0.827
1104	0.992	319.11	108.3	1.473
1115	0.994	325.72	112.6	3.153
1125	0.997	332.06	116.7	1.737
1133	0.998	336.58	119.7	1.359
1143	1.000	335.67	119.1	1.017
1166	1.003	328.34	114.3	0.877
1179	1.004	328.93	114.7	0.684
1200	1.006	330.73	115.8	0.561
1305	1.012	345.42	125.4	0.463
1406	1.017	355.33	131.9	0.453
1500	1.021	354.35	131.3	0.569

Table A.6: Swelling data for a PFOMA film with $h_0 = 179$ nm at 35 °C in CO₂

Pressure (psig)	CO₂ Activity	Thickness (nm)	Swelling %	MSE
0	0.022	178.79	0.0	1.264
261	0.375	190.05	6.3	1.435
434	0.564	199.58	11.6	1.410
601	0.715	213.48	19.4	1.285
733	0.813	228.70	27.9	1.216
858	0.890	248.75	39.1	1.298
952	0.937	270.54	51.3	1.294
1029	0.968	296.58	65.9	0.894
1097	0.990	358.39	100.5	2.506
1122	0.996	409.18	128.9	6.469
1136	0.999	433.58	142.5	7.945
1147	1.001	418.29	134.0	6.184
1155	1.002	405.16	126.6	5.120
1167	1.003	393.13	119.9	4.079
1183	1.005	387.65	116.8	3.244
1214	1.007	387.71	116.9	2.347
1315	1.013	402.62	125.2	1.590
1403	1.017	414.34	131.7	1.346
1506	1.021	416.91	133.2	1.003

Table A.7: Swelling data for a PFOMA film with $h_0 = 282$ nm at 35 °C in CO₂

Pressure (psig)	CO₂ Activity	Thickness (nm)	Swelling %	MSE
0	0.022	282.02	0.0	1.631
246	0.357	296.97	5.3	3.42
422	0.552	309.51	9.7	4.752
619	0.729	330.13	17.1	4.666
740	0.818	350.11	24.1	6.187
854	0.888	376.37	33.5	6.175
958	0.940	412.30	46.2	6.563
1041	0.973	477.65	69.4	7.713
1101	0.991	555.72	97.0	7.594
1111	0.994	580.60	105.9	7.813
1120	0.996	612.51	117.2	8.248
1131	0.998	655.76	132.5	7.948
1142	1.000	655.68	132.5	6.296
1151	1.001	628.00	122.7	5.229
1166	1.003	626.38	122.1	6.972
1180	1.004	621.35	120.3	6.867
1199	1.006	622.19	120.6	6.396
1298	1.012	649.58	130.3	5.109
1421	1.018	683.94	142.5	4.063
1509	1.021	689.05	144.3	3.249

Table A.8: Swelling data for a PFOMA film with $h_0 = 115$ nm at 50 °C in CO₂

Pressure (psig)	CO₂ Activity	Thickness (nm)	Swelling %	MSE
0	0.019	114.70	0.0	0.365
114	0.155	116.96	2.0	0.373
209	0.260	119.08	3.8	0.339
304	0.357	121.30	5.8	0.429
408	0.455	124.62	8.6	0.355
504	0.537	128.06	11.6	0.367
606	0.616	132.02	15.1	0.376
744	0.710	138.02	20.3	0.395
803	0.746	141.01	22.9	0.380
938	0.820	149.46	30.3	0.417
1012	0.855	154.71	34.9	0.448
1100	0.892	162.87	42.0	0.430
1196	0.926	172.56	50.4	0.408
1292	0.954	184.99	61.3	0.376
1395	0.977	202.58	76.6	0.504
1498	0.994	217.61	89.7	0.453
1596	1.006	228.62	99.3	0.461
1703	1.015	238.49	107.9	0.383
1796	1.021	246.43	114.8	0.347
1898	1.027	253.50	121.0	0.353
2001	1.033	260.32	127.0	0.363

Table A.9: Swelling data for a PFOMA film with $h_0 = 150$ nm at 50 °C in CO₂

Pressure (psig)	CO ₂ Activity	Thickness (nm)	Swelling %	MSE
0	0.019	150.38	0.0	1.109
107	0.147	152.84	1.6	1.009
203	0.254	155.80	3.6	0.873
305	0.358	159.41	6.0	0.632
404	0.451	163.20	8.5	0.473
513	0.544	168.09	11.8	0.370
613	0.621	172.99	15.0	0.586
709	0.688	178.28	18.6	0.887
814	0.753	184.73	22.8	1.225
888	0.794	190.87	26.9	1.437
995	0.847	199.72	32.8	1.544
1098	0.891	209.72	39.5	1.546
1198	0.927	222.21	47.8	1.338
1295	0.955	237.35	57.8	1.138
1395	0.977	257.16	71.0	0.917
1490	0.993	276.65	84.0	0.819
1592	1.005	292.99	94.8	0.747
1698	1.014	308.00	104.8	0.659
1794	1.021	319.94	112.8	0.686
1892	1.027	333.32	121.7	0.686
1991	1.032	343.92	128.7	0.801

Table A.10: Swelling data for a PFOMA film with $h_0 = 198$ nm at 50 °C in CO₂

Pressure (psig)	CO₂ Activity	Thickness (nm)	Swelling %
0	0.019	197.80	0.0
101	0.140	201.35	1.8
206	0.257	206.11	4.2
303	0.356	210.40	6.4
408	0.455	215.87	9.1
508	0.540	221.60	12.0
606	0.616	227.67	15.1
717	0.693	235.74	19.2
853	0.775	247.37	25.1
896	0.798	251.76	27.3
1000	0.849	262.35	32.6
1109	0.895	275.29	39.2
1200	0.927	291.02	47.1
1300	0.956	318.76	61.2
1402	0.979	355.88	79.9
1498	0.994	382.99	93.6
1591	1.005	398.47	101.5
1704	1.015	415.39	110.0
1798	1.021	430.14	117.5
1889	1.027	444.34	124.6
2001	1.033	459.55	132.3

Table A.11: Swelling data for a PS-b-PFOMA film with $h_0 = 100$ nm at 50 °C in CO₂

Pressure (psig)	CO₂ Activity	Thickness (nm)	Swelling %	MSE
0	0.019	100.46	0.0	0.885
118	0.160	102.16	1.7	0.982
205	0.256	103.80	3.3	1.109
300	0.353	105.60	5.1	1.238
440	0.483	108.42	7.9	1.335
514	0.545	110.03	9.5	1.443
616	0.623	112.21	11.7	1.499
707	0.686	114.04	13.5	1.556
806	0.748	116.77	16.2	1.641
889	0.795	119.65	19.1	1.684
998	0.849	125.04	24.5	1.766
1097	0.891	131.06	30.5	1.810
1200	0.927	139.01	38.4	1.754
1297	0.955	148.03	47.4	1.818
1397	0.978	157.93	57.2	1.738
1497	0.994	165.52	64.8	1.656
1597	1.006	171.23	70.4	1.614
1696	1.014	176.82	76.0	1.597
1802	1.022	182.59	81.8	1.619
1897	1.027	188.21	87.3	1.602
2005	1.033	193.57	92.7	1.639

Table A.12: Swelling data for a PS film with $h_0 = 131$ nm at 50 °C in CO₂

Pressure (psig)	CO₂ Activity	Thickness (nm)	Swelling %	MSE
0	0.019	131.24	0.00	0.980
89	0.126	132.18	0.72	1.210
179	0.228	133.24	1.52	1.294
284	0.338	134.55	2.52	1.259
403	0.450	135.80	3.47	1.354
506	0.538	136.75	4.20	1.405
609	0.618	137.39	4.69	1.492
710	0.688	138.01	5.16	1.388
804	0.747	138.78	5.75	1.453
888	0.794	139.57	6.35	1.501
1015	0.856	140.89	7.35	1.491
1100	0.892	142.11	8.28	1.478
1200	0.927	142.77	8.79	1.516
1303	0.957	143.39	9.26	1.389
1386	0.976	144.26	9.92	1.272
1480	0.992	145.51	10.87	1.073
1580	1.004	145.53	10.89	1.044
1687	1.014	145.05	10.52	1.030
1803	1.022	144.19	9.87	0.875
1914	1.028	143.88	9.63	0.784
2001	1.033	143.61	9.43	0.741

Appendix B: Supporting Information for Chapter 6

B.1 SWELLING DATA

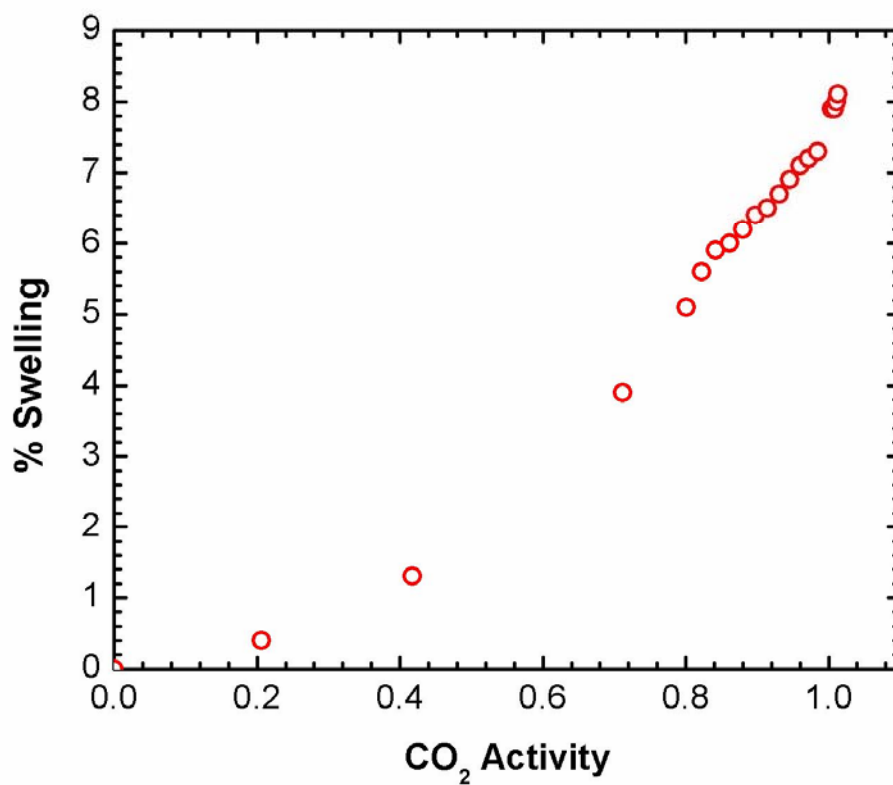


FIGURE B.1: The measured swelling % of a PS film with $h = 172$ nm in CO₂ at 25 °C.

B.2 CONTACT ANGLE DATA IN TABULATE FORM

Table B.1: Effects of CO₂ Pressure on the Contact Angle of Water on PS films with Various Thicknesses at 23 °C (typical error bar $\pm 2^\circ$)

Pressure (bar)	Activity	21 nm PS film ($^\circ$)	32 nm PS film ($^\circ$)	48 nm PS film ($^\circ$)	120 nm PS film ($^\circ$)	625 nm PS film ($^\circ$)
1.0	0.000	81	84	84	86	87
3.4	0.080	81	84	84	-	86
6.9	0.157	81	84	85	86	87
10.3	0.231	82	84	85	-	87
13.8	0.302	82	85	85	86	87
17.2	0.371	82	85	85	-	87
20.7	0.437	83	85	86	87	88
24.1	0.500	84	87	86	-	89
27.6	0.560	85	88	87	89	90
31.0	0.616	86	89	89	-	91
34.5	0.673	88	91	91	91	93
37.9	0.725	90	93	92	-	95
41.4	0.774	92	94	94	95	97
44.8	0.820	94	96	97	-	99
48.3	0.864	97	98	100	99	103
51.7	0.905	100	101	103	-	105
55.2	0.942	107	107	109	107	109
58.6	0.975	110	111	112	111	112
69.0	1.014	-	-	-	114	-
75.8	1.034	-	-	-	114	-
82.7	1.050	-	-	-	114	-
89.6	1.066	-	-	-	113	-
96.5	1.082	-	-	-	113	-
103.4	1.098	-	-	-	113	-
110.3	1.115	-	-	-	112	-
117.2	1.131	-	-	-	112	-
124.1	1.147	-	-	-	112	-
131.0	1.164	-	-	-	112	-
137.9	1.180	-	-	-	113	-

Table B.2: Contact Angles of Water on an $h = 120$ nm PS Film at $23\text{ }^{\circ}\text{C}$ during Pressurization and Depressurization

Pressurization		Depressurization	
Pressure (bar)	Contact angle ($^{\circ}$)	Pressure (bar)	Contact angle ($^{\circ}$)
1.0	86 ± 2	1.0	84 ± 2
7.4	85 ± 2	6.5	90 ± 2
14.6	86 ± 2	20.3	90 ± 2
21.2	86 ± 2	27.3	92 ± 2
27.8	88 ± 2	34.1	95 ± 2
35.1	91 ± 2	41.0	99 ± 2
41.2	95 ± 2	48.1	104 ± 2
41.1	95 ± 2	52.3	107 ± 2
48.0	100 ± 2	55.3	113 ± 2
55.4	107 ± 2	58.9	121 ± 2
58.6	113 ± 2	58.9	121 ± 2
60.7	116 ± 2		

B.3 COMPARISON BETWEEN CALCULATED PS-CO₂ INTERFACIAL TENSION IN THIS WORK AND REFERENCE

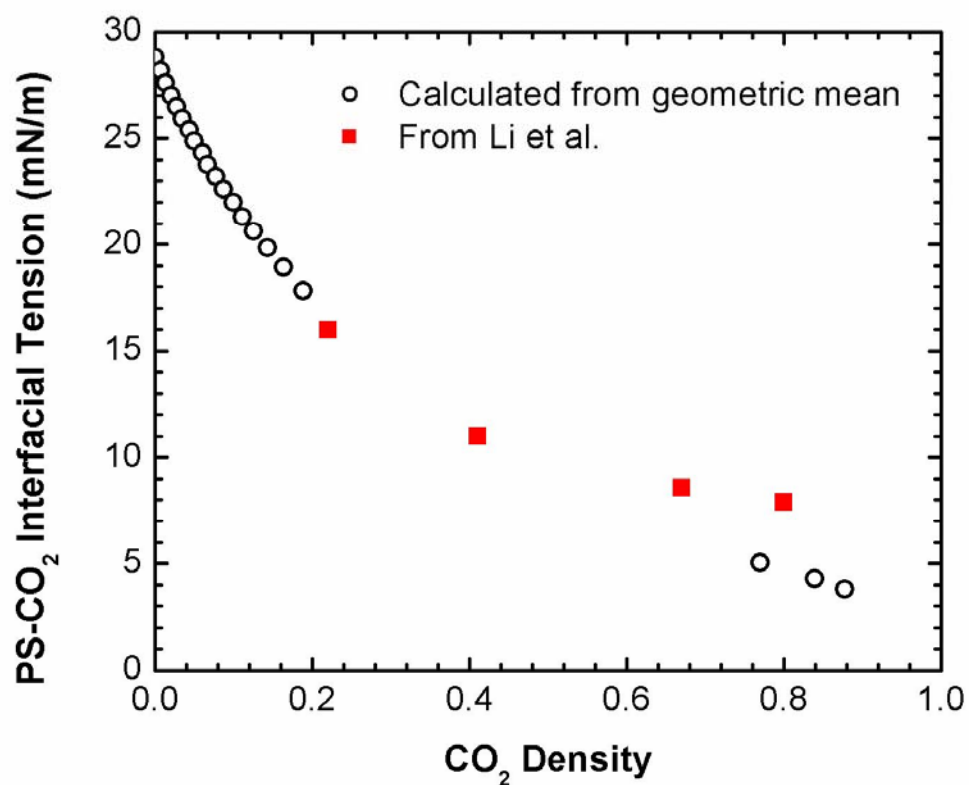


FIGURE B.2: Comparison between prediction from the geometric-mean model for PS-CO₂ interfacial tension and the work by Li et al.(Li, Y.; Meli, L.; Lim, K. T.; Green, P. F.; Johnston, K. P. *Macromolecules* **2006**, 39, 7044).

B.4 EXTENDING THE MICROSCOPIC MODEL TO CO₂ ENVIRONMENT

Table B.3: Calculation of the Hamaker Constants of PS-CO₂ Mixture (h = 120 nm)

Pressure (bar)	Volume fraction of CO ₂	CO ₂ activity	ϵ CO ₂	n CO ₂	A _{CO2} ($\times 10^{-20}$ J)	n mix	ϵ mix	A _{PS'} ($\times 10^{-20}$ J)
1.0	0.000	0.000	1.001	1	0.000	1.569*	2.550	8.802
8.5	0.004	0.206	1.008	1.004	0.001	1.566	2.545	8.723
18.5	0.013	0.417	1.019	1.008	0.003	1.560	2.535	8.573
36.0	0.038	0.712	1.041	1.019	0.013	1.544	2.507	8.164
42.7	0.049	0.801	1.053	1.024	0.021	1.537	2.494	7.996
44.4	0.053	0.822	1.056	1.025	0.023	1.535	2.489	7.928
46.1	0.056	0.842	1.060	1.027	0.026	1.533	2.486	7.889
47.8	0.057	0.862	1.063	1.028	0.029	1.533	2.485	7.878
49.5	0.059	0.880	1.067	1.030	0.033	1.531	2.483	7.850
51.2	0.060	0.898	1.072	1.032	0.037	1.531	2.482	7.833
53.0	0.061	0.914	1.076	1.034	0.043	1.530	2.480	7.821
54.8	0.063	0.931	1.082	1.036	0.048	1.529	2.479	7.800
56.5	0.065	0.946	1.087	1.038	0.054	1.528	2.477	7.775
58.3	0.067	0.960	1.094	1.042	0.065	1.527	2.474	7.751
59.9	0.067	0.972	1.101	1.046	0.077	1.527	2.473	7.747
61.8	0.068	0.985	1.111	1.050	0.092	1.527	2.473	7.744
70.6	0.073	1.004	1.436	1.175	1.049	1.536	2.478	7.965
77.9	0.073	1.008	1.452	1.181	1.123	1.537	2.479	7.984
85.2	0.074	1.011	1.463	1.186	1.174	1.537	2.479	7.986
92.3	0.075	1.013	1.472	1.189	1.217	1.537	2.478	7.980

* Calculated from the fitted Hamaker constant of the h = 120 nm PS film.

Table B.4: Calculation of the Van der Waals Contribution in the Spreading Coefficient,
 $S_{CO_2}^{vdw}$

Pressure (bar)	CO ₂ activity	A _{CO₂-W-PS'} (× 10 ⁻²⁰ J)	A _{CO₂-W-Si} (× 10 ⁻²⁰ J)	A _{CO₂-W-SiO_x} (× 10 ⁻²⁰ J)	S _{CO₂} ^{vdw} (mJ)
1.0	0.000	-2.00	-1.09	-5.34	19.5
8.5	0.206	-1.96	-1.08	-5.28	19.1
18.5	0.417	-1.88	-1.06	-5.20	18.3
36.0	0.712	-1.69	-1.03	-5.03	16.5
42.7	0.801	-1.61	-1.01	-4.94	15.7
44.4	0.822	-1.58	-1.00	-4.92	15.4
46.1	0.842	-1.56	-1.00	-4.89	15.2
47.8	0.862	-1.55	-0.99	-4.87	15.1
49.5	0.880	-1.53	-0.99	-4.84	14.9
51.2	0.898	-1.51	-0.98	-4.81	14.8
53.0	0.914	-1.50	-0.97	-4.77	14.6
54.8	0.947	-1.48	-0.97	-4.73	14.4
56.5	0.965	-1.46	-0.96	-4.69	14.3
58.3	0.983	-1.44	-0.95	-4.63	14.0
59.9	0.998	-1.42	-0.93	-4.57	13.8
61.8	1.016	-1.39	-0.92	-4.50	13.6

Table B.5: Calculation of the Polar Contribution in the Spreading Coefficient, $S_{CO_2}^P$

Pressure (bar)	CO ₂ activity	$\gamma_{CO_2}^P$ (mN/m)	$\gamma_{CO_2}^d$ (mN/m)	$\gamma_{W-CO_2}^*$ (mN/m)	$\gamma_{PS-CO_2}^P$ (mN/m)	γ_{PS-W}^P (mN/m)	$\gamma_{W-CO_2}^P$ (mN/m)	$S_{CO_2}^P$ (mJ)
1.0	0.000	0.000	0.000	71.9	4.9	40.8	50.4	-86.3
8.5	0.206	0.001	0.014	61.9	4.8	40.8	41.5	-77.5
18.5	0.417	0.005	0.073	56.6	4.6	40.8	37.5	-73.7
36.0	0.712	0.019	0.299	46.1	4.3	40.8	29.3	-65.8
42.7	0.801	0.029	0.447	42.0	4.2	40.8	26.3	-62.9
44.4	0.822	0.032	0.494	41.2	4.1	40.8	25.7	-62.4
46.1	0.842	0.035	0.545	40.3	4.1	40.8	25.1	-61.8
47.8	0.862	0.038	0.602	39.5	4.1	40.8	24.6	-61.3
49.5	0.880	0.042	0.664	38.9	4.0	40.8	24.3	-61.1
51.2	0.898	0.047	0.733	38.2	4.0	40.8	23.9	-60.7
53.0	0.914	0.052	0.811	36.2	3.9	40.8	22.2	-59.1
54.8	0.947	0.058	0.902	34.2	3.9	40.8	20.6	-57.5
56.5	0.965	0.064	1.003	32.4	3.8	40.8	19.2	-56.2
58.3	0.983	0.072	1.127	30.5	3.8	40.8	17.7	-54.7
59.9	0.998	0.080	1.259	28.6	3.7	40.8	16.3	-53.3
61.8	1.016	0.093	1.465	24.6	3.6	40.8	12.8	-50.0

* From the γ_{W-CO_2} vs. CO₂ activity curve (Figure 6.5).

Table B.6: Calculation of the Contact Angles from the Microscopic Model in CO₂

Pressure (bar)	CO ₂ activity	$S_{CO_2}^{vdw}$ (mJ)	$S_{CO_2}^P$ (mJ)	S_{CO_2} (mJ)	γ_{W-CO_2} (mN/m)	θ (°)
1.0	0.000	19.5	-86.3	-66.8	71.9	85.9
8.5	0.206	19.1	-77.5	-58.4	61.9	86.8
18.5	0.417	18.3	-73.7	-55.4	56.6	88.8
36.0	0.712	16.5	-65.8	-49.3	46.1	94.1
42.7	0.801	15.7	-62.9	-47.2	42.0	97.1
44.4	0.822	15.4	-62.4	-47.0	41.2	98.0
46.1	0.842	15.2	-61.8	-46.6	40.3	99.0
47.8	0.862	15.1	-61.3	-46.2	39.5	99.8
49.5	0.880	14.9	-61.1	-46.1	38.9	100.7
51.2	0.898	14.8	-60.7	-46.0	38.2	101.7
53.0	0.914	14.6	-59.1	-44.4	36.2	103.2
54.8	0.947	14.4	-57.5	-43.0	34.2	105.0
56.5	0.965	14.3	-56.2	-41.9	32.4	107.0
58.3	0.983	14.0	-54.7	-40.7	30.5	109.6
59.9	0.998	13.8	-53.3	-39.5	28.6	112.4
61.8	1.016	13.6	-50.0	-36.4	24.6	118.8

Bibliography

1. Abramowitz, H.; Shah, P. S.; Green, P. F.; Johnston, K. P. *Macromolecules* **2004**, 37, 7316.
2. Albalak, R. J.; Thomas, E. L.; Capel, M. S. *Polymer* **1998**, 38, 3819.
3. Arceo, A.; Green, P. F. *J. Phys. Chem. B* **2005**, 109, 6958.
4. Arnold, M. E.; Nagai, K.; Freeman, B. D.; Spontak, R. J.; E., B. D.; DeSimone, J. M.; Pinnau, I. *Macromolecules* **2001**, 34, 5611.
5. Arnold, M. E.; Nagai, K.; Spontak, R. J.; Freeman, B. D.; Leroux, D.; Betts, D. E.; DeSimone, J. M.; DiGiano, F. A.; Stebbins, C. K.; Linton, R. W. *Macromolecules* **2002**, 35, 3697.
6. Ashley, K. M.; Raghavan, D.; Douglas, J. F.; Karim, A. *Langmuir* **2005**, 21, 9518.
7. Banaszak, M.; Whitmore, M. D. *Macromolecules* **1992**, 25, 3406.
8. Bates, F. S.; Fredrickson, G. H. *Annu. Rev. Phys. Chem.* **1990**, 41, 525.
9. Beck Tan, N. C.; Wu, W. L.; Wallace, W. E.; Davis, G. T. *J. Poly. Sci. B: Polym. Phys.* **1998**, 36, 155.
10. Beckman, E.; Porter, R. S. *J. Poly. Sci. B: Polym. Phys.* **1987**, 25, 1511.
11. Besancon, B. M.; Soles, C. L.; Green, P. F. *Phys. Rev. Lett.* **2006**, 97, 057801.
12. Binks, B. P.; Clint, J. H. *Langmuir* **2002**, 18, 1270.
13. Black, C. T.; Bezencenet, O. *IEEE Transactions on Nanotechnology* **2004**, 3, 412.
14. Black, C. T.; Guarini, K. W.; Milkove, K. R.; Baker, S. M.; Russell, T. P.; Tuominen, M. T. *Appl. Phys. Lett.* **2001**, 79, 409.
15. Bockstaller, M.; Lapetnikov, Y.; Margel, S.; Thomas, E. L. *J. Am. Chem. Soc.* **2003**, 125, 5276.
16. Bockstaller, M.; Thomas, E. L. *J. Phys. Chem. B* **2003**, 107, 10017.

17. Bodycomb, J.; Funaki, Y.; Kimishima, K.; Hashimoto, T. *Macromolecules* **1999**, 32, 2075.
18. Brandrup, J.; Immergut, E. H., *Polymer Handbook*. John Wiley & Sons: **1989**.
19. Breulmann, M.; Forster, S.; Antonietti, M. *Macromol. Chem. Phys.* **2000**, 201, 204.
20. Brochard-Wyart, F.; Debrageas, G.; Fondecave, R.; Martin, P. *Macromolecules* **1997**, 30, 1211.
21. Brown, H. R.; Russell, T. R. *Macromolecules* **1996**, 29, 798.
22. Butt, H.-J.; Graf, K.; Kappl, M., *Physics and Chemistry of Interfaces*. Wiley-Vch GmbH & Co. : **2003**.
23. Cao, T.; Johnston, K. P.; Webber, S. E. *Macromolecules* **2005**, 38, 1335-1340.
24. Carbonell, R. G.; Carla, V.; Hussain, Y.; Doghieri, F. In *The Role of Gibbs Excess Adsorption on Submerged Surface in Explaining the Complex Swelling Behavior of Supported Polymeric Thin Films in Supercritical Carbon Dioxide*, Eighth Conference on Supercritical Fluids and Their Applications, Ischia, Italy, 28-31 May, **2006**.
25. Chang, S. H.; Park, S. C.; Shim, J. J. *J. Supercritical Fluids* **1998**, 13, 113.
26. Chen, J. H.; Wong, D. S. H.; Tan, C. S.; Subramanian, R.; Lira, C. T.; Orth, M. *Ind. Eng. Chem. Res.* **1997**, 36, 2808.
27. Chen, X.; Gardella, J. J. A.; Kumler, P. A. *Macromolecules* **1992**, 25, 6631-6637.
28. Chiu, J. J.; Lim, B. J.; Kramer, E. J.; Pine, D. J. *J. Am. Chem. Soc.* **2005**, 127, 5036.
29. Chou, S. Y.; Wei, M. S.; Krauss, P. R.; Fischer, P. B. *J. Appl. Phys.* **1994**, 76, 6673.
30. Cintavey, L. A.; Clarson, S. J.; Husband, D. M.; Brabander, G. N.; T., B. J. *J. Appl. Polym. Sci.* **2000**, 76, 1448.
31. Condo, P. D.; Sumpter, S. R.; Lee, M. L.; Johnston, K. P. *Ind. Eng. Chem. Res.* **1996**, 35, 1115.
32. Connell, S. D.; Collins, S.; Fundin, J.; Yang, Z.; Hamley, I. W. *Langmuir* **2003**, 19, 10449.

33. Cooper, A. I. *J. Mater. Chem.* **2000**, 10, 207.
34. Daneshvar, M.; Kim, S.; Gulari, E. *J. Phys. Chem.* **1990**, 94, 2124.
35. De Rosa, C.; C., P.; Thomas, E. L.; Lotz, B. *Nature* **2000**, 405, 433.
36. DeSimone, J. M. *Science* **2002**, 297, 799.
37. Despotopoulou, M. M.; Frank, C. W.; Miller, R. D.; Rabolt, J. F. *Macromolecules* **1996**, 29, 5797.
38. Dickson, J. L.; Gupta, G.; Horozov, T. S.; Binks, B. P.; Johnston, K. P. *Langmuir* **2006**, 22, 2161.
39. Dimitrakopoulos, C. D.; Mascaro, D. J. *IBM Journal of Research and Development* **2001**, 45, 11.
40. Efimenko, K.; Novick, B.; Carbonell, R. G.; DeSimone, J. M.; Genzer, J. *Langmuir* **2002**, 18, 6170.
41. Fasolka, M. J.; Harris, D. J.; Mayes, A. M.; Yoon, M.; Mochrie, S. G. *J. Phys. Rev. Lett.* **1997**, 79, 3018.
42. Fasolka, M. J.; Mayes, A. M. *Annu. Rev. Phys. Chem.* **2001**, 31, 323.
43. Findenegg, G. H., In *Fundamentals of Adsorption*, Myers, A. L.; Belfort, G., Eds. Engineering Foundation: New York, **1984**.
44. Fink, Y.; Winn, J. N.; Fan, S.; Michel, J.; Joannopoulos, J. D.; Thomas, E. L. *Science* **1998**, 282, 1679.
45. Flory, P. G., *Scaling Concepts in Polymer Physics*. Cornell University Press: Ithaca, NY, **1979**.
46. Fowkes, F. M. *J. Phys. Chem.* **1963**, 67, 2538.
47. Frank, C. W.; Rao, V.; Despotopoulou, M. M.; Pease, R. F.; Hinsberg, W. D.; Miller, R. D.; Rabolt, J. F. *Science* **1996**, 273, 912.
48. Fulton, J. L.; Pfund, D. M.; McClain, J. B.; Romack, T. J.; Maury, E. E.; Combes, J. R.; Samulski, E. T.; Desimone, J. M.; Capel, M. S. *Langmuir* **1995**, 11, 4241.
49. Gao, W.; Butler, D.; Tomasko, D. L. *Langmuir* **2004**, 20, 8083.
50. Giovanni, O. D.; Dorfler, W.; Mazzotti, M.; Morbidelli, M. *Langmuir* **2001**, 17, 4316.

51. Goldfarb, D. L.; de Pablo, J. J.; Nealey, P. F.; Simons, J. P.; Moreau, W. M.; Angelopoulos, M. *J. Vac. Sci. Technol. B* **2000**, 18, 3313.
52. Gorman, B. P.; Orozco-Teran, R. A.; Zhang, Z.; Matz, P. D.; W., M. D.; Reidy, R. F. *J. Vac. Sci. Technol. B* **2004**, 22, 1210.
53. Gourgouillon, D.; da Ponte, M. N. *Phys. Chem. Chem. Phys.* **1999**, 1, 5369.
54. Green, P. F. *J. Polym. Sci. B: Polym. Phys.* **2003**, 41, 2219.
55. Gross, S. M.; Roberts, G. W.; Kiserow, D. J.; DeSimone, J. M. *Macromolecules* **2000**, 33, 40.
56. Guadagno, T.; Kazarian, S. G. *J. Phys. Chem. B* **2004**, 108, 13995.
57. Guarini, K. W.; Black, C. T.; Milkove, K. R.; Sandstrom, R. L. *J. Vac. Sci. Technol. B* **2001**, 19, 2874.
58. Guarini, K. W.; Black, C. T.; Zhang, Y.; Kim, H.; Sikorski, E. M.; Babich, I. V. *J. Vac. Sci. Technol. B* **2002**, 20, 2788.
59. Gulari, E.; Serhatkulu, G. K. Method of delaminating a graphite structure with a coating agent in a supercritical fluid and its use in polymer nanocomposites. **2005**.
60. Hamley, I. W. *Adv. Polymer. Sci.* **1999**, 148, 113.
61. Hamley, I. W., *The Physics of Block Copolymer*. Oxford University Press: New York, **1998**.
62. Hamley, I. W.; Wallwork, M. L.; Smith, D. A.; A., F. L. P.; J., R. A.; Mai, S. M.; Yang, Y. M.; C., B. *Polymer* **1998**, 39, 3321.
63. Hanley, K. J.; Lodge, T. P. *J. Poly. Sci., Part B: Poly. Phys.* **1998**, 36, 3101.
64. Harrison, C.; Park, M.; P., C.; Register, R. A.; Adamson, D. H.; Yao, N. *Polymer* **1998**, 39, 2733.
65. Harrison, K. L.; da Rocha, S. R. P.; Yates, M. Z.; Johnston, K. P. *Langmuir* **1998**, 14, 6855.
66. Harrison, K. L.; Johnston, K. P.; Sanchez, I. C. *Langmuir* **1996**, 12, 2637.
67. Hebach, A.; Oberhof, A.; Dahmen, N.; Kogel, A.; Ederer, H.; Dinjus, E. *J. Chem. Eng. Data* **2002**, 47, 1540.
68. Helfand, E.; Tagami, Y. *J. Chem. Phys.* **1972**, 56, 3592.

69. Hong, S.; Macknight, W. J.; Russell, T. P.; Gido, S. P. *Macromolecules* **2001**, 34, 2876.
70. Hourri, A.; St-Arnaud, J. M.; Bose, T. K. *J. Chem. Phys.* **1997**, 106, 1780.
71. Hsu, C. C.; Prausnitz, J. M. *Macromolecules* **1974**, 7, 320.
72. Ibers, J. A.; Hamilton, W. C., *International Tables for X-Ray Crystallography*. The Kynoch Press: Birmingham, England, **1974**.
73. Ibn-Elhaj, M.; Schadt, M. *Nature* **2001**, 410, 796.
74. Inoue, R.; Kanaya, T.; Nishida, K.; Tsukushi, I.; Shibata, K. *Phys. Rev. Lett.* **2005**, 95, 056102.
75. Israelachvili, J. N., *Intermolecular and Surface Forces*. 2 ed.; Academic Press: **1992**.
76. Jaeger, P. T.; Eggers, R.; Baumgartl, H. *Journal of Supercritical Fluids* **2002**, 24, 203.
77. Johnston, K. P.; McFann, G.; Lemert, R. M. *Am. Chem. Soc. Symp. Ser.* **1989**, 140.
78. Jones, C.; Zweber, A.; DeYoung, J.; McClain, J.; Carbonell, R.; DeSimone, J. *Critical Reviews in Solid State and Materials Science* **2004**, 29, 97.
79. Kawase, T.; Siringhaus, H.; Friend, R. H.; Shimoda, T. *Digest of Technical Papers* **2001**, 32, 40.
80. Kazarian, S. G. *Polymer Science, Ser. C* **2000**, 42, 78.
81. Kazarian, S. G.; Vincent, M. F.; Bright, F.; Liotta, C. L.; Eckert, C. A. *J. Am. Chem. Soc.* **1996**, 118, 1729.
82. Keagy, J. A.; Li, Y.; Green, P. F.; Johnston, K. P.; Weber, F.; Rhoad, J. T.; Busch, E. L.; Wolf, P. J. *Submitted to J. Supercritical Fluids* **2006**.
83. Keagy, J. A.; Zhang, X.; Busch, E.; Weber, F.; Wolf, P. J.; Rhoad, T.; Martinez, H. J.; Johnston, K. P. *J. Supercritical Fluids* **2006**, in press.
84. Kim, D. H.; Jia, X.; Lin, Z.; Guarini, K. W.; Russell, T. P. *Adv. Mater.* **2004**, 16, 702.
85. Kim, D. H.; Kim, S. H.; Lavery, K.; Russell, T. P. *Nano Lett.* **2004**, 4, 1841.

86. Kim, H. K.; Shi, F. G. *Journal of Materials Science : Materials in Electronics* **2001**, 12, 361.
87. Kim, S. H.; Misner, M. J.; Russell, T. P. *Adv. Mater.* **2004**, 16, 2119.
88. Kim, S. H.; Misner, M. J.; Xu, T.; M., K.; Russell, T. P. *Adv. Mater.* **2004**, 16, 226.
89. Kim, S. O.; Solak, H. H.; Stoykovich, M. P.; Ferrier, N. J.; dePablo, J. J.; Nealey, P. F. *Nature* **2003**, 424, 411.
90. Kiselev, S. B.; Ely, J. F.; Belyakov, M. Y. *J. Chem. Phys.* **2000**, 112, 3370.
91. Koga, T.; Akashige, E.; Reinstein, A.; Bronner, M.; Seo, Y. S.; Shin, K.; Rafailovich, M. H.; Sokolov, J. C.; Chu, B.; Satija, S. K. *Physica B* **2005**, 357, 73.
92. Koga, T.; Jerome, J. L.; Seo, Y. S.; Rafailovich, M. H.; Sokolov, J. C.; Satija, S. K. *Langmuir* **2005**, 21, 6157.
93. Koga, T.; Seo, Y. S.; Hu, X.; Shin, K.; Zhang, Y.; Rafailovich, M. H.; Sokolov, J. C.; Chu, B.; Satija, S. K. *Europhysics Letters* **2002**, 60, 559.
94. Koga, T.; Seo, Y. S.; Shin, K.; Zhang, Y.; Rafailovich, M. H.; Sokolov, J. C.; Chu, B.; Satija, S. K. *Macromolecules* **2003**, 36, 5236.
95. Koga, T.; Seo, Y. S.; Zhang, Y.; Shin, K.; Kusano, K.; Nishikawa, K.; Rafailovich, M. H.; Sokolov, J. C.; Chu, B.; Peiffer, D.; Occhiogrosso, R.; Satija, S. K. *Phys. Rev. Lett.* **2002**, 89, 125506.
96. Koga, T.; Y., J.; Seo, Y. S.; Gordon, C.; Qu, F.; Rafailovich, M. H.; Sokolov, J. C.; Satija, S. K. *J. Poly. Sci. B: Polym. Phys.* **2004**, 42, 3282.
97. Kowk, D. Y.; Lam, C. N. C.; Li, A.; Zhu, K.; Wu, R.; Neumann, A. W. *Polym. Eng. Sci.* **1998**, 38, 1675.
98. Kropka, J. M.; Green, P. F. *Macromolecules* **2006**, in press.
99. Lambert, S. M.; Paulaitis, M. E. *J. Supercritical Fluids* **1991**, 4, 15.
100. Li, Y.; Loo, Y.-L.; Register, R. A.; Green, P. F. *Macromolecules* **2005**, 38, 7745.
101. Li, Y.; Meli, L.; Lim, K. T.; Green, P. F.; Johnston, K. P. *Macromolecules* **2006**, 39, 7044.
102. Li, Y.; Park, E. J.; Lim, K. T.; Johnston, K. P.; Green, P. F. *Submitted to J. Polym. Sci. B* **2006**.

103. Li, Y.; Wang, X.; Sanchez, I. C.; Green, P. F.; Johnston, K. P. *Submitted to J. Phys. Chem. B* **2006**.
104. Li, Z.; Zhao, W.; Liu, Y.; Rafailovich, M. H.; Sokolov, J.; Khougaz, K.; Eisenberg, A.; Lennx, R. B.; Krausch, G. *J. Am. Chem. Soc.* **1996**, 118, 10892.
105. Liao, X.; Wang, J.; Li, G.; He, J. *J. Polym. Sci.: B* **2004**, 42, 280.
106. Ligoure, C. *Macromolecules* **1991**, 24, 2968.
107. Lim, K. T.; Lee, M. Y.; Moon, M. J.; Lee, G. D.; Hong, S. S.; Dickson, J. L.; Johnston, K. P. *Polymer* **2002**, 43, 7043.
108. Limary, R. Block Copolymer Thin Films: Interfacial and Confinement Effects. The University of Texas at Austin, **2002**.
109. Limary, R.; Green, P. F. *Macromolecules* **2002**, 35, 2535.
110. Lin, Y.; Boker, A.; He, J.; Sill, K.; Xiang, H.; Abetz, C.; Li, X.; Wang, J.; Emrick, T.; Long, S.; Wang, Q.; Balazs, A.; Russell, T. P. *Nature* **2005**, 434, 55.
111. Lin, Z.; Kim, D. H.; Wu, X.; Boosahda, L.; Stone, D.; LaRose, L.; Russell, T. P. *Adv. Mater.* **2002**, 14, 1373.
112. Linse, P., Modelling of the self-assembly of block copolymers in selective solvent. In *Amphiphilic Block Copolymers*, Alexandridis, P.; Lindman, B., Eds. Elsevier: Amsterdam, the Netherlands, **2000**.
113. Liu, D.; Li, H.; Noon, M. S.; Tomasko, D. *Macromolecules* **2005**, 38, 4416.
114. Loo, Y. L., Templating Polymer Crystal Growth on a Nanoscale Using Phase-Separated Block Copolymers. In *The Encyclopedia of Nanoscience and Nanotechnology*, Marcel Drekker Inc.: New York, **2002**.
115. Loo, Y. L.; Register, R. A.; J., R. A. *Phys. Rev. Lett.* **2000**, 84, 4120.
116. Loo, Y. L.; Register, R. A.; J., R. A. *Macromolecules* **2002**, 35, 2365.
117. Lopes, W. A.; Jaeger, H. M. *Nature* **2001**, 414, 735.
118. Lund, R.; Willner, L.; Stellbrink, J.; Radulescu, A.; Richter, D. *Macromolecules* **2004**, 37, 9984.
119. Madsen, L. A. *Macromolecules* **2006**, 39, 1483.

120. Mansky, P.; Liu, Y.; Huang, E.; Russell, T. P.; Hawker, C. J. *Science* **1997**, 275, 1458.
121. Mansky, P.; Russell, T. P.; Hawker, C. J.; Mays, J.; Cook, D.; Satija, S. K. *Phys. Rev. Lett.* **1997**, 68, 67.
122. Mark, J.; Ngai, K.; Graessley, W.; Mandelkern, L.; Samulski, E. T.; Koenig, J.; Wignall, G. D., *Physical Properties of Polymers*. 3rd ed.; Cambridge University Press: **2004**.
123. Matsen, M. W.; Bates, F. S. *Macromolecules* **1996**, 29, 1091.
124. McClain, J. B.; Betts, D. E.; Canelas, D. A.; Samulski, E. T.; DeSimone, J. M.; Londono, D.; Cochran, H. D.; Wignall, G. D.; Chillura-Martino, D.; Triolo, R. *Science* **1996**, 274, 2049.
125. McClain, J. B.; Londono, D.; Combes, J. R.; Romack, T. J.; Canelas, D. A.; Betts, D. E.; Wignall, G. D.; Samulski, E. T.; DeSimone, J. M. *J. Am. Chem. Soc.* **1996**, 118, 917.
126. Meiners, J. C.; Quintel-Ritzi, A.; Mlynek, J.; Elbs, H.; Krausch, G. *Macromolecules* **1997**, 30, 4945.
127. Meli, L.; Li, Y.; Lim, K. T.; Johnston, K. P.; Green, P. F. *Manuscript in preparation* **2006**.
128. Meli, L.; Pham, J. Q.; Johnston, K. P.; Green, P. F. *Phys. Rev. E* **2004**, 69, 051601.
129. Morkved, T. L.; Lu, M.; Urbas, A. M.; Ehrichs, E. E.; Jaeger, H. M.; Mansky, P.; Russell, T. P. *Science* **1996**, 273, 931.
130. Mount, D. J.; Rothman, L. B.; Robey, R. J.; Ali, M. K. *Solid State Technol* **2002**, 45, 103.
131. Namatsu, H. *J. Vac. Sci. Technol. B* **2000**, 18, 3308.
132. Namatsu, H.; Yamazaki, K.; Kurihara, K. *J. Vac. Sci. Technol. B* **2000**, 18, 780.
133. O'Neill, A.; Watkins, J. J. *MRS Bulletin* **2005**, 30, 967.
134. O'Neill, M. L.; Cao, Q.; Fang, M.; Johnston, K. P.; Wilkinson, S. P.; D., S. C.; Kerschner, J. L.; Jureller, S. H. *Ind. Eng. Chem. Res.* **1998**, 37, 3067.
135. Opitz, R.; Lambrev, D. M.; de Jeu, M. h. *Macromolecules* **2002**, 35, 6930.

136. Orso, K. A.; Green, P. F. *Macromolecules* **1999**, 32, 1087.
137. Otake, K.; Webber, S. E.; Munk, P.; Johnston, K. P. *Langmuir* **1997**, 3047.
138. Pai, R. A.; Humayun, R.; Schulberg, M. T.; Sengupta, A.; Sun, J. N.; Watkins, J. *J. Science* **2004**, 303, 507.
139. Panayiotou, C. G. *Fluid Phase Equilibria* **1997**, 131, 21.
140. Park, M.; Harrison, C.; Chaikin, P. M.; Register, R. A.; Adamson, D. H. *Science* **1997**, 276, 1401.
141. Pham, J. Q.; Green, P. F. *Macromolecules* **2003**, 36, 1665.
142. Pham, J. Q.; Johnston, K. P.; Green, P. F. *J. Phys. Chem. B* **2004**, 108, 3457.
143. Pham, J. Q.; Sirard, S. M.; Johnston, K. P.; Green, P. F. *Phys. Rev. Lett.* **2003**, 91, 175503.
144. Pham, V. Q.; Rao, N.; Ober, C. K. *J. Supercritical Fluids* **2004**, 31, 323.
145. RamachandraRao, V. S.; Gupta, R. R.; Russell, T. P.; Watkins, J. J. *Macromolecules* **2001**, 34, 7923.
146. RamachandraRao, V. S.; Watkins, J. J. *Macromolecules* **2000**, 33, 5143.
147. Regenbrecht, M.; Akari, S.; Forster, S.; Mohwald, H. *J. Phys. Chem. B* **1999**, 103, 6669.
148. Reiter, G. *Langmuir* **1993**, 9, 1344.
149. Reiter, G. *J. Polym. Sci. B: Polym. Phys.* **2003**, 41, 1869.
150. Reiter, G.; Castelein, G.; Hoerner, P.; Riess, G.; Bluman, A.; Sommer, J. U. *Phys. Rev. Lett.* **1999**, 83, 3844.
151. Reiter, G.; Castelein, G.; Hoerner, P.; Riess, G.; Sommer, J. U.; Floudas, G. *Eur. Phys. J. E.* **2000**, 2, 319.
152. Reiter, G.; Castelein, G.; Sommer, J. U. *Phys. Rev. Lett.* **2001**, 87, 226101.
153. Reiter, G.; Sommer, J. U. *Phys. Rev. Lett.* **1998**, 80, 3771.
154. Robard, A.; Patterson, D.; Delmas, G. *Macromolecules* **1977**, 10, 706.
155. Rockford, L.; Liu, Y.; Mansky, P.; Russell, T. P.; Yoon, M.; Mochrie, S. G. J. *Phys. Rev. Lett.* **1999**, 88, 2602.

156. Rockford, L.; Russell, T. P.; Yoon, M.; Mochrie, S. G. J. *Macromolecules* **2001**, 34, 1487.
157. Russell, T. P. *Curr. Opin. Colloid and Interface Sci.* **1996**, 1, 107.
158. Sanchez, I. C.; Lacombe, R. H. *J. Phys. Chem.* **1976**, 80, 2352.
159. Sanchez, I. C.; Lacombe, R. H. *Macromolecules* **1978**, 11, 1145.
160. Sanchez, I. C.; Stone, M. T., Statistical Thermodynamics of Polymer Solutions and Blends. In *Polymer Blends*, Paul, D. R.; Bucknall, C. B., Eds. John Wiley & Sons: New York, **2000**.
161. Sarbu, T.; Styranec, T.; Beckman, E. J. *Nature* **2000**, 405, 165.
162. Seemann, R.; Herminghaus, S.; Jacobs, K. *Phys. Rev. Lett.* **2001**, 86, 5534.
163. Seemann, R.; Herminghaus, S.; Jacobs, K. *J. Phys.: Condens. Matter* **2001**, 13, 4925.
164. Segalman, R. A. *Materials Science and Engineering R* **2005**, 48, 191.
165. Segalman, R. A.; Hexemer, A.; Hayward, R.; Kramer, E. J. *Macromolecules* **2003**, 36, 3272.
166. Segalman, R. A.; Yokoyama, H.; Kramer, E. J. *Adv. Mater.* **2001**, 15, 1152.
167. Semenov, A. N. *Sov. Phys. JETP* **1985**, 61, 733.
168. Shah, M.; Pryamitsyn, V.; Ganesan, V. *Manuscript in preparation* **2006**.
169. Sharma, A.; Reiter, G. *J. Colloid and Interface Sci.* **1996**, 178, 383.
170. Shibayama, M.; Hashimoto, T.; Kawai, H. *Macromolecules* **1983**, 16, 16.
171. Shin, K.; Pu, Y.; Rafailovich, M. H.; Sokolov, J.; Seech, O. H.; Sinha, S. K.; Tolan, M.; Kolb, R. *Macromolecules* **2001**, 34, 5620.
172. Shull, K. R. *Macromolecules* **1996**, 29, 8487.
173. Shull, K. R.; Winey, K. I.; Thomas, E. L.; Kramer, E. J. *Macromolecules* **1991**, 24, 2748.
174. Sirard, S. M.; Castellanos, H. J.; Hwang, H. S.; Lim, K. T.; Johnston, K. P. *Ind. Eng. Chem. Res.* **2004**, 43, 525.
175. Sirard, S. M.; Green, P. F.; Johnston, K. P. *J. Phys. Chem. B* **2001**, 105, 766.

176. Sirard, S. M.; Gupta, R. R.; Russell, T. P.; Watkins, J. J.; Green, P. F.; Johnston, K. P. *Macromolecules* **2003**, 36, 3365.
177. Sirard, S. M.; Ziegler, K. J.; Sanchez, I. C.; Green, P. F.; Johnston, K. P. *Macromolecules* **2002**, 35, 1928.
178. Soles, C. L.; Douglas, J. F.; Wu, W.-L. *Macromolecules* **2004**, 37, 2901.
179. Soles, C. L.; Douglas, J. F.; Wu, W.-L. *J. Polym. Sci. B: Polym. Phys.* **2004**, 42, 3218.
180. Spatz, J. P.; Sheiko, S.; Moller, M. *Macromolecules* **1996**, 29, 3220.
181. Strubinger, J. R.; Parcher, J. F. *Anal. Chem.* **1989**, 61, 951.
182. Strubinger, J. R.; Song, H.; Parcher, J. F. *Anal. Chem.* **1991**, 63, 98.
183. Stuhn, B. *J. Polym. Sci. B: Polym. Phys.* **1992**, 30, 1013.
184. Sundararajan, N.; Yang, S.; Ogino, K.; S., V.; Wang, J.; Zhou, X.; Ober, C. K. O., S. K.; Allen, R. D. *Chem. Mater.* **2000**, 12, 41.
185. Sundrani, D.; Darling, S. B.; Sibener, S. J. *Langmuir* **2004**, 20, 5091.
186. Taylor, D. K.; Carbonell, R.; Desimone, J. M. *Annu. Rev. Energy Environ.* **2000**, 25, 115.
187. Thurn-Albrecht, T.; Schotter, J.; Kastle, G. A.; Emley, N.; Shibauchi, T.; Krusin-Elbaum, L.; Guarini, K.; Black, C. T.; Tuominen, M. T.; Russell, T. P. *Science* **2000**, 290, 2126.
188. Tompkins, H. G.; McGahan, W. A., *Spectroscopic ellipsometry and reflectometry*. Wiley: New York, **1999**.
189. Turner, M. S.; Rubinstein, M.; Marques, C. M. *Macromolecules* **1994**, 27, 4986.
190. Van Krevelen, D. W., *Properties of Polymers*. Elsevier: **1976**.
191. Villar, M. A.; Rueda, D. R.; Ania, F.; Thomas, E. L. *Polymer* **2002**, 43, 5139.
192. Vogt, B. D.; Brown, G. D.; RamachandraRao, V. S.; Gupta, R. R.; Lavery, K. A.; Francis, T. J.; Russell, T. P.; Watkins, J. J. *Macromolecules* **2003**, 36, 4029.
193. Vogt, B. D.; Brown, G. D.; RamachandraRao, V. S.; Watkins, J. J. *Macromolecules* **1999**, 32, 7907.

194. Vogt, B. D.; Soles, C. L.; Jones, R. L.; Wang, C. Y.; Lin, E. K.; Wu, W. L.; Satija, S. K. *Langmuir* **2004**, 20, 5285.
195. Volkmuth, W. D.; Austin, R. H. *Nature* **1992**, 358, 600.
196. Wang, X.; Sanchez, I. C. *Submitted to Langmuir* **2006**.
197. Watkins, J. J.; Brown, G. D.; RamachandraRao, V. S.; Pollard, M. A.; Russell, T. P. *Macromolecules* **1999**, 32, 7737.
198. Webber, G. B.; Wanless, E. J.; Armes, S. P.; Baines, F. L.; Biggs, S. *Langmuir* **2001**, 17, 5551.
199. Webber, G. B.; Wanless, E. J.; Butun, V.; Armes, S. P.; Biggs, S. *Nano Letters* **2002**, 2, 1307.
200. Webber, S. E. *J. Phys. Chem. B* **1998**, 102, 2618.
201. Weibel, G. L.; Ober, C. K. *Microelectronic Engineering* **2003**, 2003, 145.
202. Weidner, E.; Wiesmet, V.; Knez, Z.; Skerget, M. *J. Supercritical Fluids* **1997**, 10, 139.
203. Whitmore, M. D.; Noolandi, J. *J. Chem. Phys.* **1990**, 93, 2946.
204. Whitmore, M. D.; Vavasour, J. D. *Macromolecules* **1992**, 25, 2041.
205. Wissinger, R. G.; Paulaitis, M. E. *J. Poly. Sci. B: Polym. Phys.* **1987**, 25, 2497.
206. Wu, S., *Polymer Interface and Adhesion*. Marcel Dekker: New York, **1982**.
207. Xie, B.; Finstad, C. C.; Muscat, A. J. *Chem. Mater.* **2005**, 17, 1753.
208. Xie, B.; Muscat, A. J. *Microelectronic Engineering* **2004**, 76, 52.
209. Xu, T.; Hawker, C. J.; Russell, T. P. *Macromolecules* **2005**, 38, 2802.
210. Yeo, S. D.; Erdogan, K. *Journal of Supercritical Fluids* **2005**, 34, 287.
211. Yoon, J.; Lee, W.; Thomas, E. L. *MRS Bulletin* **2005**, 30, 721.
212. Zeman, L.; Patterson, D. *Macromolecules* **1972**, 5, 513.
213. Zhang, F.; Chen, Y.; Huang, H.; Hu, Z.; He, T. *Langmuir* **2003**, 19, 5563.
214. Zhang, F.; Huang, H.; Hu, Z.; Chen, Y.; He, T. *Langmuir* **2003**, 19, 10100.

215. Zhang, L.; Eisenberg, A. *J. Am. Chem. Soc.* **1996**, 118, 3168.
216. Zhang, X.; Pham, J. Q.; Martinez, H. J.; Wolf, J.; Green, P. F.; Johnston, K. P. *J. Vac. Sci. Technol. B.* **2003**, 21, 2569.
217. Zhang, X.; Pham, J. Q.; Ryza, N.; Green, P. F.; Johnston, K. P. *J. Vac. Sci. Technol. B.* **2004**, 22, 818.
218. Zhang, Y.; Gangwani, K. K.; Lemert, R. M. *J. Supercritical Fluids* **1997**, 11, 115.
219. Zhang, Z.; Handa, P. Y. *Macromolecules* **1997**, 30, 8505.
220. Zhao, N.; Xie, Q.; Weng, L.; Wang, S.; Zhang, X.; Xu, J. *Macromolecules* **2005**, 38, 8996.
221. Zhou, L.; Bai, S.; Su, W.; Yang, J.; Zhou, Y. *Langmuir* **2003**, 19, 2683.
222. Zhu, L.; Cheng, S. Z. D.; Calhoun, B. H.; Ge, Q.; Quirk, R. P.; Thomas, E. L.; Hsiao, B. S.; Yeh, F.; Lotz, B. *Polymer* **2001**, 42, 5829.
223. Zhulina, E. B.; Adam, M.; LaRue, I.; Sheiko, S. S.; Rubinstein, M. *Macromolecules* **2005**, 38, 5330.
224. Ziemelis, K. *Nature* **1998**, 393, 619.

Vita

Yuan Li was born on July 1st, 1980 in Qianjiang, Hubei, China, the daughter of Yixin Li and Ping Huang. She moved with her family to Jingzhou, Hubei in August 1994 and enrolled at Jingzhou High School. In September 1997, she was admitted to Peking University, Beijing, with the exemption from the national college entrance examination. After graduating with a Bachelor of Science degree in Chemistry in July 2001, she came to the USA in August 2001 and entered the graduate school at the Ohio State University. In August 2002, she transferred to the graduate program of Materials Science and Engineering at the University of Texas at Austin. In May 2006, she received the Master of Science and Engineering degree in Materials Science and Engineering.

Permanent address: 6th floor, #1, Building 6, 85 Jingzhong Road, Jingzhou District, Jingzhou, Hubei, China, 434100

This dissertation was typed by the author.